Flavour Physics with (semi)leptonic Decays at Forward Spectrometers

---

Dissertation

zur

Erlagung der naturwissenschaftlichen Doktorwürde

(Dr. sc. nat.)

vorgelegt der

Mathematisch-naturwissenschaftlichen Fakultät

der

Universität Zürich

von

Elena Graverini

aus

Italien

Promotionskommission

Prof. Dr. Ulrich Straumann (Leitung der Dissertation)
Prof. Dr. Nicola Serra
Prof. Dr. Olaf Steinkamp
Dr. Barbara Storaci
Prof. Dr. Andrey Golutvin (Externer Gutachter)

Zürich, 2018

Abstract

Particle physics is going through a very unusual and intriguing period. All particles predicted by the Standard Model (SM) have been found; nevertheless, strong experimental evidence suggests that some pieces of the puzzle are still missing. The key issue addressed in this thesis is the use of flavour physics to shed light on the yet unknown components of matter. Three different projects are reported on. The first is a detailed simulation of the behaviour of hidden particles predicted by some of the most acknowledged New Physics theories, aimed at estimating the discovery potential of a newly proposed beam dump experiment, Search for HIdden Particles (SHiP). SHiP is aimed at looking for weakly interacting hidden particles, and has the unique capability of providing the combination of energy and intensity required to probe the validity of several theories designed to explain most of the currently not understood phenomena. The work presented here assesses SHiP's sensitivity to Heavy Neutral Leptons (HNL) and Dark Photons, and explores its possible synergy with a Future Circular Collider (FCC) experiment in the search for HNLs.

Another possible way to look for new physics exists. One can challenge the Standard Model by testing the properties of known particles up to very high precision. LHCb is a forward spectrometer dedicated to the study of flavour-changing processes at the Large Hadron Collider (LHC), and it is the experiment the second and third projects reported here focus on. The second project addresses the challenges of operating a high-precision silicon microstrip tracker, such as the one used by LHCb, in the remarkably radioactive environment of the LHC. This thesis describes two methods to monitor the evolution of silicon properties due to radiation damage, reporting in particular on the outcome of dedicated Charge Collection Efficiency (CCE) scans performed at regular intervals during the LHCb operation. The results are compared to the predicted evolution of the detector properties based on phenomenological models, proving that the ageing of the LHCb Silicon Tracker is under control.

The universality of lepton flavour is arguably one of the most interesting consequences of the Standard Model. Contrary to this prediction, recently published results suggest that the three generations of fermions may behave slightly differently. These anomalies detected in the flavour sector sparked interest for the analysis of semileptonic $b \to c\ell\bar{\nu}_\ell$ transitions. The last project described in this thesis undertakes the first study of Lepton Flavour Universality (LFU) in a baryonic occurrence of this transition, analysing the $\Lambda_b \to \Lambda_c^*\ell\bar{\nu}_\ell$ decay. The ratio $R\left(\Lambda_c^*\right)$ between the rate of semitauonic and that of semimuonic transitions is a powerful probe for LFU. In this thesis, preparatory studies defining the strategy for such an analysis are described, and the level of background due to faulty identification of particles and to their incorrect combination is evaluated. A SM calculation predicting the value of the $R\left(\Lambda_c^*\right)$ ratio

is not available yet, due to lack of information on the hadronic component of the underlying processes. Therefore, another study is presented, aimed at providing all the necessary experimental and theoretical ingredients to calculate $R\left(\Lambda_c^*\right)$ in the SM. The measurement of the form factor parameters governing the $\Lambda_b \to \Lambda_c^*$ transition would enable a precise estimation of $R\left(\Lambda_c^*\right)$. The sensitivity of such a measurement is reported here, together with an estimate of the resulting uncertainty on the theoretical value of $R\left(\Lambda_c^*\right)$.

Zusammenfassung

Die Teilchenphysik durchläuft eine sehr ungewöhnliche und faszinierende Zeit. Alle von dem Standardmodell (SM) vorhergesagten Teilchen wurden gefunden; dennoch deuten starke experimentelle Befunde darauf hin, dass einige Teile des Puzzles noch fehlen. Das zentrale Thema dieser Arbeit ist der Einsatz der Flavour-Physik, um Licht auf die noch unbekannten Komponenten der Materie zu werfen. Es wird über drei verschiedene Projekte berichtet. Das Erste ist eine detaillierte Simulation des Verhaltens von versteckten Teilchen, die von einigen der anerkanntesten Theorien der neuen Physik vorhergesagt werden, mit dem Ziel, das Entdeckungspotential eines neu vorgeschlagenen Strahldump-Experiments, Search for HIdden Particles (SHiP), zu ermitteln. SHiP zielt auf die Suche nach schwach wechselwirkenden, verborgenen Teilchen ab, und hat das einzigartige Potential, die Kombination aus Energie und Intensität zu liefern, die erforderlich ist, um die Gültigkeit von einigen dieser Theorien zu untersuchen, die die meisten derzeit nicht verstandenen Phänomene erklären würden. Die hier vorgestellte Arbeit bewertet SHiPs Sensitivität für Heavy Neutral Leptons (HNL) und Dark Photons und untersucht die mögliche Synergie mit einem Future Circular Collider (FCC) Experiment auf der Suche nach HNLs.

Es gibt eine andere Möglichkeit, nach neuer Physik zu suchen. Man kann dass Standardmodell überprüfen, indem man die Eigenschaften bekannter Teilchen mit sehr hoher Präzision testet. LHCb ist ein Vorwärtsspektrometer, das sich der Erforschung von Flavour-changing Processes am Large Hadron Collider (LHC) widmet, und es ist das Experiment, auf das sich das zweite und dritte Projekt, über das hier berichtet wird, konzentriert. Das zweite Projekt befasst sich mit den Herausforderungen, die der Betrieb eines hochpräzisen Silizium-Microstrip-Spurdetektors in der bemerkenswert radioaktiven Umgebung des LHC mit sich bringt. Diese Arbeit beschreibt zwei Methoden zur Überwachung der Entwicklung von Silizium-Eigenschaften aufgrund von Strahlenschäden und berichtet insbesondere über die Ergebnisse von dedizierten Ladungserfassungs-Effizienz-Scans, die in regelmäßigen Abständen während des LHCb-Betriebs durchgeführt werden. Die Ergebnisse werden mit der vorhergesagten Entwicklung der Detektoreigenschaften verglichen, die auf phänomenologischen Modellen basieren und beweisen, dass die Alterung des LHCb Silizium-Spurdetektors unter Kontrolle ist.

Die Flavour-Universalität der Leptonen ist eine der Interessantesten Konsequenz der Standardmodells. Entgegen dieser Voraussage, deuten kürzlich veröffentlichte Ergebnisse darauf hin, dass sich die drei Generationen von Fermionen leicht unterschiedlich verhalten. Diese im Flavour-Sektor entdeckte Anomalien weckten Interesse für die Analyse semileptonischer $b \to c\ell\bar{\nu}_\ell$ Übergänge. Das letzte Projekt, das in dieser Arbeit beschrieben wird, führt die

erste Studie der leptonischen Flavour-Universalität (LFU) in einem baryonischen Auftreten dieses Übergangs durch und analysiert den Zerfall von $\Lambda_b \to \Lambda_c^* \ell \bar{\nu}_\ell$. Das $R\left(\Lambda_c^*\right)$-Verhältnis zwischen der Rate der semi-tauonischen und der Rate der semi-myonischen Übergänge ist eine wichtiger Test der LFU. In dieser Arbeit werden Vorstudien, die die Strategie für eine solche Analyse definieren, beschrieben und der Hintergrund aufgrund fehlerhafter Identifikation von Teilchen und deren falschen Kombinationen evaluiert. Eine SM-Rechnung, die den Wert des $R\left(\Lambda_c^*\right)$-Verhältnisses vorhersagt, ist noch nicht verfügbar, da keine Information über die hadronische Komponente der zugrunde liegenden Prozesse vorliegt. Daher wird eine weitere Studie vorgestellt, die darauf abzielt, alle notwendigen experimentellen und theoretischen Zutaten für die Berechnung von $R\left(\Lambda_c^*\right)$ im SM bereitzustellen. Die Messung der Formfaktor-Parameter für den $\Lambda_b \to \Lambda_c^*$ Übergang würde eine präzise Schätzung von $R\left(\Lambda_c^*\right)$ ermöglichen. Die Sensitivität einer solchen Messung wird hier angegeben, zusammen mit einer Schätzung der daraus resultierenden Unsicherheit des theoretischen Wertes von $R\left(\Lambda_c^*\right)$.

Contents

CHAPTER 1

Introduction

Contents

The Standard Model (SM) of particle physics is a self-consistent and elegant theory describing our knowledge of particle interactions at the sub-nuclear level. Describing most physics phenomena with great precision, the SM has been standing for over 30 years as "the" theory of particle physics, with experiments validating it to a remarkable degree. The most recent, compelling experimental confirmation of a SM prediction came to light with the discovery of a Higgs boson-like particle, jointly announced by the CMS and ATLAS collaborations in 2012 [1, 2].

However, the SM is unable to accomodate all phenomena observed in nature. We can estimate from cosmological observation that a striking 96% of the energy in the Universe is not accounted for by the SM. About 27% of the unforeseen energy is observed to interact gravitationally, but not electromagnetically nor through weak interaction. As these particles do not emit any light, we call them Dark Matter. The remaining 68%, referred to as Dark Energy (DE), seems to have gravitational effects only on a global scale, influencing the expansion rate of the universe. Gravity, itself, does not fit into the SM formalism. And, what is more, it is unclear how the "ordinary" 4% of energy content of the universe that is nicely described by the SM survived the matter-antimatter annihilation processes that took place just after the Big Bang: charge-parity (CP) violation, the mechanism responsible for the asymmetry between matter and antimatter, can occur in the SM, but only up to a level about 10 orders of magnitude smaller than what would be required to explain the observed proportion between matter and antimatter [3]. In addition, evidence for neutrino oscillation [4] prove that neutrinos have non-zero mass, contrary to what predicted by the SM. All of these observations provide compelling arguments to state that the SM is not a complete theory; a number of theoretical puzzles, as well, like the apparent *fine-tuning* of the mass of the Higgs boson, suggest that we are still short of a more fundamental description.

This thesis focusses on the search for new particles that could complement the SM and provide for all or part of its shortcomings. These particles can be searched for in the product

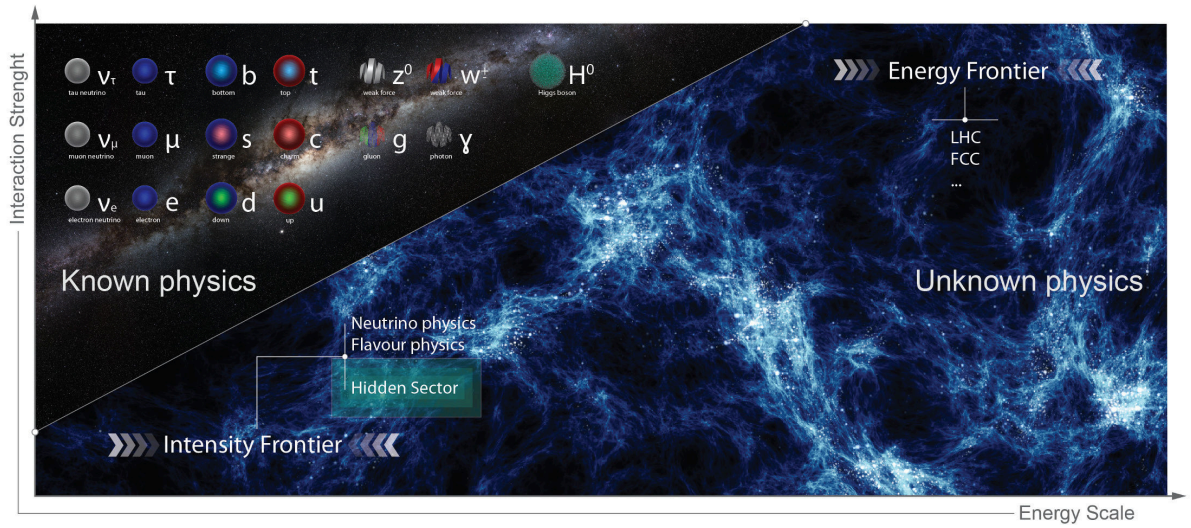

Figure 1.1: Sketch depicting the search for new particles at the intensity and energy frontiers. Courtesy of R. Jacobsson and D. Dominguez [8].

of decays of – or collisions among – known particles. However, particle physics experiments have not seen any new particle as of today. Hence, if such new particles exist, the strenght of their interaction with SM particles must be very small: therefore we need an enormous amount of decay or collision events in order to detect their signal. This kind of search has a limit: new particles can only be produced if their mass is smaller than the energy available in the production process. The search for light, weakly interacting unknown particles is central to Part I of this thesis, which describes the proposed SHiP experiment [5] and its physics reach.

Yet, there is another possible way to look for new particles: one can examine SM processes in detail and compare measured quantities to those that the SM predicts. If a new particle happens to be involved in these processes as a virtual mediator[1], we can expect some measured observables to differ from the corresponding theory predictions. This approach is sensitive to a slightly different kind of hidden particles: their coupling to the SM should be sizeable, otherwise their effect would be too small to be seen; in the case of virtual particles, however, their mass can be very high, as they are not bound to be on shell. In fact, if these particles had small mass (order of few to hundred GeV) and sizeable coupling, most likely they would have already been detected by past or current experiments.

We refer to these two approaches as *intensity frontier* and *energy frontier*, respectively. Figure 1.1 depicts an artist's representation of the landscape for the search of new particles.

Quarks and leptons, the fundamental fermions of the SM, exist in three generations, differing only in mass. Each generation contains two members: the three charged leptons e, μ and τ are paired with a very low mass, electrically neutral counterpart, the ν_e, ν_μ and ν_τ neutrinos,

[1] We call *mediator* or *virtual particle* a particle that borrows energy from vacuum for a time short enough to preserve the Heisenberg Uncertainty Principle [6], being allowed to be off-shell. For further details see *e.g.* [7].

respectively; similarly, each generation of quarks contains an up- and a down-type quark. The property that distinguishes the fundamental fermions from one another is called "flavour". The only known difference between the three generations of fermions is mass, emerging from Yukawa couplings between the fermions and the Higgs field. The Yukawa couplings are also responsible for all interactions that transform a quark flavour into another. Section 1.1 will give an overview of flavour physics in the SM.

LHCb [9] is a forward spectrometer operating at the LHC accelerator, dedicated to the study of flavour changing processes. Thanks to the high energy of the LHC collisions, it has access to a large number of hadrons containing heavy flavoured quarks. Part II of this thesis focusses on the LHCb experiment. In particular, Chapter 6 concentrates on the LHCb Silicon Tracker (ST), showing the possible problems connected with operating a detector in the high-radiation environment of the LHC, and describing how to monitor its performance.

One of the fundamental properties of the SM is that the interactions of charged leptons differ only up to kinematic effects due to their different masses. This concept is referred to as Lepton Universality (LU). Precision tests of LU have been performed by many experiments. While the analyses of processes involving only the first two generation of leptons and quarks yielded results compatible with the Standard Model, recent studies on processes involving heavier flavours resulted in a 4 σ tension with the assumption of LU, seemingly favouring *e.g.* tau couplings with respect to those of lower mass leptons. This problem is taken on in Chapter 7, that reports on preliminary studies of $\Lambda_b \to \Lambda_c^* \ell \nu$ decays aimed at further testing the assumption of Lepton Universality in the SM. Chapter 8 then presents a work aimed at determining a parametrization for the hadronic interaction involved in the $\Lambda_b \to \Lambda_c^*$ transition, and assesses the sensitivity of LHCb to the numerical values of the parameters of this model.

1.1. Flavour physics in the Standard Model

In the Standard Model all of the fundamental fermions obtain their masses through Yukawa couplings to the Higgs field[2]. The Higgs mechanism is described by the Lagrangian

$$\mathcal{L}_{\text{Higgs}} = -\left(D_\mu \phi\right)^\dagger \left(D^\mu \phi\right) - V\left(\phi^\dagger \phi\right) + \mathcal{L}_Y, \tag{1.1}$$

where:

- $\phi = \begin{pmatrix} \phi^+ \\ \phi^0 \end{pmatrix}$ represents the Higgs doublet, composed of an electrically charged (ϕ^+) and an electrically neutral (ϕ^0) scalar field,
- $-\left(D_\mu \phi\right)^\dagger \left(D^\mu \phi\right)$ is a kinetic term,

[2] This section is written following the approach of [10, 11].

- $V\left(\phi^\dagger\phi\right)$ is the Higgs potential, and
- $\mathcal{L}_Y$ is the Lagrangian describing the Yukawa interactions, described in the following.

The Higgs potential is described by

$$V\left(\phi^\dagger\phi\right) = \lambda\left(\phi^\dagger\phi\right)^2 - \mu^2\left(\phi^\dagger\phi\right) + \frac{\mu^4}{4\lambda}, \tag{1.2}$$

where λ is the Higgs self-coupling and μ is the Higgs mass parameter. The minimum of this potential changes according to the value of the complex parameter μ: if $\mu^2 < 0$, the minimum is attained at $\phi = 0$, around which the electroweak Lagrangian is symmetric; for $\mu^2 > 0$, the minimum shifts to

$$|\phi| = \sqrt{\frac{\mu^2}{2\lambda}}, \tag{1.3}$$

which breaks the symmetry of the electroweak Lagrangian. As the point $\phi = 0$ is not stable against quantum fluctuations, the expectation value of the Higgs field in vacuum is $\langle|\phi|\rangle = \sqrt{\mu^2/2\lambda} \equiv v/\sqrt{2}$, spontaneously breaking the electroweak symmetry. The parameter v, called the vacuum expectation value (vev), was measured to be $v = 246$ GeV [12]. The v parameter also represents the "electroweak scale", *i.e.* the scale at which electroweak symmetry is broken. Performing an arbitrary change of coordinates, we can choose the represent the vev as

$$\langle\phi\rangle = \frac{1}{\sqrt{2}}\begin{pmatrix} 0 \\ v \end{pmatrix} \tag{1.4}$$

This choice is referred to as "unitary gauge". The physical Higgs boson corresponds in this gauge to a neutral scalar field produced by excitations around this minimum, represented in the unitary gauge by:

$$\phi = \frac{1}{\sqrt{2}}\begin{pmatrix} 0 \\ v + H \end{pmatrix}. \tag{1.5}$$

While the Yukawa Lagrangian for interactions between the Higgs doublet and a charged lepton ℓ is generically defined as

$$\mathcal{L}_Y^\ell = -g_\ell\left(\bar{\ell}_L\phi\ell_R + \bar{\ell}_R\phi^\dagger\ell_L\right), \tag{1.6}$$

in unitary gauge this becomes

$$\mathcal{L}_Y^\ell = -\frac{1}{\sqrt{2}}vg_\ell\left(\bar{\ell}_L\ell_R + \bar{\ell}_R\ell_L\right) = -\frac{1}{\sqrt{2}}vg_\ell\left(\bar{\ell}\ell\right), \tag{1.7}$$

where $\ell_{L,R}$ are the left- and right-handed components of the lepton field and g_ℓ is the magnitude of the Yukawa coupling between the Higgs field and the lepton ℓ. A leptonic mass term of

$$m_\ell = \frac{1}{\sqrt{2}} v g_\ell \tag{1.8}$$

arises from this Lagrangian. Similarly, in this gauge the Yuakawa interaction Lagrangian for quarks can be written as:

$$\mathcal{L}_Y^q = -\bar{u}_{Li} m_{ij}^u u_{Rj} - \bar{d}_{Li} m_{ij}^d d_{Rj} + \text{h.c.}, \tag{1.9}$$

where the indices i, j run over the three quark generations, u and d represent the up- and down-type components of the quark doublets, and L and R represent the left- and right-handed components of the quark fields. Mass matrices for the up- and down-type quarks arise in this parametrisation and are represented by the m_{ij}^u and m_{ij}^d notations, respectively. As the $\mathcal{L}_Y^q$ Lagrangian represents flavour interactions, the mass matrices are built in the flavour basis. They contain off-diagonal terms to account for flavour-changing interactions, and therefore they do not directly represent the mass basis. To diagonalize these matrices and move into the mass basis, we introduce four unitary matrices $V_{L,R}^{u,d}$, obtaining:

$$M_u = V_L^{u\dagger} m_u V_R^u \tag{1.10}$$

$$M_d = V_L^{d\dagger} m_d V_R^d \tag{1.11}$$

where M_u and M_d are now diagonal matrices and have the form

$$M_u = \begin{pmatrix} m_u & 0 & 0 \\ 0 & m_c & 0 \\ 0 & 0 & m_t \end{pmatrix}, \tag{1.12}$$

$$M_b = \begin{pmatrix} m_d & 0 & 0 \\ 0 & m_s & 0 \\ 0 & 0 & m_b \end{pmatrix}. \tag{1.13}$$

In the flavour basis, the Lagrangians for weak interactions between the quarks and the $W^\pm$ bosons ($\mathcal{L}_{CC}$) and between the quarks and the Z^0 boson ($\mathcal{L}_{NC}$) can be written as[3]:

$$\mathcal{L}_{CC} = \frac{i g_2}{\sqrt{2}} \left(W_\mu^+ \bar{u}_{Lj} \gamma^\mu d_{Lj} + W_\mu^- \bar{d}_{Lj} \gamma^\mu u_{Lj} \right) \tag{1.14}$$

$$\mathcal{L}_{NC} = \frac{i g_2}{\sqrt{2}} \left(Z_\mu \bar{u}_{Lj} \gamma^\mu u_{Lj} + Z_\mu \bar{d}_{Lj} \gamma^\mu d_{Lj} \right) \tag{1.15}$$

[3] In this notation, *CC* and *NC* stand for "charged current" and "neutral current" interations, respectively.

where g_2 is the weak coupling strenght and $W_\mu^\pm$ and Z_μ represent the charged and neutral currents associated to the $W^\pm$ and Z^0 bosons, respectively. In order to rotate onto the mass basis, we insert the diagonalization matrices as follows:

$$\mathcal{L}_{CC} = \frac{ig_2}{\sqrt{2}} \left[W_\mu^+ \bar{u}_{Lj} \left(V_L^u V_L^{d\dagger} \right) \gamma^\mu d_{Lj} + W_\mu^- \bar{d}_{Lj} \left(V_L^d V_L^{u\dagger} \right) \gamma^\mu u_{Lj} \right] \tag{1.16}$$

$$\mathcal{L}_{NC} = \frac{ig_2}{\sqrt{2}} \left[Z_\mu \bar{u}_{Lj} \left(V_L^u V_L^{u\dagger} \right) \gamma^\mu u_{Lj} + Z_\mu \bar{d}_{Lj} \left(V_L^d V_L^{d\dagger} \right) \gamma^\mu d_{Lj} \right]. \tag{1.17}$$

The product $V_L^u V_L^{d\dagger} \equiv V_{CKM}$ intervening in charged-current interactions is called Cabibbo-Kobayashi-Maskawa (CKM) matrix [13] and transforms between the flavour and mass quark eigenstates:

$$\begin{pmatrix} d' \\ s' \\ b' \end{pmatrix} = \begin{pmatrix} V_{ud} & V_{us} & V_{ub} \\ V_{cd} & V_{cs} & V_{cb} \\ V_{td} & V_{ts} & V_{tb} \end{pmatrix} \begin{pmatrix} d \\ s \\ b \end{pmatrix}, \tag{1.18}$$

with d, s, b and d', s', b' representing the flavour and mass eigenstates, respectively. The off-diagonal elements of the CKM matrix are non-zero, hence weak charged current interactions couple quarks with different flavours. The CKM matrix can be written in the so-called Wolfenstein parametrisation [14]:

$$\begin{pmatrix} V_{ud} & V_{us} & V_{ub} \\ V_{cd} & V_{cs} & V_{cb} \\ V_{td} & V_{ts} & V_{tb} \end{pmatrix} = \begin{pmatrix} 1 - \lambda^2/2 & \lambda & 0 \\ -\lambda & 1 - \lambda^2/2 & A\lambda^2 \\ 0 & -A\lambda^2 & 1 \end{pmatrix} + O\left(\lambda^3\right), \tag{1.19}$$

where A is a parameter of order 1 and λ represents the Cabibbo angle[4]. The CKM matrix has thus a peculiar hierarchical structure, with elements closer to its diagonal much larger than those further off.

Due to the unitarity of the $V_{L,R}^{u,d}$ rotation matrices, the products $V_L^u V_L^{u\dagger}$ and $V_L^d V_L^{d\dagger}$ intervening in the neutral current interaction Lagrangian are both identity. Therefore, neutral current interactions conserve flavour.

1.2. Addressing the shortcomings of the Standard Model

We summarize here the main shortcomings of the theory that best describes our understanding of nature.

- Only about 4% of the energy content of the Universe undergoes interactions predicted

[4] In particular, $\lambda = \sin\theta_C \simeq 0.23$ [15], where θ_C is the Cabibbo angle, historically used to describe the rotation between flavour and mass basis before the third quark generation was discovered [16].

by the SM, the rest is not visible. There is evidence for Dark Matter (DM, 27% of the Universe' content) to be composed of particles, while the origin of Dark Energy (DE, the remaining 68%) is not clear [17].

- The SM does not incorporate gravity, one of the forces that governs our universe from very small scales to galatic interactions, until the Planck scale [18]. The latter, also called Grand Unification scale, is of the order $E_P = \sqrt{\hbar c^5/G} \approx 10^{19}$ GeV, where $\hbar$ is the reduced Planck constant, c is the speed of light and G is the gravitational constant.

- A source of CP violation arises from the $O\left(\lambda^3\right)$ terms of the CKM matrix. However, the observed abundance of matter as opposed to the scarcity of antimatter suggests that another source of CP violation should exist, about 10 times as large [3].

- Neutrino oscillations are now an established experimental fact [4], but they can only happen if neutrinos have mass. Neutrinos are massless in the SM.

Besides the tension between theory and the above mentioned experimental facts, there are a number of theoretical problems within the SM itself. The SM contains as many as 19 free parameters with no theoretical prediction; 13 of these lie in the Yukawa sector (*e.g.* the quark and lepton masses). These parameters happen to take values in an extremely wide range. The masses of the electron and of the top quark differ by a factor as large as 10^6. Theory cannot explain the reason for this huge difference, nor the underlying structure that causes the hierarchy of the CKM matrix and the existence of three generations of fundamental fermions. Another problem is related to the mass of the physical Higgs boson. While in vacuum this is determined only by the Higgs self-interaction, quantum corrections (*i.e.* interactions between the Higgs and the other fermions and gauge bosons) shift the Higgs mass by an amount that grows quadratically with increasing energy. Therefore, at high energy, the observed light mass of the Higgs boson can be obtained only if a substantial amount of cancellation happens between the quantum corrections and the Higgs self-interaction. A theory that requires its parameters to be fine-tuned for it to agree with experimental data is often referred to as "unnatural". It is in fact unclear whether such seemingly perfect fine tuning, together with the greatly varying magnitudes of the SM parameters, arises by chance[5] or if they are the only visible hints of an underlying, wider theory not yet developed.

Several theories or extensions to the SM were devised to cope with the unexplained phenomena and to try to attain a greater level of naturalness. These theories are often referred to as New Physics (NP) or Physics Beyond the SM (BSM). In particular, models that include a "hidden sector" (HS) of particles interacting very weakly with the SM through a mediator provide a natural explanation for Dark Matter. A minimalistic example is the νMSM [19], where three massive right-handed neutrinos complement the left-handed SM neutrinos, addressing all the known experimental shortcomings of the SM except gravity.

[5] Argument sometimes accepted as is, based upon the so-called "Anthropic Principle".

Depending on the masses and couplings of the right-handed neutrinos, the lightest one would provide a Dark Matter candidate in the keV region, while the two others, in the MeV - GeV range, would provide mass to the SM neutrinos through the seesaw mechanism, and generate the matter-antimatter asymmetry through leptogenesis. This theory is presented in detail in Section 2.1.1.

Modern experiments at the LHC hunt down NP by looking directly for undiscovered particles and discrepancies between measurements and the SM predictions. General purpose experiments like CMS [20] and ATLAS [21] are most suited to look directly for new particles, while a sigle-arm precision spectroscope like LHCb operates precision measurements to test SM predictions and search for possible contributions of virtual NP particles to B- and D-meson decays.

The fact that the SM is a self-consistent weakly coupled theory up to very high scale does not point to a particular energy scale for NP [22–24]. A possibility is that new particles are light, or in the same range as known particles, but they have a very feeble interaction with SM particles. To test this hypotesis, very high intensity beams are needed, allowing to look for very rare events. Fixed target experiments provide lower centre-of-mass energy, but allow to look for much rarer events with respect to circular collider, due to their much larger luminosity. The proposed SHiP experiment [5] has been devised in order to explore the HS at the intensity frontier, looking primarily for right-handed heavy neutrinos.

References

[1] Serguei Chatrchyan et al. “Observation of a new boson at a mass of 125 GeV with the CMS experiment at the LHC”. In: *Phys. Lett.* B716 (2012), pp. 30–61. DOI: 10.1016/j.physletb.2012.08.021. arXiv: 1207.7235 [hep-ex].

[2] Georges Aad et al. “Observation of a new particle in the search for the Standard Model Higgs boson with the ATLAS detector at the LHC”. In: *Phys. Lett.* B716 (2012), pp. 1–29. DOI: 10.1016/j.physletb.2012.08.020. arXiv: 1207.7214 [hep-ex].

[3] Glennys R. Farrar and M. E. Shaposhnikov. “Baryon asymmetry of the Universe in the standard model”. In: *Phys. Rev. D* 50 (2 July 1994), pp. 774–818. DOI: 10.1103/PhysRevD.50.774. URL: https://link.aps.org/doi/10.1103/PhysRevD.50.774.

[4] Y. Fukuda et al. “Evidence for oscillation of atmospheric neutrinos”. In: *Phys. Rev. Lett.* 81 (1998), pp. 1562–1567. DOI: 10.1103/PhysRevLett.81.1562. arXiv: hep-ex/9807003 [hep-ex].

[5] M. Anelli et al. “A facility to Search for Hidden Particles (SHiP) at the CERN SPS”. In: (2015). arXiv: 1504.04956 [physics.ins-det].

[6] Werner Heisenberg. “Über den anschaulichen Inhalt der quantentheoretischen Kinematik und Mechanik”. In: *Z. Phys.* 43 (1927), pp. 172–198. DOI: 10.1007/BF01397280.

[7] Mark Thomson. *Modern particle physics*. New York: Cambridge University Press, 2013. ISBN: 9781107034266. URL: http://www-spires.fnal.gov/spires/find/books/www?cl=QC793.2.T46::2013.

[8] "SHiP sets a new course in intensity-frontier exploration". In: *CERN Courier* 56.2 (Mar. 2016), pp. 25–27. URL: https://cds.cern.ch/record/2232554.

[9] A. Augusto Alves Jr. et al. "The LHCb Detector at the LHC". In: *JINST* 3 (2008), S08005. DOI: 10.1088/1748-0221/3/08/S08005.

[10] C. P. Burgess and G. D. Moore. *The standard model: A primer*. Cambridge University Press, 2006. ISBN: 9780511254857, 9781107404267, 9780521860369.

[11] Gregory Ciezarek and Mitesh Patel. "Searches for lepton number violation, and flavour violation beyond the Yukawa couplings at LHCb". Presented 10 Jun 2014. May 2014. URL: http://cds.cern.ch/record/1755654.

[12] Richard Keith Ellis, William James Stirling, and Bryan R Webber. *QCD and collider physics*. Cambridge monographs on particle physics, nuclear physics, and cosmology. Photography by S. Vascotto. Cambridge: Cambridge University Press, 2003. URL: https://cds.cern.ch/record/318585.

[13] Makoto Kobayashi and Toshihide Maskawa. "CP Violation in the Renormalizable Theory of Weak Interaction". In: *Prog. Theor. Phys.* 49 (1973), pp. 652–657. DOI: 10.1143/PTP.49.652.

[14] Lincoln Wolfenstein. "Parametrization of the Kobayashi-Maskawa Matrix". In: *Phys. Rev. Lett.* 51 (1983), p. 1945. DOI: 10.1103/PhysRevLett.51.1945.

[15] K. A. Olive et al. "Review of Particle Physics". In: *Chin. Phys.* C38 (2014), p. 090001. DOI: 10.1088/1674-1137/38/9/090001.

[16] Nicola Cabibbo. "Unitary Symmetry and Leptonic Decays". In: *Phys. Rev. Lett.* 10 (1963). [,648(1963)], pp. 531–533. DOI: 10.1103/PhysRevLett.10.531.

[17] P. A. R. Ade et al. "Planck 2015 results. XIII. Cosmological parameters". In: *Astron. Astrophys.* 594 (2016), A13. DOI: 10.1051/0004-6361/201525830. arXiv: 1502.01589 [astro-ph.CO].

[18] Joseph Polchinski. "Quantum gravity at the Planck length". In: *eConf* C9808031 (1998). [,209(1998)], p. 08. DOI: 10.1142/S0217751X99001329. arXiv: hep-th/9812104 [hep-th].

[19] Takehiko Asaka, Steve Blanchet, and Mikhail Shaposhnikov. "The nuMSM, dark matter and neutrino masses". In: *Phys. Lett.* B631 (2005), pp. 151–156. DOI: 10.1016/j.physletb.2005.09.070. arXiv: hep-ph/0503065 [hep-ph].

[20] S. Chatrchyan et al. "The CMS experiment at the CERN LHC". In: *JINST* 3 (2008), S08004. DOI: 10.1088/1748-0221/3/08/S08004.

[21] G. Aad et al. “The ATLAS Experiment at the CERN Large Hadron Collider”. In: *JINST* 3 (2008), S08003. DOI: 10.1088/1748-0221/3/08/S08003.

[22] Dario Buttazzo et al. “Investigating the near-criticality of the Higgs boson”. In: *JHEP* 12 (2013), p. 089. DOI: 10.1007/JHEP12(2013)089. arXiv: 1307.3536 [hep-ph].

[23] Giuseppe Degrassi et al. “Higgs mass and vacuum stability in the Standard Model at NNLO”. In: *JHEP* 08 (2012), p. 098. DOI: 10.1007/JHEP08(2012)098. arXiv: 1205.6497 [hep-ph].

[24] Fedor Bezrukov et al. “Higgs Boson Mass and New Physics”. In: *JHEP* 10 (2012), p. 140. DOI: 10.1007/JHEP10(2012)140. arXiv: 1205.2893 [hep-ph].

PART I

The intensity frontier: SHiP

CHAPTER 2

The proposed SHiP experiment

Contents

2.1. Introduction and physics case

SHiP is a newly proposed general purpose fixed target facility at the CERN SPS accelerator, with the aim of looking for very weakly interacting long living particles. The SHiP experiment setup is described in Section 2.2. The search for right-handed neutrinos, also known as Heavy Neutral Leptons (HNL) or Majorana neutrinos, represents its primary goal. A flux of 2×10^{20} proton-target collisions in five years of activity, together with a very large decay volume, will allow SHiP to probe a variety of New Physics models in largely unexplored region of the corresponding parameter spaces. The redundant system of background tagging detectors will make it a zero-background experiment and a very efficient tool to discover light hidden particles produced in decays of charm mesons. The peculiar layout of the SHiP facility also make it a Standard Model neutrino factory. Therefore, a dedicated detector (nicknamed νSHiP) will be installed, that will offer the first opportunity to discover the tau antineutrino $\bar{\nu}_\tau$ and allow to perform measurements of active neutrino cross-sections and angular distributions [1, 2]. The νSHiP detector is also well suited to search for Light Dark Matter (LDM) in the sub-GeV region, looking for hints of LDM particles produced by decay of virtual dark photon or scattering off electrons and nuclei of the detector itself [3]. Finally, the large amount of τ leptons produced at the SHiP target suggests that an additional facility nicknamed τSHiP could be installed at the SHiP beam dump. This would allow to search for the Lepton Flavour

violating decay $\tau \rightarrow 3\mu$ with a sensitivity of 10^{-10} or better.

Chapter 3 focusses on studies of the SHiP sensitivity to sterile neutrinos and to dark photons. Sections 2.1.1 and 2.1.2 will introduce these two physics scenarios.

The author's contributions to the SHiP experiment are described in Section 2.3 and in Chapter 3. In particular, the author developed a fast Monte Carlo simulation to study the sensitivity of the SHiP experiment to HNLs and to dark photons (Sections 3.1.1 and 3.3). These studies have been verified and complemented with the analysis of HNL signal simulated by means of the full SHiP simulation (Section 3.1.2). The latter allowed to devise a set of offline selections capable of maintaining the level of background lower than 0.1 event candidates in 5 years of operation, while retaining high efficiency for signal events (Sections 3.1.3-3.1.4). The author also contributed to the design of the experiment by optimizing the shape of the vacuum vessel (Section 2.3), and implementing the physics of HNLs in the SHiP simulation framework (Section 3.1.2).

2.1.1. Sterile neutrinos in the νMSM

The "Neutrino Minimal Standard Model" (νMSM) is a minimalistic model that attempts at explaining the pattern of neutrino masses, dark matter and the matter-antimatter asymmetry observed in the present Universe by introducing three Heavy Neutral Leptons (HNLs) [4, 5]. These states are SU(2) × U(1) singlets, insensitive to the electroweak interaction (thus the *sterile* nickname). Therefore, the SM lagrangian would extend to:

$$\mathcal{L} = \mathcal{L}_{SM} + \bar{N}_i i\partial\!\!\!/ N_i - f_{i\alpha}\Phi\bar{N}_i L_\alpha - \frac{M_i}{2}\bar{N}_i N_i + h.c. \tag{2.1}$$

where Φ and $L_\alpha(\alpha = e, \mu, \tau)$ are respectively the Higgs and lepton doublets, f is a matrix of Yukawa couplings and M_i is a Majorana mass term. N_i represents the sterile neutrino fields.

As the Majorana masses are assumed to be of the order of the electroweak scale or below, the model can only be consistent with the neutrino experiments if the Yukawa couplings are very small, $f_i^2 \sim O(m_\nu M_i/v^2)$, where m_ν are the masses of active neutrinos and v is the vacuum expectation value of the Higgs field [5]. Hereinafter, as often in literature, the mixing couplings f_i^2 will be referred to as U_α^2, with $\alpha = e, \mu, \tau$.

One of the new states, N_1, is a dark matter (DM) candidate with lifetime possibly greater than the age of the Universe, and a mass of O(keV) [6]. This hypothesis can be verified by looking for a monochromatic line coming from the decay $N_1 \rightarrow \nu\gamma$. A possible hint of such a decay was recently reported in [7, 8], but it is not clear yet if this signal could be attributed to other astrophisical sources. The other two HNLs are degenerate in mass, with m_N in the MeV-GeV range, and are responsible for the baryon-antibaryon asymmetry of the Universe through a process of leptogenesis made possible by their lepton number violating Majorana mass term [5, 9–11]. The two heavy states also allow for the observed pattern of neutrino masses through the type I see-saw mechanism, first introduced in the context of Grand Unified

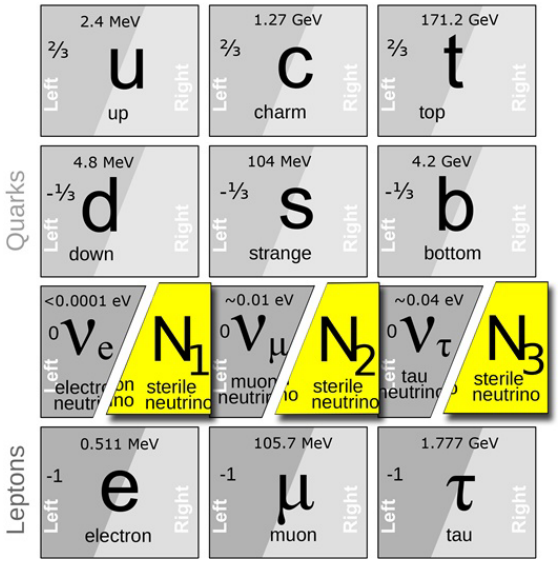

Figure 2.1: The SM foresees massless and only left-handed neutrinos. In the νMSM, three right-handed counterparts N_1, N_2 and N_3 are added to the particle content of the SM [2].

Theories [12–15], made possible by the cohexistence of Dirac and Majorana mass terms.

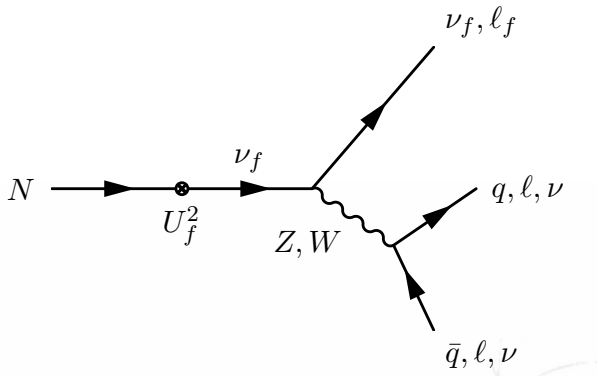

Figure 2.2: Decay of a HNL through mixing with a SM neutrino.

The phenomenology of sterile neutrino production is described in [16–20]. HNLs can be produced in decays where a SM neutrino is replaced by an HNL through kinetic mixing. They then decay to SM particles by mixing again with a SM neutrino. These massive neutrino states can decay to a variety of final states through the emission of a $W^{\pm}$ or Z^0 boson (see Figure 2.2). Branching ratios for the production and decay of HNLs can be obtained from the Dirac neutrino case [21] as shown in [17] and reported in Appendix A.

2.1.2. Dark Photons

A variety of NP models that naturally explain DM predict the existence of an hidden sector of particles which are singlet under the SM gauge group. These SM-neutral, unobserved particles do not interact with SM particles, except through a "messenger" particle belonging to the hidden sector. Minimalistic models consist of a $U(1)'$ gauge symmetry in the hidden sector, whose gauge boson γ' is called a *dark photon*. If $U(1)'$ is broken by a Higgs-like mechanism, the dark photon can acquire a non-zero mass.

The SM Lagrangian $\mathcal{L}_{SM}$ can be extended to:

$$\mathcal{L} = \mathcal{L}_{SM} - \frac{1}{4}F'_{\mu\nu}F'^{\mu\nu} + \frac{\epsilon}{2}F'_{\mu\nu}F^{\mu\nu} + \frac{m^2_{\gamma'}}{2}A'_{\mu}A'^{\mu}, \tag{2.2}$$

where A'_μ is the gauge field of the $U(1)'$ group, $F'_{\mu\nu} \equiv \partial_\mu A'_\mu - \partial_\nu A'_\mu$, and ϵ represents the parameter of kinetic mixing between the dark photon and pairs of charged SM particles.

Current phenomenological limits in the parameter space of the dark photon mass and kinetic mixing are shown in Figure 2.3.

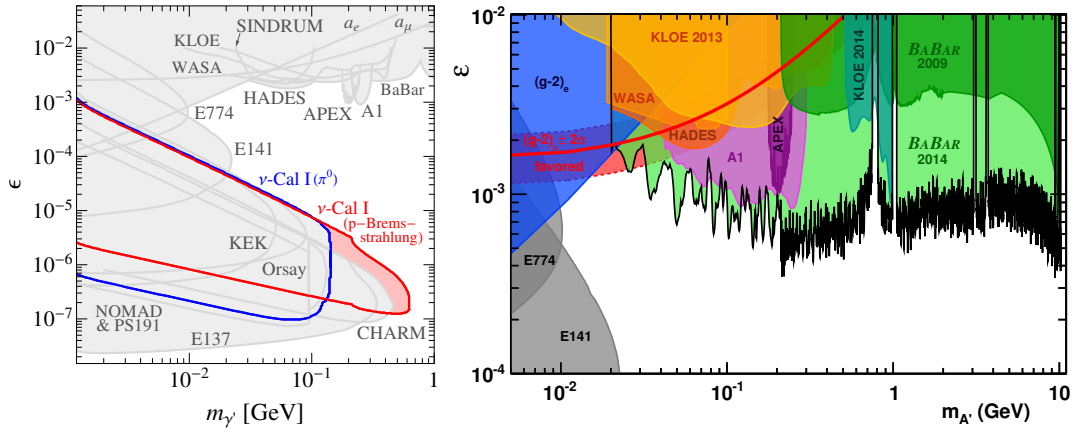

Figure 2.3: Exclusion bounds on the parameter space of dark photons. Beam dump experiments and collider experiments can access complementary regions. The latest BABAR limits from 2014 are shown on the right [22–24].

Such dark photons may be searched for at SHiP in neutral di-lepton and di-meson final states: γ' may mix to the SM photon through loops of particles charged both under $U(1)$ and $U(1)'$. Assuming γ' is the lightest particle of the hidden sector, it would then decay to $\ell^+\ell^-$ and $q\bar{q}$ final states through a virtual photon. [25]

The partial decay width of the dark photon into a lepton pair is given by:

$$\Gamma(\gamma' \to l^+l^-) = \frac{1}{3}\alpha_{\text{QED}} m_{\gamma'} \epsilon^2 \sqrt{1 - \frac{4m_l^2}{m_{\gamma'}^2}} \left(1 + \frac{2m_l^2}{m_{\gamma'}^2}\right), \tag{2.3}$$

where m_l is the lepton mass and α_{QED} is the fine-structure constant of Quantum Electro-Dynamics [26]. Following the approach used by the authors of [27], we compute the partial decay width into $q\bar{q}$ pairs as:

$$\Gamma(\gamma' \rightarrow \text{ hadrons}) = \frac{1}{3}\alpha_{\mathrm{QED}} m_{\gamma'} \epsilon^2 R\left(m_{\gamma'}\right) \ , \tag{2.4}$$

where

$$R\left(\sqrt{s}\right) = \frac{\sigma(e^+e^- \rightarrow hadrons)}{\sigma(e^+e^- \rightarrow \mu^+\mu^-)} \tag{2.5}$$

is the energy-dependent R-ratio quantifying the hadronic annihilation in e^+e^- collisions [28].

In a fixed target experiment dark photons can be generated by bremsstrahlung of scattering protons, in analogy with the ordinary photon bremmstrahlung. Let us consider a proton beam with initial momentum and energy P and E_p respectively. Let $E_{\gamma'}$ and p be the energy and momentum of the generated dark photon. If z denotes the fraction of the proton momentum carried away by the dark photon parallel to the original direction of the proton, so that $zP = p_{\parallel}$, the differential γ' production rate per proton interaction, calculated in the Fermi-Weizsäcker-Williams approximation, reads [24, 29]

$$\frac{dN}{dzdp_\perp^2} = \frac{\sigma_{pA}(s')}{\sigma_{pA}(s)} w_{ba}(z, p_\perp^2) \, , \tag{2.6}$$

where $s' = 2m_p(E_p - E_{\gamma'})$, $s = 2m_p E_p$ and

$$w_{ba}(z, p_\perp^2) = \frac{\epsilon^2 \alpha_{QED}}{2\pi H} \left[\frac{1 + (1-z)^2}{z} - 2z(1-z)\left(\frac{2m_p^2 + m_{\gamma'}^2}{H} - z^2 \frac{2m_p^4}{H^2} \right) \right. \tag{2.7}$$

$$\left. + 2z(1-z)\left(1 + (1-z)^2\right) \frac{m_p^2 m_{\gamma'}^2}{H^2} + 2z(1-z)^2 \frac{m_{\gamma'}^4}{H^2} \right] \tag{2.8}$$

with $H(p_\perp^2, z) = p_\perp^2 + (1-z)m_{\gamma'}^2 + z^2 m_p^2$, $p_\perp$ and $p_{\parallel}$ being the components of the γ' momentum orthogonal and parallel to the direction of the proton, respectively. The hadronic cross section σ_{pA} relates to the proton-proton scattering cross section σ_{pp} by a function $f(A)$ such that $\sigma_{pA}(s) = f(A)\sigma_{pp}(s)$, with $f(A)$ depending only on the atomic number A. Thus, it drops out when computing the event rate through Eqn 2.6, leaving us with:

$$\frac{dN}{dzdp_\perp^2} = \frac{\sigma_{pp}(s')}{\sigma_{pp}(s)} w_{ba}(z, p_\perp^2) \, . \tag{2.9}$$

However, the above formula does not take into account possible QCD contribution when the transferred momentum q^2 exceeds the QCD scale. Studies about how to address the

multi-GeV regime of dark photon production in proton bremsstrahlung are ongoing[1]. In this work, when the mass of the dark photon is much in excess of 1 GeV, we include the standard dipole form factor [31] in the proton - dark photon vertex:

$$G_D(q^2) = \left(1 + \frac{q^2}{0.71\,\mathrm{GeV}^2}\right)^{-2} \tag{2.10}$$

The q^2 in this vertex is given by the mass of the dark photon. When its mass is much in excess of the QCD scale, then there is a strong suppression of the production. Therefore, a "penalty" factor of

$$\mathrm{penalty}(m_{\gamma'}) = \left(\frac{m_{\gamma'}^2}{0.71\,\mathrm{GeV}^2}\right)^{-4} \quad \text{for} \quad m_{\gamma'}^2 > 0.71\,\mathrm{GeV}^2 \tag{2.11}$$

is applied, leading to a rescaled production rate:

$$\frac{dN}{dz dp_\perp^2} = \frac{\sigma_{pp}(s')}{\sigma_{pp}(s)}\, w_{ba}(z, p_\perp^2) \times \mathrm{penalty}(m_{\gamma'})\,. \tag{2.12}$$

In addition, dark photons can emerge in the decay of secondary mesons, depending on the γ' mass, through mixing with the SM photon. For the electromagnetic decay of the π^0 meson we can estimate a branching ratio

$$\mathrm{Br}(\pi^0 \to \gamma'\gamma) \simeq 2\epsilon^2 \left(1 - \frac{m_{\gamma'}^2}{m_{\pi^0}^2}\right)^3 \mathrm{Br}(\pi^0 \to \gamma\gamma) \tag{2.13}$$

that differs from the SM decay channel due to the presence of a phase space factor depending on the γ' mass, and is reduced by the mixing parameter ϵ [32]. Branching ratios for the decay of other neutral pseudo-scalar mesons such as η^0 can be obtained from 2.13 by replacing the meson mass. Similarly, for decays of vector mesons (e.g. $\rho^\pm, \rho^0, \omega$) into γ' and a pseudoscalar meson P (e.g. $\pi^\pm, \pi^0, \pi^0$) we use:

$$\mathrm{Br}(V^\pm \to P\gamma') \simeq \epsilon^2 \times \mathrm{Br}(V^\pm \to P\gamma) \tag{2.14}$$

$$\times \frac{(m_V^2 - m_{\gamma'}^2 - m_P^2)^2 \sqrt{(m_V^2 - m_{\gamma'}^2 + m_P^2)^2 - 4m_V^2 m_P^2}}{(m_V^2 - m_{\gamma'}^2)^3}\,, \tag{2.15}$$

where m_V is the mass of the decaying vector meson and m_P is the mass of the pseudoscalar meson [29].

[1] A first study postdates this work and was presented in [30].

Experiment	PS191	NuTeV	CHARM	SHiP
Proton energy (GeV)	19.2	800	400	400
Protons on target ($\times 10^{19}$)	0.86	0.25	0.24	20
Decay volume (m^3)	360	1100	315	1780
Decay volume pressure (bar)	1 (He)	1 (He)	1 (air)	10^{-6} (air)
Distance to target (m)	128	1400	480	80-90
Off beam axis (mrad)	40	0	10	0

Table 2.1: Comparison of the experimental conditions for HNL search experiments [1].

2.1.3. Previous searches and experimental prospects

Previous experiments have made important contributions to constrain the parameter space for hidden particles, in particular dark photons and HNLs. The most significant limits below the charm mass have been obtained in the fixed target experiments PS191 [33–35], CHARM [36] and NuTeV [37]. Searches in B and Z^0 decays, and in electron beam dump experiments, are in general sensitive but cover a different region of the parameter space. Table 2.1 lists the relevant design parameters of these three experiments, in comparison with those planned for SHiP [1].

The pioneering accelerator experiment PS191 was specifically designed to search for HNLs at the CERN Proton Synchrotron (PS). The high energies available at the CERN Super Proton Synchrotron (SPS) and the Fermilab Tevatron accelerators allowed extending the searches to higher masses looking for HNL produced via mixing to active neutrinos from charmed decays. The CHARM experiment searched for HNL decays in $e^+e^-\nu$, $\mu^+\mu^-\nu$ and $e^\pm\mu^\mp\nu$ final states. NuTeV searched for events with a muon and a charged track originating from a common decay vertex in the helium volume. For each one of these experiments, no signal candidates were found. Regions of the HNL parameter space were excluded down to couplings U^2 as low as 10^{-6} (CHARM, NuTeV) or even 10^{-8} (PS191), limited to masses below 450 GeV due to the low energy of the PS beam.

SHiP will greatly improve the sensitivity of the previous experiments using the production of heavy hadrons at the SPS. In particular, a data sample of 8×10^{17} D mesons is expected in about 5 years of nominal SPS operation, as well as a data sample of 3×10^{15} τ leptons. Despite being suppressed in production by four orders of magnitude with respect to the charmed hadrons, beauty hadrons will also contribute to the physics sensitivity between the beauty hadron and the charm hadron masses. Beauty hadrons will also be the dominant source of light scalars mixing with the Higgs boson. Below the beauty mass, the SHiP experiment will be able to exceed the sensitivity of previous experiments for HNLs by several orders of magnitude. This will allow SHiP to explore a range of phenomena with unprecedented reach. HNL couplings could be probed close to the ultimate seesaw limit. The sensitivities of

other existing or planned experiments to hidden sector particles are more than an order of magnitude lower compared to SHiP, even under the experimentally challenging assumption of zero background [1].

2.2. The SHiP beam and detector

The SHiP experiment will make use of a new, dedicated beam line branched off the SPS extraction line at the CERN North Area. The proposed location of the beam dump and underground complex (Figure 2.4(a)) allows for possible future extensions of the experimental hall [38].

Figure 2.4(b) shows a 3D rendering of the current foreseen configuration of the SHiP detector. A 400 GeV/c proton beam will be stopped in a heavy target, at a centre-of-mass energy $\sqrt{s} = \sqrt{2E_b m_p} \simeq 27$ GeV[2]. The target must maximize the production of heavy mesons (containing b- or c-quarks) while reducing that of pions and kaons which, decaying into muons and neutrinos, would be a large source of background. The target should thus be made of a material with the shortest possible interaction length, for a total size capable of containing the proton shower. A detailed study proved that the desired performance can be achieved with a segmented target made of layers of titanium-zirconium doped molybdenum and of pure tungsten, alternated with thin slits for water cooling. This design would allow the target to withstand the foreseen thermal and mechanical stress with a peak power of 2.5 MW. Under nominal SPS conditions, the SPS will deliver 2×10^{20} protons onto the SHiP target in 5 years of operation [1].

The target will be followed by a hadron stopper in iron, aimed at absorbing secondary hadrons and residual non-interacting protons, followed by a magnetized layer of steel. Muons emerging from the beam dump will be further deflected from the detector fiducial volume by means of an active shielding system based on magnets of alternate polarity, designed to cope with the expected muon spectrum. Detailed simulations prove the efficiency of this configuration, capable of reducing the flux of muons in the solid angle of the Hidden Sector (HS) detector to a negligible level in only 45 m of space.

2.2.1. The *i*SHiP facility

The SHiP collaboration will install a facility nicknamed *i*SHiP in front of the Hidden Sector detector. This facility will be aimed at studying the ν_τ properties, also providing the first experimental observation of the $\bar{\nu}_\tau$, and at looking for light dark matter candidates produced in the decay or scattering of (virtual) dark photons onto the material of the ν_τ detector.

The *i*SHiP facility is smaller than the HS detector and can be placed in front of it, still

[2] Refer to Chapter 5, Section 5.1.2 for details about the centre of mass energy of beam dump and collider experiments.

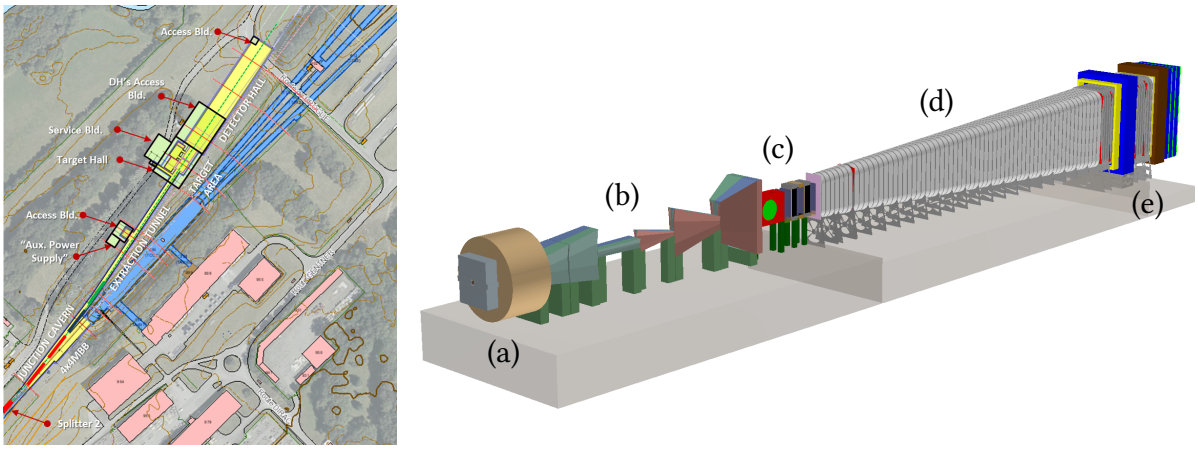

Figure 2.4: Left: design overview of the SHiP facility at the CERN North Area [1]. The SHiP tunnel and buildings are highlighted in yellow and green. The facilities drawn in blue correspond to the current SPS beam test area. Right: detailed view of the current baseline SHiP experimental layout (GEANT4 implementation). The view shows, from left to right: the target complex and hadron absorber (a), the active muon shield (b), the *i*SHiP facility (c), the HS decay volume (d) and the HS detector (e). Details are given in the text.

benefitting of the muon-cleared area. It will consist of a target made of bricks of laminated lead and emulsions placed in magnetic field, similar to those used by the OPERA experiment [39], followed by a target tracker and by a muon magnetic spectrometer. Details about the ν_τ detector and its physics case are given in [3, 40].

2.2.2. Hidden Sector detector

The hidden sector detector will search for evidence of hidden particles decaying in a large evacuated decay volume. The studies that lead to the choice of a cylindrical shape with elliptical cross section as baseline layout for the vacuum vessel enclosing the decay volume are discussed in Section 2.3. The length of the tube was set to 62 m, consisting of 50 m of fiducial decay volume and a 12 m long magnetic spectrometer, while its transversal dimensions were chosen to be 5×10 m [1]. This was the baseline configuration proposed to the CERN SPS committee [1]. While this thesis is in preparation, further studies are looking into the option of an elliptical or pyramidal frustum, the latter being preferred and shown in Figure 2.4. The probability that neutrinos interact with the residual gas inside the decay volume is negligible if the vacuum pressure is set to 10^{-6} bar [1]. A deeper analysis showed that many of these background events can be rejected by making use of the surrounding veto tagger and the geometric requirement of pointing back to the primary proton target, which would allow to relax the requirements on the vacuum pressure to about 10^{-3} bar. The final layout of the vessel will be described in the SHiP Comprehensive Design Report (CDR), currently in preparation; the rest of this section, as well as the studies presented in Chapter 3, describes the HS detector assuming the Technical Proposal vessel layout [1].

The vessel will be instrumented with a background tagger. The 30 cm of gap inside the double external wall of the decay volume will be filled with liquid scintillator, separated into 863 sections of approximately 1.5 m^2 of surface, each read out by two large-area photodetectors.

An important source of background is represented by neutral kaons produced in neutrino and muon interactions upstream of the vacuum vessel. Since the last layer of the muon spectrometer of the ν_τ detector does not cover the full HS detector acceptance, another upstream veto tagger is foreseen. This detector will consist of a 4×12 m^2 array of plastic scintillator bars.

Background originating in the entrance window of the vacuum vessel is tagged by a straw veto tagger, located in vacuum at 5 m from the entrance window. The same technology is used for the magnetic spectrometer tracker. The HS spectrometer must be able to reconstruct charged tracks from the decay of hidden particles with maximum efficiency, while also providing accurate measurements of the track momentum and direction of flight. Background rejection in SHiP can deeply benefit of high precision timing, good quality vertices, and of a good resolution in the reconstructed invariant mass and track direction. The tracker will consist of four stations symmetrically arranged around a large aperture dipole magnet providing an integrated field of 0.65 Tm. Each station provides two stereo views and two views in y, the direction perpendicular to the magnetic field. The R&D of the straw tracker will benefit from the positive performances recorded in NA62 [41], the only difference being the need for 5 m long straw tubes.

Outside of the vacuum vessel, a timing detector with a resolution of at least 100 ps will allow to efficiently tag events originating from random combinations of two muons. Two technologies are currently under investigation, both capable of achieving the required performance: plastic scintillator bars and multi-gap resistive plate chambers (MRPC).

The electromagnetic calorimeter will identify electrons, photons and neutral pions and provide precise energy measurements by means of a shashlik structure of interleaved lead and plastic scintillator layers read out by plastic wavelength-shifting fibers. It will be followed by a hadronic calorimeter aimed at providing pion identification and tagging neutral hadrons not seen by the other detectors. The same shashlik technology will be used, with an optimal segmentation devised through dedicated simulation studies.

The last component of the particle identification system will be a muon detector composed of four 6×12 m^2 stations, made of extruded plastic scintillator strips read out by wavelength-shifting fibers, separated by three muon filters [1].

The SHiP coordinate system is a right-handed Cartesian system with the $\hat{z}$ direction lying on the central axis of the vacuum vessel, and proceeding from the target towards the muon chambers.

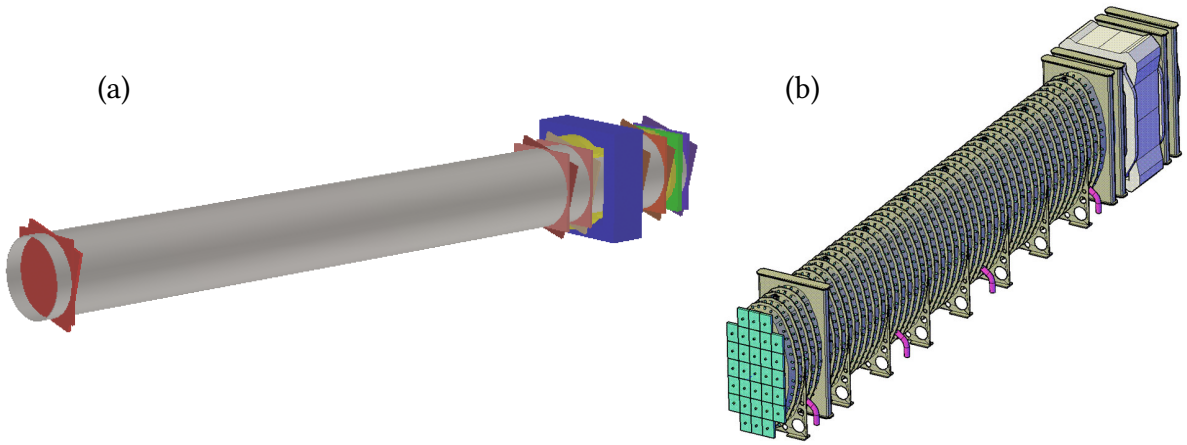

Figure 2.5: Rendering of one of the two identical HS detector elements described in the SHiP EoI in 2013 (a) [42]. Technical design of the reoptimized single vacuum vessel proposed in the SHiP TP in 2015 following the studies presented in Section 2.3 (b) [1].

2.3. Optimization of the vacuum vessel

This section presents the studies that led to the choice of the elliptical cylinder-shaped vacuum vessel presented in the Technical Proposal [1]. The results presented here seeded further optimization effort, with ongoing studies demonstrating how a pyramidal frustum-shaped vessel could be a better choice[3].

The originally proposed design, at the time when the SHiP Expression of Interest (EoI) was submitted to the SPS Committee, comprised two identical detector elements placed in sequence. Each detector element was made of a 50 m long cylindrical 5 m diameter vacuum vessel, including a 10 m long tracking system placed at its far end, followed by a calorimeter system and muon detector [42]. Figure 2.5(a) shows one of the two decay vessel elements foreseen at the time of the EoI. It soon appeared clear that such design would not be optimal in terms of cost and acceptance. Due to the divergence of the hidden particles, the second element would increase the acceptance by only about 60%. The second vessel would also get considerably more background from muons deflected by the sweeping magnet or scattering on the cavern walls. Moreover, the total required length of the experimental hall would be of the order of 150 m, in order to accomodate the muon shield, the tau neutrino detector and the two Hidden Sector detector elements. The civil engineering cost would be high. A larger, single-element detector would provide the same acceptance at a smaller cost, and it would leave room for possible future extensions of the facility.

However, there are some constraints to the redesign of the decay vessel:

- the vessel dimension in the bending plane of the muons should be kept as small as needed to achieve a muon-depleted entry lid at the position where the vessel is placed;

[3] The final layout of the vacuum vessel will be described in the SHiP Comprehensive Design Report (CDR), currently in preparation.

- the dimension of the vessel should allow a dipole magnet to be placed around the vessel in the middle of the tracking system.

The first requirement is satisfied with an elliptical cylinder, or an elliptical frustum, whose dimension along $\hat{x}$ does not exceed 5 m at 45 m from the target. Likewise, a parallelepipoidal or pyramidal frustum-shaped vessel with the same dimensions as the ellipse axes would meet the requirements. Studies demostrate that a dipole magnet with inner dimensions of 5×10 m^2 is feasible [1]. To be conservative, we kept 10 m as the maximum dimension of the exit face of the vacuum tank.

An elliptical or pyramidal frustum with semiaxes increasing in length as the distance from the target increases would allow to obtain the maximum acceptance, naturally mimicking the divergence of the hidden particles. However, if the required dimensions of the vessel prove the tracking system, currently foreseen to adopt the straw technology, to be unfeasible due to the dimension and gravitational bending of the straws, a major redesign of the tracking system would be needed.

Given these constraints, the dimensions of the vessel have been optimized with acceptance studies performed by means of the Monte Carlo simulation presented in Section 3.1.1. Figure 2.6 shows the results of an analysis aimed at defining the ellipticity of the vessel cross section, and the required length of the decay region. The same studies were performed for a vessel with rectangular cross-section, and are shown in Figure 2.7. A sample of HNLs of mass $m_{HNL} = 1$ GeV and lifetime $\tau_{HNL} = 128$ µs, generated at the SHiP target and decaying within a cylinder of diameter 12 m and length 200 m, was produced. HNLs are let decay into a two-body final state ($HNL \to \pi\mu$) and a three-body final state ($HNL \to \mu\mu\nu$). Once a test shape for the SHiP vacuum vessel is defined, events are marked as in acceptance if:

- the HNL decay vertex is inside the vessel;
- the vertex is at least 5 m downstream of the entry lid, as extra protection against background events originating from the upstream material;
- the two charged daughter tracks cross the exit lid of the vessel;
- the two charged daughter tracks are fully contained in the vacuum vessel (i.e. their xy projection lies within the vessel cross section at every z position).

The last requirement makes sure that tracks are not kicked back into the vessel by the magnetic field of the spectrometer magnet, as the used simulation does not include the vessel walls. The daughter tracks are propagated through a magnetic field of 1 T m along the $\hat{x}$ axis, centered 5 m before the exit lid.

Figures 2.6 and 2.7 show that it is possible to achieve the same sensitivity prospected in the EoI [42] with a single, larger decay volume. Moreover, no significant differences are observed between the foreseen acceptances for two bodies and three bodies decays. The studies shown

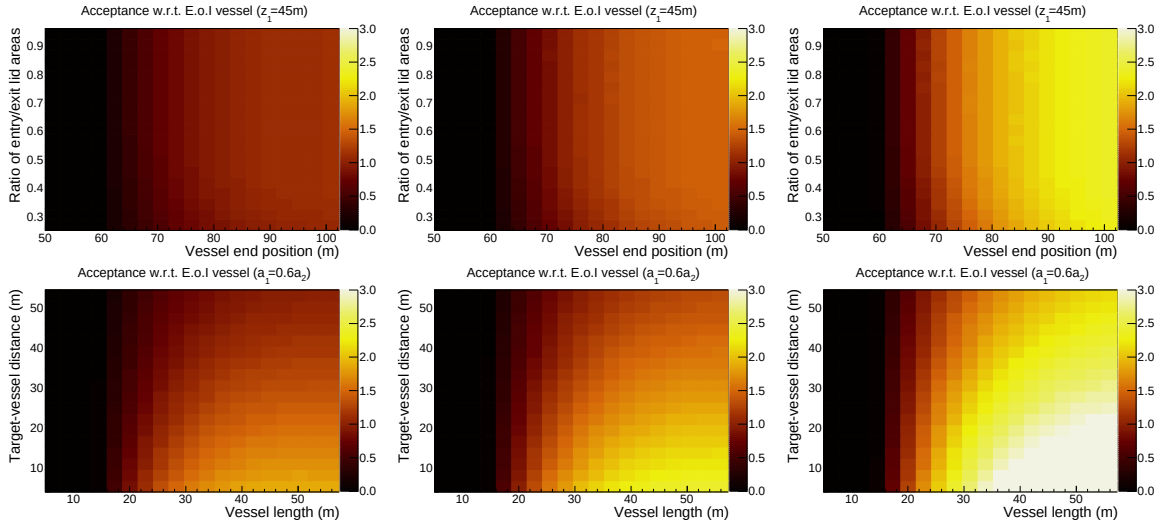

(a) 2-bodies, exit face: 4×10 m **(b)** 2-bodies, exit face: 5×10 m **(c)** 2-bodies, exit face: 8×10 m

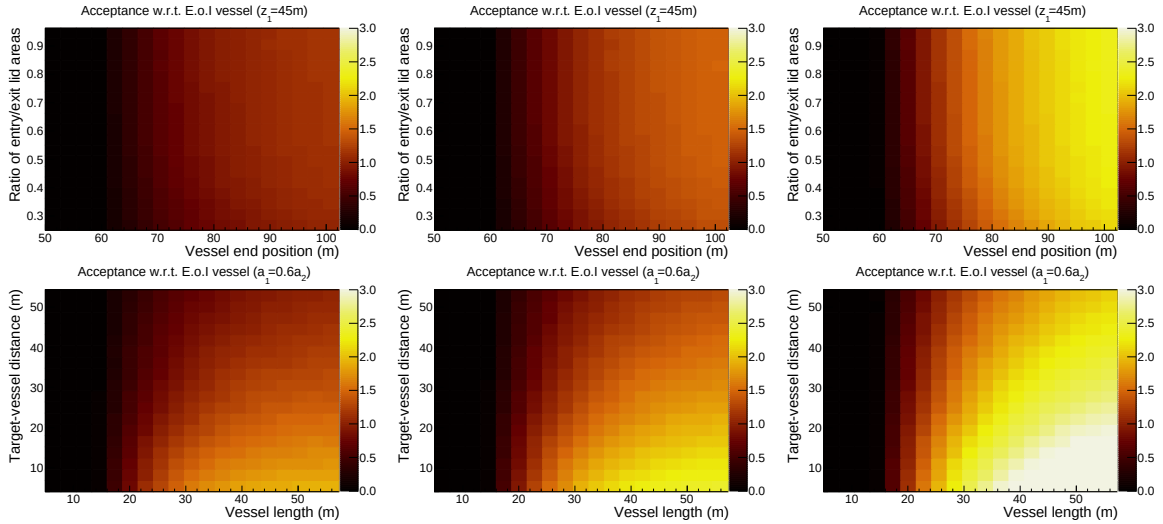

(d) 3-bodies, exit face: 4×10 m **(e)** 3-bodies, exit face: 5×10 m **(f)** 3-bodies, exit face: 8×10 m

Figure 2.6: Acceptance studies for a truncated conical vessel with elliptical cross section. The three series of plots show the ratio between the acceptance of the conical vessel rescaled to the acceptance of the vessel proposed in the Expression of Interest [42] as a function of the vessel length and of the ratio between the surfaces of the entry and exit lids at fixed distance from the target, and as a function of the vessel length and of its distance from the target at fixed ratio between the two lids, respectively, for three different proportions between the ellipse axes. No significant differences are observed between two-body decays $HNL \to \pi\mu$ **(a-c)** and three bodyes decays $HNL \to \mu\mu\nu$ **(d-f)**.

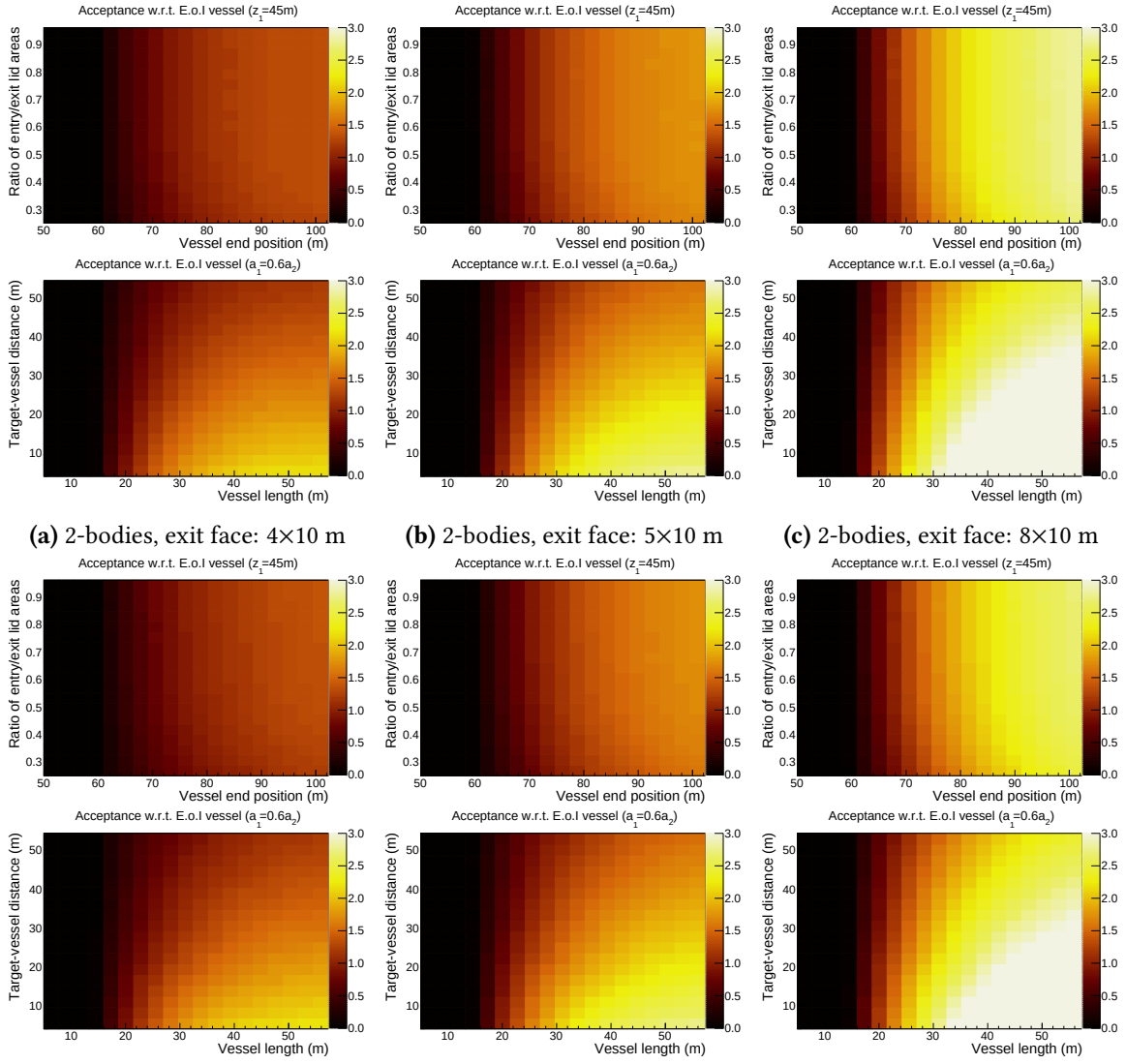

(a) 2-bodies, exit face: 4×10 m **(b)** 2-bodies, exit face: 5×10 m **(c)** 2-bodies, exit face: 8×10 m

(d) 3-bodies, exit face: 4×10 m **(e)** 3-bodies, exit face: 5×10 m **(f)** 3-bodies, exit face: 8×10 m

Figure 2.7: Acceptance studies for a vessel with pyramidal frustum shape. The three series of plots show the ratio between the acceptance of the pyramidal vessel rescaled to the acceptance of the vessel proposed in the Expression of Interest [42] as a function of the vessel length and of the ratio between the surfaces of the entry and exit lids at fixed distance from the target, and as a function of the vessel length and of its distance from the target at fixed ratio between the two lids, respectively, for three different proportions between the x and y dimensions. No significant differences are observed between two-body decays $HNL \to \pi\mu$ **(a-c)** and three bodyes decays $HNL \to \mu\mu\nu$ **(d-f)**.

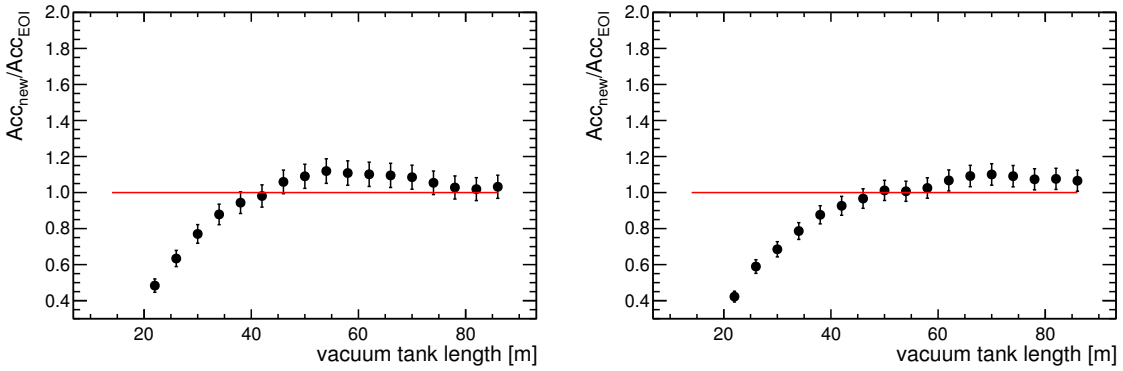

(a) Acceptance w.r.t. EoI configuration ($\pi\mu$)

(b) Acceptance w.r.t. EoI configuration ($\mu\mu\nu$)

Figure 2.8: Ratio between the acceptance of the single cylindrical decay volume and that of the two-volumes original configuration, as a function of the volume length, for $HNL \to \pi\mu$ **(a)** and $HNL \to \mu\mu\nu$ **(b)**.

assume a truncated conical shape (Figure 2.6), or a pyramidal frustum (Figure 2.7), with the entry lid smaller than the exit lid. A maximum cross-section of 8 m $\times$ 10 m is investigated, due to the vessel construction cost and to the design of the spectrometer magnet. However, the decision to insert a ν_τ detector in front of the Hidden Sector detector freezes the transversal shape of the vessel to a cylinder of axes 5 m $\times$ 10 m, since a 5 m wide muon-free area along $\hat{x}$ will be anyway provided to the *i*SHiP facility. Hence, a cylindrical or parallelepipoidal volume with the entry and exit lids of the same dimensions is chosen as baseline layout, as it would prove more feasible from the engineering point of view, without losing too much acceptance with respect to the conycal/pyramidal case. The magnetic muon sweeping system proposed in [1] proved able to provide a 5 m muon-free width at a distance of about 60 m from the target, thus moving the Hidden Sector decay volume to 63.8 m from the target as baseline solution[4].

Considering the transversal dimensions fixed to 5 m along x and 10 m along y, and the position of the entrance lid set to $z_0 = 65$ m, Figure 2.8 shows that the same acceptance as with the original configuration [42] is achieved with a vessel longer than 45 m for two-bodies final states and longer than 50 m for three-bodies final states. We therefore conservatively set the length of the vacuum vessel to 60 m.

The option of a parallelepipoidal vessel was evaluated against the cylindrical solution. The gain in acceptance with respect to the cylindrical option was computed by means of the fast simulation and amounts to $\Delta A = (16 \pm 7)\%$. This solution is under discussion and should consider also the increased cost due to the required larger area of the calorimeter systems. We considered optimal, at the Technical Proposal stage, the solution of a 60 m long cilyndrical vessel with elliptical cross section of axes 5 m $\times$ 10 m [1]. A 3D rendering of the reoptimized

[4] Further work on the magnetic muon shield proved that the distance between the target and the vacuum vessel can be reduced to 45 m. These studies will be presented in the SHiP Comprehensive Design Report, currently in preparation.

vacuum tank is visible in Figure 2.5(b).

Further optimization can happen in two ways.

1. It is reasonable to assume that the muon-free area extends with the distance from the target. If one releases the constraint of a maximum spectrometer magnet size of 10×5 m^2, there would be room for a conical or trapezoidal vessel, with a larger exit lid along the x axis (the direction of muon sweeping). The studies reported in Figure 2.9 show that the acceptance can increase by more than 90% if the length of the shorter axis of the exit lid is increased to 10 m. However, further studies are necessary in order to better understand the flux of muons at this distance from the target, and how muon collisions in the cavern walls can influence the Hidden Sector sensitivity.

2. If the muon sweeping system could be redesigned in order to clear muons from the Hidden Sector detector acceptance in a shorter distance, the vessel could be moved closer to the target. This possibility is being investigated while this thesis is in preparation. This configuration would result in an overall increase in acceptance and the required vessel length would be shorter (see Figure 2.10). Moreover, going closer to the target could allow a reduction in the transverse size of the vessel without any loss in acceptance. The acceptance could be even higher if a conical or pyramidal vessel is reintroduced, never exceeeding 5 m $\times$ 10 m in transverse size (see Figure 2.11).

Finally, the Monte Carlo simulation for dark photons presented in Section 3.3 allowed to test the new baseline geometry of the decay vessel on dark photon events as well. The result is shown in Figure 2.12. Although the geometry was decided in order to optimize the HNL yield, the changes introduced increase the γ' acceptance by a factor greater than 2. Moreover, the result presented in Figure 2.12 would support the choice of a shorter vacuum vessel. However, even if the dark photon acceptance seems to be favoured by a vessel length around 45 m, this study is sensitive to the dark photon spectrum. Therefore, a more accurate theory calculation including QCD contributions is required.

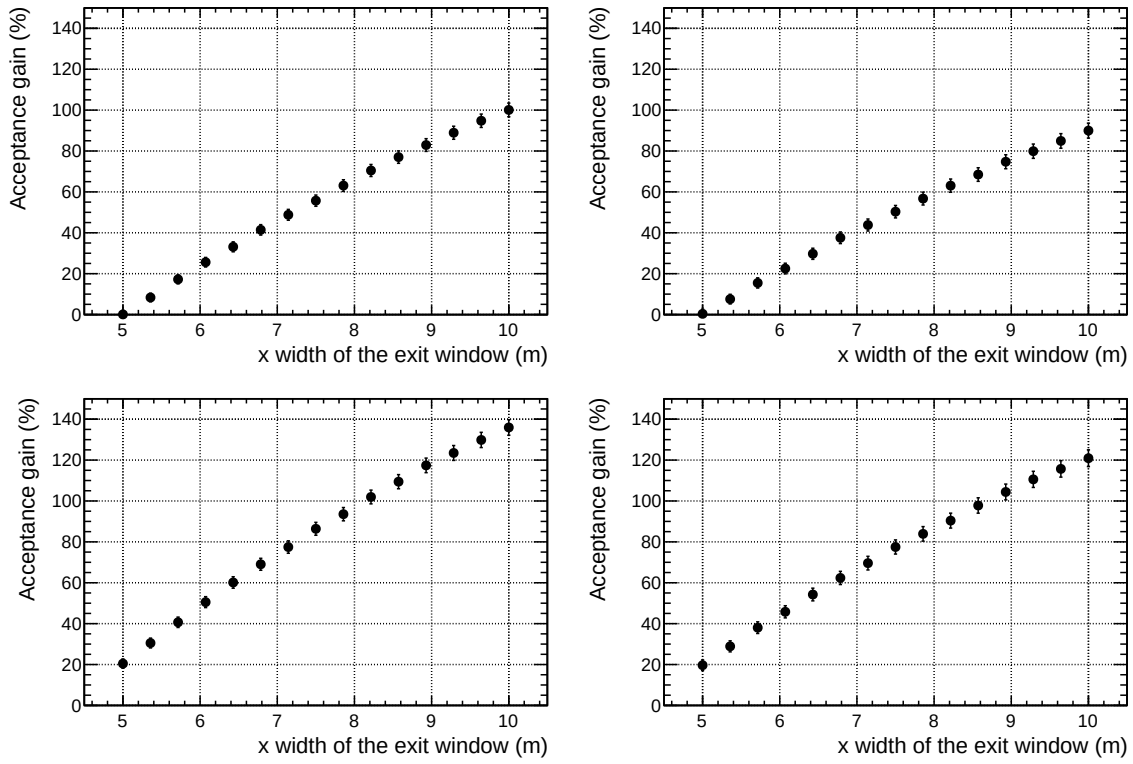

Figure 2.9: Possible increase in yield with a conical vessel (first row) or a pyramidal frustum (second row) which width along x increases with the distance to the target, computed for two-body (left) and three-body (right) decays. The vessel length is set to 60 m for this study.

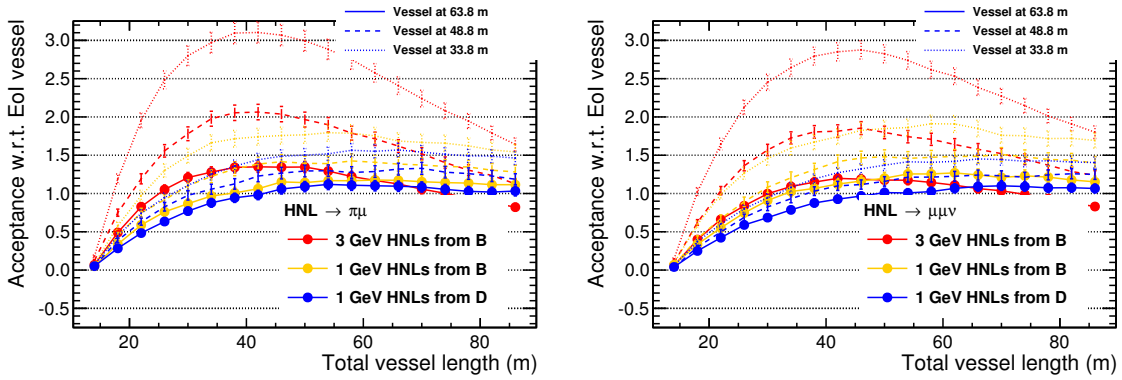

Figure 2.10: Acceptance studies for vessels placed at various distances from the target: 63.8 m (solid line), 48.8 m (dashed line) and 33.8 m (dotted line). The vessel is a cylinder with elliptical cross section, with axes of 5 m and 10 m. The color code represents the sample of HNLs: 1 GeV HNLs from decays of charm mesons (blue), 1 GeV HNLs from decays of beauty mesons (yellow), 3 GeV HNLs from decays of beauty mesons (red).

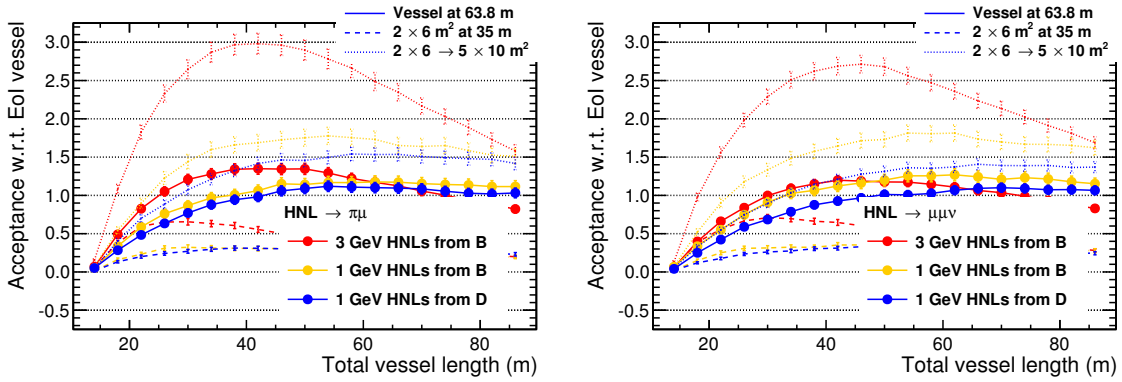

Figure 2.11: Acceptance studies for different elliptical vessels: baseline solution [1] (solid line), a vessel with smaller cross section (with axes of 2 m and 6 m) at 35 m from the target (dashed line), and the latter with a conical shape (exit lid with axes of 5 m and 10 m, dotted line). The color code represents the sample of HNLs: 1 GeV HNLs from decays of charm mesons (blue), 1 GeV HNLs from decays of beauty mesons (yellow), 3 GeV HNLs from decays of beauty mesons (red).

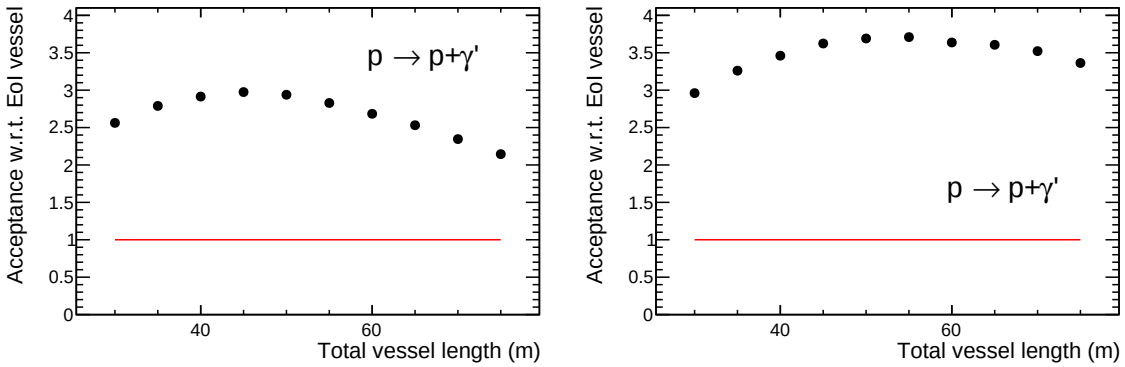

Figure 2.12: Geometrical acceptance as a function of the the total vessel length for dark photons of mass 1 GeV and coupling to the SM of $\epsilon = 10^{-7}$. Only proton bremsstrahlung is used as source of γ'. The vessel cross section is elliptical (left) or rectangular (right) with axes of 5 m along $\hat{x}$ and 10 m along $\hat{y}$. The entry lid is placed at 60 m from the target.

CHAPTER 3

SHiP sensitivities in the Hidden Sector

Contents

This chapter presents studies of SHiP's sensitivity in two physics channels (HNLs and dark photons) that, for their variety of possible final states, can be representative for the whole portion of the SHiP physics program dealing with particles with a lifetime much longer than the size of the experiment [2].

One of the main challenges for this kind of experiments is to maintain the background to a controlled level. The ambitious goal of the SHiP experiment is to suppress all backgrounds to a total of less than 0.1 expected events in 5 years of operation. Section 3.1.4 will discuss in detail the case of background induced by Standard Model neutrino interactions.

The sensitivity plots presented in Section 3.1.5 and Section 3.3 assume a level of background of 0.1 events for a foreseen total exposure of 2×10^{20} proton-target collisions. This way, they can be interpreted in two ways. If no event is observed, the plots represent the area of the parameter space that SHiP can rule out at 90% C.L. (confidence level). On the other hand, those plots also represent the 3σ evidence contour if 2 candidate events are observed.

The studies presented in this chapter have been published in the SHiP Technical Proposal [1] and as SHiP public notes [43, 44]. Section 3.2 extends this work in order to assess the possible synergy between SHiP and a possible future circular collider. The results presented in Section 3.2 have been published in [25, 45].

3.1. The search for Heavy Neutral Leptons

The free parameters for any model with HNLs are four: the three mixing parameters U_e^2, U_μ^2, U_τ^2, and the HNL mass m_N. Usually the total coupling to the SM $U_{\text{tot}}^2 = \sum_i U_i^2$ is used to present the results, since this is the important parameter from the cosmological point of view. Moreover, the interpretation of the limits in the parameter space depends on the hierarcy of the active neutrino masses. In this work, only the total coupling U^2 is left free to vary over the whole parameter space. The relative strenght of the HNL coupling to the three SM flavours are fixed according to five benchmark scenarios (*models*), conforming to existing theoretical works [10, 17]:

I. $U_e^2 : U_\mu^2 : U_\tau^2 \sim 52 : 1 : 1$, inverted hierarchy [17]

II. $U_e^2 : U_\mu^2 : U_\tau^2 \sim 1 : 16 : 3.8$, normal hierarchy [17]

III. $U_e^2 : U_\mu^2 : U_\tau^2 \sim 0.061 : 1 : 4.3$, normal hierarchy [17]

IV. $U_e^2 : U_\mu^2 : U_\tau^2 \sim 48 : 1 : 1$, inverted hierarchy [10]

V. $U_e^2 : U_\mu^2 : U_\tau^2 \sim 1 : 11 : 11$, normal hierarchy [10]

The sensitivity limits obtained for the above scenarios are shown and discussed in Section 3.1.5.

In order to extract SHiP's sensitivity, two techniques are combined. The official experiment software FairShip is used to precisely evaluate the final state acceptance and the reconstruction efficiency, and to devise a signal selection strategy. FairShip has the advantage of containing a detailed description of the material and the geometry of the detector (Geant4 [46]), as well as a realistic description of the magnetic fields. A fast Monte Carlo simulation was additionally developed to estimate the signal yield as a function of the position in the HNL parameter space.

Scenario II, with a total coupling to the SM of $U^2 = 9.3 \cdot 10^{-9}$ and a HNL mass of 1 GeV/c^2, was chosen to investigate SHiP's acceptance in detail in order to tune the fast simulation, and will be referred to as *benchmark scenario* throughout this section.

3.1.1. Estimation of the HNL sensitivity

The number of sterile neutrinos that are detectable by SHiP in the nominal data taking period depends on their production rate and the corresponding experimental acceptance. It is given by:

$$n(HNL) = N(\text{p.o.t}) \times \chi(pp \to HNL) \times \mathcal{P}_{\text{vtx}} \times \mathcal{A}_{\text{tot}}(HNL \to \text{visible}), \tag{3.1}$$

where

- $N(\text{p.o.t}) = 2 \times 10^{20}$ is the number of proton on target collisions expected in five years of SHiP operation at nominal conditions.

- $\chi(pp \to HNL)$ is the total production rate of sterile neutrinos per proton-target interaction. It is equal to:

$$\begin{aligned}\chi(pp \to HNL) = \; 2\times \big[&\chi(pp \to c\bar{c}) \times \text{Br}\,(c \to HNL) \\ &+ \chi(pp \to b\bar{b}) \times \text{Br}\,(b \to HNL)\big]\end{aligned} \tag{3.2}$$

  where $\chi(pp \to c\bar{c}) = 1.7 \times 10^{-3}$ and $\chi(pp \to b\bar{b}) = 1.6 \times 10^{-7}$ are the production fractions of c- and b-mesons for a 400 GeV proton beam colliding on a Molybdenum target. Sterile neutrinos are mainly produced in $D_{(s)}$ meson decays, but $B_{(s)}$ mesons also contribute and they are the only source of sterile neutrinos for masses above 2 GeV. The fractions of heavy-meson decays into sterile neutrinos $\text{Br}\,(c \to HNL)$ and $\text{Br}\,(b \to HNL)$ take into account all the dominant kinematically allowed decay channels of $D_{(s)}$ and $B_{(s)}$ mesons into sterile neurinos:

$$\begin{aligned}&D \to K\ell + HNL \\ &D_s \to \ell + HNL \\ &D_s \to \tau\nu_\tau \text{ followed by } \tau \to \ell\nu + HNL \text{ or } \tau \to \pi + HNL \\ &B \to \ell + HNL \\ &B \to D\ell + HNL \\ &B_s \to D_s\ell + HNL\end{aligned} \tag{3.3}$$

  The widths of these channels are proportional to U^2_{tot} and are parametrised as shown in Appendix A according to [17], as a function of the sterile neutrino mass and couplings. Other decays with smaller branching ratios represent a small correction and therefore they are not included. The factor two is added to take into account the fact that each of the quarks in the pair can hadronise individually and result in the production of an HNL.

- $\mathcal{P}_{\text{vtx}}$ is the probability that the decay vertex of a sterile neutrino of given mass and couplings is located inside the SHiP fiducial volume. Its estimation is presented in detail in the following.

- $\mathcal{A}_{\text{tot}}(HNL \to \text{visible})$ is the experimental acceptance of all the visible final states, i.e. the fraction of sterile neutrinos decaying in SHiP fiducial volume that result in a detectable final state. It is defined as:

$$\mathcal{A}_{\text{tot}}(HNL \to \text{visible}) = \sum_{i=\text{visible channel}} \text{Br}\,(HNL \to i) \times \mathcal{A}(i) \tag{3.4}$$

where the index i runs over final states with two charged particles. The estimation of the final state acceptance $\mathcal{A}(i)$ is explained in detail in the following.

Geometrical acceptance

The software package Pythia8 [47] is used to build a sample of charm and beauty mesons produced in the SHiP target. For every meson, all of the kinematically allowed decays into massive sterile neutrinos from Equation 3.3 are simulated using the ROOT TGenPhaseSpace class.

A two-dimensional binned Probability Density Function (PDF) for the momentum p and polar angle θ of sterile neutrinos produced in the proton-target interaction is obtained with the fast simulation. The PDF is built from simulated events, weighted with the branching ratio of the meson decay in which the HNL is produced. This PDF corresponds to the four-momentum spectrum of sterile neutrinos detectable by SHiP.

The sterile neutrino lifetime is estimated as the sum of the widths of its main decay channels:

$$\begin{aligned} HNL &\longrightarrow 3\nu \\ HNL &\longrightarrow \pi^0\nu \\ HNL &\longrightarrow \pi^{\pm}\ell \\ HNL &\longrightarrow \rho^0\nu \\ HNL &\longrightarrow \rho^{\pm}\ell \\ HNL &\longrightarrow \ell^+\ell^-\nu \end{aligned} \tag{3.5}$$

The branching ratios for these channels are computed according to the formulas in Appendix A [17] and shown in Figure 3.1 as a function of the HNL mass. The formulas in Ref. [17] for the decay of the HNL into mesons are valid up to $m_{HNL} \sim 1$ GeV/c^2. If the sterile neutrino mass is much larger than the QCD scale, $m_{HNL} \gg \lambda_{QCD}$, the two quarks from $HNL \longrightarrow q\bar{q}\nu$ and $HNL \longrightarrow q\bar{q}\ell$ decays tend to hadronize individually. For masses in the region of 1 - 5 GeV/c^2, the inclusive $HNL \longrightarrow q\bar{q}\nu$ decay width is extrapolated from the parametrisation of $HNL \longrightarrow \ell^+\ell^-\nu$ with appropriate corrections.

For every bin of the PDF, the probability that an HNL with the corresponding four-momentum decays within the acceptance of SHiP is computed as

$$\mathcal{P}_{vtx}\left(p, \theta \,\middle|\, m_N, U_f^2\right) = \int_{\text{SHiP}} \frac{e^{-l/\gamma c\tau}}{\gamma c\tau}\, dl. \tag{3.6}$$

Hence, a new PDF is built, in which the content of each bin of the four-momentum spectrum is weighted according to Eqn. 3.6. The new spectrum is further corrected with a geometrical factor $A(\theta)$, selecting only sterile neutrinos in the angular acceptance of a cylinder strictly containing the SHiP vacuum vessel.

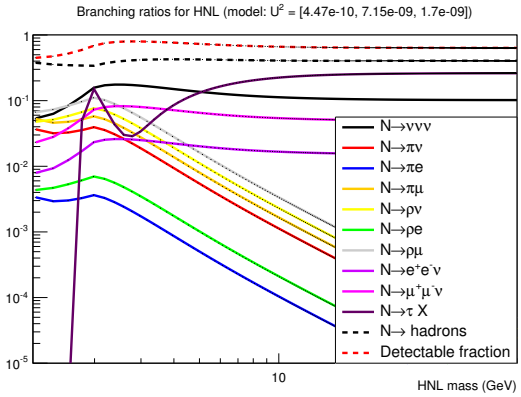

Figure 3.1: Sterile neutrino branching ratios as a function of its mass for the benchmark scenario [1].

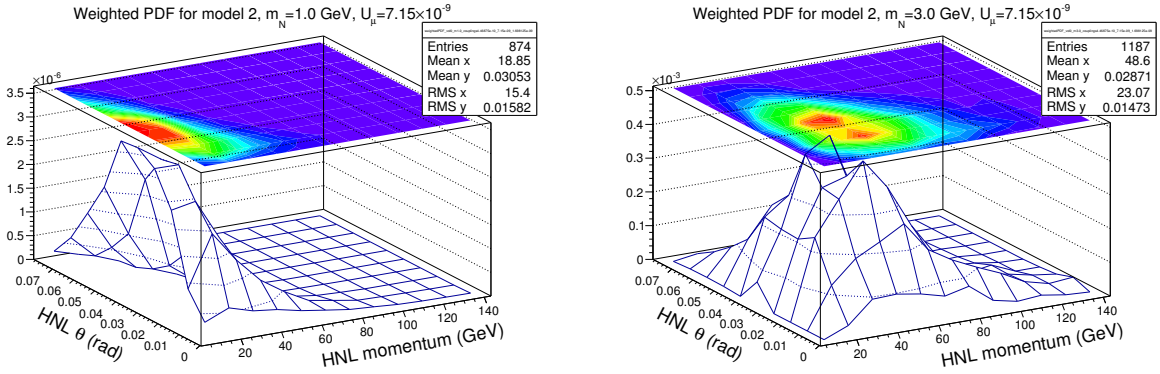

Figure 3.2: Binned probability density function in momentum and polar angle for the benchmark scenario, for $m_N = 1$ GeV (left) and for $m_N = 3$ GeV (right).

The resulting weighted spectrum represents the distribution in (p, θ) of sterile neutrinos that are detectable at SHiP. An example is shown in Figure 3.2 for the benchmark scenario. Its integral over the four-momentum spectrum represents the total probability that an HNL of given mass and couplings produces a vertex inside the fiducial decay volume:

$$\mathcal{P}_{vtx}(m_N, U_f^2) = \int \mathcal{P}_{vtx}\left(p, \theta \,\middle|\, m_N, U_f^2\right) \, dp \, d\theta \tag{3.7}$$

In the benchmark scenario, this probability corresponds to roughly 4.5×10^{-5} (0.96×10^{-2}) for HNLs of mass 1 GeV (3 GeV), which PDF is shown in Figure 3.2.

Final state acceptance

The visible fraction of sterile neutrinos $\mathcal{A}_{tot}(HNL \rightarrow \text{visible})$ is a function of the branching ratio and of the final state acceptance of the visible HNL decay channels (see Equation 3.4). All the decay channels providing two charged particles in the final state are considered detectable. Decays such as $HNL \rightarrow \rho^0 \nu$ followed by $\rho^0 \rightarrow \pi^+\pi^-$ are also included. However, final states

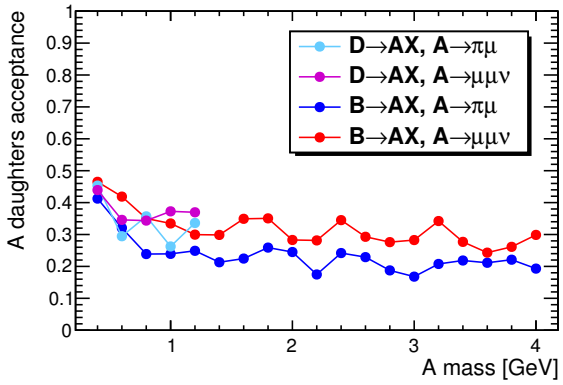

Figure 3.3: Final-state acceptance for HNLs decaying into $\pi\mu$ with a vertex inside the SHiP vacuum vessel.

with one charged and one neutral pion are conservatively considered not reconstructable and hence are not included.

For every detectable and kinematically allowed channel, a sample of events is simulated using ROOT TGenPhaseSpace. The four-momentum of the decaying HNL is sampled from the weighted spectrum described in Section 3.1.1. The position of the decay vertex is sampled from an exponential distribution with the sterile neutrino lifetime as parameter. The daughter tracks are propagated through the spectrometer magnetic field until they cross the exit lid of the vacuum vessel. The effect of the magnetic field is simulated as a momentum kick along the y axis at the z position of the centre of the magnet.

A detailed event selection is put in place by means of the FairShip framework and is described in Section 3.1.2. In the fast Monte Carlo, simulated events are considered reconstructable if:

- the vertex is within the fiducial volume of the vacuum vessel, that is, it is located at least 5 m downstream of the entrance lid and upstream of the first spectrometer straw tracker station. This corresponds to the requirement that the HNL daughters do not cross the straw veto tagger, used offline to suppress the background originating from neutrino interactions in the material upstream of the vessel.

- The daughter tracks are contained within the vacuum vessel at the z of the centre of the spectrometer magnet.

- The daughter tracks are contained within the vacuum vessel at the z position of the exit lid.

The selection ensures that the tracks that exit from the fiducial volume and re-enter as a result of the magnetic kick are discarded. Overall, depending on the HNL mass, the daughter tracks are in acceptance in 20%-50% of the cases, as shown in Figure 3.3.

The final state acceptance is computed as

$$\mathcal{A}(i) = \frac{\#\text{ reconstructable}}{\#\text{ simulated}}. \tag{3.8}$$

The intrinsic uncertainty of the toy Montecarlo on the total HNL acceptance, given by the product $\mathcal{P}_{\text{vtx}} \times \mathcal{A}(i)$, was found to be of the order of 30% relative to a single simulation test. This explains in part the fluctuations shown in Table 3.1 (more details are given in Section 3.1.2).

3.1.2. HNLs in the full SHiP simulation

The official SHiP computing framework, named FairShip [1], is based on FairROOT [48], based in turn on the ROOT package [49]. Detectors and other material are defined with the ROOT `TGeo` classes; particle transport and detector response is simulated through Geant4 [46], while track reconstruction makes use of Genfit [50]. Events are produced using the following generators: Pythia8 [47] for the proton-target collision, Genie [51] for SM neutrino interactions, and Pythia6 [52] for inelastic muon scattering.

The physics parameters of Pythia8 were modified to allow the generation of HNLs. To generate signal, all the leptonic and semi-leptonic decays of $D^{\pm}$, D^0, D_s, Λ_c and of the τ lepton were set to include an HNL in place of the SM neutrino. The HNL decay table is dinamically produced on the basis of the HNL mass and couplings: the kinematically available decay channels are activated, with their amplitudes computed as described in Appendix A, and used to determine the HNL lifetime. It is possible to activate and deactivate selected HNL decay channels in order to study the corresponding final states. The full list of possible final states is analogue to that of the toy simulation (Eqn. 3.5):

$$\begin{aligned}
&HNL \longrightarrow 3\nu \\
&HNL \longrightarrow \pi^0 \nu_\alpha \quad \text{with } \alpha = e, \mu, \tau \\
&HNL \longrightarrow \pi^{\pm} \ell \quad \text{with } \ell = e, \mu \\
&HNL \longrightarrow \rho^0 \nu_\alpha \quad \text{with } \alpha = e, \mu, \tau \\
&HNL \longrightarrow \rho^{\pm} \ell \quad \text{with } \ell = e, \mu \\
&HNL \longrightarrow \ell^+ \ell^- \nu_\alpha \quad \text{with } \ell, \alpha = e, \mu, \tau \text{ and } \alpha \neq \ell \\
&HNL \longrightarrow \ell^+ \ell'^- \nu_\ell \quad \text{with } \ell, \ell' = e, \mu, \tau \text{ and } \ell' \neq \ell
\end{aligned} \tag{3.9}$$

In FairShip, the $\mathcal{P}_{\text{vtx}}$ factor in Equation 3.1 corresponds to weights applied to each generated HNL to account for the probability that such particle leaves a decay vertex inside the SHiP fiducial volume. The weights are computed as in Eqn. 3.6. The total geometrical acceptance $\mathcal{P}_{\text{vtx}} \times \mathcal{A}$ is equal to the ratio of the sum of the weights of HNL candidates satisfying geometrical selection criteria, divided by the total number of HNLs generated. The error on the acceptance

is calculated by generating various independent HNL signal samples, and by taking the root-mean-square deviation of the computed acceptances as error. It is found to be of order $\sim 10\%$. The following selection criteria were used to estimate the total acceptance with FairShip:

- the HNL decay vertex is located between the straw veto tagger and the exit lid of the vacuum vessel;
- the x, y position of the sterile neutrino decay vertex is inside the elliptical fiducial volume ($r_x = 250$ cm, $r_y = 500$ cm);
- both HNL daughters leave a signal in one of the straw stations before the magnet (1 or 2) and in station 4 after the magnet. These hits are within the elliptical fiducial volume ($r_x = 250$ cm, $r_y = 500$ cm);
- 150 MeV of energy are deposited in the ECAL (only for $HNL \to \mu\pi$ and $HNL \to eev$);
- muons from HNL decays leave a signal in the first two muon stations (only for $HNL \to \mu\pi$ and $HNL \to \mu\mu\nu$).

No reconstruction nor further track selection criteria were applied to compare the geometrical acceptances for HNLs obtained with FairSHiP and with the fast simulation [1].

Comparisons of signal acceptances between the fast MC and FairShip

Comparisons between the fast MC and the full simulation are shown in Table 3.1, for the $HNL \to \mu\pi$ decay channel and for HNL masses ranging from 0.3 GeV/c^2 to 1.1 GeV/c^2 and various couplings, and in Figure 3.4. The test observable in Table 3.1 is the total detector acceptance $\mathcal{A} \equiv \mathcal{A}_{tot}(HNL \to \text{visible}) \times \mathcal{P}_{\text{vtx}}$. The results show good agreement between the fast and the full simulation. The signal acceptance results obtained with the FairShip software and the fast Monte Carlo, without applying further offline selection criteria, are in agreement within errors. The signal acceptance for the benchmark scenario in the $\pi\mu$ channel is found to be $\mathcal{A} = (5.8 \pm 1.8) \times 10^{-6}$ for the fast Monte Carlo and $\mathcal{A} = (5.6 \pm 0.6) \times 10^{-6}$ for FairShip.

Figure 3.4 compares the sterile neutrino momentum and polar angle distributions obtained with FairShip and with the fast Monte Carlo for the benchmark scenario. A good level of agreement is observed for the momentum distribution. Even if the two procedures result in slightly different polar angle spectra, a systematic overestimation of the acceptance will be prevented by means of an acceptance correction factor. Such factor is computed as the ratio between the acceptance computed with FairShip and the acceptance computed with the fast MC. This factor is used in the sensitivity studies described in this chapter in order to provide a more realistic estimate of the detector acceptance, together with the reconstruction and selection efficiencies. In the fast Monte Carlo, all the kinematically allowed decay channels of the $D_{(s)}$ and $B_{(s)}$ mesons are included in the simulation and contribute to the sterile neutrino spectrum with relative contributions that vary according to the sterile neutrino couplings

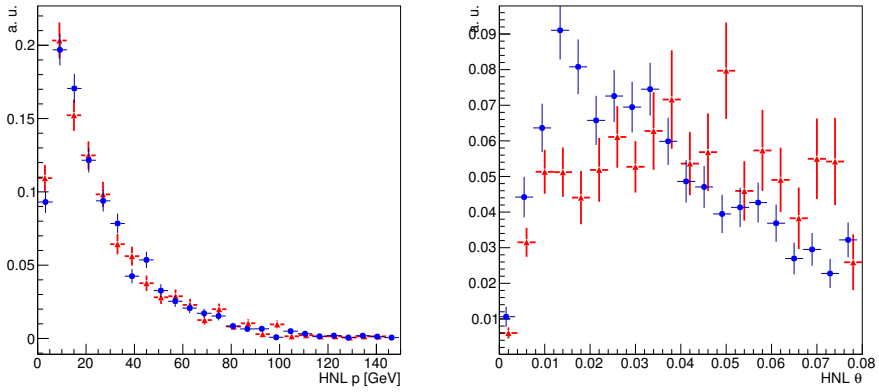

Figure 3.4: Sterile neutrino momentum (left) and polar angle (right) distributions obtained in FairShip (red) and in the fast Monte Carlo (blue) [1].

and mass. In the FairShip software, only the charm contribution was initially included, and the mass/coupling dependence of the branching ratios was neglected (see Section 3.1.2). To achieve a fair comparison between the two techniques, only sterile neutrinos coming from D_s mesons were used, both in the fast Monte Carlo and in FairShip, to produce Table 3.1 and Figure 3.4.

3.1.3. Reconstruction efficiency and offline selection

In this section the offline selection of HNL is studied. The main background, consisting of SM neutrinos interacting in the vicinity of the decay volume, is used as a case study to optimize the selection criteria. The remaining background, mainly coming from cosmic muons or residual muons from the proton-target interaction, is sub-dominant. Two-charged particles events due to cosmic rays interacting in the material will be reduced to a negligible level by the liquid scintillator tagger and by the requirement of a reasonably small impact parameter with respect to the target. Combinatorial background will also be identified, thanks to the dedicated timing detector. Signal-like events due to the decay of a V^0 produced in the interaction of a neutrino with the upstream material are also efficiently vetoed thanks to a system of several tagging detectors [1].

Figures 3.5-3.7 show distributions of number of degrees of freedom (ndf), reduced chi-square χ^2/ndf, distance of closest approach of the daughter tracks, z position of the decay vertex, reconstructed candidate mass and reconstructed mass for events with $\chi^2/ndf < 5$ and $ndf > 15$, and impact parameter to the target. These observables are shown for $HNL \to \mu\pi$, $HNL \to \mu\mu\nu$ and $HNL \to ee\nu$ decays, respectively, and superimposed to the same observables for neutrino-induced background [1].

The main criterion to design the selection is the goal to achieve an estimate of less than one background event in the whole data taking period, keeping an high efficiency for both the

	m_N [GeV/c^2]	U_e^2	U_μ^2	U_τ^2	Model	fMC $\mathcal{A} \times \mathcal{P}_{\text{vtx}}$	FairShip $\mathcal{A} \times \mathcal{P}_{\text{vtx}}$	Ratio fMC/FairShip
$HNL \to \pi\mu$	1.1	6.25×10^{-10}	1.00×10^{-8}	2.38×10^{-9}	2	2.96×10^{-5}	2.64×10^{-5}	1.12
	1.1	3.13×10^{-9}	5.00×10^{-8}	1.19×10^{-8}	2	1.44×10^{-4}	1.45×10^{-4}	0.99
	1.0	4.47×10^{-10}	7.15×10^{-9}	1.70×10^{-9}	2	5.76×10^{-6}	5.55×10^{-6}	1.04
	1.0	6.25×10^{-9}	1.00×10^{-7}	2.38×10^{-8}	2	8.04×10^{-5}	7.85×10^{-5}	1.02
	1.0	1.00×10^{-9}	1.92×10^{-11}	1.92×10^{-11}	1	7.23×10^{-7}	7.07×10^{-7}	1.02
	1.0	9.09×10^{-10}	1.00×10^{-8}	1.00×10^{-8}	5	1.04×10^{-5}	8.98×10^{-6}	1.16
	0.6	6.25×10^{-10}	1.00×10^{-8}	2.38×10^{-9}	2	4.48×10^{-7}	5.63×10^{-7}	0.80
	0.6	3.64×10^{-9}	4.00×10^{-8}	4.00×10^{-8}	5	2.33×10^{-6}	3.11×10^{-6}	0.75
	0.5	6.25×10^{-10}	1.00×10^{-8}	2.38×10^{-9}	2	1.89×10^{-7}	2.26×10^{-7}	0.84
	0.5	6.25×10^{-9}	1.00×10^{-7}	2.38×10^{-8}	2	1.85×10^{-6}	2.62×10^{-6}	0.71
	0.5	6.25×10^{-8}	1.00×10^{-6}	2.38×10^{-7}	2	1.79×10^{-5}	2.58×10^{-5}	0.69
	0.5	1.00×10^{-8}	1.92×10^{-10}	1.92×10^{-10}	1	1.86×10^{-7}	2.05×10^{-7}	0.91
	0.3	5.00×10^{-9}	8.00×10^{-8}	1.90×10^{-8}	2	1.09×10^{-7}	1.25×10^{-7}	0.87
$\mu\mu\nu$	1.0	4.47×10^{-10}	7.15×10^{-9}	1.70×10^{-9}	2	6.44×10^{-6}	5.88×10^{-6}	1.10
$ee\nu$	1.0	1.00×10^{-6}	1.92×10^{-8}	1.92×10^{-8}	1	3.36×10^{-10}	2.42×10^{-10}	1.39

Table 3.1: Comparison of signal acceptances for the $HNL \to \pi\mu$, $\mu\mu\nu$ (in the benchmark scenario) and $ee\nu$ (in a scenario with couplings $O(10^{-6})$ and $m_N = 100$ MeV/c^2) decay channels using the fast Monte Carlo and FairShip. The first four columns specify the position in the HNL parameter space. The fifth column identifies the scenario among those presented in this section. The sixth column is the result obtained with the fast Monte Carlo simulation, and the seventh column is the FairShip result. Finally, the last column shows the ratio between the two results. Most ratios are compatible with unity within the uncertainty. The oscillation are due to the fact that the HNL physics is represented only partially in the FairShip software, and to the poor statistical significance obtainable with the fast MC [1].

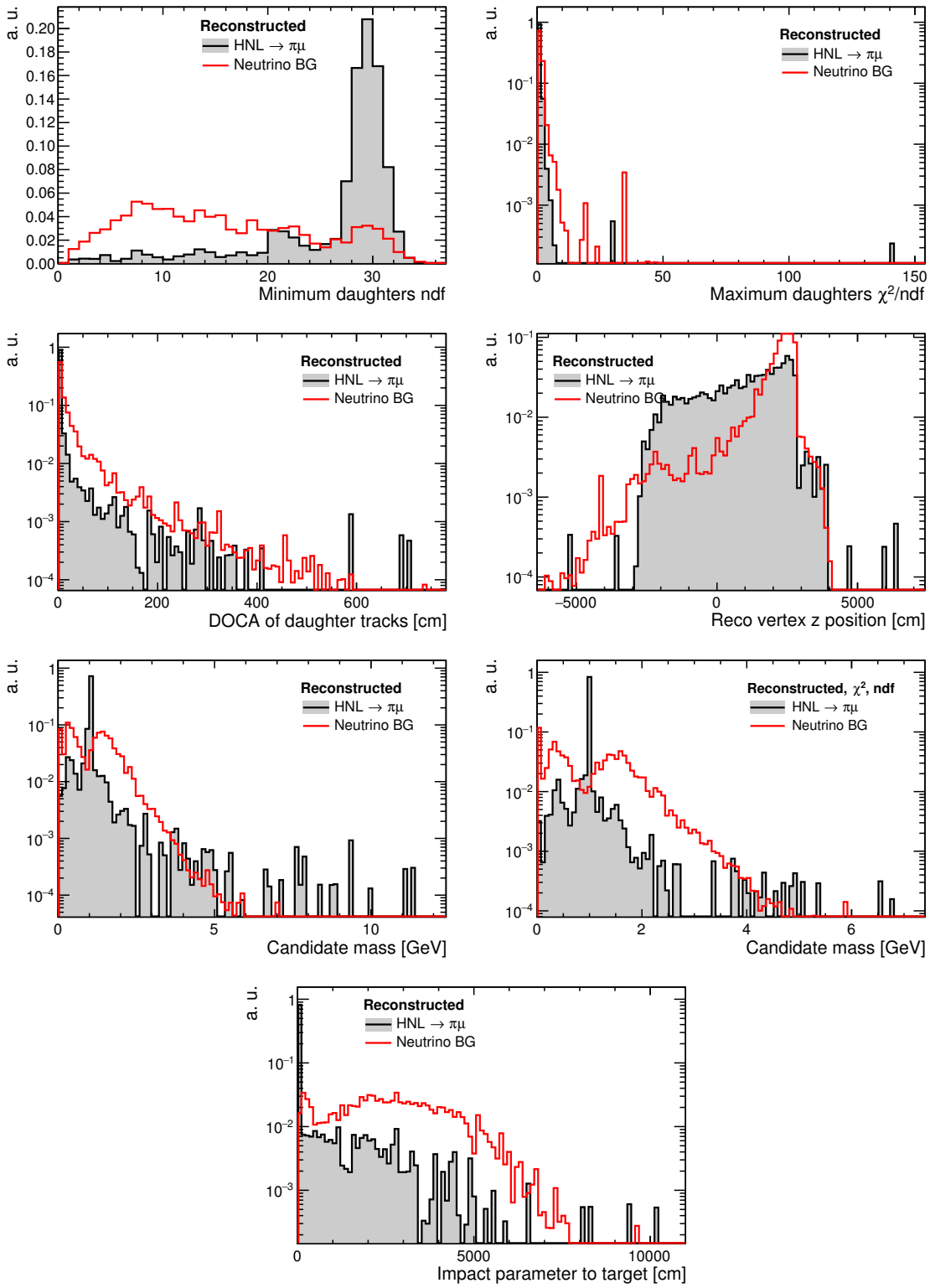

Figure 3.5: χ^2/ndf, ndf, distance of closest approach of the daughter tracks, z position of the decay vertex, reconstructed candidate mass and reconstructed mass for events with $\chi^2/ndf < 5$ and $ndf > 15$, and impact parameter to the target distributions for 2-track signal candidates in the $HNL \rightarrow \mu\pi$ channel (solid black line). The red line represents neutrino-induced reconstructed background events [1].

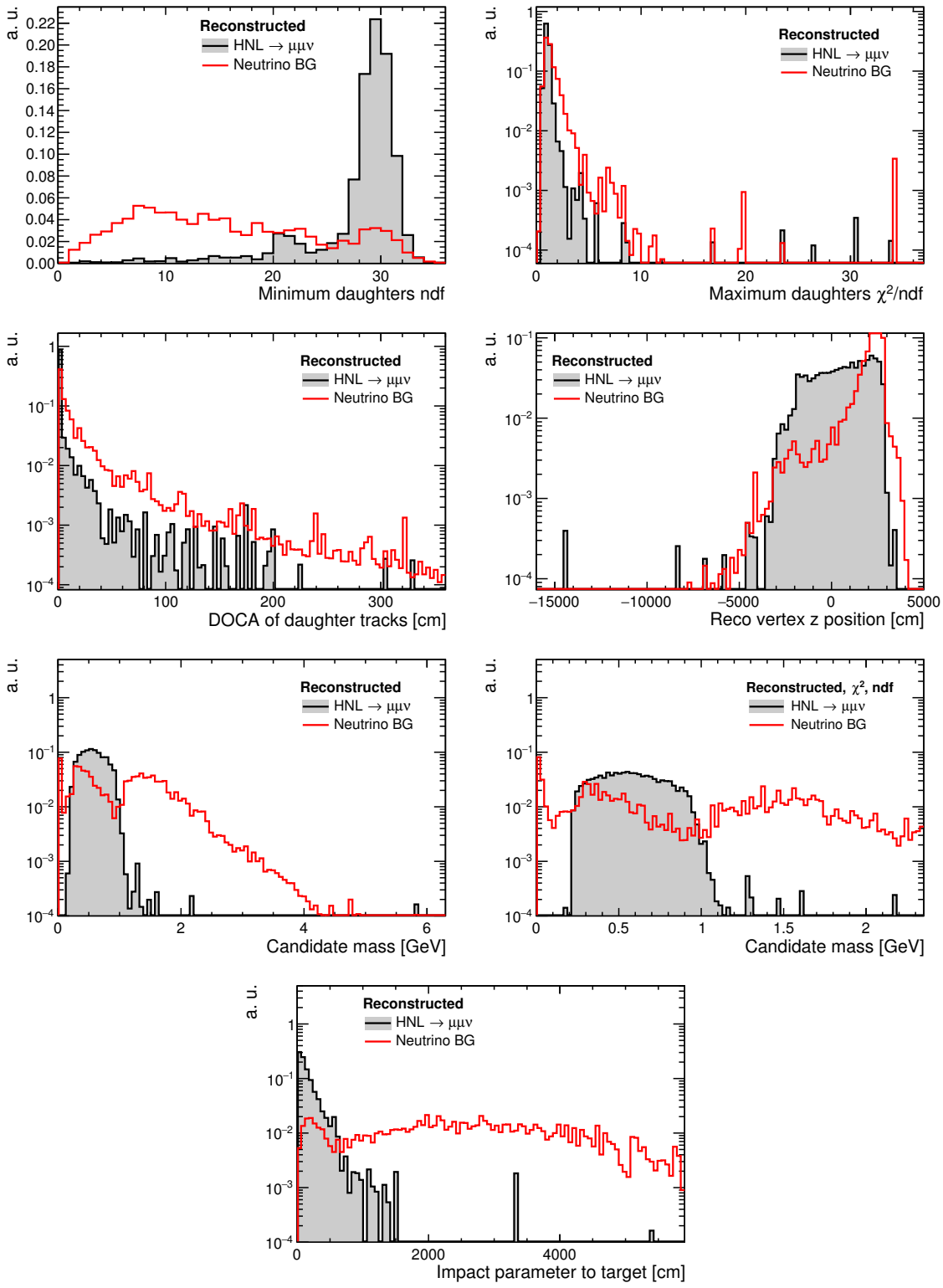

Figure 3.6: χ^2/ndf, ndf, distance of closest approach of the daughter tracks, z position of the decay vertex, reconstructed candidate mass and reconstructed mass for events with $\chi^2/ndf < 5$ and $ndf > 15$, and impact parameter to the target distributions for 2-track signal candidates in the $HNL \to \mu\mu\nu$ channel (solid black line). The red line represents neutrino-induced reconstructed background events [1].

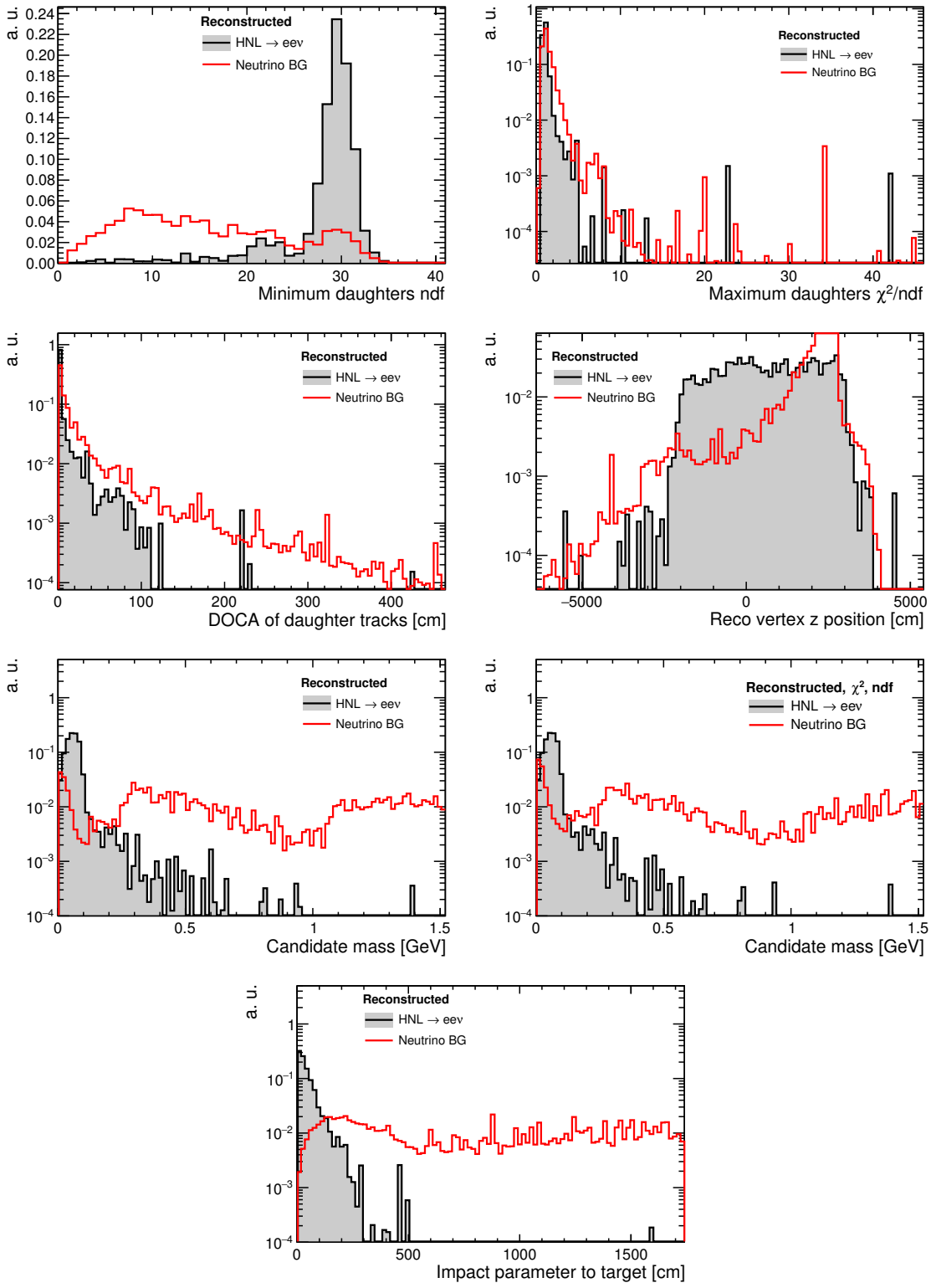

Figure 3.7: χ^2/ndf, ndf, distance of closest approach of the daughter tracks, z position of the decay vertex, reconstructed candidate mass and reconstructed mass for events with $\chi^2/ndf < 5$ and $ndf > 15$, and impact parameter to the target distributions for 2-track signal candidates in the $HNL \rightarrow eev$ channel (solid black line). The red line represents neutrino-induced reconstructed background events [1].

fully reconstructed (mainly $HNL \to \pi\mu$) and the partially reconstructed signal ($HNL \to \ell\ell\nu$). The following four kinds of selection criteria have been devised:

- Track multiplicity:
  - "1 HNL candidate": only one candidate is reconstructed, i.e. the event contains only two charged tracks.
- Fiducial cuts:
  - "Vtx in fiducial vol.": the vertex is located in the fiducial volume, at least 20 cm downstream of the straw veto, and at least 20 cm upstream of the first tracker station (which longitudinal vertex resolution is $\sigma_z \sim 9$ cm). It is contained in the elliptical shape of the vessel, with a 1 cm tolerance at the border (the transversal vertex resolution is $\sigma_{x,y} \sim 0.3$ cm).
  - "Tracks in fiducial vol.": the tracks forming the HNL candidate are fully contained in the vessel, with a 1 cm tolerance at the border.
- Track quality cuts:
  - "Event reconstructed": the track fit converged for both daughter tracks. FairShip only creates a reconstructed HNL candidate if two reconstructed tracks of opposite charge create a vertex with a maximum closest-approach distance of 30 cm.
  - "N.d.f. > 25": number of degrees of freedom > 25. This ensures a sufficient amount of hits in each tracking station. Tracks not crossing all the 4 tracking stations are not reconstructed.
  - "DOCA < 1 cm": distance of closest approach between the two charged tracks < 1 cm: the average for signal events is 3.6 mm.
  - "$\chi^2/\text{ndf} < 5$": the reduced chi-square of the track fit is less than 5 for both daughters.
- Background-suppressing cuts:
  - daughters track momentum > 1.5 GeV: this helps suppressing the combinatorial background.
  - "IP < 10 cm": impact parameter to the target < 10 cm: the average for fully reconstructed signal events is 1.65 cm. This cut is released to 2.5 m for partially reconstructed final states.
  - "Event not vetoed": it corresponds to the online selection, i.e. no activity in any of the VETO detectors: upstream veto, straw veto, liquid scintillator and the ν_τ RPC muon spectrometer, which can act as a background tagger for HS searches.
- Particle identification:

– for final states including one (two) muons, the efficiency of a selection based on the presence of one (two) muon track(s) in the first two muon stations is evaluated.

The number of sterile neutrino candidates selected after the different requirements is given in Tables 3.2 to 3.4 for signal samples, and in Table 3.5 for a sample of neutrino-induced background events (see Section 3.1.4). The online selection ("Event not vetoed") is applied at the end of the selection chain, with the purpose of increasing the statistical significance of the computed efficiencies on the neutrino background of the offline selections. The efficiency of each cut is computed with respect to the preceding cut. In particular, Table 3.6 shows the effect of the online selection alone on the neutrino background.

Selection	**Entries**	**Acceptance**	**Selection efficiency**
Event reconstructed	4471	6.43×10^{-6}	–
1 HNL candidate	4386	6.27×10^{-6}	97.6 %
Vtx in fiducial vol.	3777	5.37×10^{-6}	85.7 %
Tracks in fiducial vol.	3508	4.77×10^{-6}	88.8 %
N.d.f. > 25	3345	4.45×10^{-6}	93.2 %
DOCA < 1 cm	3161	4.15×10^{-6}	93.3 %
χ^2/N.d.f. < 5	3161	4.15×10^{-6}	100.0 %
Daughters $P > 1$ GeV	3160	4.15×10^{-6}	99.9 %
IP < 10 cm	3137	4.11×10^{-6}	99.1 %
Event not vetoed	2969	3.91×10^{-6}	95.1 %
1 muon in 1^{st} muon station	2955	3.89×10^{-6}	99.4 %
1 muon in 2^{nd} muon station	2916	3.82×10^{-6}	98.2 %

Table 3.2: Effect of the offline selection on $HNL \to \pi\mu$. The second column lists the number of events selected from the original sample. The third column corresponds to the sum of weights (see text) of the selected events divided by the original sample size. The fourth column lists the individual efficiency on signal candidates for each cut of the selection chain, calculated relative to the weighted acceptance yielded by all preceding cuts.

The resulting acceptance after all selection criteria are applied is compared with the raw acceptance computed with the fast Monte Carlo. The ratio between these two values is applied as efficiency factor to the fast simulation in order to take into account the reconstruction and selection efficiencies when providing estimates for the SHiP sensitivity to sterile neutrinos.

3.1.4. Background studies

The principal background to the hidden particle decay signal originates from the inelastic scattering of neutrinos and muons in the vicinity of the detector, producing long-lived neutral mesons. Another source of background are random combinations of tracks from the residual muon flux, or other charged particles from inelastic interactions in the proximity, which enter

Selection	Entries	Acceptance	Selection efficiency
Event reconstructed	4856	7.64×10^{-6}	–
1 HNL candidate	4855	7.63×10^{-6}	100.0 %
Vtx in fiducial vol.	4184	6.6×10^{-6}	86.4 %
Tracks in fiducial vol.	4063	6.33×10^{-6}	95.9 %
N.d.f. > 25	3791	5.62×10^{-6}	88.8 %
DOCA < 1 cm	3475	5.05×10^{-6}	89.9 %
χ^2/N.d.f. < 5	3475	5.05×10^{-6}	100.0 %
Daughters $P > 1$ GeV	3469	5.04×10^{-6}	99.7 %
IP < 2.5 m	3231	4.3×10^{-6}	85.3 %
Event not vetoed	3151	4.14×10^{-6}	96.3 %
2 muons in 1^{st} muon station	3092	4.02×10^{-6}	97.1 %
2 muons in 2^{nd} muon station	2996	3.84×10^{-6}	95.6 %

Table 3.3: Effect of the offline selection on $HNL \to \mu\mu\nu$. The second column lists the number of events selected from the original sample. The third column corresponds to the sum of weights (see text) of the selected events divided by the original sample size. The fourth column lists the individual efficiency on signal candidates for each cut of the selection chain, calculated relative to the weighted acceptance yielded by all preceding cuts.

Selection	Entries	Acceptance	Selection efficiency
Event reconstructed	2755	1.78×10^{-10}	–
1 HNL candidate	2753	1.78×10^{-10}	99.9 %
Vtx in fiducial vol.	2232	1.46×10^{-10}	82.0 %
Tracks in fiducial vol.	2232	1.46×10^{-10}	100.0 %
N.d.f. > 25	2080	1.29×10^{-10}	88.0 %
DOCA < 1 cm	1652	9.13×10^{-11}	71.1 %
χ^2/N.d.f. < 5	1652	9.13×10^{-11}	100.0 %
Daughters $P > 1$ GeV	1590	8.44×10^{-11}	92.4 %
IP < 2.5 m	1590	8.44×10^{-11}	100.0 %
Event not vetoed	1538	8.21×10^{-11}	97.3 %

Table 3.4: Effect of the offline selection on $HNL \to ee\nu$. The second column lists the number of events selected from the original sample. The third column corresponds to the sum of weights (see text) of the selected events divided by the original sample size. The fourth column lists the individual efficiency on signal candidates for each cut of the selection chain, calculated relative to the weighted acceptance yielded by all preceding cuts.

Selection	Entries	Events / 5 years	Selection efficiency
Event reconstructed	79547	2.11×10^4	–
1 HNL candidate	60469	1.67×10^4	79.1 %
Vtx in fiducial vol.	13687	3.61×10^3	21.6 %
Tracks in fiducial vol.	13291	3.5×10^3	97.0 %
N.d.f. > 25	7064	1.65×10^3	47.1 %
DOCA < 1 cm	752	228	13.9 %
χ^2/N.d.f. < 5	751	228	99.9 %
Daughters $P > 1$ GeV	519	137	60.2 %
IP < 10 cm (2.5 m)	1 (265)	0.139 (47)	0.1 % (34.2 %)
Event not vetoed	0	0	0.0 %

Table 3.5: Effect of the offline selection on neutrino-induced background. The second column lists the number of events selected from the original sample. The third column corresponds to the sum of weights (see text) of the selected events divided by the original sample size. The fourth column lists the individual efficiency on signal candidates for each cut of the selection chain, calculated relative to the weighted acceptance yielded by all preceding cuts.

Selection	Entries	Events / 5 years	Selection efficiency
Event reconstructed	79547	2.11×10^4	–
Event not vetoed	215	64.2	0.3 %

Table 3.6: Effect of the online selection on neutrino-induced background. The second column lists the number of events selected from the original sample. The third column corresponds to the sum of weights (see text) of the selected events divided by the original sample size. The fourth column lists the individual efficiency on signal candidates for each cut of the selection chain, calculated relative to the weighted acceptance yielded by all preceding cuts.

the decay volume and together mimic signal events. Cosmic muons can contribute to both types of background, but their yield is expected to be small [1, 38].

Studies performed using the full SHiP Monte Carlo simulation indicate that a level of background of 0.1 events for 5 years of data taking is achievable, thanks to the redundant system of veto detectors [1, 30].

The flux of neutrinos is estimated to be 10^{11} neutrinos per spill. Background studies were performed with an energy spectrum ranging from 2 GeV to about 100 GeV[1]. Neutrinos are mainly produced in decays of pions and kaons produced at the SHiP target. A large sample of neutrino interactions with the detector material was simulated, corresponding to the amount of neutrino interactions expected in five years of SHiP operation.

Neutrino interactions were found to take place mainly in the muon magnetic spectrometer of the tau neutrino detector, and in the entrance window and the surrounding walls of the vacuum vessel. The probability that neutrinos interact with the residual gas inside the decay volume is negligible. Overall we expect about 10^7 neutrino interactions in 5 years; about 10^4 such events have two tracks of opposite charge reconstructed in the HS spectrometer as potential signal candidates [1]. The topology of these events is such that the relatively loose signal selection criteria introduced in Section 3.1.3, together with the online preselection operated by the veto detectors, allow to reject the totality of the simulated background-induced candidate events: the interaction products do not point at the target, do not have a reconstructed vertex inside the decay volume, and have very poor track quality. This is true, in general, for all background sources [1, 30].

At the level of online selection, the requirement of having at least one veto detector with a positive response, together with a loose requirement on the pointing of the interaction products to the target, rejects about 99.7% of tracks coming from neutrino interactions (see Table 3.6). If no online selection was applied, the signal selection criteria introduced in Section 3.1.3, with an impact parameter lower than 10 cm (2.5 m) with respect to the proton target, would allow anyway the rejection of 99.99% (99.77%) of the reconstructed neutrino-induced candidates (see Table 3.5). Figures 3.5-3.7 show a comparison of the distributions of the observables used in the offline selection for the HNL signal and the neutrino background. The set of selections applied is higly redundant and can be trimmed down to study specific channels.

3.1.5. Sensitivity to HNLs

The signal acceptance of $\mathcal{A} = (5.6 \pm 0.6) \times 10^{-6}$ quoted in Section 3.1.2 decreases to $\mathcal{A} = (4.4 \pm 1.8) \times 10^{-6}$ at the reconstruction level, following the offline selections. This reduction is accounted for in the fast Monte Carlo.

[1] Neutrinos with energy lower than 2 GeV have negligible impact on the background studies, since they mostly interact through elastic scattering.

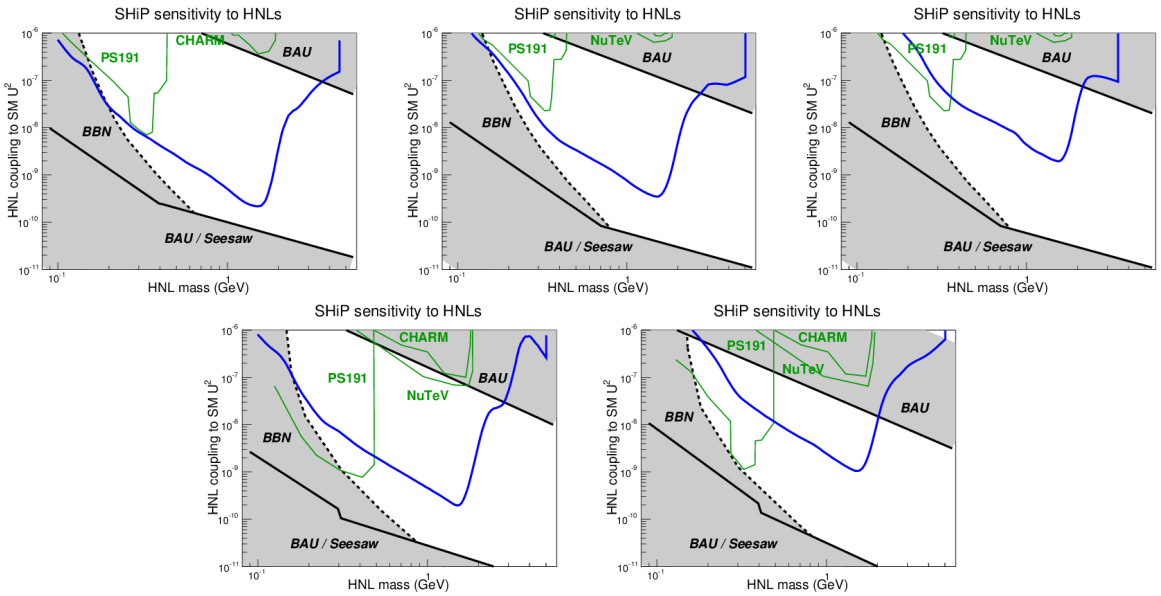

Figure 3.8: Sensitivity contours in the parameter space of the νMSM for scenarios I–V introduced in Section 3.1. They can be interpreted as 90% C.L. exclusion limits if no event will be observed, assuming a level of background of 0.1 events in 5 years, and as 3σ discovery potential if two events are observed.

Having validated the fast Monte Carlo results against those of the full simulation (Section 3.1.2), it can be used to assess the sensitivity contours in the sterile neutrino mass-couplings parameter space. The fast Monte Carlo technique has the advantage of being computationally faster and easier to configure with respect to a change of coordinates in the HNL parameter space. It can also be used to completely determine the expected number of signal events in five years of SHiP operation, because it provides algorithms to estimate both the rate of sterile neutrinos produced at the target and the acceptance to the sterile neutrino decay products. On the other hand, the accuracy of the result is of the order of 30%. Fluctuations due to fine tunings of the selection criteria would be subdominant with respect to statistic fluctuations. Therefore, following the analysis of Tables 3.2-3.4, averaging over the reconstruction and selection efficiencies of the different final states, we apply a correction factor of

$$f_{\text{reco}} = \begin{cases} 40\% & \text{if } m_N < 2m_\mu \\ 60\% & \text{otherwise} \end{cases} \tag{3.10}$$

to the final result of the fast simulation in order to account at once for the efficiency of the track reconstruction algorithms and for that of the selection criteria.

The SHiP sensitivity, evaluated for the five scenarios introduced in Section 3.1, is shown in the five plots of Figure 3.8, respectively. The figures also show the variation of the νMSM parameter space for different relative strengths of the cuplings to the three SM flavours.

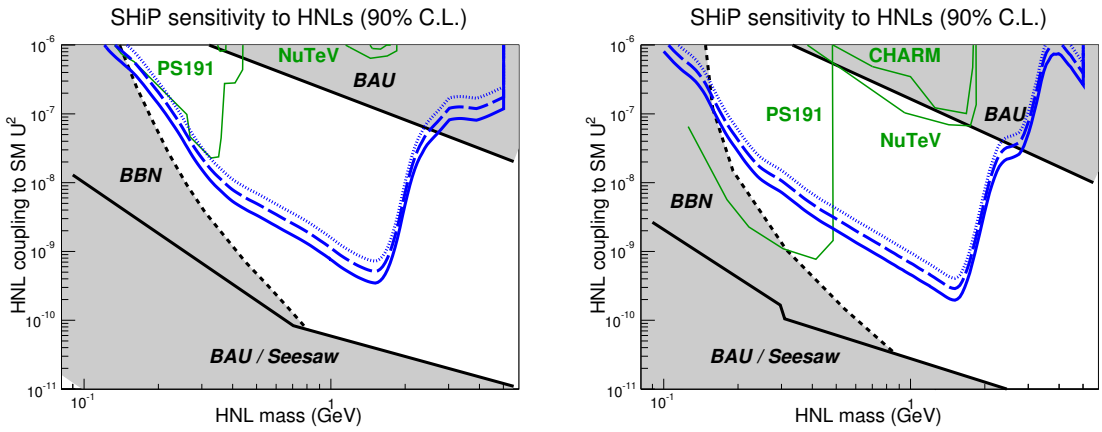

Figure 3.9: Variation of the sensitivity contours for scenarios II (left) and IV (right) as a function of the background estimates. The solid blue curve represents the 90% C.L. upper limit assuming 0.1 background events in 2×10^{20} proton-target collisions. The dashed blue curve assumes 10 background events. The dotted blue curve assumes a systematic uncertainty of 60% on the level of background, i.e. 10 ± 6 background events [30, 38].

Regions of large coupling and mass ("BAU") are greyed out because a HNL with those parameters would not suffice to explain the level of matter-antimatter asymmetry in the Universe. Observations of Big Bang nucleosynthesis would find a natural explanation in the νMSM if the two massive HNLs lie in the region to the right of the "BBN" curve. Finally, couplings that are too low would not allow the SM neutrino masses to be generated through the seesaw mechanism ("Seesaw" curve in the plots). The exclusion limits set by previous experiments are also shown in the plots [10, 17].

Finally, Figure 3.9 shows the impact on the sensitivity of a higher level of background in SHiP. The assumption of 10 background events in the nominal data taking period (a yield 100 larger than the expected), and even with a systematic uncertainty of 60%, would only marginally affect the HNL sensitivity, compared to the significant improvement with respect to the limits set by previous experiments. Moreover, the estimates shown in Figure 3.9 do not take into account that the invariant mass can be used as additional selection criterium, once an hypotesis on the HNL mass is made.

3.2. HNL search at future circular colliders

Heavy right-handed neutrinos can also be searched for at high luminosity lepton colliders, such as the Future e^+e^- Circular Collider (FCC-ee), currently being studied within the "Future Circular Collider Study" project at CERN [53]. The machine being studied would fit in a 100 km tunnel and would be able to address centre-of-mass energies in the 90-350 GeV range, allowing precision tests of the Standard Model and accurate measurements of the characteristics of the Higgs boson. FCC-ee would represent a first step towards the ultimate goal of a 100 TeV

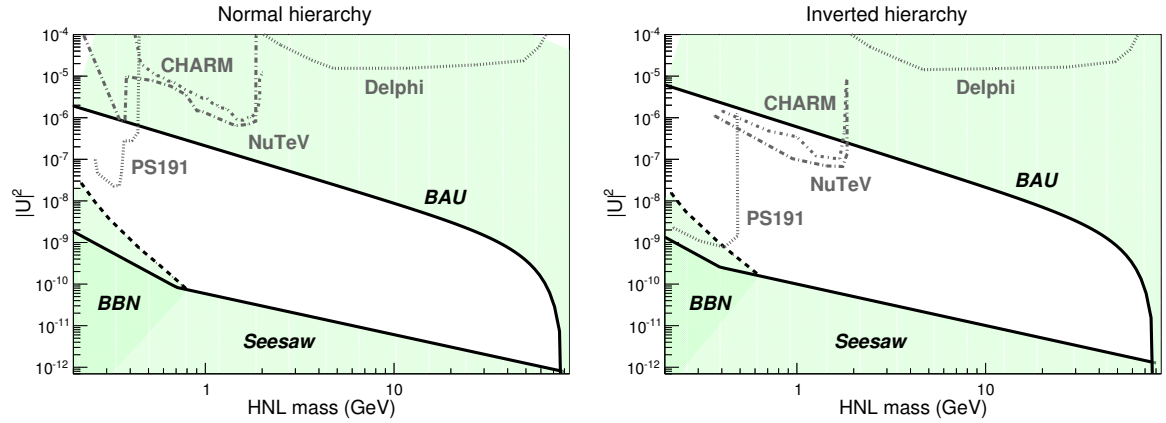

Figure 3.10: Interesting domains in the mass-coupling parameter space of heavy neutrinos and current experimental limits, for normal and inverted hierarchy of the left-handed neutrino masses [45].

proton collider that would fit in the same tunnel. Luminosity studies show that such e^+e^- machine, operated at the centre-of-mass energy corresponding to the Z resonance, could produce 10^{12} to 10^{13} Z bosons per year with the "crab-waist" scheme, and thus allow to investigate extremely rare decays [54–56].

The portion of the νMSM parameter space accessible for the SHiP experiment was described in Section 3.1.5. In [45] we extend the mass range up to the mass of the W boson. For HNL masses $m_N \gtrsim m_W$, the rate of interactions is enhanced due to the now kinematically allowed decay channel $HNL \to \ell W$, leading to stronger constraints on the mixing parameter resulting from baryon-antibaryon asymmetry (BAU) [57]. The resulting parameter space (Figure 3.10) is bound on all sides, due to the intersection of the BAU and seesaw constraints.

A review of possible methods to perform HNL searches at future e^+e^- colliders is given in [45]. Hints of the existence of sterile neutrinos can be found in the discrepancy between the measured number of neutrino families – the ratio of the Z invisible width to its leptonic decay width – and that of the SM lepton flavours. The former, $N_\nu = 2.9840 \pm 0.0082$ [58], appears to be about two standard deviations lower than three, and such decifit could be compatible with the presence of sterile neutrinos. However, for small mixing angles between sterile and active neutrinos as those predicted by all models trying to explain the BAU, the most efficient way to look for sterile neutrinos at a lepton collider is to operate it as a Z factory.

HNLs can be produced in $Z \to \nu\bar{\nu}$ decays with a SM neutrino kinematically mixing to an HNL, therefore producing $Z \to \nu HNL$. At very small couplings, the lifetime of the HNL becomes substantial, giving the possibility to suppress background arising from W^*W^*, Z^*Z^* and $Z^*\gamma^*$ processes with the requirement of a displaced secondary vertex.

A method analogous to the one outlined in Section 3.1.1 was used to estimate the expected HNL yield at an hypotetical general purpose experiment at the FCC-ee. A simple detector with spherical symmetry and 100% reconstruction efficiency is assumed. All di-lepton final

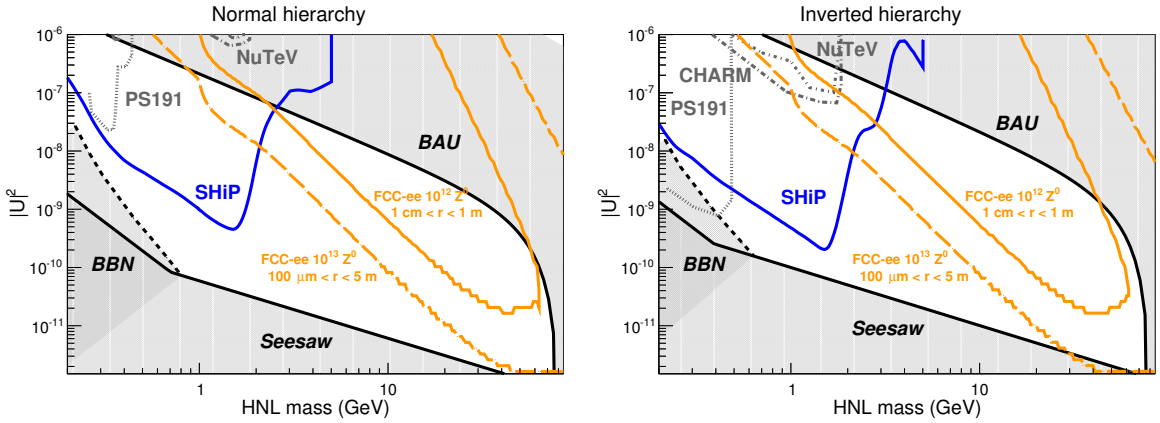

Figure 3.11: Physics reach in the HNL parameter space for SHiP and two realistic FCC-ee configurations for νMSM scenarios II (left) and IV (right). Previous searches are shown in green. Greyed-out areas represent the cosmological boundaries of the scenario [25, 45].

states $\ell^+\ell^-\nu$ are considered detectable. The expected HNL yield is computed as

$$n(HNL) = n(Z) \times 2\,\mathrm{Br}(Z \to \nu\bar{\nu}) \times U_{tot}^2 \times \mathcal{P}_{vtx} \times \mathrm{Br}(HNL \to \text{visible}) \tag{3.11}$$

where $n(Z)$ is the integrated Z yield and the factor 2 accounts for the fact that both neutrinos can mix to the HNL. The $\mathrm{Br}(HNL \to \text{visible})$ factor is the total visible leptonic branching ratio of the HNL and includes, depending on the HNL mass, $ee\nu$, $\mu\mu\nu$, $e\mu\nu$, $e\tau\nu$, $\tau\tau\nu$, and $\mu\tau\nu$ final states. $\mathcal{P}_{vtx}$ is simply computed as:

$$\mathcal{P}_{vtx}\left(m_N, U_f^2\right) = \int_{r_{min}}^{r_{max}} \frac{e^{-l/\gamma c\tau}}{\gamma c\tau}\, dl\,, \tag{3.12}$$

assuming that the detector has spherical symmetry. The integration boundaries r_{min} and r_{max} correspond to the minimum and maximum vertex displacement, which are given in turn by the tracking detector vertex resolution and by its overall size. If the accelerator operates at $\sqrt{s} = m_Z$, Z bosons decay at rest and the HNL lifetime is boosted by a factor $\gamma = m_Z/2m_N + m_N/2m_Z$ [25].

Figure 3.11 compares the sensitivities of SHiP and of an hypotetical FCC-ee experiment in the parameter space of the νMSM, for two realistic FCC-ee configurations. The minimum and maximum displacements of the secondary vertex in FCC-ee depend on the characteristics of the tracking detectors of the hypotetical general purpose experiment. For the first (second) FCC-ee configuration, an inner tracker with resolutions of 100 μm (1 mm) and an outer tracker with diameter of 1 m (5 m) have been considered. The production of 10^{12} (10^{13}) Z bosons is assumed.

The SHiP experiment will be able to scan a large part of the parameter space below the B meson mass. On the other hand, the results shown in Figure 3.11 show that heavier HNLs

can be searched for at a future Z factory. The synergy between SHiP and a future Z factory would allow the exploration of most of the νMSM parameter space [25].

3.3. Sensitivity in the Vector Portal

A method similar to the one presented in Section 3.1.1, and analogous the one used by the authors of [24], is used to estimate SHiP's sensitivity to dark photons. The expected number of recorded dark photon events at SHiP is given by:

$$n(\gamma') = N(p.o.t.) \times \chi(pp \to \gamma') \times \mathcal{P}_{\text{vtx}} \times \mathcal{A}_{\text{tot}}(\gamma' \to \text{visible}), \tag{3.13}$$

in analogy with Eqn. 3.1 for HNLs.

To compute the production rate $\chi(pp \to \gamma')$, two dark photon production processes are considered: proton bremsstrahlung and decays of secondary mesons (see Section 2.1.2).

3.3.1. Production in proton bremsstrahlung

For production via $p \to p + \gamma'$, the differential production rate is analytically determined through Eqn. 2.12 within the limits given by the beam and the geometry of the SHiP detector. We take the inelastic proton-proton cross-section from experimental data:

$$\sigma_{pp}(s') = Z + B \cdot \log^2\left(\frac{s'}{s_0}\right) + Y_1\left(\frac{s_1}{s'}\right)^{\eta_1} - Y_2\left(\frac{s_1}{s'}\right)^{\eta_2}, \tag{3.14}$$

where $Z = 35.45$ mb, $B = 0.308$ mb, $Y_1 = 42.53$ mb, $Y_2 = 33.34$ mb, $\sqrt{s_0} = 5.38$ GeV, $\sqrt{s_1} = 1$ GeV, $\eta_1 = 0.458$ and $\eta_2 = 0.545$ [28].

In Eqn. 2.12, z is the fraction of the proton momentum P_p carried away by the γ' in the direction of incoming proton and $p_\perp$ is the transverse momentum of the dark photon. In particular:

$$P_p^\mu = \left(E_p,\ P_p,\ \vec{P_{p\perp}} = \vec{0}\right) \qquad \text{Proton four-momentum} \tag{3.15}$$

$$p^\mu = \left(E\left(z, P_p, \theta\right),\ zP_p,\ \vec{p_\perp}\left(\theta\right)\right) \qquad \text{Dark photon four-momentum} \tag{3.16}$$

Eqn. 2.12 was rewritten as a function of the dark photon angle and total momentum, by means

Mass interval (GeV)	Process	$n_{\gamma'}/p.o.t/\epsilon^2$
$m_{\gamma'} < 0.135$	$\pi^0 \to \gamma\gamma'$	5.41
$0.135 < m_{\gamma'} < 0.548$	$\eta \to \gamma\gamma'$	0.23
$0.548 < m_{\gamma'} < 0.648$	$\omega \to \pi^0\gamma'$	0.07
$0.648 < m_{\gamma'} < 0.958$	$\eta' \to \gamma\gamma'$	10^{-3}

Table 3.7: Dominating modes for γ' production in meson decays at SHiP.

of the following transformations:

$$\frac{dN}{dpd\theta} = \frac{dN}{dzdp_\perp^2}\frac{dp_\perp^2}{d\theta}\frac{dz}{dp} \tag{3.17}$$

$$\theta = p_\perp / zP_p \tag{3.18}$$

$$\frac{dp_\perp^2}{d\theta} = 2p_\perp \frac{dp_\perp}{d\theta} = 2p_\perp zP_p = 2\theta z^2 P_p^2 \tag{3.19}$$

$$p = \sqrt{p_\perp^2 + z^2P_p^2} = \sqrt{z^2P_p^2\left(\theta^2+1\right)} \tag{3.20}$$

$$\frac{dp}{dz} = \frac{zP_p^2\left(\theta^2+1\right)}{\sqrt{z^2P_p^2\left(\theta^2+1\right)}} = P_p\sqrt{\theta^2+1} \quad \Longrightarrow \quad \frac{dz}{dp} = \frac{1}{P_p\sqrt{\theta^2+1}} \tag{3.21}$$

This way we obtain a two-dimensional probability density function in $f(p,\theta)$. The integral of f in the kinematically allowed range of momenta, restricted to a solid angle accessible to SHiP, provides an estimate of the total dark photon production rate through proton bremsstrahlung at the SHiP facility. The conditions of validity of the Fermi-Weizsäcker-Williams approximation [59, 60] used to derive the formulas of Section 2.1.2 require us to set the momentum lower bound to $p_{min} = 0.14P_p$ [24]. The effect of a momentum upper bound lower than the kinematically allowed one is negligible for the integration of $f(p,\theta)$ over the γ' spectrum accessible at SHiP.

The product $\chi(pp \to \gamma') \times \mathcal{P}_{\text{vtx}}$ is computed at once (see Section 3.3.3).

3.3.2. Production in decays of secondary mesons

For meson decays, a Monte Carlo approach is used:

1. A Pythia8 simulation is used to estimate the number of times per proton-target collision a photon in the final state is made available for kinetic mixing with γ'. The available channels vary according to the γ' mass. The dominating production channels and the amount of potential dark photons per pp collision are shown in Table 3.7.

2. According to the given $m_{\gamma'}$, the appropriate production channel is enabled in Pythia8 by resetting the decay table of the corresponding meson to a single channel with a SM

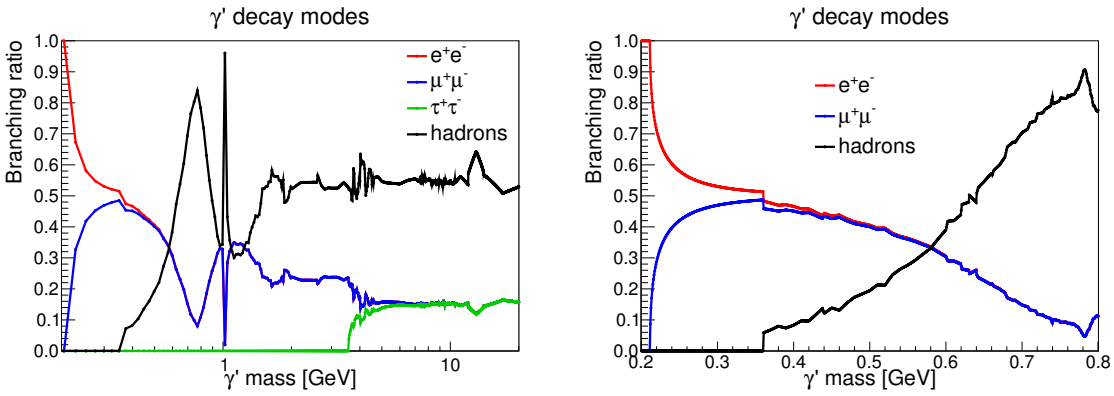

Figure 3.12: Branching ratios for the decay of dark photons as a function of the dark photon mass. The right hand plot shows the 0.2 - 0.8 GeV region in detail.

photon and a γ' in the final state;

3. 400 GeV/c^2 proton-target collisions are simulated until the amount of recorded dark photons reaches a statistically acceptable amount ($n_{\gamma'} > 10^3$);

4. the dark photons four-momenta are stored in an ntuple, and a two-dimensional PDF is built out of the dark photons within SHiP's geometrical acceptance.

The production rate is then computed as:

$$\chi(pp \to \gamma') = \frac{n_{\gamma'}/p.o.t}{\epsilon^2} \times \mathrm{Br}(M \to \gamma'), \tag{3.22}$$

where:

- M is the decaying meson;
- the first term is taken from Table 3.7 according to the γ' mass, and already takes into account the multiplicity of M mesons produced in a proton-target collision;
- the last term is computed according to Eqn. 2.13, 2.15.

3.3.3. Geometrical and final state acceptance

Once a four-momentum probability density function for dark photons is obtained, according to one of the preceding methods, each bin is re-weighted with the probability that dark photons with such four-momentum decay inside the SHiP decay volume, in analogy with Section 3.1.1, Eqn. 3.6:

$$\mathcal{P}_{vtx}\left(p, \theta | m_{\gamma'}, \epsilon\right) = \int_{\mathrm{SHiP}} \frac{e^{-l/\gamma c\tau}}{\gamma c\tau}\, dl. \tag{3.23}$$

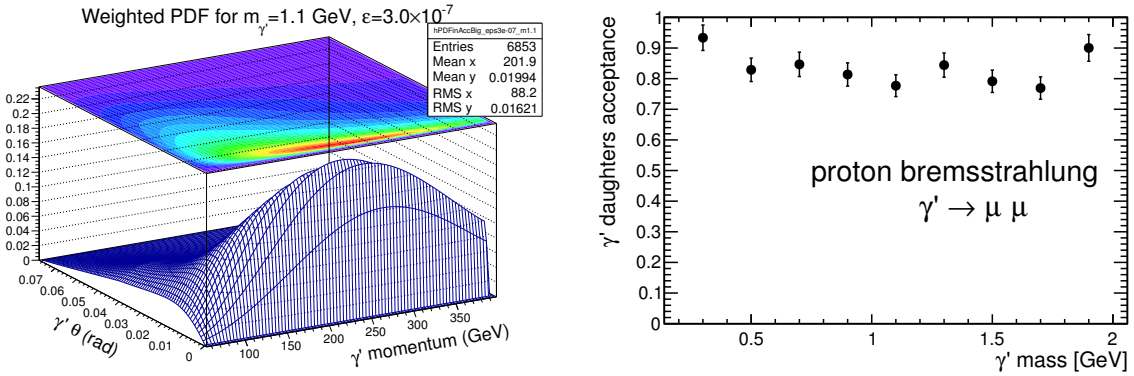

(a) Reweighted PDF for γ' produced by proton bremsstrahlung

(b) Final-state acceptance for γ' produced by proton bremsstrahlung decaying into $\mu^+\mu^-$

Figure 3.13: Details of the simulation outcome for dark photons produced by proton bremsstrahlung. The acceptance for the γ' decay products is high with respect to what seen for HNLs (see Section 3.1.1). This is due to the high boost obtained by dark photons in the $p \to p + \gamma'$ process.

The mean life of the dark photon is calculated by the inverse of the total decay width $\Gamma_{tot} = \sum_i \Gamma_i$, using the widths from Section 2.1.2. The ratio $R\left(\sqrt{s}\right)$ is interpolated from experimental values [28]. A plot of the obtained branching ratios is shown in Figure 3.12.

The integral in p, θ of the reweighted PDF represents the probability that dark photons with such mass and couplings decay with a vertex in the SHiP decay region:

$$\mathcal{P}_{vtx}(m_{\gamma'}, \epsilon) = \int \mathcal{P}_{vtx}\left(p, \theta | m_{\gamma'}, \epsilon\right)\, dp\, d\theta \tag{3.24}$$

In the case of γ' production by proton bremsstrahlung, the integral in p, θ of $\mathcal{P}_{vtx}\left(p, \theta | m_{\gamma'}, U_f^2\right)$ gives, using the boundaries described in Section 3.3.1, the whole product $\chi(pp \to \gamma') \times \mathcal{P}_{\text{vtx}}$, due to the analytical form of the γ' production rate.

According to the γ' mass, we simulate leptonic decays $\gamma' \to e^+e^-$ and $\gamma' \to \mu^+\mu^-$ in the rest frame of the γ'. For each event:

1. a decay vertex is generated inside the fiducial volume

2. the leptons are boosted according to a γ' four-momentum sampled from the re-weighted PDF

3. if both leptons go through the end cap of the fiducial volume, the event is considered in acceptance

The fraction $\mathcal{A}_i$ of events with both leptons in the acceptance is computed. The final state acceptance $\mathcal{A}_{\text{tot}}(\gamma' \to \text{visible})$ is computed from this fraction and the corresponding branching

ratio:

$$\mathcal{A}_{\text{tot}}(\gamma' \to \text{visible}) = \sum_{i=\text{visible channel}} \mathcal{BR}(\gamma' \to i) \times \mathcal{A}(i) \tag{3.25}$$

The above sum is operated on the leptonic modes only. In order to take hadronic decays into account, for which we do not have the exclusive branching ratios, an approximate rescaling is done by increasing the final result by the product $\text{Br}(\gamma' \to q\bar{q}) \times \chi(q\bar{q}\text{ visible})$, where $\chi(q\bar{q}\text{ visible})$ approximates the visible fraction of the hadronic final states and is set to:

$$\chi(q\bar{q}\text{ visible}|m_{\gamma'}) = \begin{cases} 1 & \text{if } m_{\gamma'} > 2 \times m_c \\ 2/3 & \text{otherwise} \end{cases}, \tag{3.26}$$

where m_c is the mass of the charm quark.

Finally, the result is further rescaled to account for SHiP's reconstruction and selection efficiencies in the way described in Section 3.1.5. The FairShip package is used to evaluate the effect of the signal selections on $\gamma' \to \mu\mu$ events. As dark photon phenomenology is currently[2] not implemented in the software package, we used the HNL and dark photon fast simulations to study the four-momentum distribution of the final-state particles in the two processes $\gamma' \to \mu\mu$, with the γ' produced by proton bremsstrahlung, and $HNL \to \pi\mu$. The ratio between the two distributions is applied as weighting factor to final-state $\pi\mu$ pairs from HNL decays simulated in FairShip, in order to emulate the spectrum of $\mu\mu$ pairs from dark photon decays. The simulated events are then filtered with the same set of selection applied to fully reconstructed HNL decays (see Table 3.2). The number of selected γ' candidates is shown in Table 3.8. The third column shows the evolution of the expected number of reconstructed $\gamma' \to \mu\mu$ events per proton-target collision after each selection step. The yield after all selections is reduced by 75%, a factor that is applied as correction factor to the fast simulation in order to account for reconstruction and selection efficiency.

Figure 3.14 shows SHiP's expected sensitivity to dark photons, compared to previous searches. The constraints from supernovae cooling [62] and big bang nucleosynthesis, and the most up-to-date limits established by previous experiments up to July 2014 [61], are shown in grey [25]. Another production mechanism that is relevant at high masses is the QCD production at the parton level, which has been studied in a subsequent work [30]. Assuming the same efficiency as for the low mass, according to preliminary theoretical calculation [2], taking parton bremsstrahlung into account would extend the sensitivity to masses of about 10 GeV, as shown in Figure 3.14b.

[2] At the time of writing.

Selection	Entries	$n(\gamma')/N(p.o.t.)$	Selection efficiency
Event reconstructed	59222	2.51×10^{-16}	-
1 HNL candidate	58211	2.5×10^{-16}	99.5 %
Vtx in fiducial vol.	50160	2.16×10^{-16}	86.4 %
Tracks in fiducial vol.	46600	2.13×10^{-16}	98.7 %
N.d.f. > 25	44519	2.1×10^{-16}	98.6 %
DOCA < 1 cm	41799	2.01×10^{-16}	95.8 %
χ^2/N.d.f. < 5	41799	2.01×10^{-16}	100.0 %
Daughters $P > 1$ GeV	41752	2.01×10^{-16}	100.0 %
IP < 10 cm	41477	2×10^{-16}	99.7 %
Event not vetoed	39457	1.89×10^{-16}	94.3 %
1 muon in 1st muon station	39225	1.88×10^{-16}	99.7 %
1 muon in 2nd muon station	38780	1.87×10^{-16}	99.4 %

Table 3.8: Effect of the offline selection on $\gamma' \to \mu\mu$ produced in proton bremsstrahlung. The second column lists the number of events selected from the original sample. The third column corresponds to the expected γ' yield per proton-target collision. The fourth column lists the individual efficiency on signal candidates for each cut of the selection chain, calculated relative to the weighted acceptance yielded by all preceding cuts.

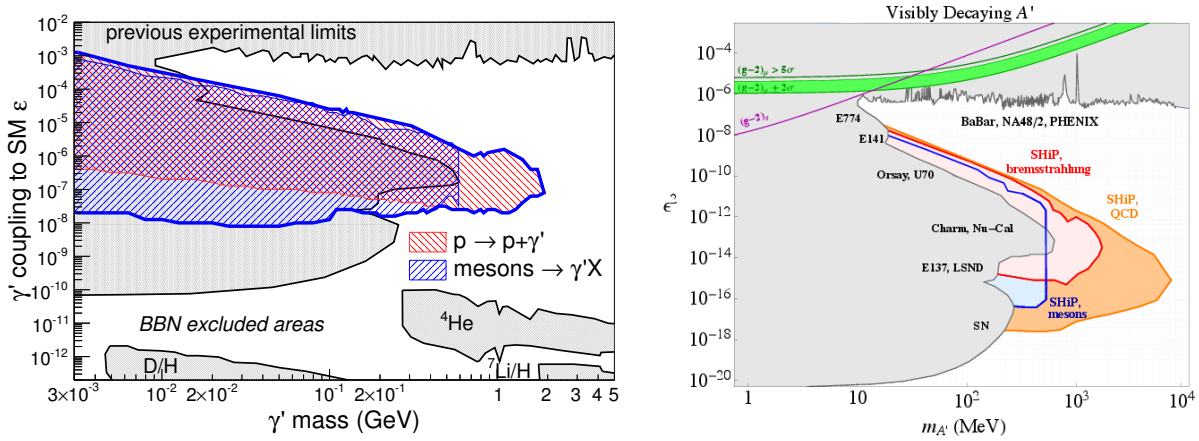

(a) γ' produced in p-bremsstrahlung and meson decays **(b)** γ' produced in parton-level QCD interaction

Figure 3.14: SHiP sensitivity to dark photons produced in proton bremsstrahlung and secondary meson decays **(a)** [1, 25] and by direct QCD interaction **(b)** [30]. Previous searches [61] explored the greyed-out area. Low-coupling regions are excluded by Big Bang Nucleosynthesis observations and by data from the SN1987A supernova [61, 62].

CHAPTER 4

Conclusions

The high intensity of the CERN SPS 400 GeV beam allows probing a wide variety of models containing light long-lived particles with masses below $O(10)$ GeV/c^2, which are capable of providing solutions to most of the observed shortcomings and theoretical problems of the Standard Model.

The proposed SHiP experiment, with a 60 m long evacuated decay volume with a magnetic spectrometer, and calorimeters and muon detectors at the far end, offers the possibility of exploring cosmologically interesting and previously unexplored regions of the parameter space for several theories beyond the Standard Model at a nearly null background level. The robustness against various types of background is guaranteed by background taggers and a dedicated timing detector. Selection criteria capable of isolating signal while drastically reducing the rate of residual backgrounds were studied in Sections 3.1.3 and 3.1.4. These criteria define the strategy for HNL search adopted in the SHiP Technical Proposal [1]. The acceptance studies presented in Section 2.3 led to the current design of the vacuum vessel enclosing the SHiP decay volume and spectrometer.

Hidden particles are predicted by a large number of theories beyond the Standard Model. In particular, the physics reach that SHiP can achieve in theories including HNLs and dark photons is calculated in Chapter 3. The work reported in this document demonstrates how, under nominal conditions (an integrated total of 2×10^{20} protons on target in five years of operation at the SPS), SHiP can access a significant fraction of the previously unexplored parameter space for both dark photons and HNLs up the the mass of the B meson. SHiP can improve the limits established by previous experiments by several orders of magnitude. These results were published in the SHiP Technical Proposal [1] and as SHiP public notes [43, 44]. In addition, heavier HNLs can be found in direct searches at a future Z factory. In Section 3.2 the HNL sensitivity of a hypotetical future experiment at the FCC-ee lepton collider is analysed. This work, published in [25, 45], shows that the synergy between SHiP and future accelerator experiments could lead to the exploration of the whole parameter space of the νMSM, allowing to prove or rule out the theory that sterile neutrinos are the only missing piece of the SM, explaining at the same time the SM neutrino masses, the observed matter-antimatter asymmetry, and the origin of dark matter.

The proposed SHiP experiment represents a unique opportunity for physics at the intensity frontier: the discovery of a very weakly interacting Hidden Sector would lead to a dramatic breakthrough in our understanding of particle physics and of the Universe.

References for Part I

[1] M. Anelli et al. “A facility to Search for Hidden Particles (SHiP) at the CERN SPS”. In: (2015). arXiv: 1504.04956 [physics.ins-det].

[2] Sergey Alekhin et al. “A facility to Search for Hidden Particles at the CERN SPS: the SHiP physics case”. In: (2015). arXiv: 1504.04855 [hep-ph].

[3] Annarita Buonaura. “Study of nu-tau properties with the SHiP experiment”. Presented 2017. PhD thesis. 2017. URL: https://cds.cern.ch/record/2268663.

[4] Takehiko Asaka, Steve Blanchet, and Mikhail Shaposhnikov. “The nuMSM, dark matter and neutrino masses”. In: *Phys. Lett.* B631 (2005), pp. 151–156. DOI: 10.1016/j.physletb.2005.09.070. arXiv: hep-ph/0503065 [hep-ph].

[5] Takehiko Asaka and Mikhail Shaposhnikov. “The nuMSM, dark matter and baryon asymmetry of the universe”. In: *Phys. Lett.* B620 (2005), pp. 17–26. DOI: 10.1016/j.physletb.2005.06.020. arXiv: hep-ph/0505013 [hep-ph].

[6] Alexey Boyarsky, Oleg Ruchayskiy, and Mikhail Shaposhnikov. “The Role of sterile neutrinos in cosmology and astrophysics”. In: *Ann.Rev.Nucl.Part.Sci.* 59 (2009), pp. 191–214. DOI: 10.1146/annurev.nucl.010909.083654. arXiv: 0901.0011 [hep-ph].

[7] Esra Bulbul et al. “Detection of An Unidentified Emission Line in the Stacked X-ray spectrum of Galaxy Clusters”. In: *Astrophys.J.* 789 (2014), p. 13. DOI: 10.1088/0004-637X/789/1/13. arXiv: 1402.2301 [astro-ph.CO].

[8] Alexey Boyarsky et al. “An unidentified line in X-ray spectra of the Andromeda galaxy and Perseus galaxy cluster”. In: (2014). arXiv: 1402.4119 [astro-ph.CO].

[9] Evgeny K. Akhmedov, V.A. Rubakov, and A. Yu. Smirnov. “Baryogenesis via neutrino oscillations”. In: *Phys.Rev.Lett.* 81 (1998), pp. 1359–1362. DOI: 10.1103/PhysRevLett.81.1359. arXiv: hep-ph/9803255 [hep-ph].

[10] Laurent Canetti and Mikhail Shaposhnikov. “Baryon Asymmetry of the Universe in the NuMSM”. In: *JCAP* 1009 (2010), p. 001. DOI: 10.1088/1475-7516/2010/09/001. arXiv: 1006.0133 [hep-ph].

[11] Laurent Canetti, Marco Drewes, and Mikhail Shaposhnikov. “Matter and Antimatter in the Universe”. In: *New J. Phys.* 14 (2012), p. 095012. DOI: 10.1088/1367-2630/14/9/095012. arXiv: 1204.4186 [hep-ph].

[12] Peter Minkowski. “$\mu \to e\gamma$ at a Rate of One Out of 1-Billion Muon Decays?” In: *Phys.Lett.* B67 (1977), p. 421. DOI: 10.1016/0370-2693(77)90435-X.

[13] Tsutomu Yanagida. "HORIZONTAL SYMMETRY AND MASSES OF NEUTRINOS". In: *Conf.Proc.* C7902131 (1979), pp. 95–99.

[14] Murray Gell-Mann, Pierre Ramond, and Richard Slansky. "Complex Spinors and Unified Theories". In: *Conf.Proc.* C790927 (1979), pp. 315–321. arXiv: 1306.4669 [hep-th].

[15] Rabindra N. Mohapatra and Goran Senjanovic. "Neutrino Mass and Spontaneous Parity Violation". In: *Phys.Rev.Lett.* 44 (1980), p. 912. DOI: 10.1103/PhysRevLett.44.912.

[16] Michael Gronau, Chung Ngoc Leung, and Jonathan L. Rosner. "Extending Limits on Neutral Heavy Leptons". In: *Phys.Rev.* D29 (1984), p. 2539. DOI: 10.1103/PhysRevD.29.2539.

[17] Dmitry Gorbunov and Mikhail Shaposhnikov. "How to find neutral leptons of the νMSM?" In: *JHEP* 10 (2007). [Erratum: JHEP11,101(2013)], p. 015. DOI: 10.1007/JHEP11(2013)101,10.1088/1126-6708/2007/10/015. arXiv: 0705.1729 [hep-ph].

[18] Anupama Atre et al. "The Search for Heavy Majorana Neutrinos". In: *JHEP* 0905 (2009), p. 030. DOI: 10.1088/1126-6708/2009/05/030. arXiv: 0901.3589 [hep-ph].

[19] C. Garcia Cely et al. "Higgs Decays in the Low Scale Type I See-Saw Model". In: *Phys.Lett.* B718 (2013), pp. 957–964. DOI: 10.1016/j.physletb.2012.11.026. arXiv: 1208.3654 [hep-ph].

[20] Wai-Yee Keung and Goran Senjanovic. "Majorana Neutrinos and the Production of the Right-handed Charged Gauge Boson". In: *Phys.Rev.Lett.* 50 (1983), p. 1427. DOI: 10.1103/PhysRevLett.50.1427.

[21] Loretta M. Johnson, Douglas W. McKay, and Tim Bolton. "Extending sensitivity for low mass neutral heavy lepton searches". In: *Phys. Rev.* D56 (1997), pp. 2970–2981. DOI: 10.1103/PhysRevD.56.2970. arXiv: hep-ph/9703333 [hep-ph].

[22] J. P. Lees et al. "Search for a Dark Photon in e^+e^- Collisions at BaBar". In: *Phys. Rev. Lett.* 113.20 (2014), p. 201801. DOI: 10.1103/PhysRevLett.113.201801. arXiv: 1406.2980 [hep-ex].

[23] Sarah Andreas, Carsten Niebuhr, and Andreas Ringwald. "New Limits on Hidden Photons from Past Electron Beam Dumps". In: *Phys. Rev.* D86 (2012), p. 095019. DOI: 10.1103/PhysRevD.86.095019. arXiv: 1209.6083 [hep-ph].

[24] Johannes Blümlein and Jürgen Brunner. "New Exclusion Limits on Dark Gauge Forces from Proton Bremsstrahlung in Beam-Dump Data". In: *Phys. Lett.* B731 (2014), pp. 320–326. DOI: 10.1016/j.physletb.2014.02.029. arXiv: 1311.3870 [hep-ph].

[25] Elena Graverini, Nicola Serra, and Barbara Storaci. "Search for New Physics in SHiP and at future colliders". In: *JINST* 10 (2015), p. 7007. DOI: 10.1088/1748-0221/10/07/C07007. arXiv: 1503.08624 [hep-ex].

[26] Rouven Essig et al. "Discovering New Light States at Neutrino Experiments". In: *Phys. Rev.* D82 (2010), p. 113008. DOI: 10.1103/PhysRevD.82.113008. arXiv: 1008.0636 [hep-ph].

[27] James D. Bjorken et al. "New Fixed-Target Experiments to Search for Dark Gauge Forces". In: *Phys. Rev.* D80 (2009), p. 075018. DOI: 10.1103/PhysRevD.80.075018. arXiv: 0906.0580 [hep-ph].

[28] K. A. Olive et al. "Review of Particle Physics". In: *Chin. Phys.* C38 (2014), p. 090001. DOI: 10.1088/1674-1137/38/9/090001.

[29] D. Gorbunov, A. Makarov, and I. Timiryasov. "Decaying light particles in the SHiP experiment: Signal rate estimates for hidden photons". In: *Phys. Rev.* D91.3 (2015), p. 035027. DOI: 10.1103/PhysRevD.91.035027. arXiv: 1411.4007 [hep-ph].

[30] M. Anelli et al. *Addendum to Technical Proposal: A Facility to Search for Hidden Particles (SHiP) at the CERN SPS*. Tech. rep. CERN-SPSC-2015-040. SPSC-P-350-ADD-2. Geneva: CERN, Oct. 2015. URL: https://cds.cern.ch/record/2060742.

[31] L. N. Hand, D. G. Miller, and Richard Wilson. "Electric and Magnetic Form Factors of the Nucleon". In: *Rev. Mod. Phys.* 35 (2 Apr. 1963), pp. 335–349. DOI: 10.1103/RevModPhys.35.335. URL: http://link.aps.org/doi/10.1103/RevModPhys.35.335.

[32] Brian Batell, Maxim Pospelov, and Adam Ritz. "Exploring Portals to a Hidden Sector Through Fixed Targets". In: *Phys. Rev.* D80 (2009), p. 095024. DOI: 10.1103/PhysRevD.80.095024. arXiv: 0906.5614 [hep-ph].

[33] G. Bernardi et al. "Search for Neutrino Decay". In: *Phys. Lett.* B166 (1986), p. 479. DOI: 10.1016/0370-2693(86)91602-3.

[34] G. Bernardi et al. "FURTHER LIMITS ON HEAVY NEUTRINO COUPLINGS". In: *Phys. Lett.* B203 (1988), p. 332. DOI: 10.1016/0370-2693(88)90563-1.

[35] F. Vannucci. "Sterile neutrinos: From cosmology to the LHC". In: *J. Phys. Conf. Ser.* 136 (2008), p. 022030. DOI: 10.1088/1742-6596/136/2/022030.

[36] F. Bergsma et al. "A Search for Decays of Heavy Neutrinos in the Mass Range 0.5-GeV to 2.8-GeV". In: *Phys. Lett.* B166 (1986), p. 473. DOI: 10.1016/0370-2693(86)91601-1.

[37] A. Vaitaitis et al. "Search for neutral heavy leptons in a high-energy neutrino beam". In: *Phys. Rev. Lett.* 83 (1999), pp. 4943–4946. DOI: 10.1103/PhysRevLett.83.4943. arXiv: hep-ex/9908011 [hep-ex].

[38] Elena Graverini. "SHiP: a new facility with a dedicated detector to search for new long-lived neutral particles". In: *European Physical Society conference on High Energy Physics*. 2015. URL: http://pos.sissa.it/cgi-bin/reader/conf.cgi?confid=234.

[39] R. Acquafredda et al. "The OPERA experiment in the CERN to Gran Sasso neutrino beam". In: *JINST* 4 (2009), P04018. DOI: 10.1088/1748-0221/4/04/P04018.

[40] Giovanni De Lellis. "SHiP: a new facility with a dedicated detector for neutrino physics". In: vol. EPS-HEP2015. CERN-SHiP-PROC-2016-009. July 2015, p. 037. URL: https://cds.cern.ch/record/2131204.

[41] Edoardo Cortina Gil et al. "The Beam and detector of the NA62 experiment at CERN". In: *JINST* 12.05 (2017), P05025. DOI: 10.1088/1748-0221/12/05/P05025. arXiv: 1703.08501 [physics.ins-det].

[42] W. Bonivento et al. "Proposal to Search for Heavy Neutral Leptons at the SPS". In: (2013). arXiv: 1310.1762 [hep-ex].

[43] Elena Graverini. "SHiP sensitivity to Heavy Neutral Leptons". In: (Sept. 2016). URL: https://cds.cern.ch/record/2214085.

[44] Elena Graverini. "SHiP sensitivity to Dark Photons". In: (Sept. 2016). URL: https://cds.cern.ch/record/2214092.

[45] Alain Blondel et al. "Search for Heavy Right Handed Neutrinos at the FCC-ee". In: *37th International Conference on High Energy Physics*. Valencia, Spain, July 2014. arXiv: 1411.5230 [hep-ex]. URL: http://inspirehep.net/record/1328783/files/arXiv:1411.5230.pdf.

[46] S. Agostinelli et al. "GEANT4: A Simulation toolkit". In: *Nucl. Instrum. Meth.* A506 (2003), pp. 250–303. DOI: 10.1016/S0168-9002(03)01368-8.

[47] Sjöstrand, Torbjörn and Mrenna, Stephen and Skands, Peter Z. "A Brief Introduction to PYTHIA 8.1". In: *Comput. Phys. Commun.* 178 (2008), pp. 852–867. DOI: 10.1016/j.cpc.2008.01.036. arXiv: 0710.3820 [hep-ph].

[48] M Al-Turany et al. "The FairRoot framework". In: *Journal of Physics: Conference Series* 396.2 (2012), p. 022001. URL: http://stacks.iop.org/1742-6596/396/i=2/a=022001.

[49] Rene Brun and Fons Rademakers. "{ROOT} — An object oriented data analysis framework". In: *Nuclear Instruments and Methods in Physics Research Section A: Accelerators, Spectrometers, Detectors and Associated Equipment* 389.1–2 (1997). New Computing Techniques in Physics Research V, pp. 81–86. ISSN: 0168-9002. DOI: http://dx.doi.org/10.1016/S0168-9002(97)00048-X. URL: http://www.sciencedirect.com/science/article/pii/S016890029700048X.

[50] C. Höppner et al. "A novel generic framework for track fitting in complex detector systems". In: *Nuclear Instruments and Methods in Physics Research Section A: Accelerators, Spectrometers, Detectors and Associated Equipment* 620.2–3 (2010), pp. 518–525. ISSN: 0168-9002. DOI: http://dx.doi.org/10.1016/j.nima.2010.03.136. URL: http://www.sciencedirect.com/science/article/pii/S0168900210007473.

[51] C. Andreopoulos et al. "The GENIE Neutrino Monte Carlo Generator". In: *Nucl. Instrum. Meth.* A614 (2010), pp. 87–104. DOI: 10.1016/j.nima.2009.12.009. arXiv: 0905.2517 [hep-ph].

[52] Sjöstrand, Torbjörn and Mrenna, Stephen and Skands, Peter Z. "PYTHIA 6.4 physics and manual". In: *Journal of High Energy Physics* 2006.05 (2006), p. 026. URL: http://stacks.iop.org/1126-6708/2006/i=05/a=026.

[53] *The FCC design study*. http://cern.ch/fcc.

[54] A. Bogomyagkov, E. Levichev, and D. Shatilov. "Beam-beam effects investigation and parameters optimization for a circular e^+e^- collider at very high energies". In: *Phys. Rev. ST Accel. Beams* 17 (4 Apr. 2014), p. 041004. DOI: 10.1103/PhysRevSTAB.17.041004.

[55] M. Koratzinos et al. "TLEP: A High-Performance Circular e+ e- Collider to Study the Higgs Boson". 2013.

[56] M. Bicer et al. "First Look at the Physics Case of TLEP". In: *JHEP* 1401 (2014), p. 164. DOI: 10.1007/JHEP01(2014)164. arXiv: 1308.6176 [hep-ex].

[57] Mikhail Shaposhnikov. "The νMSM, leptonic asymmetries, and properties of singlet fermions". In: *JHEP* 0808 (2008), p. 008. DOI: 10.1088/1126-6708/2008/08/008. arXiv: 0804.4542 [hep-ph].

[58] S. Schael et al. "Precision electroweak measurements on the Z resonance". In: *Phys.Rept.* 427 (2006), pp. 257–454. DOI: 10.1016/j.physrep.2005.12.006. arXiv: hep-ex/0509008 [hep-ex].

[59] K.J. Kim and Y.S. Tsai. "An improved Weizsacker Williams method and photoproduction of lepton pairs". In: *Physics Letters B* 40.6 (1972), pp. 665–670. ISSN: 0370-2693. DOI: 10.1016/0370-2693(72)90622-3.

[60] K.J. Kim and Y.-. Tsai. "Improved Weizsaecker–Williams method and its application to lepton and W- boson pair production". In: *Phys. Rev., D, v. 8, no. 9, pp. 3109-3125* (Nov. 1973).

[61] Anthony Fradette et al. "Cosmological Constraints on Very Dark Photons". In: *Phys.Rev.* D90.3 (2014), p. 035022. DOI: 10.1103/PhysRevD.90.035022. arXiv: 1407.0993 [hep-ph].

[62] Demos Kazanas et al. "Supernova Bounds on the Dark Photon Using its Electromagnetic Decay". In: *Nucl.Phys.* B890 (2014), pp. 17–29. DOI: 10.1016/j.nuclphysb.2014.11.009. arXiv: 1410.0221 [hep-ph].

PART II

Precision measurements at the energy frontier: LHCb

CHAPTER 5

The LHCb experiment

Contents

This Chapter introduces the LHCb experiment at the CERN Large Hadron Collider. The CERN laboratory and its accelelator system is introduced in Section 5.1. The LHCb detector is then described in detail in Section 5.2. Finally, Section 5.3 offers an overview of how information from the various detector components is interpreted and filtered before being used for physics analysis.

5.1. CERN and the LHC

CERN, whose name stands for the French *Conseil Européen pour la Recherche Nucléaire*[1], was provisionally founded in 1952 by eleven european States and then established as a research organization based in Geneva in 1954 [1]. The laboratory now extends over the French-Swiss border in the Geneva area, between the Léman lake and the Jura massif, and counts 22 member States. CERN's facilities are used by over 600 research institutes and universities from all over the world [2].

The Large Hadron Collider (LHC) [3, 4] is at present the world's largest and most powerful particle accelerator. It lies in the 26.7 km long tunnel that previously hosted the Large Electron Positron (LEP) collider [5], at a depth of about 100 m underground. Two beams of particles of

[1] European Council for Nuclear Research.

the same charge circulate in two parallel beam pipes, where they are accelerated in opposite directions and set to collide in four interaction points along the LHC ring. The interaction points, sketched in Figure 5.1(b), host the seven LHC experiments: ATLAS [6] and LHCf [7], CMS [8] and TOTEM [9], LHCb [10] and MoEDAL [11], and ALICE [12].

5.1.1. The LHC experiments

ATLAS and CMS ATLAS (A Toroidal Lhc ApparatuS) and CMS (Compact Muon Solenoid) are two general-purpose detectors with cylindrical geometry around the beam line. They were designed to look for new particles at the TeV scale, and are therefore optimised for the detection and reconstruction of high energy objects.

ALICE ALICE (A Large Ion Collider Experiment) was designed to study Pb-Pb collisions and the high energy density objects generated by ion collisions.

TOTEM and LHCf TOTEM (TOTal Elastic and inelastic cross-section Measurement) and LHCf (LHC forward) are forward detectors placed in the CMS and ATLAS halls, respectively. Their purpose is the study of diffractive physics, *e.g.* the measurement of the total pp cross section, a necessary reference for every other LHC experiment.

MoEDAL MoEDAL (Monopole and Exotics Detector At the Lhc) is a passive detector located in the same hall as LHCb. It was designed to search for magnetic monopoles and other highly ionizing, very long lived massive particles.

LHCb LHCb (LHC beauty) is a forward spectrometer dedicated to the study of heavy flavoured particles, *i.e.* hadrons containing heavy quarks. It will be thoroughly described in Section 5.2.

5.1.2. The accelerator complex

The proton acceleration chain, illustrated in Figure 5.1(a), begins with the extraction of protons as nuclei of hydrogen atoms. These are accelerated to an energy of 50 keV and guided to a linear accelerator (LINAC2) where they reach an energy of 50 MeV. A Proton Synchrotron Booster (PSB) raises the energy to 1.4 GeV before injecting the proton beam into the Proton Synchrotron (PS). At 26 GeV the protons are transferred to the Super Proton Synchrotron (SPS), where they are accelerated to 450 GeV. At this stage, part of the beam is extracted and delivered to the CERN North Area experiments[2]. Two transfer lines finally inject the proton

[2] The CERN North Area, located in Prevessin (France), hosts a number of beam dump experiments. The currently running facilities are: NA61/SHINE [14], aimed at exploring the wide variety of final states produced by different particles colliding onto fixed targets; NA62 [15], studying the rare decay $K \to \pi\nu\nu$; COMPASS [16],

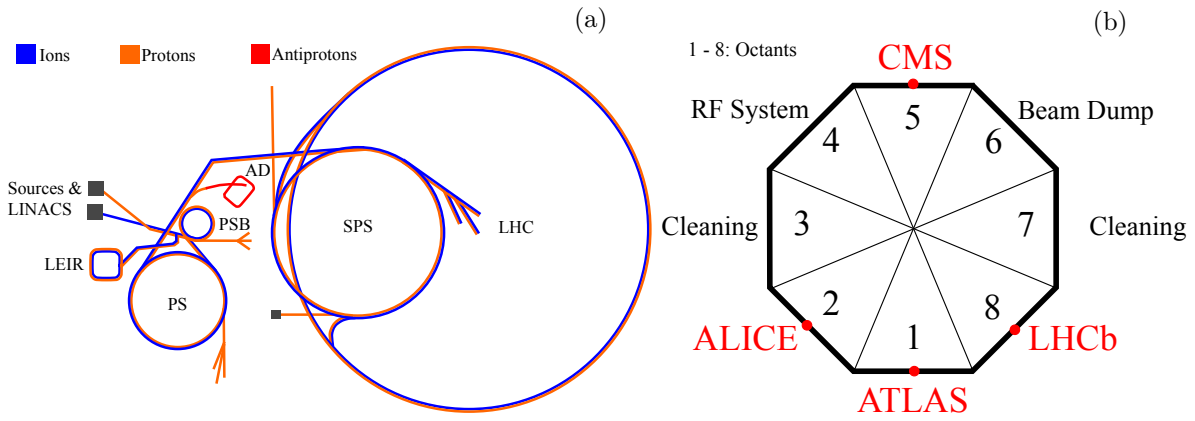

Figure 5.1: CERN's accelerator complex, highlighting the various acceleration stages (a). Scheme of the LHC layout, showing the eight sectors and their main purposes (b) [13].

beam into the two LHC beam pipes, where protons are accelerated in opposite directions up to the collision energy and finally directed to collide in the four interaction points (IP).

Accelerators are mainly characterised by their luminosity $\mathcal{L}$ and collision energy $\sqrt{s}$. The latter is defined as the energy available in the collision centre of mass:

$$\sqrt{s} = \left[(p_{b1} + p_{b2})^{\mu} (p_{b1} + p_{b2})_{\mu} \right]^{\frac{1}{2}}, \tag{5.1}$$

where $p_{b1,2}$ are the four-momenta of the particles involved in the collision. For a fixed-target experiment, such as SHiP (*cf.* Chapters 2 and 3), this quantity amounts to $\sqrt{s} \simeq \sqrt{2E_b m_p}$ where E_b is the energy of the beam and m_p is the mass of the target proton, which we assume at rest. For two colliding beams of equal energy E_b and opposite directions like in LHC, on the other hand, we have $\sqrt{s} = 2E_b$. LHC operated at $\sqrt{s} = 7$ and 8 TeV during LHC Run I, between 2010 and 2012, and at $\sqrt{s} = 13$ TeV since the start of LHC Run II in 2015.

Luminosity is a measure of the number of occurrences per time unit for a process with a given cross-section σ. It is related to the rate R of events featuring the given process and to the process cross section by

$$R(t) = \sigma \mathcal{L}(t) . \tag{5.2}$$

Here, $\mathcal{L}(t)$ represents the instantaneous luminosity of the machine. The integrated luminosity $\mathcal{L} = \int dt \mathcal{L}(t)$ is a measure of the amount of pp collisions delivered by the LHC. The luminosity depends on the design and parameters of the collider. The LHC beam is not continuous: it is composed of a maximum of 2808 proton bunches, each with a maximum intensity of 1.15×10^{11} protons per bunch. By design, LHC bunches collide every 25 ns. During Run I, however, bunches were collided every 50 ns. Assuming a Gaussian beam profile, the

investigating the nucleon spin structure; NA63 [17], focussed on radiation processes in strong electromagnetic fields.

instantaneous luminosity is given by

$$\mathcal{L} = \frac{f\gamma N_p^2 n_b}{4\pi\epsilon_n\beta^*}F, \tag{5.3}$$

where:

n_b	is the number of proton bunches,
N_p	is the number of protons per bunch,
f	is the revolution frequency of the proton bunches,
γ	is the relativistic gamma factor,
ϵ_n	is the normalized transverse beam emittance,
β^*	is the value of the beta function at the IP, and
F	is a geometrical reduction factor due to the beams crossing angle.

The beta function β^* appearing in Eqn. 5.3 is a quantity related to the transverse dimensions of the beam.

Particles emerging from a collision are mainly emitted in the forward region, due to the asymmetry in the fraction of proton momentum carried by the colliding partons. High occupancy can degrade the tracking performance of forward detectors like LHCb, which was designed to work at a lower luminosity with respect to the general purpose detectors CMS and ATLAS. Hence, the luminosity at the LHCb interaction point is reduced by increasing the transversal distance between the two beams. While collisions decrease the beam intensity during an LHC fill, the distance between the beams in LHCb is reduced, keeping the instantaneous luminosity stable within a ±5 % range, as shown in Figure 5.2(a). This technique, named "luminosity levelling", minimises the effects of luminosity decay, allowing to maintain the same trigger configuration during a fill and to reduce systematic uncertainties due to changes in the detector occupancy [18].

5.2. The LHCb detector

The large centre-of-mass energy $\sqrt{s}$ and the high rate of pp interactions at the LHC result in an unprecedented yield of heavy quarks. The LHCb experiment [19] was designed with the purpose of making use of the large sample of charm and beauty hadrons by analysing their decays to spot possible signs of New Physics. As the production of $b\bar{b}$ quark pairs takes predominantly place in the forward region, *i.e.* at low angle from the beam axis, as shown in Figure 5.2(b), LHCb has been designed as a single arm spectrometer covering the

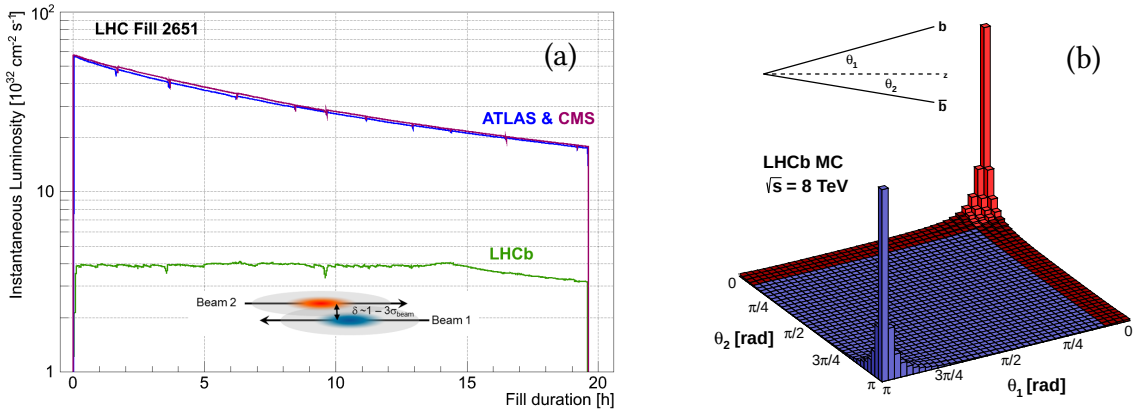

Figure 5.2: Instantaneous luminosity for ATLAS, CMS and LHCb during a long LHC fill (a). After ramping to the desired value of 4×10^{32} cm^{-2} s^{-1} for LHCb, the luminosity is kept stable for about 15 hours by adjusting the transversal beam overlap [18]. Distribution of angles between the b or $\bar{b}$ quark momentum and the beam axis, as simulated for pp collisions at $\sqrt{s} = 8$ TeV (b). The region highlighted in red corresponds to the acceptance of the LHCb detector [10].

pseudorapidity[3] range $2 < \eta < 5$.

Figure 5.3 gives an overview of the whole LHCb detector and of the position of every subdetector in the LHCb cavern. The next sections will describe each subdetector in detail. One of the distinguishing characteristics of b-hadrons is their long lifetime. In LHCb, they travel on average a distance of few mm before decaying. A crucial requirement for the design of an experiment aimed at b-physics is therefore the ability to reconstruct the trajectory of the decaying hadron, *i.e.* the separation between the primary pp interaction vertex (PV) and the secondary b-hadron decay vertex (SV), and to distinguish different b-hadron decay modes from each other. This criterion drove the design of the LHCb Vertex Locator (VELO), described in Section 5.2.1, and of a system of two tracking stations. In addition, in order to distinguish the decay of a b-hadron from that of a different particle, a good mass resolution and an efficient particle identification system are needed. The former can be attained by means of a performant tracking system, requirement satisfied in LHCb by a system of two tracking detectors and a warm dipole magnet, descibed in Section 5.2.1. A system composed of two Cherenkov light-based detectors, a muon detector, and a calorimeter system (see Section 5.2.2) meets the particle identification requirements needed to reconstruct the particles emitted in the decays of heavy hadrons.

The various components of the LHCb detector are hereinafter described in detail, with particular attention to the aspects related to the interpretation of data aimed at performing physics analyses: the tracking procedure is introduced, as well as the way particles are identified.

[3] Pseudorapidity is defined as $\eta = -\log(\tan\theta/2)$, where θ is the polar angle measured with respect to the beam axis.

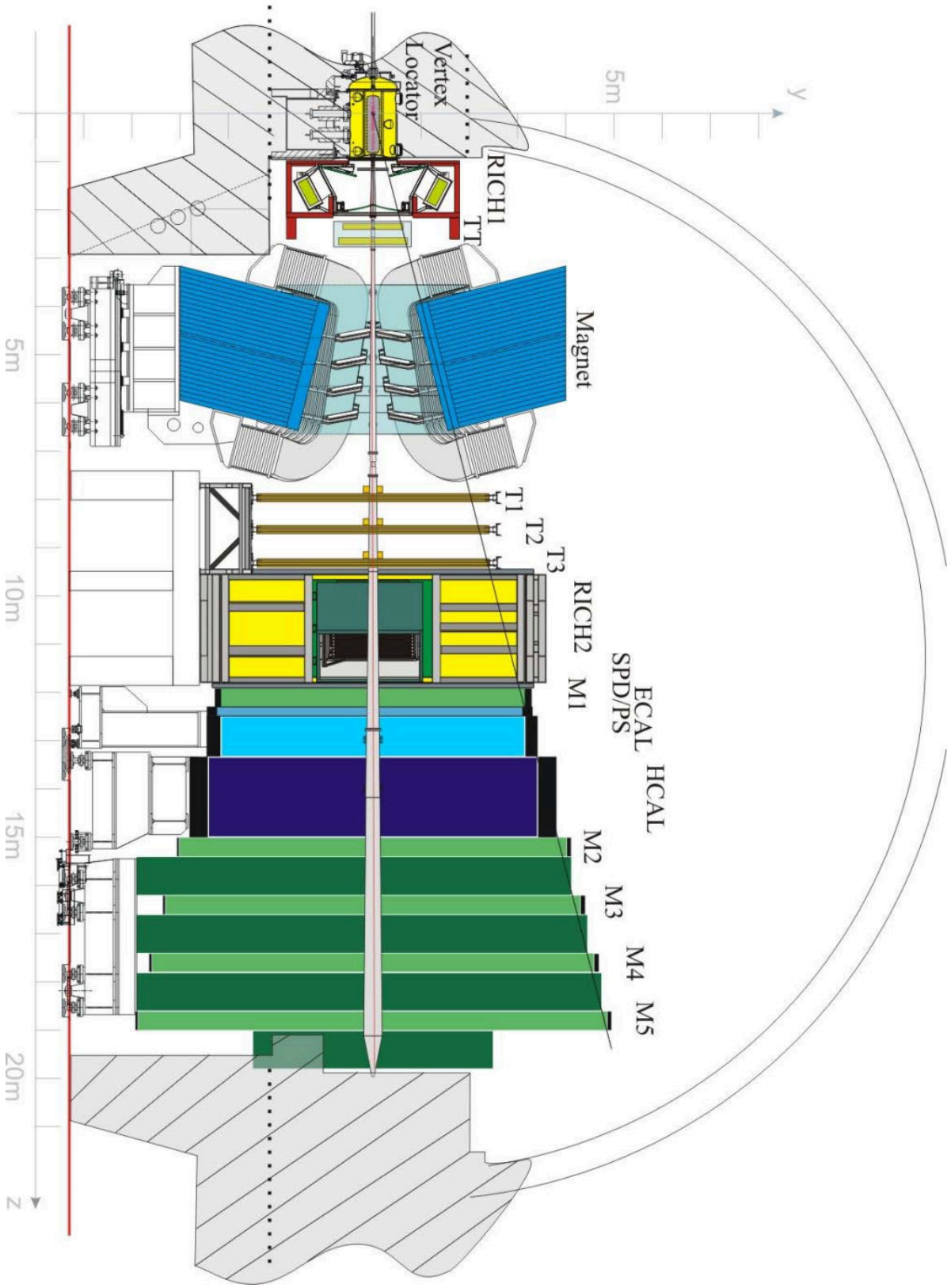

Figure 5.3: Schematics of the LHCb detector [10].

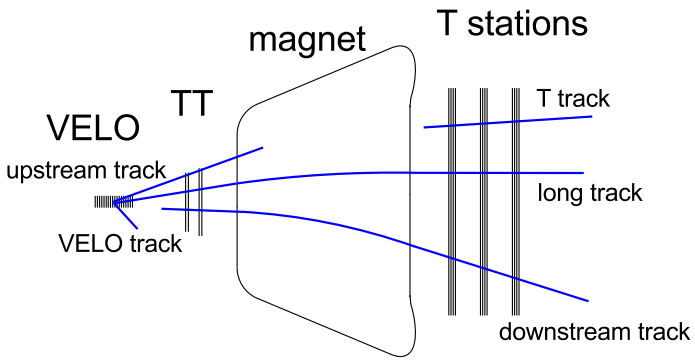

Figure 5.4: Track types reconstructed in LHCb [20].

5.2.1. Tracking system

The LHCb tracking system is composed of a vertex detector, the VELO, and a system of forward tracking stations: the Tracker Turicensis, TT, placed in front of a warm dipole magnet, and three stations T1–3 downstream of the magnet, collectively referred to as T-stations. VELO and TT both use silicon microstrips. The T stations employ two different technologies, due to the large difference in occupancy between the inner and outer regions of the detector. The central part, referred to as Inner Tracker (IT), uses a silicon strip technology similar to that used by the TT, while the Outer Tracker (OT) consists of straw-drift tubes. The VELO enables the reconstruction of the trajectory of the decaying hadron, by identifying the PV and any potential SV. Combining the information from the VELO with that from the other tracking detectors then provide a measurement of the charge and momentum of the charged decay products, by tracing them through a magnetic field. Pieces of information from the various tracking subdetectors are combined in order to associate each track to a vertex.

Not all charged particles create hits in all tracking subdetectors. At the PV and SV, some particles are produced in the backward direction, or with large transverse momentum, and leave hits only in the VELO before flying out of the LHCb acceptance. These tracks are crucial for vertex reconstruction, but not very useful for further analysis. Forward-produced low momentum particles can reach the TT and then be deflected by the magnetic field, failing to hit the T stations. Furthermore, decay products of long-lived particles like the K_s^0 are often produced outside of the VELO. These particles would leave traces only in the other tracking stations. Figure 5.4 schematically shows the different kinds of tracks reconstructed in LHCb, *i.e.*:

- *VELO* tracks consisting only of VELO hits,
- *UPSTREAM* tracks, combining VELO and TT hits,
- *T* tracks reconstructed only by the T-stations,

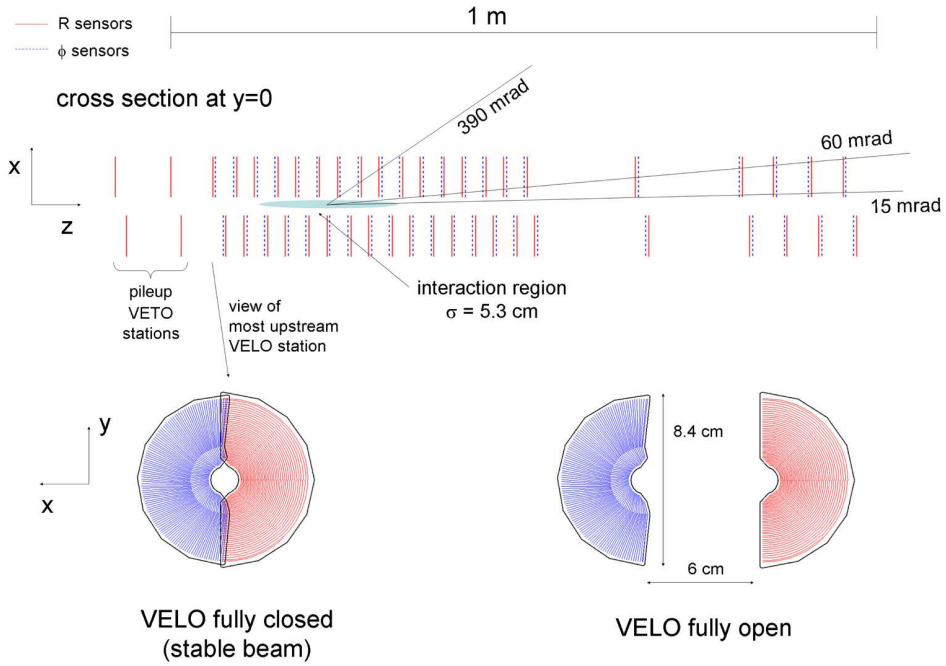

Figure 5.5: Layout of the VELO detector [22].

- *LONG* tracks, including hits in all tracking detectors (VELO, TT and T-stations), and
- *DOWNSTREAM* tracks, combining hits from the TT and T-stations.

Different pattern recognition algorithms are employed to reconstruct different track types. Then, tracks are fitted with a Kalman filter [21] algorithm accounting for effects due to multiple scattering and ionization energy loss. Finally, the fitted tracks are filtered based on their ghost probability. A neural network is employed to this aim, whose response is calibrated on input quality variables like the track χ^2 and the number of hits in each subdetector.

The most useful track types for physics analyses are *LONG* and *DOWNSTREAM* tracks. The tracking efficiency varies according to the track momentum and the number of tracks in the same event, but it is always above 95% for *LONG* tracks.

The Vertex Locator (VELO)

The VELO consists of 21 modules of silicon microstrip sensors [23]. Each module is composed of two sensors, one with strips in the radial direction (r-sensors) and one with strips in the azimutal direction (ϕ-sensors). The strip pitch, and hence the resolution, varies with the distance from the beam line, going from 40 μm in the innermost part to 100 μm in the outermost part.

A defining characteristic of the LHCb VELO detector is that it surrounds the beam at only 8 mm from its axis. This is the operating mode in stable beams conditions, *i.e.* while taking physics data. However, during the injection of protons into the LHC the beam position is not

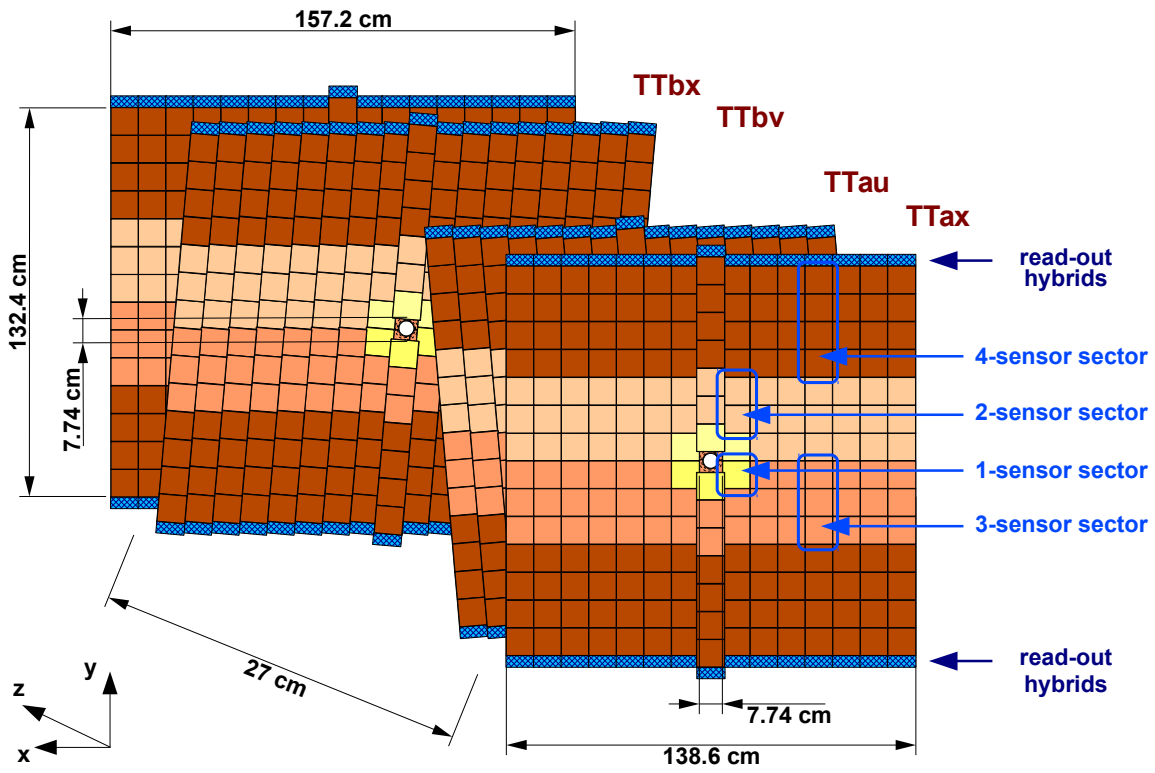

Figure 5.6: Schematic view of the TT detector [26].

as stable, making it unsafe for the VELO to be so close to the beam axis. Therefore, the VELO is split in two halves, slightly overlapping to ensure full ϕ coverage, that are mechanically retracted during the beam injection phase and in the event of a beam loss. The VELO operates in vacuum, within the beam vessel.

The Silicon Tracker (ST) and the magnet

The ST consists of two subdetectors, TT [24] and IT [25], positioned upstream and downstream of the magnet, respectively. The LHCb magnet is a warm magnet with a bending power of 4 T m. The polarity is periodically inverted, with the purpose of evaluating and minimizing systematic effects on the tracking procedure.

The upstream detector is named Tracker Turicensis (TT), after the design effort made by the University of Zurich. It consists of four layers of silicon microstrip sensors, with a strip pitch of 183 µm. The strips of the outer layers are vertically oriented, giving a measurement along the x direction; the strips of the inner layers are rotated by $\pm 5^\circ$ in order to provide stereo information (u, v).

Each TT layer is composed of a number of vertical (or stereo) modules holding fourteen 10×10 cm^2 sensors each. The central modules are divided into two halves, placed above and

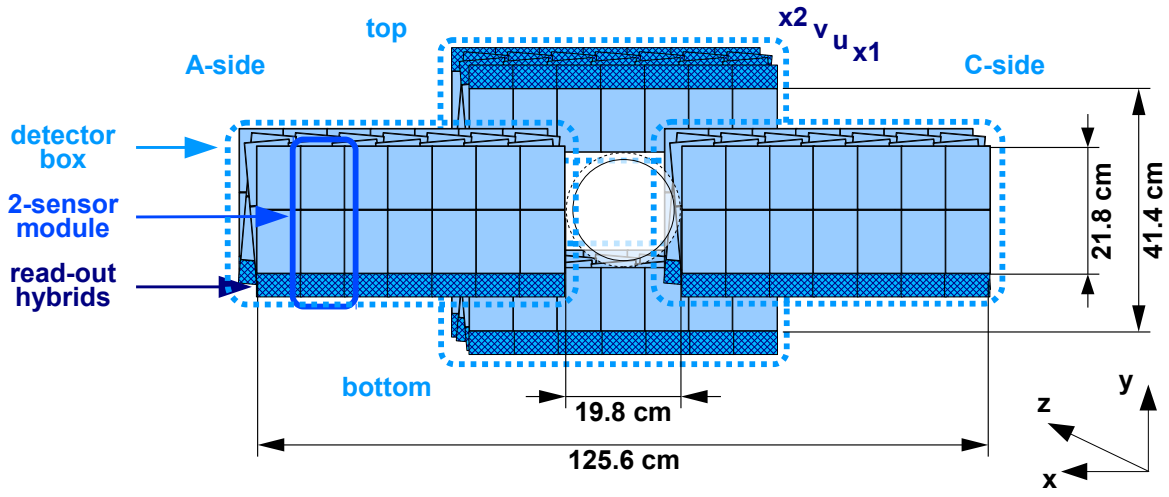

Figure 5.7: Schematic view of an IT station [26].

below the beam pipe. The readout partitioning of the TT reflects the spatial occupancy of the detector: sensors in the innermost region are read out individually, whereas those in the outer regions are wire bonded together in sets of two or three, as illustrated in Figure 5.6. This allows to reduce the total number of channels.

The Inner Tracker (IT) constitutes the central part of the T-stations. Each station shares the same 4-layer layout as the TT. The modules are arranged in four detector boxes, on the two sides of the beam pipe and on its top and bottom, as shown in the sketch in Figure 5.7. The sensors of the IT have a 198 µm strip pitch, and are read out either individually (top and bottom modules) or in pairs (side modules).

Both the TT and IT have a hit resolution of about 50 µm.

The Outer Tracker (OT)

The outer region of the T-stations is referred to as Outer Tracker (OT) [28]. The technology employed by the OT consists in 5 mm diameter Kapton straw drift tubes containing a gold-plated Tungsten anode wire. Each of the four stations consists of four layers, arranged in the same stereo layout as the TT and IT. A gas mixture of 70% Ar, 28.5% CO_2 and 1.5% O_2 is used, resulting in a drift time short enough to minimize spill-over (*i.e.* signal residuals extending in time to the following bunch crossing) and achieve a spatial resolution of 200 µm.

The top and bottom modules are made of two rows of staggered 2425 mm long straw tubes read out at the top and bottom edges, respectively. The left and right modules consist of straw tubes twice as long, interrupted in the middle ($y = 0$) and read out from both top and bottom. Figure 5.8 summarizes the LHCb forward tracking system, highlighting the TT and the three IT/OT stations.

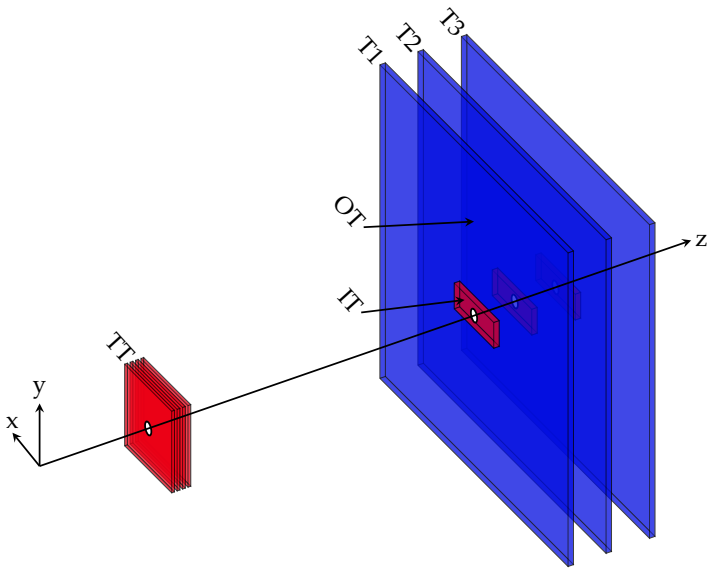

Figure 5.8: Schematic layout of the LHCb forward tracking system, highlighting the TT on the left and the three IT/OT stations on the right [27].

5.2.2. Particle identification

Particle identification (PID) is performed combining information from two RICH detectors, the calorimeter system and the muon system. In each event, mass hypotheses are assigned to every particle, and the relative likelihoods are calculated via multivariate likelihood classifiers combining information from the PID subdetectors. The classifiers are trained to compare the various particle hypoteses against the pion hypotesis. One can then estimate *e.g.* if a reconstructed track belongs more likely to a kaon or pion based on the difference between the log-likelihoods[4] of the kaon and pion hypotheses, respectively. The particle identification efficiency of this classifier varies depending on the track momentum.

In LHCb, PID information is further refined by the use of a neural network combining the output of the PID classifiers and information from the other subdetectors, *e.g.* the tracking stations. The output of the neural network is a variable taking values between 0 and 1, that can be interpreted as the absolute probability of a particle to be of a certain species.

The Ring Imaging Cherenkov (RICH) detectors

LHCb has two RICH detectors [30]. These detectors can measure the Cherenkov radiation emitted by charged particles traversing a medium faster than the speed of light in that medium.

[4] The log-likelihood is the natural logarithm of the likelihood. It has the same discriminating power as the likelihood itself, as it is a strictly monotonic function.

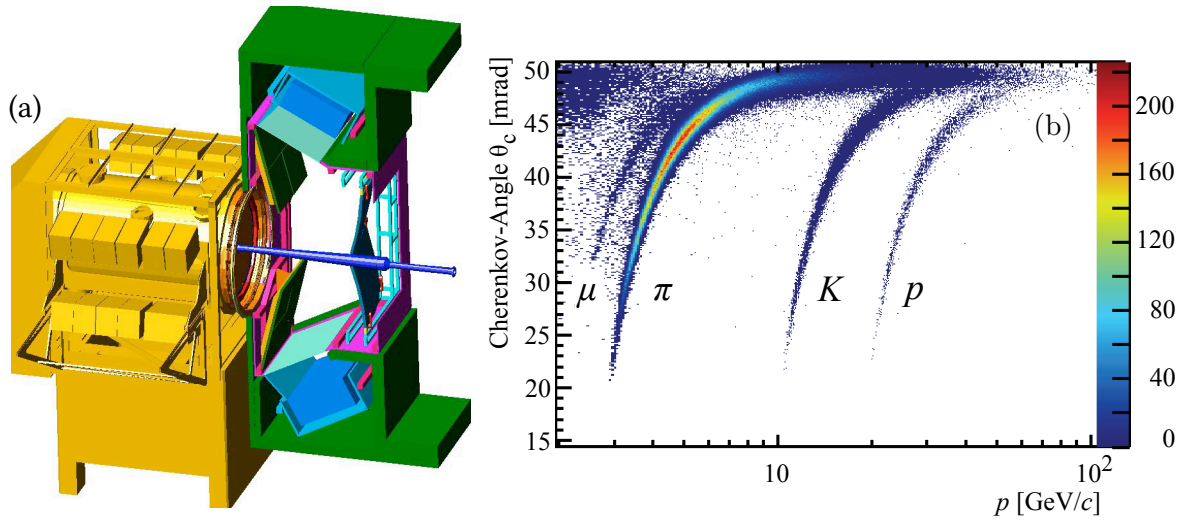

Figure 5.9: Cut-away 3D model of the RICH1 detector, attached on the left to the VELO tank (a) [10]. Reconstructed Cherenkov angle as a function of the track momentum in a C_4F_{10} radiator (b) [29].

The emission angle of Cherenkov radiation is given by:

$$\cos\theta_C = \frac{1}{n\beta} \tag{5.4}$$

where θ_C is the angle between the direction of the emitted light and the trajectory of the particle, n is the refractive index of the medium and β is the particle velocity in units of c. Knowing n and measuring $\cos\theta_C$, one can calculate the speed of the particle: combining this information with the momentum measurement given by the tracking system, the mass of the particle can be determined. The Cherenkov angle dependence on the particle momentum is shown in Figure 5.9(b) for different particle species.

Both RICH detectors record Cherenkov light by means of a system of two mirrors that deflect photons outside of the LHCb acceptance. Hybrid Photon Detectors (HPD) are employed to read out the signal [10]. The first RICH detector, RICH1 (Figure 5.9(a)), is located between the VELO and the TT. It uses a C_4F_{10} radiator, covering the momentum range $1 < p < 60$ GeV. RICH2 is situated downstream of the T stations and covers the momentum range $15 < p < 100$ GeV using CF_4 as radiator. RICH2 covers only a central region ($\eta < 3$) of the LHCb acceptance, where high momentum particles are most abundant.

The calorimeter system

The calorimeter system [31] is composed of four subdetectors, as sketched in Figure 5.10(a). A Scintillating Pad Detector (SPD), consisting of fine-granularity scintillator pads, is followed by a 15 mm thick lead absorber plane and by another scintillating pad detector with Pre-Shower function (PS). The aim of the SPD layer is to help distinguishing between calorimeter charge

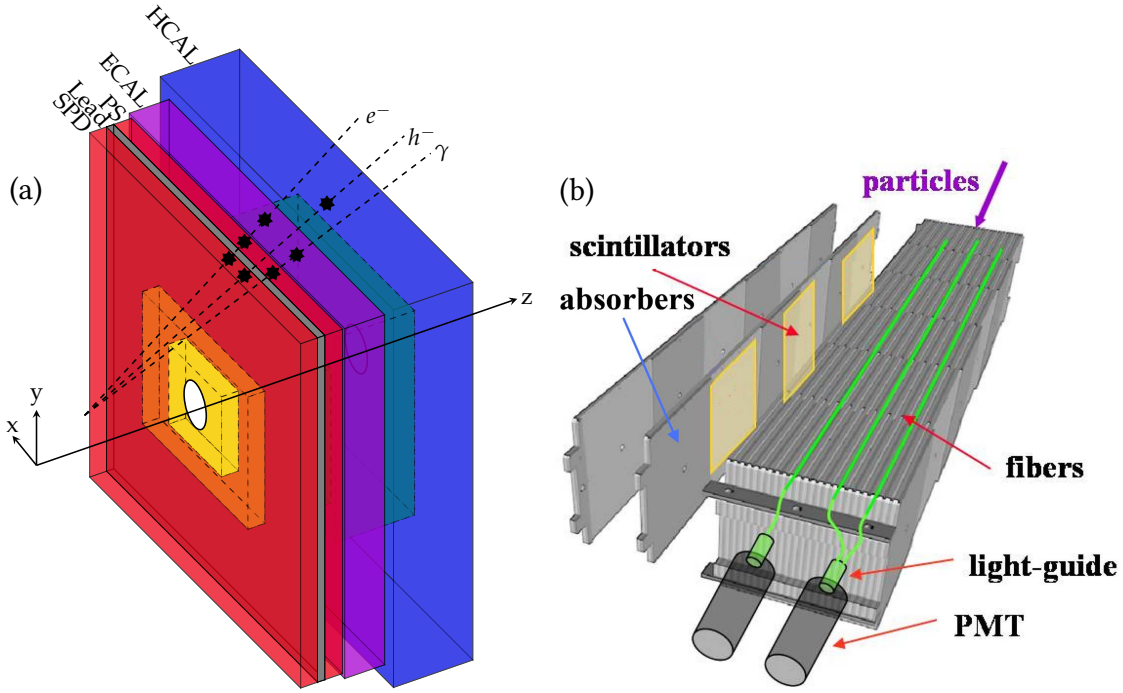

Figure 5.10: Layout of the calorimeter system highlighting its segmentation and the interactions of different particles (a). The z dimension of the SPD/PS is exaggerated for clarity [27]. Exploded 3D view of an HCAL module (b) [10].

deposits initiated by charged and neutral particles, *e.g.* separating photons and π^0 from $e^{\pm}$. The electromagnetic showering process then initiates in the PS, which has the same function of the ECAL but provides much finer granularity. The radiation length[5] of SPS and PS combined amounts to 2.5 X_0.

The remainder of the ECAL, built as a sampling calorimeter, has a length of 25 X_0 in order to fully contain the whole electromagnetic shower. It is composed of 66 alternating layers of 2 mm thick lead and 4 mm thick scintillator tiles. The latter are wrapped in reflecting Tyvek paper with the purpose of increasing the light collection efficiency. Wavelength shifting fibres collect the light generated in the scintillator and guide it to Multi-Anode Photomultiplier Tubes (MAPMT). The same readout technology is shared by the SPD, PS and ECAL, but in the ECAL 64 fibres are read out together by a single photomultiplier.

The HCAL is also made of alternating layers of scintillating tiles and absorbing material (for the HCAL, 1 cm thick iron) for a length of 19.7 cm, but the tiles are oriented parallel to the beam pipe, as shown in Figure 5.10(b). The readout technology uses wavelength shifting fibres and PMTs, which are placed at the downstream end of the HCAL. Figure 5.11 pictures the HCAL as seen from the front, behind the two open halves of the ECAL.

[5] The radiation length X_0 is a property of the material, defined as the mean distance over which a high-energy electron reduces its energy by a factor $1/e$, losing energy by bremsstrahlung.

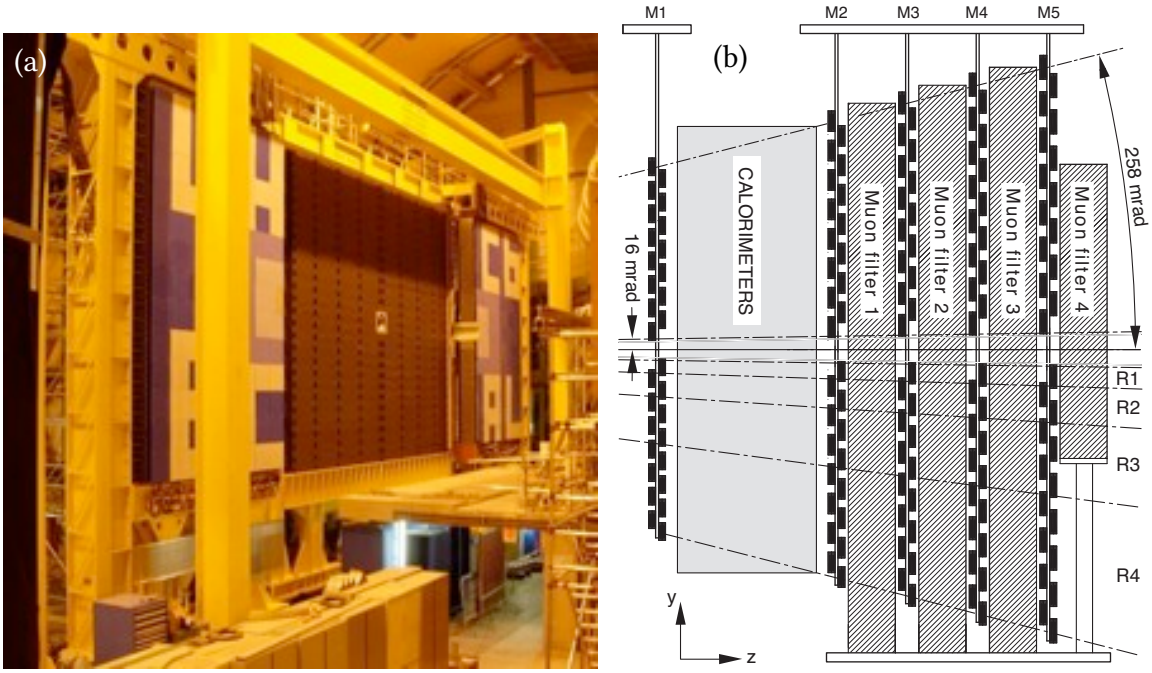

Figure 5.11: View from upstream of the HCAL detector installed behind the two retracted ECAL halves in the LHCb cavern (a). Side view of the muon system (b) [10].

The energy resolution of the calorimeters has an energy dependence measured to be

$$\frac{\sigma_E}{E} \simeq \frac{9\%}{\sqrt{E\,(\text{GeV})}} \oplus 0.8\% \qquad \text{for the ECAL, and} \tag{5.5}$$
$$\frac{\sigma_E}{E} \simeq \frac{69\%}{\sqrt{E\,(\text{GeV})}} \oplus 10\% \qquad \text{for the HCAL,}$$

where the first term accounts for stochastic effects in the development of the shower, and the second one is due to the intrinsic resolution of the detector [10].

The addition of the preceding SPD/PS layer largely improves the PID performance of the calorimeter system. Electrons are separated from hadrons with an efficiency of 92% and a misidentification rate of hadrons as electrons of 4.5% [32].

The muon system

The muon system [33] is composed of five Multi-Wire Proportional Chamber (MWPC) detectors (M1–5). The first one (M1), aimed at improving the transverse momentum (p_T) resolution for use in the trigger, is located in front of the calorimeter system. The other four stations (M2–5) are placed downstream of the HCAL and interleaved by 80 cm thick layers of iron, acting as absorber stopping all particles except muons and neutrinos. A side view of the muon system is sketched in Figure 5.11(b).

The muon stations have finer granularity in the region closest to the beam pipe, and are composed of Multi-Wire Proportional Chambers (MWPC). The innermost part of M1 uses triple-GEM (Gas Electron Multiplier) detectors, which are more suited to cope with the higher occupancy of that region.

The identification of muons is implemented in two ways. One provides information used by the likelihood classifier mentioned in Section 5.2.2. The other one is a binary classifier based on a minimum number of hits in the muon stations depending on the track momentum. Both classifiers were shown to provide very high identification efficiency at the same time as very tight background rejection.

5.3. The LHCb data flow

5.3.1. Simulation

The LHCb simulation software [34] runs in three subsequent steps: event generation, simulation of the detector response, and event reconstruction. The first stage makes use of dedicated packages: EvtGen implements the decay kinematics based on various physical models [35], and the rest of the *pp* interaction is simulated with a version of Pythia [36, 37] specifically tuned on data and configured for LHCb [38]. In the second stage, particles are propagated through the detector using Geant4 [39, 40]. At this time, the detector response is simulated, and signals are digitized converting data into the same format provided by the actual DAQ system. Finally, at the last stage, the same reconstruction algorithm that is used on real data is applied.

5.3.2. Data acquisition and trigger system

The LHC collides bunches of protons at a rate of 40 MHz. The raw data rate recorded at LHCb is way too large to be stored. A Data Acquisition (DAQ) system is employed to build information from the detector data. A system of pre-selections is used to reduce the disk size of the collected data, filtering out uninteresting events. In particular, a series of hardware- and software-based selection algorithms, called *trigger*, is employed to reduce the data rate down to a few kHz [41, 42].

The first level trigger (L0) is implemented in hardware, and uses information from the calorimeters and the muon system. Raw data are processed by the front-end electronics, placed close to the detectors themselves. To cope with the large amount of data, a maximum latency of 4 μs is imposed between the *pp* collision and the final L0 trigger decision. The logic implemented in the front-end electronics selects events with a high transverse momentum energy deposit in the calorimeter, or with a high-p_T track segment in the muon stations, and passes them on to the readout boards. In order to cope with the high-radiation environment and with the large number of readout channels, custom Application-Specific Integrated

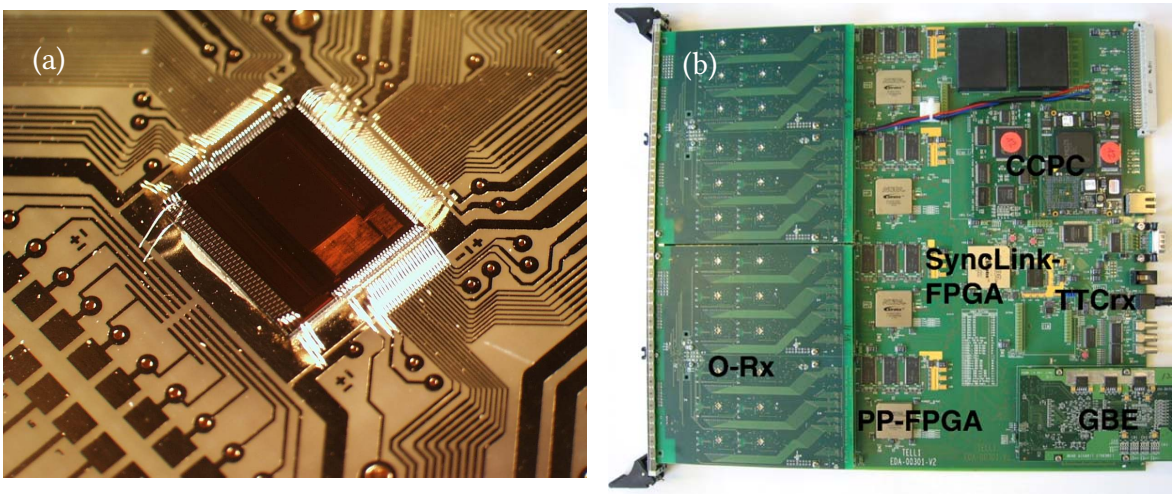

Figure 5.12: The Beetle chip (a) [47] and the TELL1 board (b) [48].

Circuits (ASICs) are used. In particular, all of the silicon subdetectors employ the radiation-hard Beetle chip [43–45], shown in Figure 5.12(a), specifically developed for LHCb [46]. Each of the 128 channels of the Beetle chip consists of a preamplifier/shaper, a programmable analogue pipeline and a serial read-out compatible with a 1 MHz read-out rate.

LHCb's custom-made readout boards, called TELL1 [48], are placed behind a shielding wall to minimize radiation effects. TELL1 boards are motherboards hosting several mezzanine cards; their main data processing elements are five Field Programmable Gate Arrays (FPGA) mounted on each board. The TELL1s are synchronized to the front-end electronics by means of the LHC-wide 40 MHz clock and of dedicated firmware to deal with each subdetector's specific latency, as well as with the specific event format and processing algorithms. Event digitization, noise filtering and zero suppression[6] are performed in the TELL1 boards, which then trasmit compressed data packages to the Event Filtering Farm (EFF) where the rest of the trigger is run. A TELL1 board is pictured in Figure 5.12(b).

The High Level Trigger (HLT) is fully implemented in software and runs on a farm consisting of about 29000 CPU cores. It consists of several trigger lines, dedicated to the various kinds of physics analyses, and it is further divided into two stages. HLT1 implements a partial event reconstruction, tracking particles in the VELO and tracking system and matching them to the calorimeter and muon track segments used in the L0. Thanks to the VELO information, new criteria are available to select tracks based *e.g.* on their impact parameter (IP) with respect to the primary pp interaction vertex. Selected events are transferred to the HLT2, which performs a full event reconstruction with offline-quality output. In Run II, in particular, upgrades to the computing infrastructure allow for high quality decay information to be calculated by the HLT software, making a separate offline event reconstruction unnecessary [42]. HLT2, more than HLT1, is composed of a large number of trigger lines. Each physics analysis uses data

[6] Removal of empty data packets, leading to an event size of about 40 kB.

selected by a specific subset of HLT lines, based on the topological and kinematic features of the seeked events.

5.3.3. Stripping

Even with an output rate of few kHz, the dataset saved to disk is very large. It is computationally too demanding to work on the whole dataset in order to perform physics analyses. Therefore, further selections collectively referred to as *stripping* are applied to data. The stripping software is run twice a year, and it serves the purpose of making smaller datasets available to analysts. The stripping selections are tuned according to the type of decays needed by each analysis.

CHAPTER 6

Radiation damage in the LHCb silicon tracker

Contents

After the first observation of jets [49–52] — *i.e.* cones of hadrons and other particles produced by the hadronization of a single quark or gluon — and following the discovery of the $W^{\pm}$ and Z^0 bosons [53–58] at the UA1 [59] and UA2 [60] experiments, it became clear that particle physics could advance only if experimenters found a way to tag the flavour of quarks.

The lifetime of a particle reflects into the distance between the main interaction vertex, where the particle is produced, and its decay vertex. Therefore, the ability to measure the distance between primary and secondary vertices is of paramount importance, especially to discriminate events containing a pair of b quarks, which are characterized by a long lifetime. This method was first introduced by the DELPHI [61] experiment, and then by

all of the following collider experiments. Particles containing heavy quarks[1] have lifetimes of the order of 1 ps, translating *e.g.* into a flight distance in the mm regime at the LHC. Track reconstruction must then be precise enough to resolve primary and secondary vertices, extrapolating emerging tracks back to the interaction region. Silicon detectors provide the needed level of resolution, and their layers are thin enough to control multiple scattering. LHCb adopts a silicon-based tracking system: the VELO, TT and IT detectors described in Chapter 5 all use silicon sensors.

Operating silicon detectors in a high-radiation environment like that of the LHC, however, must take into account the fact that radiation can modify the crystalline structure of silicon. Being able to predict and monitor radiation damage induced on silicon sensors is crucial. This chapter will introduce the basic principles of silicon detectors (Section 6.1) and the effect of radiation (Section 6.2), and then report in Sections 6.3 to 6.8 on the *in-situ* measurements performed in dedicated LHCb runs aimed at measuring the evolution of the Silicon Tracker properties with irradiation.

The studies presented in this chapter will be published in [62], currently in preparation.

6.1. Principles of silicon detectors

> *The Bible teaches us "In the beginning God created heaven and earth". Today, we still do not know for sure what heaven is made of, but earth consists of, at least the upper crust, silicon and oxygen with some dirt (in the form of the other 90 elements) thrown in for added value.*
>
> F. Hartmann, in [63].

Silicon is a solid semiconductor whose specific conductance ranges between $10^{-9}\ \Omega^{-1}\,\mathrm{cm}^{-1}$ and $10^{-2}\ \Omega^{-1}\,\mathrm{cm}^{-1}$, somewhere between metals and insulators [63]. Electrical conductance is known to derive from the covalent bonds in the crystal lattice: the energy band structure of semiconductors presents a forbidden region, called the *band gap*, separating the valence band from the conduction band. If an electron absorbs sufficient energy, $E > E_{gap}$, it can enter the conduction band, leaving a so-called *hole*[2] in the valence band. Both electron and hole can move if an external electric field is applied. In absence of lattice impurities, the concentration of electrons in the conduction band, n, and that of holes in the valence band, p, are both equal to the intrinsic concentration n_i, which is a function of temperature. By adding impurities, one can effectively insert additional energy levels within the band gap. This process, called *doping*, increases the probability of electrons moving to the conduction band and of holes moing to the valence band. Silicon is a type-IV material[3], meaning that it has four valence electrons (*cf.* Mendeleev's periodic table, schematically depicted in Figure 6.1). The addition

[1] Typically c and b quarks.
[2] A positively charged ionized atom.
[3] According to the original and to the CAS naming conventions.

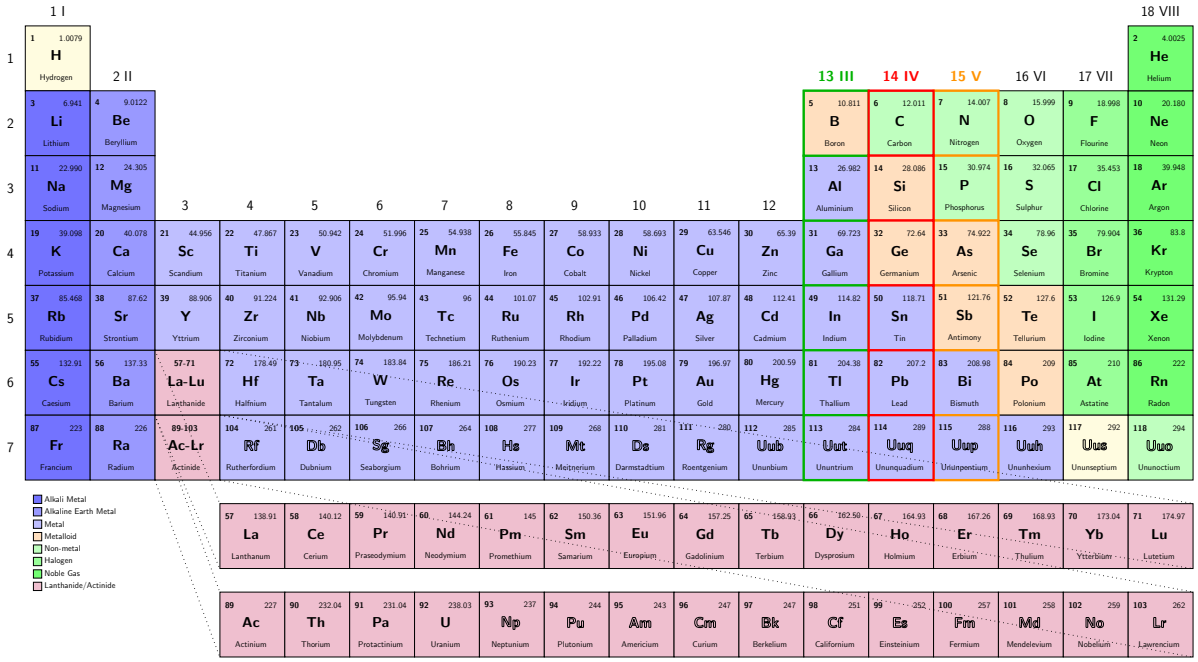

Figure 6.1: Mendeleev's periodic table of the elements. Highlighted are type-III, type-IV and type-V elements. Silicon is a type-IV element, and its crystalline structure can be doped with type-III acceptors or type-V donors in order to alter its conductivity properties.

of type-V impurities, *i.e.* donor materials with excess of electrons, produces n-type silicon; p-type silicon is obtained by the addition of acceptor material, *i.e.* type-III elements with three valence electrons. A typical donor material is phosphorus; widespread is the use of boron and aluminum as acceptors.

For doped silicon, the concentration of charge carriers is dominated by the concentration of dopant, and has a temperature dependence following the mass action law:

$$np = n_i^2 = N_C N_V e^{-\frac{E_{gap}}{k_B T}} \tag{6.1}$$

where N_C and N_V represent the density of states in the conduction and energy band, respectively, $E_{gap} = E_C - E_V$ is the width of the band gap, k_B is the Boltzmann constant and T is the silicon temperature. The conductivity σ of the material is given by

$$\sigma = e\left(\mu_e n + \mu_h p\right) \tag{6.2}$$

where e is the electron charge, and the electron and ion mobilities μ_e and μ_h derive from their drift velocities $v_D^{e,h}$ and from the applied electric field E with $\mu = v_D/E$. The drift velocity is proportional to the mean time τ_L between scattering processes. Scattering can happen in correspondence of crystal defects, impurities, and thermally stimulated phonons (lattice vibrations). The electron and ion mobilities depend on the characteristics of the material. For

a given material, the drift velocity is proportional to the applied electric field.

Semiconductors, especially silicon, are widely used as base material for electronic components and microelectronic circuits. It is then convenient to adapt the already developed industrial processes for the production of silicon-based detectors. Moreover, the intrinsic high mobility of electrons and holes in silicon makes silicon detectors convenient for use in High Energy Physics (HEP) applications, due to their excellent signal collecting time (O (10 ns) for a 100 μm thick sensor).

6.1.1. The *pn*-junction

Silicon substrate maintains a dynamical equilibrium. Electron-hole pairs are created and recombine continuously. In a typical HEP sensor at room temperature the number of free charge carriers is $O\left(10^9\right)$, whereas the number of pairs created by a minimum ionizing particle (MIP) is of the order of 10^4 (further details will be given in Section 6.1.4) [63]. As the detection of any signal would be unpractical in these conditions, the number of thermally created free charge carriers must be reduced by several orders of magnitude. This can be done by either cooling down the device, which however is problematic for large detectors, or by depleting the silicon volume exploiting the properties of a *pn*-junction. Silicon sensors are, in fact, diodes operated in reverse-bias mode.

Joining *n*-type and *p*-type silicon substrates together creates in fact a space charge region, where the majority charge carriers from each side diffuse to the opposite region. By leaving behind charged ionized atoms, they create an electric field and oppose further charge diffusion, inducing once more a dynamical equilibrium. The difference of potential in the space charge region at this stage is called *intrinsic* or *built-in* voltage and is given by

$$V_{in} = \frac{e}{2\epsilon\epsilon_0} N_{eff} w^2, \tag{6.3}$$

where:

- $\epsilon\epsilon_0$ is the effective permittivity of silicon,
- w is the width of the depleted area,
- N_{eff} represents the effective dopant concentration, and it is defined as

$$N_{eff} = \left(n w_n^2 + p w_p^2\right) / w^2, \tag{6.4}$$

  where w_n and w_p are the width of the depleted areas on the *n*- and *p*-side of the junction, respectively, and $w = w_n + w_p$.

Conversely, the width of the depleted region around a *pn*-junction can be calculated based on

the properties of the material:

$$w = \sqrt{\frac{2\epsilon\epsilon_0}{eN_{eff}} V_{in}}. \tag{6.5}$$

The application of an external voltage V_{bias} will disturb the equilibrium and increase or reduce – depending on the polarity – the width of the depleted region:

$$w = \sqrt{\frac{2\epsilon\epsilon_0}{eN_{eff}} (V_{in} + V_{bias})}. \tag{6.6}$$

If the external voltage is of reverse polarity with respect to the junction, the depleted area expands with V_{bias} until the whole thickness of the sensor is depleted. This condition is called *full depletion* and the corresponding bias voltage is given by

$$V_{depl} = \frac{e}{2\epsilon\epsilon_0} N_{eff} W^2 - V_{in} \tag{6.7}$$

where W is the thickness of the sensor. V_{in} is ormally much smaller than V_{depl}, allowing for the approximation

$$V_{depl} \approx \frac{e}{2\epsilon\epsilon_0} N_{eff} W^2. \tag{6.8}$$

6.1.2. Leakage current

Eqn. 6.2 describes the impact of the charge carrier mobility μ on the conductivity of silicon. The mean time τ_L between scattering processes, which is proportional to the charge carriers drift velocity and therefore to their mobility, is mainly influenced by second-order Shockley-Read-Hall processes [64, 65]. It can be expressed as:

$$\tau_L = \frac{1}{\sigma_c v_{th} N_t} \tag{6.9}$$

where σ_c is the cross-section of the charge carriers, v_{th} their thermal velocity and N_t the concentration of impurities, acting as traps. In a fully depleted sensor, thermally generated pairs are separated and swept towards the sensor boundaries by the electric field induced by the external voltage. This is an undesired effect, and the resulting current I_L is called *reverse* or *leakage current*. This current is proportional to the volume of the sensor and grows with decreasing τ_L according to the relation

$$I_L = \frac{e}{2} \frac{n_i}{\tau_L} wA, \tag{6.10}$$

where A is the surface of the junction.

6.1.3. Silicon oxide interface

Pure silicon is too chemically reactive to be of use in a particle detector. Silicon dioxide (SiO_2), on the other hand, is a dielectric material, one of the best insulators [63]. Modern silicon strip sensors employ a thin SiO_2 layer to protect the silicon strips. The Si-SiO_2 interface density of energy states in the band gap is very low, preventing combination of charge carriers between the two sides of the interface. A metal strip, connected to the readout electronics, is placed on top of the oxide layer[4]: this way, a capacitive coupling between the sensor and the metal contact is created, which can then be integrated with the front-end electronics. The condition of the Si-SiO_2 interface is determined by the oxide charge and by the voltage of the metal strips, which is typically zero during normal operation of a silicon strip detector. Sensors intended for use in HEP are designed such that the surface charge has the same polarity as the majority charge carriers, which are therefore driven into the bulk. This configuration is referred to as *surface depletion*.

Charges accumulating on the oxide surface can alter the electric field in the vicinity of the strips, and affect the insulation and capacitance between neighbouring strips.

6.1.4. Detection of charged particles

Pairs of charge carriers are released in the material of the detector by traversing charged particles that lose part of their energy through elastic collisions with the electrons of the material. The rate of ionisation energy loss for charged particles is described by the Bethe-Bloch relation [66–68]

$$\frac{dE}{dx} = -2\pi N_A r_e^2 m_e c^2 \rho \frac{Z}{A}\frac{z^2}{\beta^2}\left[\ln\frac{2m_e c^2\beta^2 W_{max}}{I^2\,(1-\beta^2)} - 2\beta^2 - \delta - 2\frac{C}{Z}\right], \tag{6.11}$$

[4] The acronym indicating the traditional MOS structure stands, in fact, for Metal-Oxide-Semiconductor.

where:

x is the path length normalized to the density, in $\mathrm{g\,cm^{-2}}$;
N_A is the Avogadro constant ($6.022 \times 10^{23}\,\mathrm{mol^{-1}}$);
r_e $= e^2/4\pi m_e c^2$ is the classical electron radius (2.817×10^{-15} m);
$m_e c^2$ is the electron mass (511 keV);
ρ is the density of the material in $\mathrm{g\,cm^{-3}}$;
Z is the atomic number of the material;
A is the atomic weight of the material;
z is the charge of the traversing particle in units of e, the electron charge;
β $=$ is the velocity of the traversing particle in units of c, the speed of light;
γ $= 1/\sqrt{1-\beta^2}$;
W_{max} is the maximum energy transfer in a single collision;
I is the effective ionisation potential of the medium, averaged over all electrons;
δ accounts for the polarization of the medium due to the traversing particle, and
C accounts for the fact that collisions with the inner shells electrons are rare [69].

The energy loss per unit lenght is expressed in Eqn. 6.11 as a function of the particle velocity β. The latter is related to the particle energy by relativistic kinematics:

$$E = \gamma mc^2 = \frac{mc^2}{\sqrt{1-\beta^2}}. \tag{6.12}$$

The energy loss per unit length can therefore be analysed as a function of the particle energy or of any of its kinematic properties. Figure 6.2(a) shows the energy loss per unit length of a charged pion traversing silicon as a function of its kinetic energy. For non-relativistic energies the energy loss is inversely proportional to the particle energy. A minimum is reached, followed by a logarithmic rise at relativistic energies leading to saturation at very high energy, due to the so-called "density effect": the traversing particle polarizes the media, whose atoms can no longer be considered independent targets. Particles depositing a minimum of energy per unit path length are called Minimum Ionizing Particles (MIP) [69, 70]. Detectors need to keep their noise level small compared to the energy deposit of a MIP in order to be used as efficient particle detectors. Furthermore, statistical fluctuations cause the energy deposit per scattering event to vary, an effect described by a straggling function first derived by Landau [71]. In some cases, electrons excited by the traversing particle have enough energy to cause further ionization by scattering themselves on other atoms. These are called δ-rays, and cause the large asymmetric tail on the right-hand side of the energy deposit distribution, showcased in Figure 6.2(b). As a consequence, the most probable energy loss is about 30%

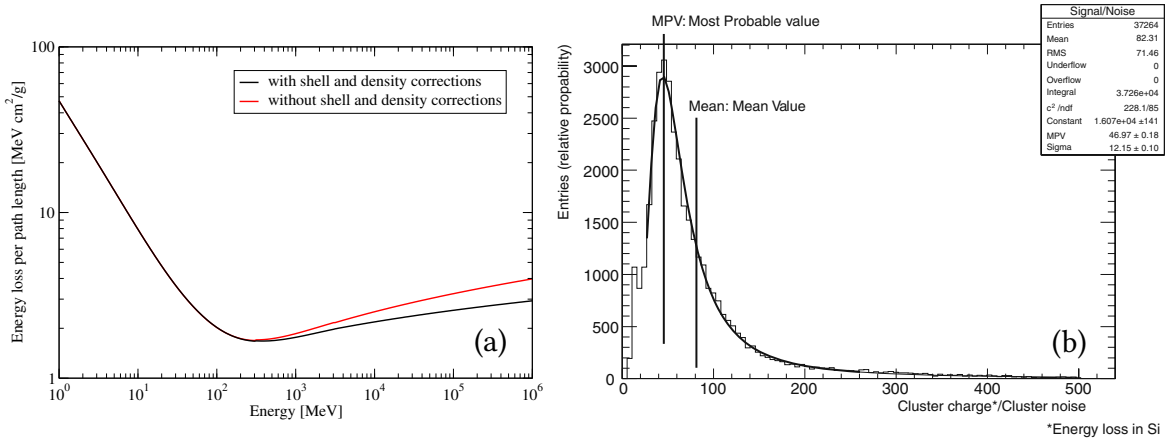

Figure 6.2: Energy loss per unit length of a charged pion traversing silicon as a function of its kinetic energy (a) [70]. Charge deposited by ionization from cosmic muons at MIP energies traversing a 500 µm thick silicon sensor (b) [63].

smaller than the average energy loss. In silicon at room temperature, the average energy lost in ionizing collisions is $\bar{E}_{ion} = 3.62$ eV. This is larger than the silicon band gap $E_{gap} = 1.12$ eV: in fact, part of the deposited energy is lost in phonon creation (vibrational modes of the crystalline lattice), and electrons can generally absorb more energy than the amount needed to cross the band gap.

Figure 6.3 demonstrates the working principle of a silicon sensor. Unlike gas detectors, silicon sensors do not use electron avalanche-based methods to amplify the charge read out at the electrodes. However, the raw signal created in silicon devices is large enough to be measured without intrinsic charge amplification. The number of pairs created by a MIP oscillates about a mean value $\bar{n}_{pairs}$ given by

$$\bar{n}_{pairs} = \frac{E}{\bar{E}_{ion}}, \tag{6.13}$$

where E is the energy deposited by the traversing particle, which can be calculated by integrating Eqn. 6.11 over the thickness of the depleted sensor. Given the high density of silicon, $\rho = 2.33\,\mathrm{g\,cm^{-3}}$, the average energy loss of a MIP is about $390\,\mathrm{eV\,\mu m^{-1}}$, while the most probable energy loss is about $270\,\mathrm{eV\,\mu m^{-1}}$. The latter results in the creation of about 75 charge carriers per µm. For a 300 µm thick sensor, the most probable signal exceeds 22000 electrons (holes). The variance of the number of released charge carriers can be parametrized as

$$\sigma^2\left(n_{pairs}\right) = F \times n_{pairs}, \tag{6.14}$$

where F is the so-called Fano factor [64, 72], indicating the fraction of the total deposited energy that contributes to ionize the material. For silicon, $F = 0.115$ [73]: such a small factor

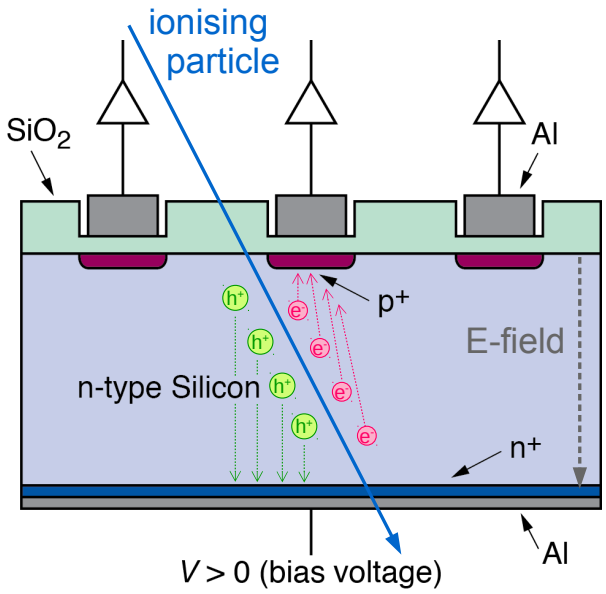

Figure 6.3: Sketch demonstrating the working principle of a p^+-in-n silicon sensor such as the type used for the LHCb Silicon Tracker.

indicates that ionization dominates over phonon excitation.

6.2. Effect of radiation on a silicon sensor

LHC experiments need to maximize the flux of recorded particles, in order to achieve the large statistical samples necessary for the analysis of rare processes. Their detectors, therefore, operate in a very high radiation environment. Particles traversing silicon detectors can damage the silicon lattice. This effect is commonly referred to as *radiation damage*, or *ageing* of the detector. Ageing effects on silicon depend on the type and energy of the traversing particle. Therefore, it is convenient to normalize fluence to a reference type of particles, typically neutrons of 1 MeV kinetic energy (fluence is then measured in units of '1 MeV neutron equivalent'). Empirical models describing radiation damage rescale contributions from different types of radiation by applying damage coefficients measured with different types of particles over a wide energy range, and characterize silicon ageing as a function of the fluence $\Phi_{1\text{ MeV-}n,\text{eq}}$ of slow neutrons. Hereinafter, as in literature, the ionizing dose collected by the sensor is normalized to units of 1 MeV neutron equivalent fluence. Two main types of radiation damage can be distinguished for silicon devices, described below.

Surface damage

Surface damage occurs when electron-hole pairs are produced in the insulating oxide layer. Since charge carriers cannot drift to the electrodes, they remain trapped in the oxide, increasing

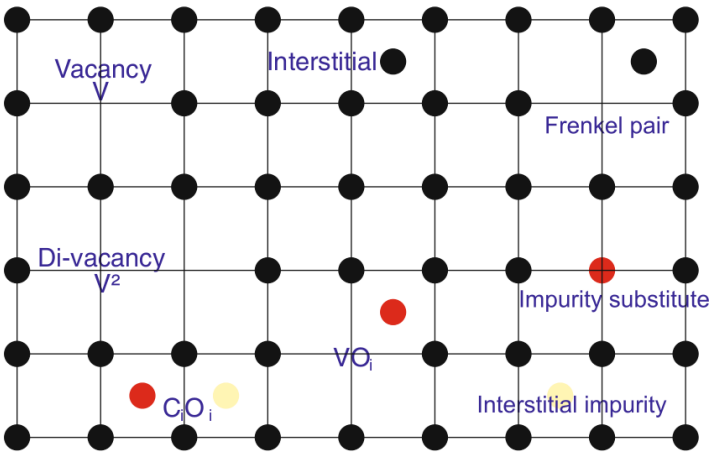

Figure 6.4: Effects of bulk radiation damage on a silicon detector [63].

its charge. In dielectric material the rate of recombination can be very low, leading to irreversible damage. In SiO_2, highly mobile electrons are attracted to the metal implant, while slowly moving holes drift to the Si-SiO_2 interface. Consequences of this effect include an increase of interstrip capacitance, leading to higher noise, and an increase in cross-talk, due to lower interstrip resistance.

This type of damage tends to saturate after a rather low irradiation dowse, and to then remain constant in time.

Bulk damage

Bulk damage occurs due to changes in the silicon lattice. Particles crossing the silicon detector can have non-ionising interactions with a recoiling atom in the lattice. Atoms may be displaced from their lattice positions, and subsequently diffuse (Figure 6.4). The creation of so-called Frenkel pairs, *i.e.* interstitials and vacancies (space charge) leads to:

- increase of the leakage current I_L due to the creation of defects acting as scattering centres, which effectively reduce the lifetime τ_L;
- the removal of donors and the creation of additional energy levels acting as acceptors, modifying the effective dopant concentration and thus changing the voltage V_{depl} needed to deplete the sensor;
- defects in the lattice which may act as traps for charged particles, decreasing the charge collection efficiency. At effective fluences above 10^{15} equivalent 1 MeV-n, eq charges may no longer arrive at the collecting electrodes in 300 µm thick sensors.

The doping of the LHCb ST was chosen in such a way that exposure to radiation has an effect of first decreasing the effective doping (and thus the depletion voltage V_{depl}) until the point of type inversion, and subsequently increasing both the effective doping and V_{depl}.

Parameter	Value	Description
$n_{c,0}$	$(3.28 \pm 0.26) \times 10^{-10}\,\mathrm{cm}^{-3}$	Initial concentration of donors
c_c	$2.29 \times 10^{-13}\,\mathrm{cm}$	Donors removal rate
g_c	$(1.60 \pm 0.04) \times 10^{-2}\,\mathrm{cm}^{-1}$	Acceptors growth rate
g_a	$(1.40 \pm 0.14) \times 10^{-2}\,\mathrm{cm}^{-1}$	Annealing coefficient
$k_{a,0}$	$(2.4 \pm 1.0) \times 10^{15}\,\mathrm{s}^{-1}$	Annealing frequency factor
E_{aa}	$(1.09 \pm 0.03)\,\mathrm{eV}$	Annealing activation energy
g_r	$(5.70 \pm 0.09) \times 10^{-2}\,\mathrm{cm}^{-1}$	Reverse annealing coefficient
$k_{r,0}$	$(1.5 \pm 1.1) \times 10^{15}\,\mathrm{s}^{-1}$	Reverse annealing frequency factor
E_{ar}	$(1.31 \pm 0.03)\,\mathrm{eV}$	Reverse annealing activation energy

Table 6.1: Parameters used for the Hamburg model predictions. Their values were measured in dedicated irradiation campaigns and can be found in literature [74].

6.2.1. The Hamburg model

Phenomenological models have been developed to describe the evolution of effect of radiation damage on silicon detectors in known radiation environments. In particular, the Hamburg model [74] describes the change of the effective doping concentration N_{eff} as a function of fluence. This model, whose parameters were determined in irradiation campaign of silicon sensors, is composed of three terms:

- **Stable damage term**: a radiation-induced change in the silicon band structure, provoking a removal of donor atoms with an exponential behaviour with fluence, and a linear increase in the number of stable acceptors:

$$n_c\left(\Phi_{1\text{ MeV-}n,\,\mathrm{eq}}\right) = n_{c,0}\left[1 - \exp\left(-c_c\Phi_{1\text{ MeV-}n,\,\mathrm{eq}}\right)\right] + g_c\Phi_{1\text{ MeV-}n,\,\mathrm{eq}}, \tag{6.15}$$

  where $n_{c,0}$ represent the initial concentration of donors, c_c their exponential removal rate, and g_c the linear acceptors increase rate.

- **Annealing term**: after irradiation, sensors undergo a temperature-dependent process of annealing of induced defects (e.g. by recombination) that can be modeled by an exponential form:

$$n_a\left(\Phi_{1\text{ MeV-}n,\,\mathrm{eq}}, t, T\right) = g_a\Phi_{1\text{ MeV-}n,\,\mathrm{eq}}\exp\left(-t/\tau_a\left(T\right)\right) \tag{6.16}$$

  where g_a represents the annealing introduction rate, and the time scale τ_a is given by the Arrhenius relation

$$1/\tau_a\left(T\right) = k_{a,0}\exp\left(-E_{aa}/k_BT\right), \tag{6.17}$$

  where E_{aa} is the average activation energy of annealing processes.

- **Reverse annealing term**: the combination of individual defects into defect clusters is also possible, and leads to a change in N_{eff} on a different time scale, typically larger than that of positive annealing:

$$n_r\left(\Phi_{1\text{ MeV-}n,\text{eq}}, t, T\right) = g_r \Phi_{1\text{ MeV-}n,\text{eq}}\left(1 - 1/(1 + t/\tau_r(T))\right) \tag{6.18}$$

with g_r describing the reverse annealing introduction rate, and τ_r given by

$$1/\tau_r(T) = k_{r,0}\exp\left(-E_{ar}/k_B T\right), \tag{6.19}$$

E_{ar} being the activation energy of reverse annealing processes.

The evolution with time of N_{eff} depends on the integrated fluence $\Phi_{1\text{ MeV-}n,\text{eq}}$ and on the sensor temperature T, which can be measured. The values of all the model parameters, used in the simulation described in Section 6.7, can be found in Table 6.1. During the LHC operation, irradiation periods extend over long time scales, and are not always sequentially followed by annealing periods. Therefore, a differential approach [13] is used in order to predict the evolution of the effective doping ΔN_{eff} and thus ΔV_{depl}:

$$\begin{aligned}\left.\frac{dN_{eff}}{dt}\right|_{t=0} =& c \times n_{0,c}\exp\left(-c\Phi_{1\text{ MeV-}n,\text{eq}}\right) \times \frac{d\Phi_{1\text{ MeV-}n,\text{eq}}}{dt} \\ &+ \Phi_{1\text{ MeV-}n,\text{eq}} \times \left(\frac{g_r}{\tau_r(T)} - \frac{g_a}{\tau_a(T)}\right) + \frac{d\Phi_{1\text{ MeV-}n,\text{eq}}}{dt} \times (g_a + g_c)\,.\end{aligned} \tag{6.20}$$

6.3. Monitoring of the radiation damage in the LHCb ST

An integrated luminosity of about 3 fb^{-1} was collected by LHCb during the LHC Run I (2010–2012) at proton-proton collision energy $\sqrt{s} = 7$ and 8 TeV. An additional 3.7 fb^{-1} was collected at $\sqrt{s} = 13$ TeV since the beginning of LHC Run II (2015–2017); 2 fb^{-1} more are expected in 2018. After the end of Run II, LHCb plans to replace both the TT and the IT with new detectors, capable of coping with an instantaneous luminosity about five times larger than that achieved during Run II, and compatible with a 40 MHz readout rate. A finer granularity silicon strip-based Upstream Tracker (UT) will replace the TT, and a Scintillating Fibre (SciFi) detector will take the place of the three T-stations now composed by the IT in the inner region and the OT in the outer region [75].

Radiation damage, and its impact on the ST performance, is monitored in two independent ways. One uses the observed change in the sensors leakage current, and the other one measures the change in full depletion voltage. The leakage current method is presented in Section 6.4 and thoroughly described in [13, 62].

Due to the detector being currently installed in the LHCb cavern, and contained in detector boxes for temperature regulation, it is not possible to perform an in-situ measurement of the

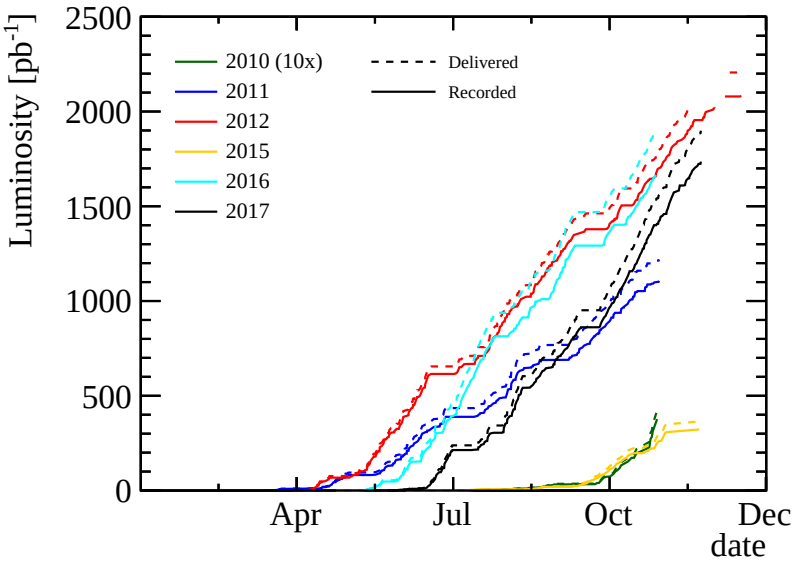

Figure 6.5: Sketch showing the evolution of the integrated luminosity for each year of LHC operation, highlighting the delivered luminosity (dashed line) and the luminosity recorded by LHCb (solid line).

depletion voltage V_{depl} through a capacitance scan. A viable way to probe the evolution of the effective concentration N_{eff} is to monitor the dependence on the applied bias voltage V_{bias} of the amount of charge collected by the sensor when hit by a charged particle. This quantity increases with the bias voltage for $V_{bias} \leq V_{depl}$, and saturates for $V_{bias} > V_{depl}$. Such approach requires dedicated data taking runs, named Charge Collection Efficiency (CCE) scans. The operational conditions of the CCE scans are incompatible with normal data taking due to the variation of V_{bias}; the scans are therefore performed in regular intervals two to four times a year, following the end of the physics run and before its restart, and after shorter technical stops. Sections 6.5 and 6.6 will describe this method in detail. The outcome is compared in Section 6.7 with the expected evolution of V_{depl} according to the Hamburg model, based on the measured fluence and temperature.

6.4. Leakage current

The continuous measurement of the ST leakage currents provides a reliable method to monitor the radiation-induced damage in the silicon sensors bulk.

For the LHCb Silicon Tracker, we define the leakage current as the value of the current measured at the end of each LHC fill in each bias voltage channel. Bias voltage is distributed to multiple ST readout sectors through patch panels implementing a higher granularity partitioning in the central detector regions, and coarser partitioning in the outher regions. In the IT, each channel is connected to four readout sectors, each composed of either one or two sensors. In the TT, each channel serves either one, two or three readout sectors, for a total

Parameter	Value	Description
$\alpha_{I,0}$	$(6.67 \pm 0.09) \times 10^{-17}\,\mathrm{A\,cm^{-1}}$	Normalization of the linear term
$\alpha_{I,1}$	$(7.23 \pm 0.06) \times 10^{-17}\,\mathrm{A\,cm^{-1}}$	Normalization of the exponential term
$\alpha_{I,2}$	$(3.08 \pm 0.07) \times 10^{-18}\,\mathrm{A\,cm^{-1}}$	Normalization of the logarithmic term
$k_{I,0}$	$(4.2 \pm 0.5) \times 10^{13}\,\mathrm{s^{-1}}$	Frequency factor
$E_{a,I}$	$(1.11 \pm 0.05) \times 10^{13}\,\mathrm{eV}$	Activation energy
t_0	$1.5 \times 10^{7}\,\mathrm{s}$	Annealing time scale

Table 6.2: Parameters used for the leakage currents predictions. Their values, taken from [76], were measured in dedicated irradiation campaigns. The value of t_0 was set to about 170 days after the start of the LHC Run I.

number of sensors ranging from 1 to 12. Overall, each HV channels serves a silicon volume going from 4.55 cm^3 to 54.60 cm^3.

Measured currents are cleaned by removing LHCb runs with special configurations (*e.g.* CCE or timing scans) and by removing erroneous measurements such as null ones and outliers due to glitches in the control software. The ambient temperature is measured using sensors placed in the detector boxes. As it is due to the excitation of electron-hole pairs, the leakage current has a temperature dependence that can be described by the relation

$$\frac{I_L(T_1)}{I_L(T_2)} = \left(\frac{T_1}{T_2}\right)^2 \exp\left[\frac{E_g}{2k_B}\left(\frac{1}{T_2} - \frac{1}{T_1}\right)\right], \tag{6.21}$$

where $T_{1,2}$ are two arbitrary temperatures and E_g is the silicon band gap energy [62]. In the remainder of this section, current measurements taken at different times are combined through normalization to a temperature of 8°C.

Figure 6.6 and 6.7 show the leakage current per silicon volume, respectively for TT sectors and for IT sectors, as a function of the fluence each sector has been exposed to. The fluence is calculated by means of the FLUKA simulation described in Section 6.7. The change in leakage current per silicon volume $\Delta I_L/V$ can be modeled as a linear function of the fluence Φ with $\Delta I_L/V = \alpha(t,T)\,\Phi$. The coefficient α shows an evolution with time, due to the alternating periods of irradiation and annealing, and a temperature dependence. It can be parametrized as the sum of a constant and of an exponential term, with the addition of a logarithmic term describing long-term annealing [76], as:

$$\alpha\left(t, T|\alpha_{I,0}, \alpha_{I,1}, \alpha_{I,2}, t_0\right) = \alpha_{I,0} + \alpha_{I,1} e^{-t/\tau_L(T)} + \alpha_{I,2} \log\left(t/t_0\right), \tag{6.22}$$

where the time constant τ_L has a temperature dependence given by the Arrhenius relation $1/\tau_L(T) = k_{I,0} \exp\left(-E_{a,I}/k_B T\right)$, whose parameters are listed in Table 6.2. The time scale t_0, corresponding to about 170 days after the start of the LHC Run I, was chosen such to ensure a nonnegligible level of irradiation before annealing starts to take place.

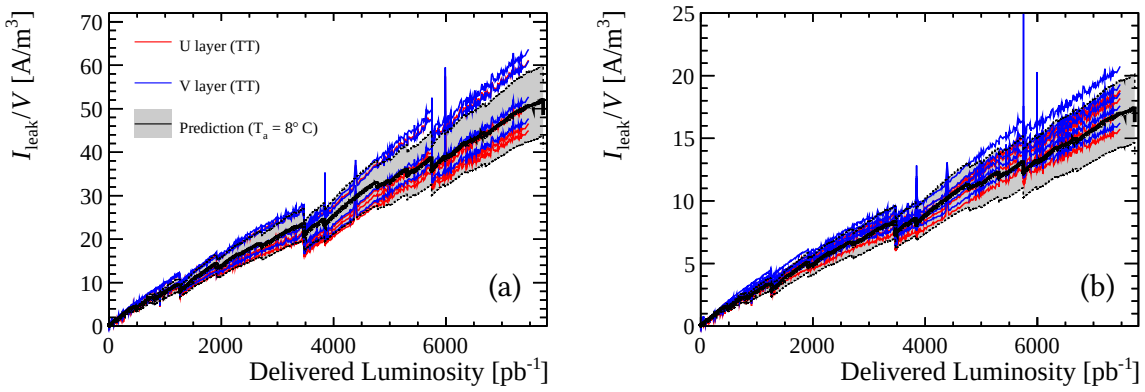

Figure 6.6: Evolution of the leakage current for the different HV channels connected to (a) one-sensor and (b) two-sensor read-out sectors in TT as a function of the delivered integrated luminosity measured. The red curves show channels in the detector layer TTaU, the blue one in TTbV. The predicted evolution is shown in black while the grey band shows its uncertainty, computed from the uncertainty on the model parameters, on the FLUKA simulation and on the temperature measurements. The uncertainty does not account for the range of fluence expected across the sectors shown.

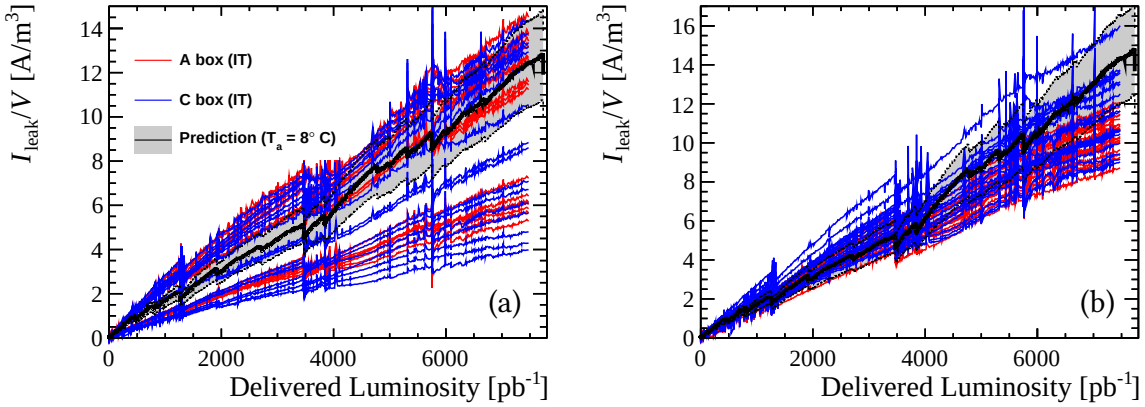

Figure 6.7: Evolution of the leakage current in the different HV channels connected to (a) one-sensor and (b) two-sensor read-out sectors in IT. The red lines show HV channels in the A-side detector box and the bottom detector box in (a) and (b), respectively, the blue lines the HV channels in the C-side detector box and the top detector box in (a) and (b), respectively.

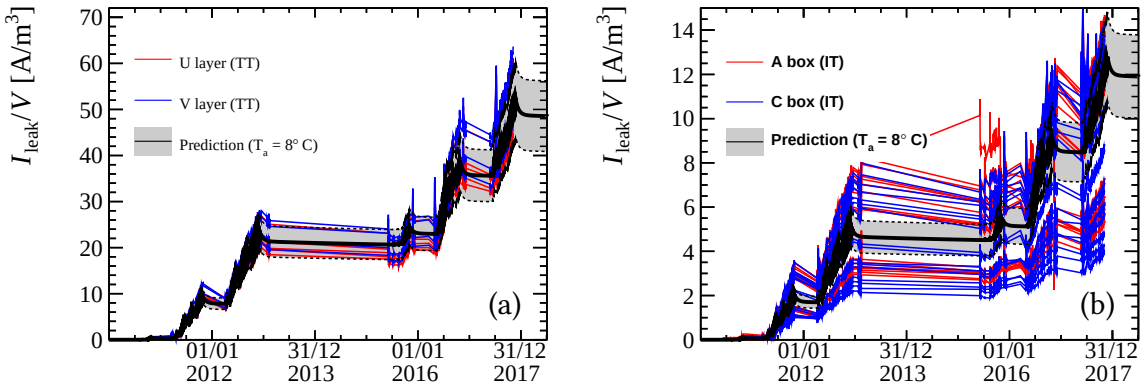

Figure 6.8: Evolution of the leakage current with time in the HV channels connected to one-sensor read-out sectors of the TT (a) and of the IT (b).

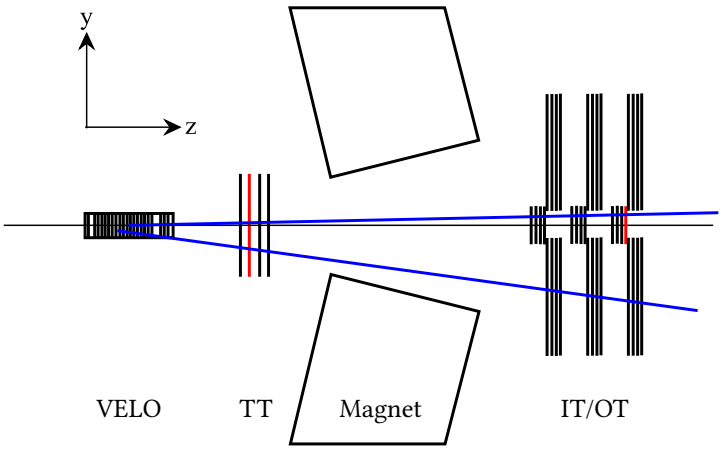

Figure 6.9: Sketch depicting the LHCb tracking system during a CCE scan: the bias voltage of the layers drawn in red is scanned, while the other layers are used for track reconstruction [13].

Figure 6.6 and 6.7 also show, based on this formalism, the predicted evolution of the leakage currents, using the actual LHCb running conditions (peak luminosity, used in the fluence calculation, and detector temperature). Data show good agreement with the prediction. As expected, periods corresponding to LHC shutdowns (*i.e.* the LS1, end-of-the-year stops, or shorter technical stops) are visible, that lead to a decrease in ΔI_L.

Figure 6.8 highlights the time evolution of the leakage current for TT and IT one-sensor readout sectors. The periods of irradiations and those corresponding to the LHC shutdowns are clearly distinguishable. The annealing effect of long-term shutdowns reduces the magnitude of the bulk currents, until irradiation restarts.

6.5. CCE scans

This method was initially developed to monitor radiation damage during the LHC Run I [13]. It has since been extended to Run II, and it has undergone continuous improvements refining the algorithms used for the analysis of CCE scan data and the treatment of the corresponding statistical and systematic uncertainties.

Radiation damage is probed for in one layer of the TT (TTaU) and one of the IT (T3X2) only. The other layers are used for track reconstruction. The reconstructed tracks are extrapolated to the probed layer, where we look for a cluster of deposited charge in a search window around the track position. The setup is sketched in Figure 6.9.

Depending on the detector (TT and IT sensors have different thickness), different V_{bias} ranges are probed as listed in Table 6.3. The bias voltage also influences the charge collection speed. In order to make sure the whole deposited charge is collected, a timing scan is performed for every voltage step, reading data at a time $t_0 + \delta t$ where δt takes the values in

TT V_{bias} steps	60, 100, 125, 150, 175, 200, 225, 250, 300, 350, 400 V
IT V_{bias} steps	20, 40, 60, 75, 90, 105, 120, 140, 170, 200, 400 V
Timing steps in 2011	0, -6.25, -3.125, +3.125, +6.25, +9.375 ns
Timing steps since 2012	0, -9.375, -4.69, +4.69, +9.375, +14.06 ns

Table 6.3: Bias voltage steps and sampling time shifts cycled during CCE scans.

Table 6.3 and t_0 is the nominal Beetle chip signal sampling time, used in physics data taking[5]. The Beetle sampling time is shifted through the ST Control Boards as described in [77]. A change in the software governing the detector control system in early 2012 lead to a change in the width of the timing steps, resulting in a broader probed time window.

Data are read out non zero-suppressed, *i.e.* the *ADC* values of all channels are saved, regardless of the presence of a nearby cluster of deposited charge. A custom tracking algorithm is run, which excludes the scanned layers from the track reconstruction. Tracks are then extrapolated to the scanned layers using a parabolic track extrapolator [78]. The *ADC* values of the strip closest to the extrapolated track and that of the two (TT) or six (IT) closest neighbours is summed, giving an estimate of the signal amplitude. We use a larger set of neighbouring strips for the IT due to track extrapolation being less precise in T3X2, which is the most downstream layer of the IT. Finally, a sample of noise-induced clusters is collected as well. This is obtained by recording the *ADC* value of random combinations of 3 (7) neighbouring strips from events in which no extrapolated tracks hit the corresponding TT (IT) readout sector.

Table 6.4 summarizes the CCE scans performed between 2011 and 2017.

6.6. Estimation of the depletion voltage

6.6.1. Track selection

Data collected in CCE scans is prepared for analysis by removing spurious tracks, and tracks which could not be correcly reconstructed. Tracks not associated to real particles result in low-charge signals that pollute the *ADC* distributions used to estimate the detector's charge collection efficiency. Examples of *ADC* distributions before any track selection are shown in Figure 6.12 (dotted lines). The latter present a noise contribution centred at about 0 *ADC* counts and with a Gaussian shape; signal tracks, on the other hand, tend to deposit more charge.

We found that a threshold of 16 *ADC* counts is optimal to separate the contributions of noise and signal in both subdetectors. Using this threshold, the characteristics of signal-like

[5] With *sampling time* we refer to the delay implemented in the readout electronics such that information recorded at a certain point in time by a certain subdetector is correctly associated with data from the other subdetectors recorded during the same LHC bunch crossing.

Date	Fill number	Integrated luminosity (fb^{-1})		
		7 TeV	8 TeV	13 TeV
2011-07-14	1944	0.48	–	–
2011-09-07	2083	0.81	–	–
2011-10-25	2252	1.24	–	–
2012-04-05	2472	1.26	–	–
2012-07-02	2797	1.26	0.66	–
2012-09-28	3108	1.26	1.46	–
2013-01-22	3478	1.26	2.21	–
2015-06-03	3820	1.26	2.21	–
2015-10-20	4518	1.26	2.21	0.23
2015-11-22	4643	1.26	2.21	0.37
2016-04-23	4856	1.26	2.21	0.37
2016-08-04	5162	1.26	2.21	1.34
2017-06-05	5746	1.26	2.21	2.28
2017-07-12	5934	1.26	2.21	2.51
2017-09-12	6238	1.26	2.21	3.21
2017-10-27	6336	1.26	2.21	3.81
2017-11-21	6404	1.26	2.21	4.16

Table 6.4: Summary of CCE scans, and integrated delivered luminosity at the time of each CCE scans.

and noise-like tracks are analysed. In particular, two properties are used to develop a first track selection:

- **Ghost probability.** Ghost tracks are collections of unrelated hits and/or track segments. A multivariate classifier is used in LHCb to determine the probability that a track is a ghost [79]. This classifier takes into account kinematical variables as well as hit residuals, *i.e.* the differences between the position of the hit on a given tracking plane and its expected position based on the track extrapolation.

- **Track quality.** The χ^2 per degree of freedom of the track is used as an indicator of the fit quality. Large χ^2/ndf means large residuals, and tracks with $\chi^2/ndf \gtrsim 5$ are generally rejected for physics analyses.

For each location of a 2-dimensional space in these two variables, the ratio between the amount of signal-like tracks ($ADC > 16$) and that of noise-like tracks $ADC < 16$ is shown in Figure 6.10 for four sets of data: tracks extrapolated to the TT and to the IT during the LHC Run I and Run II.

Only data lieing in a region of this space characterized by a high signal to background (S/N) ratio is used for further analysis. The shape of the *ADC* distribution changes as a function of the bias voltage (*cf.* Figure 6.12), therefore the selection was calibrated on data acquired with

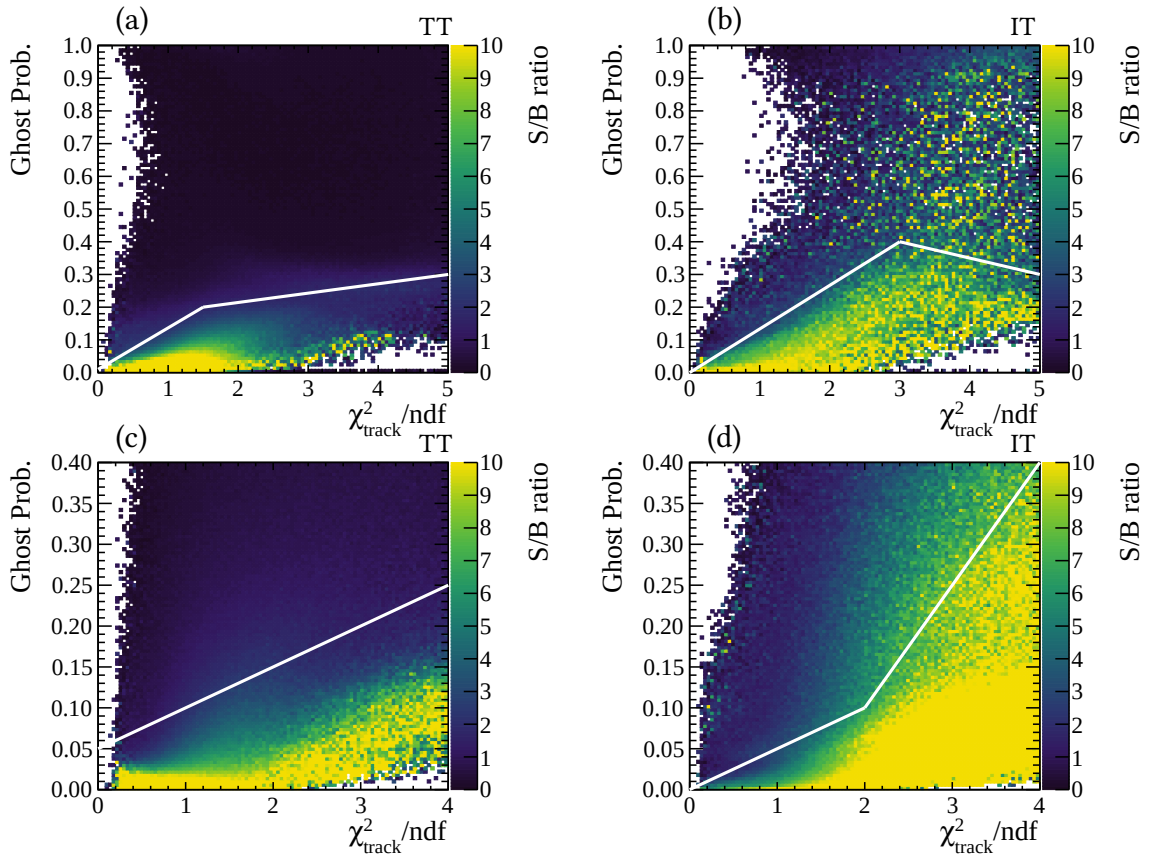

Figure 6.10: Observed signal ($ADC > 16$) to background ($ADC < 16$) ratio as a function of the track reduced χ^2 and ghost probability for $V_{bias} > 300$ V for the TT (left) and for $V_{bias} > 170$ V for the IT (right); the area corresponding to the selected tracks is bounded on top by the white lines. The track selection was optimized separately for Run I **(a, b)** and Run II **(c, d)** data, following a change in the definition of ghost probability in the LHCb track reconstruction software (note the different axis ranges between the two sets of data).

$V_{bias} \geq 300$ V for the TT, and $V_{bias} \geq 170$ V for the IT. The LHCb software undergoes constant updates: a major change between Run I and Run II led to the redefinition of the quantity used to determine the probability for a track to be a ghost track [79]. Furthermore, the ghost probability and reduced χ^2 thresholds used in track reconstruction were lowered from 1.0 and 5 to 0.4 and 4, respectively. Therefore, the track selection for CCE scans was optimized again at the beginning of Run II. The area below the white lines in Figure 6.10 corresponds to the calibrated track selection, which is intentionally kept loose in order to maximise the amount of signal in the used data sample.

The effect of this selection is to reduce the importance of the noise contribution: *cf.* the filtered *ADC* distributions, where this selection was applied, drawn as solid lines in Figure 6.12. Signal and noise will be further discriminated with a fit, described in Section 6.6.2.

Figure 6.11 shows the signal retention and noise rejection efficiencies of the track selection as a function of the distance between the beam pipe and the extrapolated position of the tracks on the scanned TT (IT) layer. Figure 6.12 shows the ADC distributions recorded in

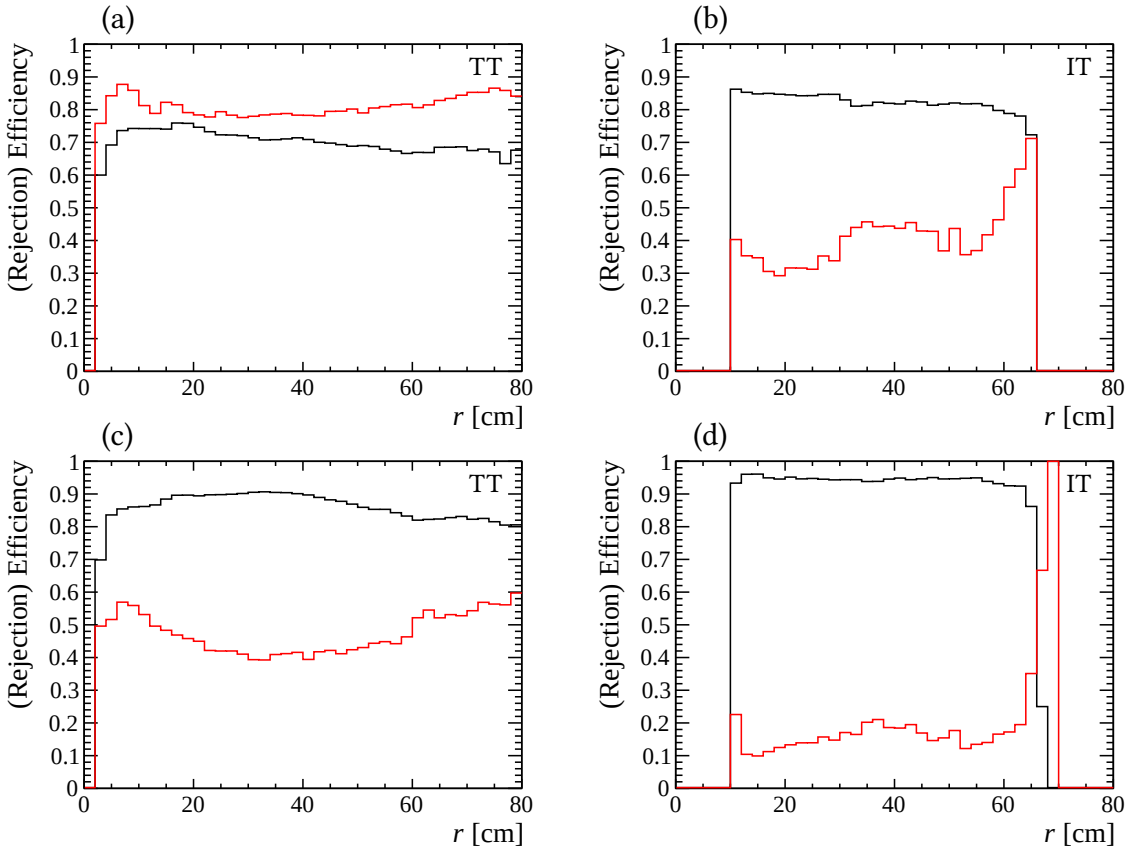

Figure 6.11: Performance of the selection on tracks recorded with $V_{bias} > 300$ V for the TT and with $V_{bias} > 170$ V for the IT. The red line shows the noise ($ADC < 16$) rejection efficiency as a function of the track distance from the beam axis, while the black line shows the signal ($ADC > 16$) retention efficiency. Plots **(a, b)** and **(c, d)** are elaborated on Run I and Run II data, respectively.

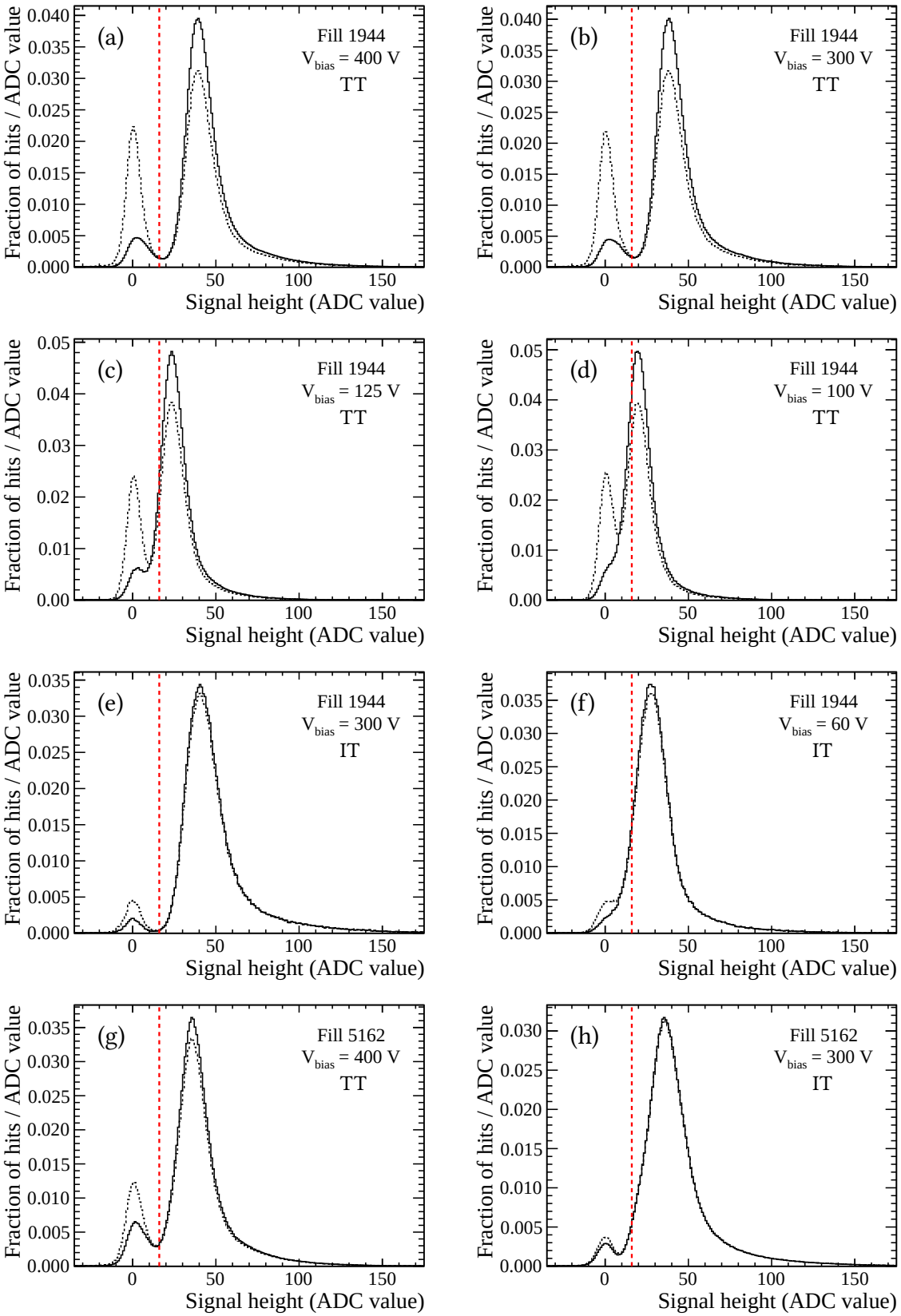

Figure 6.12: Shape of the *ADC* distribution recorded in TT **(a–d)** and IT sectors **(e–f)** in Run I with changing bias voltage; shapes in Run II (**(g)** for the TT and **(h)** for the IT). The red dashed line shows the threshold of 16 ADC used to separate signal from noise. The dotted and solid lines show the *ADC* distribution before and after the track selection described in the text. The collected charge is integrated among all the readout sectors of the considered detector layer.

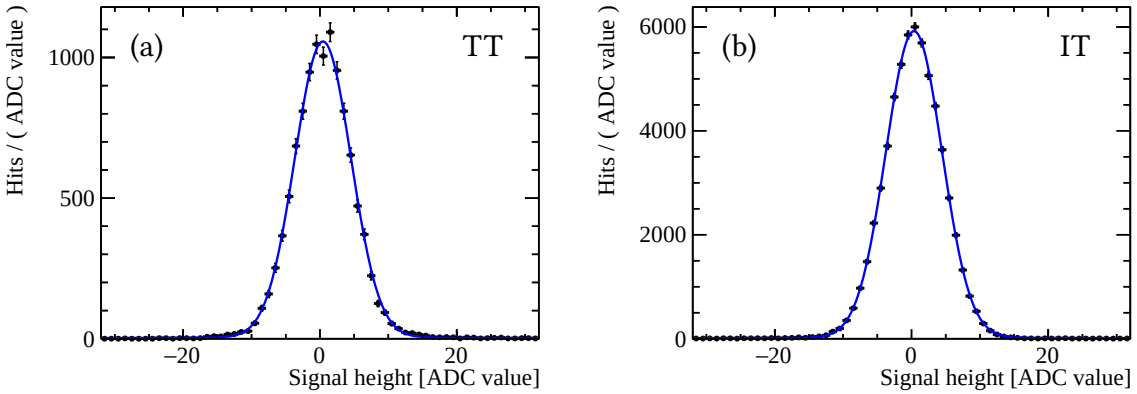

Figure 6.13: *ADC* distribution of noise hits in the TT (a) and IT (b). The blue lines represent the double Gaussian fit model.

the 3 (7) strips adjacent to the extrapolated track position for TT (IT) before and after the track selection is applied, for different bias voltages. The selection seems to perform worse in Run II. However, this is due to the fact that the average data quality is better in Run II, with a larger signal to noise ratio, due to the new software and running conditions. Compare, as an example, the change of noise level before the track selection is applied between Figure 6.12(b) and Figure 6.12(h).

6.6.2. Estimation of the amount of collected charge

A maximum likelihood fit is used to estimate the most probable value (MPV) of the signal height for each voltage and timing step. The noise component is modeled by a double Gaussian distribution G_2, defined as

$$G_2\left(x|f,\mu,\sigma_1,\sigma_2\right) = fG\left(x|\mu,\sigma_1\right) + (1-f)\,G\left(x|\mu,\sigma_2\right), \tag{6.23}$$

where $G\left(x|\mu,\sigma_1\right)$ and $G\left(x|\mu,\sigma_2\right)$ are two single Gaussians sharing the same mean μ and with standard deviations σ_1 and σ_2, respectively. The parameters of G_2 are estimated separately for each readout sector with a fit to the pure noise data sample. Figure 6.13 shows the noise distributions in TT and IT for a CCE scan taken in 2016.

The *ADC* distribution for hits associated to extrapolated tracks is described by the convolution of a Landau distribution L [71] with the noise distribution G_2. The parameters of G_2 are set to those extracted from the fit of the noise shape for the corresponding readout sector. The Landau distribution is described by:

$$L\left(x|m,s\right) = \int_0^\infty e^{-t}\cos\left(\frac{x-m}{s}t + \frac{2t}{\pi}\ln\frac{t}{s}\right)dt, \tag{6.24}$$

where m is the location parameter, corresponding to the most probable *ADC* value (MPV),

and s is a scale parameter representing the spread of the distribution. Photons can convert into an e^+e^- pair in the material of the VELO. The e^+e^- pair is produced with a very small opening angle, being detected as a single track until the magnetic field separates electron and positron by bending them in opposite directions. If an e^+e^- pair crosses the TT, both electrons generate signal in the same TT readout channels, inducing twice as much charge as a single MIPs. To account for this possibility, a second Landau distribution with MPV $2m$ and spread $2s$ is added to the fit model. This effect is negligible in the IT, which is downstream of the magnet.

The final fit model for signal reads:

$$\begin{aligned} f\left(x|f,g,\mu,\sigma_1,\sigma_2,m,s\right) = g\,L\left(x|m,s\right) * G_2\left(x|f,\mu,\sigma_1,\sigma_2\right) \\ + \left(1-g\right)L\left(x|2m,2s\right) * G_2\left(x|f,\mu,\sigma_1,\sigma_2\right), \end{aligned} \tag{6.25}$$

where the $*$ symbol denotes a convolution, and:

- f is fixed to the value found by fitting the noise sample,
- μ, σ_1 and σ_2 are initially set to the values found by fitting the noise sample, but let free to float[6],
- the other parameters m, s and g are free to float; g is fixed to 0 for the IT.

All parameters are determined individually for each readout sector. For the TT readout sectors closest to the LHC beam pipe, dedicated measurements only including tracks traversing the sensors within 75 mm from the beam axis are additionally performed. Figure 6.14 shows the fit of this model to the *ADC* distributions recorded in a TT sector and an IT sector during a CCE scan taken in 2016.

Having determined the signal MPV for each δt, from the MPV *vs.* δt samplings we reconstruct the pulse shape, which we integrate in order to estimate the total amount of charge collected by the detector. For each V_{bias}, we model the pulse shape as a function of δt with an empirical "half Gaussian" function with parameters t_0 and τ and normalization A, motivated by the use of a CR-RC shaper in the Beetle chip [80]:

$$f\left(\delta t|\tau,t_0,A\right) = A \times \exp\left(-\frac{\delta t - t_0}{\tau}\right) \times \left[\frac{1}{2}\left(\frac{\delta t - t_0}{\tau}\right)^2 - \frac{1}{6}\left(\frac{\delta t - t_0}{\tau}\right)^3\right] \tag{6.26}$$

The amount of collected charge is estimated by computing the integral of the fitted pulse shape between its two zeros t_0 and $t_0 + 3\tau$. Figure 6.15 demonstrates this fit for various bias voltage values for data recorded in a CCE scan taken in 2016. The signal amplitude results smaller at low bias voltage, when sensors are only partially depleted.

[6] We found that this makes the fit more stable and results in fitted parameter values compatible, within uncertainty, to those found by fitting the noise sample.

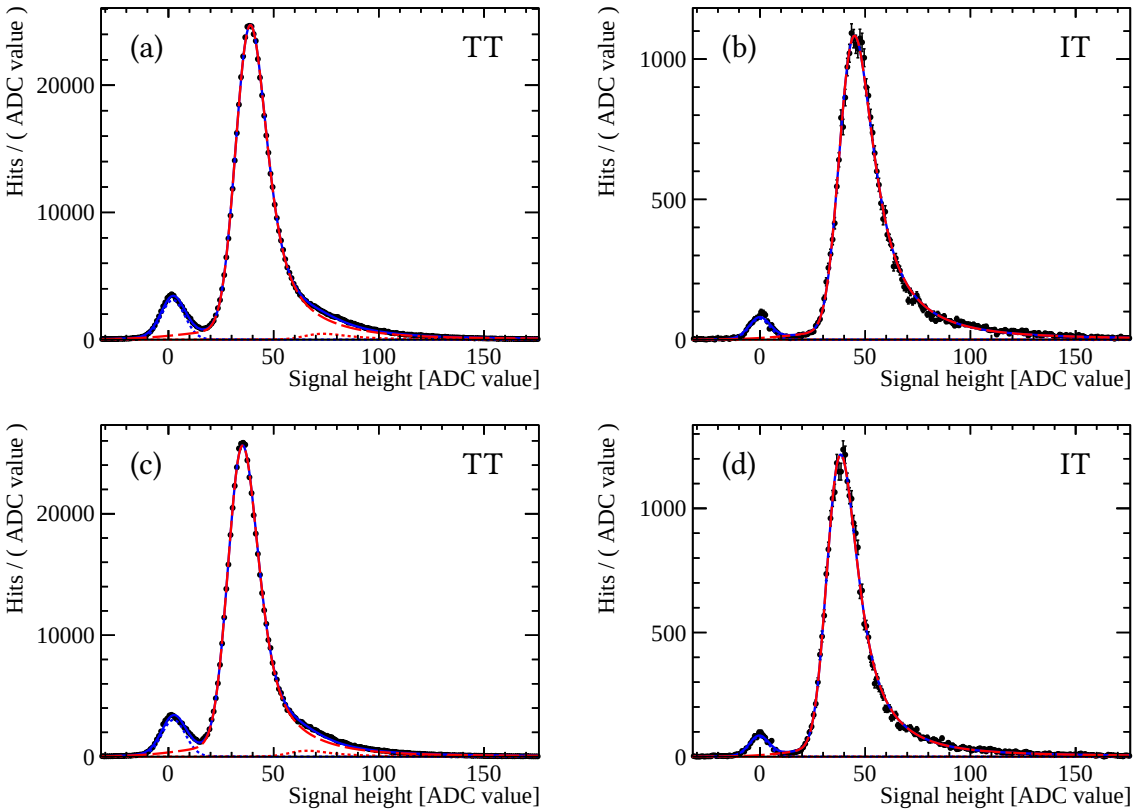

Figure 6.14: *ADC* distribution of hits associated to tracks extrapolated to the TT (a, c) and IT (b, d) for a CCE scan taken in 2016. The applied bias voltages are 350 V (a) and 225 V (c) for the TT, and 200 V (b) and 120 V (d) for the IT. The blue lines correspond to the total fit model. The dashed blue lines represent the double Gaussian modelling the noise distribution. The solid red lines correspond to the signal distributions, fitted with a Landau convoluted with the noise distribution. Finally, the dotted red lines are the noise-convoluted Landau distribution with location and scale parameters equal to twice those of the signal Landau, accounting for the contribution of $\gamma \rightarrow e^+e^-$ in the TT.

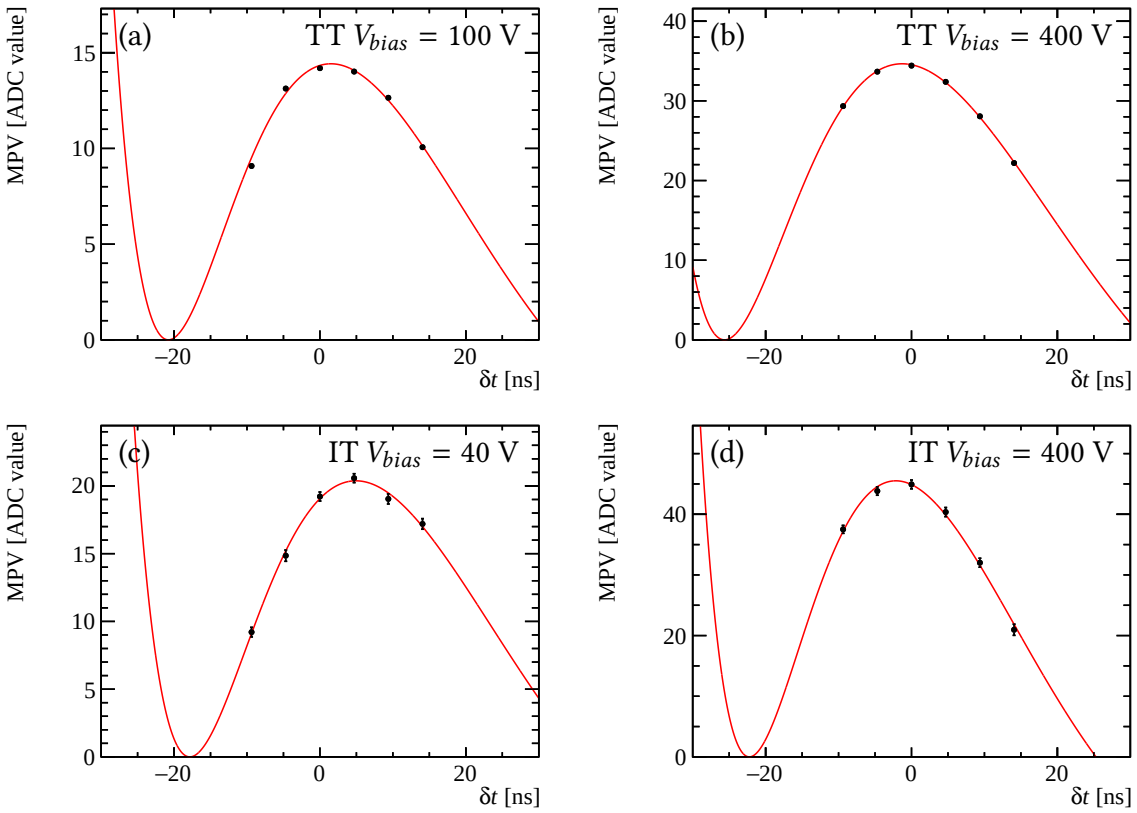

Figure 6.15: Pulse shape for the TT sector 2634 (a–b) and for the IT sector 7299 (c–d) for different bias voltages, for a CCE scan taken in August 2016. The fitted distribution, described in the text, reflects the use of a CR-RC shaper in the Beetle readout chip.

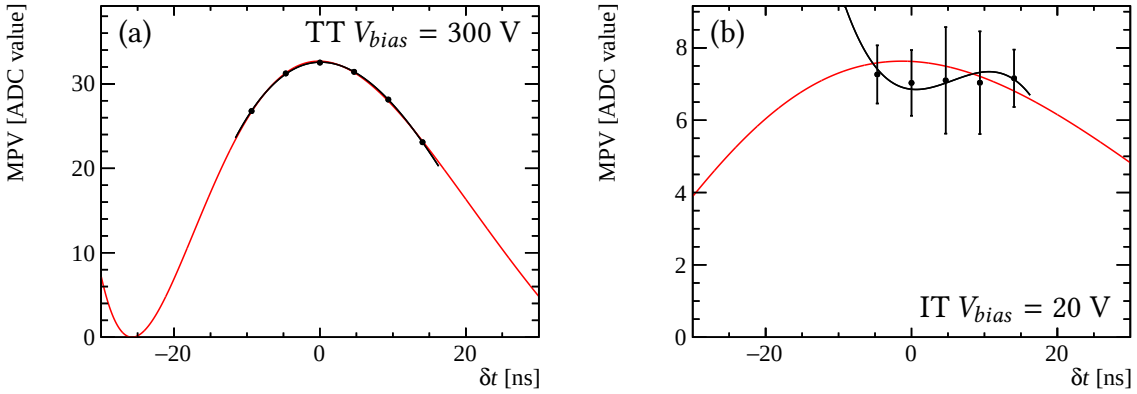

Figure 6.16: Third order polynomial fit to the pulse shape. The fitted polynomial in (a) presents only one flat point, corresponding to the pulse maximum, hence the data set is kept. The polynomial fitting the data in (b) has a minimum, a maximum and a saddle point: these data, taken at a too low bias voltage, are therefore discarded for further analysis.

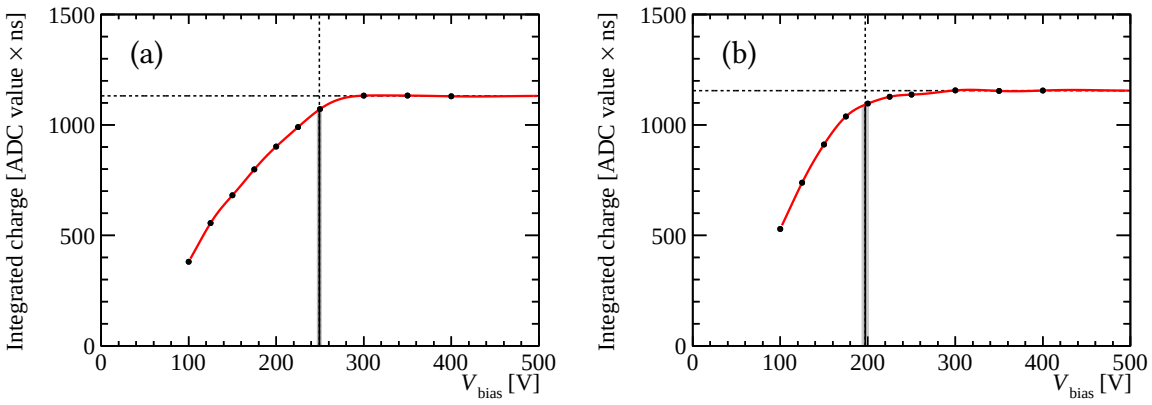

Figure 6.17: Integrated collected charge as a function of the applied bias voltage for a central TT read-out sector measured in CCE scans in April 2012 (a) and September 2017 (b).

At very low bias voltages sometimes it is not possible to reconstruct the pulse shape, because the charge collection efficiency is too low and therefore the *ADC* signal is so small that it overlaps too much with the noise distribution to be well discriminated with the fit model discussed above. Such data are characterized by very low MPVs like those visible in Figure 6.16(b). To prevent these data points from polluting further analysis, we perform a fit to the MPV *vs.* δt samplings with a third order polynomial, whose first and second derivatives are stored. If the polynomial has more than one flat point, or at least one saddle point, the measurements set is discarded for further analysis. Figure 6.16 shows the polynomial fit (black solid line) for an accepted set of measurements and for a discarded one.

6.6.3. Extraction of the depletion voltage

The depletion voltage V_{depl} is determined by analyzing the collected charge *vs.* V_{bias} characteristics, of which examples are shown in Figure 6.17 for the TT and in Figure 6.18 for the IT. V_{depl} is determined in a three-step process:

1. First, data points with $V_{bias} > 280$ V (TT) or 160 V (IT) are averaged to determine the maximum amount of collected charge S_{max}, corresponding to the saturation achieved when the sensor is fully depleted.

2. Then, a fifth-order spline $S(V_{bias})$ with continuous derivative at all nodes is used to interpolate the data points. Each data point is used as a node. This method is rather insensitive, in the $V_{bias} \approx V_{depl}$ region, to fluctuations at low V_{bias}.

3. Finally, we extract the depletion voltage V_{depl} as the bias voltage where a fraction $r \simeq 93\,\%$ of the saturation charge S_{max} is collected.

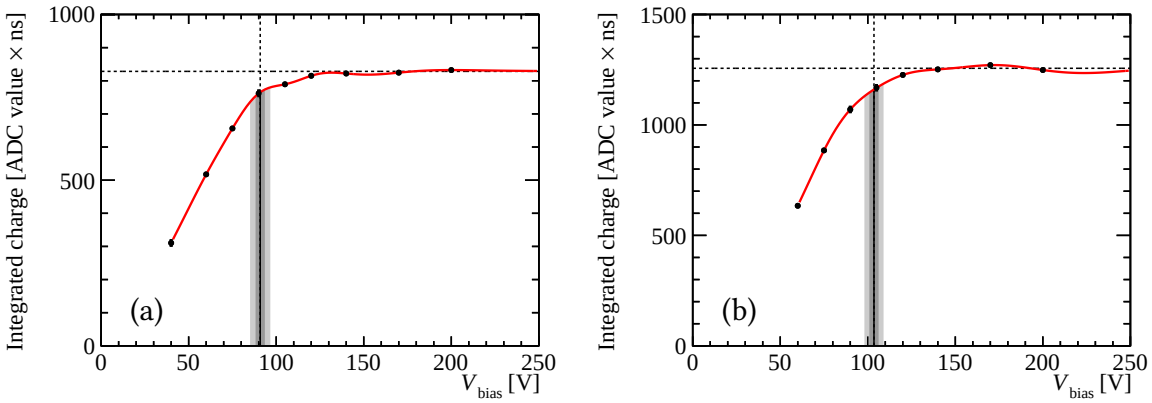

Figure 6.18: Integrated collected charge as a function of the applied bias voltage for a central IT read-out sector measured in CCE scans in October 2011 (a) and September 2017 (b). The larger uncertainty with respect to the TT case is due to the larger uncertainties on the individual r ratios used for the IT sectors. The smaller maximum amount of charge collected in 2011 is due to the narrower sampling time window (*cf.* Table 6.3).

The fraction r differs between IT and TT, and it was calibrated in an early CCE scan, taken in July 2011, from a sector-by-sector comparison between the maximum amount of collected charge and the charge collected at bias voltage V_{cal} corresponding to the initial depletion voltage:

$$S_i\left(V_{cal}\right) = r_i \times S_{i,max}, \tag{6.27}$$

where the index i runs over the various ST sectors analyzed in the CCE scan. In turn, the initial depletion voltage V_{cal} is determined by scaling V^0_{depl}, the depletion voltage measured in the laboratory with CV scans before the sensors were assembled in the detector, according to the amount of radiation damage predicted by the Hamburg model at the time t_{cal} of the calibration CCE scan, obtaining $V_{cal} \equiv V^0_{depl}\left(t_{cal}\right) \lesssim V^0_{depl}$[7]. For the TT, we find that averaging out the value of r among the various readout sectors reduces the impact of statistical fluctuations occurred during the July 2011 CCE scan on the determination of the full depletion voltage in subsequent CCE scans. To this aim, we weight each measurement of r by the square of its uncertainty. The latter is calculated by propagating the statistical uncertainties on the values of $S_i\left(V_{cal}\right)$ and S_{max}. We then perform a weighted average among all sectors in order to determine the value of r that will be used for the analysis of subsequent CCE scans. For the IT, on the other hand, the smaller number of readout sectors, and in general the lower amount of collected data, makes it more convenient to adopt a specific calibration ratio for each sector. Distributions of the r ratios for all of the analyzed TT and IT sectors are shown

[7] Please note that, in the notation used in this Chapter, V^0_{depl} as well as $V^0_{depl}\left(t\right)$ are theoretical values derived from our knowledge of the sensors laboratory-measured initial depletion voltages, and by the predicted amount of radiation damage at time t, while $V_{depl}\left(t\right)$ indicates the depletion voltage measured in a CCE scan at time t.

in Figure 6.19(a–b).

As the depletion voltage is determined by interpolating the available data points, we assign to $S\left(V_{depl}\right)$ a statistical uncertainty $\sigma\left[S\left(V_{depl}\right)\right]$ calculated from the statistical uncertainties of the adjacent data points with a weighted average taking into account the distance between each of the adjacent data points and the measured V_{depl}:

$$\sigma\left[S\left(V_{depl}\right)\right] \equiv \frac{\sigma_i}{|V_{depl} - V_i|} + \frac{\sigma_{i+1}}{|V_{depl} - V_{i+1}|}, \tag{6.28}$$

where V_i is the largest among the tested bias voltage values that is smaller than V_{depl}, σ_i is the statistical uncertainty on the ADC measurement at V_i, and the index $i+1$ denotes the next data point (which is taken, by construction, at a bias voltage $V_{i+1} > V_{depl}$). The uncertainty $\sigma\left[S\left(V_{depl}\right)\right]$ on the ADC value corresponding to V_{depl} is then converted into a statistical uncertainty on V_{depl} by constructing a bias voltage interval $\left(V_{low}, V_{high}\right)$ such that

$$\begin{aligned} &S\left(V_{low}\right) = S\left(V_{depl}\right) - \sigma\left[S\left(V_{depl}\right)\right], \quad \text{and} \\ &S\left(V_{high}\right) = S\left(V_{depl}\right) + \sigma\left[S\left(V_{depl}\right)\right]. \end{aligned} \tag{6.29}$$

We then define $\sigma_{stat}\left(V_{depl}\right) \equiv \left(V_{high} - V_{low}\right)/2$.

The systematic uncertainty on the extracted V_{depl} is dominated by the uncertainty on r, and by the extraction procedure of V_{depl} from the charge equivalent *vs.* bias voltage characteristic. The systematics from r mainly arises, in the TT analysis, from the fact that we average the ratio among all of the readout sectors of the TTaU layer. To estimate the error introduced by the use of the averaged ratio in determining each single sector's depletion voltage, we compare V_{cal} to the depletion voltage value obtained in the calibration CCE scan using the averaged r. The relative difference between V_{cal} and $V_{depl}\left(t_{cal}\right)$ is histogrammed in Figure 6.19(c); the spread of this distribution is taken as relative systematic uncertainty on each measurement of V_{depl}. In the case of the IT, the uncertainty on each sector's r ratio has a statistical nature, and arises from the amount of data available in the calibration CCE scan. This uncertainty is then propagated to the analysis of all subsequent scans.

The depletion voltage can be extracted from the charge equivalent *vs.* bias voltage characteristic using different procedures. In particular, the use of a fifth-order spline with the constraint that the derivative is continuous at all nodes is motivated by the fact that its parameters at each node are sensitive to the position of the neighbouring nodes through the constraint on the spline derivatives. However, this choice is arbitrary, and similar results can be obtained by interpolating with lower order splines, or by fitting with a functional form. We therefore assign the difference between the result obtained with a fifth-order spline and that obtained by linear interpolation (Figure 6.20) as a systematic uncertainty, arising from our arbitrary the choice of the model. This systematic uncertainty is summed in quadrature with that arising from the r ratio.

As an additional control method, we extract the depletion voltage as the abscissa of a

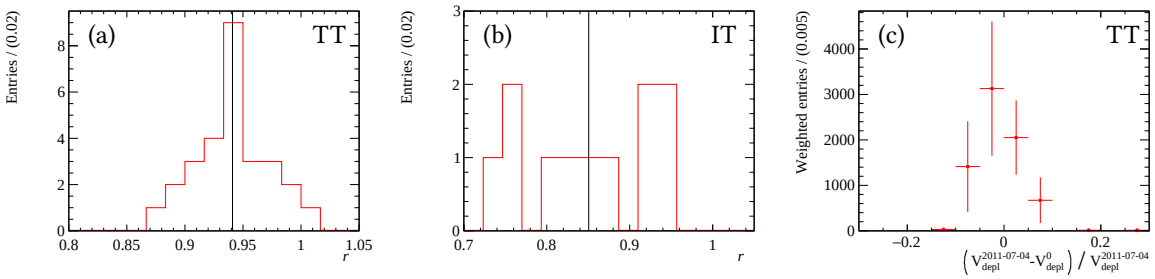

Figure 6.19: Ratio r between the collected charge at $V_{depl} = V_{cal}$ and the maximum amount of collected charge, calculated for TT (a) and IT (b) readout sectors during the July 2011 CCE scan. The r values for TT sectors are weighted by the inverse of the square of the associated uncertainties, in order to extract their weighted average. Relative difference between V_{cal} and V_{depl} (t_{cal}) obtained in the July 2011 CCE scan by using the fraction r averaged among all the readout sectors of the studied TT layer (c).

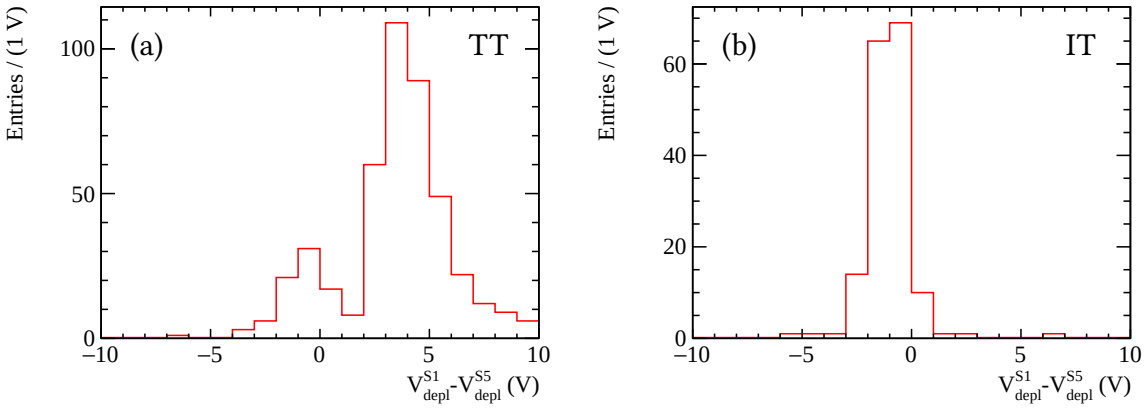

Figure 6.20: Histogram of the differences between the values of V_{depl} obtained by interpolation with a fifth-order spline and by linear interpolation for the TT (a) and the IT (b), calculated for all CCE scans.

straight line ℓ, used to fit the rising edge of the characteristics, corresponding to S_{max}:

$$V'_{depl} \equiv V \quad \text{such that} \quad \ell\,(V) = S_{max}. \tag{6.30}$$

The results found with this method are similar to those obtained with the spline. However, a level of arbitrarity is introduced with the selection of the data points lying on the rising edge of the curve. Further details on this cross-check can be found in Appendix B.3.

6.7. Comparison with the Hamburg model predictions

Figures 6.23 to 6.24 gather the evolution of the depletion voltage for selected TT sectors and for all the sectors of the TT ad IT. V_{depl} is plotted against the integrated average fluence withstood by those sectors at the time of the CCE scan. The fluence is estimated based on

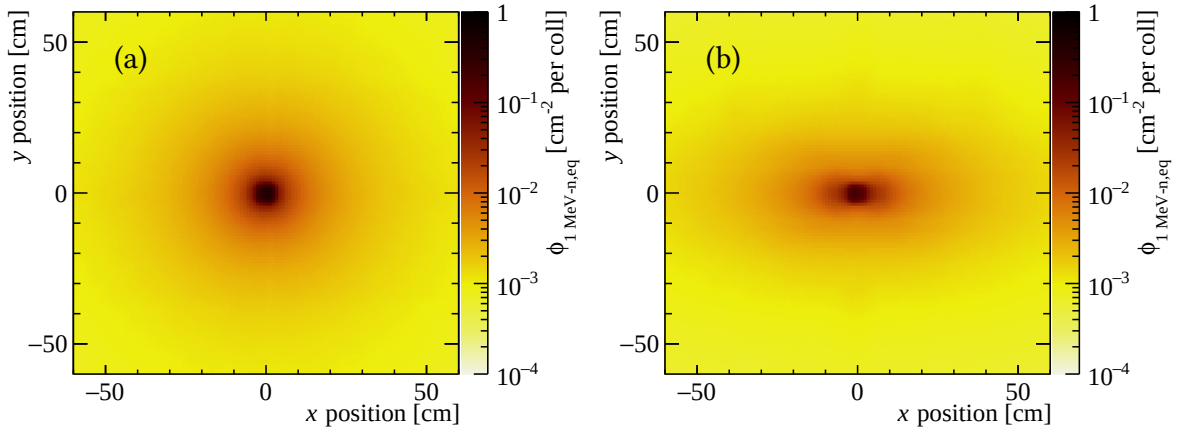

Figure 6.21: Expected 1-MeV neutron equivalent fluence per proton-proton collision at the z position of the TT centre (a) and of the IT centre (b). These results were obtained from a FLUKA simulation of the LHCb detector, assuming a proton-proton collision energy of 13 TeV [62]. The difference between the TT and IT radiation maps can be appreciated: charged particles are swept towards larger $|x|$ positions after crossing the TT.

the LHC delivered luminosity (*cf.* Figure 6.5) at the time of each CCE scan and on simulated detector irradiation maps. In particular, a FLUKA [81, 82] simulation is used to determine the 1 MeV-n, eq fluence as a function of the x, y position in the two detectors. Different fluence maps are used for data collected at $\sqrt{s} = 7, 8, 13$ TeV. Figure 6.21 shows the TT and IT fluence maps for $\sqrt{s} = 8$ TeV as an example. For $\sqrt{s} = 7, 8$ TeV the simulated radiation maps have a scoring of 1×1 cm^2 in the transversal (x, y) plane for the TT and of 5×5 cm^2 for the IT, for statistical reasons. For $\sqrt{s} = 13$ TeV both maps have a scoring of 2.5×2.5 cm^2 and are linearly interpolated in order to obtain a 1×1 cm^2 scoring. The statistical uncertainty of the FLUKA simulation is modeled with a power law as a function of the radial distance from the beam pipe:

$$\frac{\sigma\left(\Phi_{1\ \mathrm{MeV\text{-}}n,\mathrm{eq}}\right)}{\Phi_{1\ \mathrm{MeV\text{-}}n,\mathrm{eq}}} \equiv a_0 \left(\frac{r}{r_0}\right)^{\alpha}, \tag{6.31}$$

with $a_0 = 0.7 \times 10^{-2}\,\mathrm{cm}^{-2}$, $r_0 = 1$ cm and $\alpha = 0.918$ [13]. Figure 6.22 compares the one-dimensional profiles of the expected TT and IT fluence. A difference between the TT and IT irradiation is visible: after crossing the TT detectors, charged particles are swept towards larger $|x|$ positions. Therefore, in the IT irradiation results broader along $\hat{x}$, and generally lower than what experienced by the TT.

Predictions from the Hamburg model based on the stable damage term are also shown in black in Figures 6.23 to 6.24. The gray bands represent the statistical error on the Hamburg prediction due to the uncertainties on the simulated fluence and on the model parameters listed in Table 6.1 in Section 6.2.1. In Figure 6.24, the Hamburg prediction is calculated from an initial depletion voltage $\bar{V}^0_{depl}$ averaged among all sectors. The black dashed lines correspond

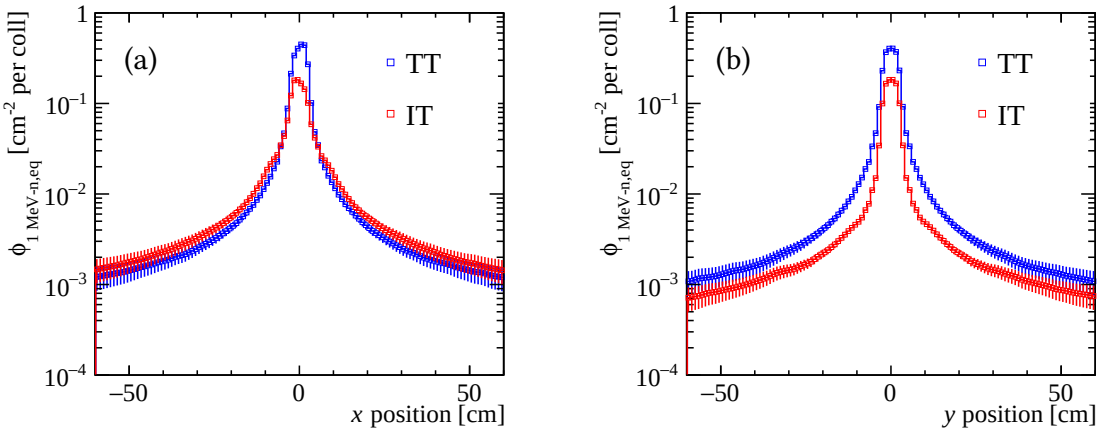

Figure 6.22: Expected 1-MeV neutron equivalent fluence per proton-proton collision at $\sqrt{s}$ = 13 TeV: $\hat{x}$-profiles (a) and $\hat{y}$-profiles (b) for the TT and IT.

to the standard deviation of the distribution of the initial depletion voltages.

The predicted V_{depl} evolution is also calculated using the full Hamburg model (Eqn. 6.20) for selected readout sectors, using the actual running conditions including the detector temperature, measured to a precision of 2 °C by means of dedicated temperature sensors placed in the centres of the detector boxes. Figures 6.25 and 6.26 show the experimental data obtained in CCE scans superimposed to the Hamburg model predition as a function of time, respectively for two TT sectors – whose location is sketched in Figure 6.27(a) – and two IT sectors. Here the gray bands also include the uncertainty on the measured temperature. The dashed lines account for the uncertainty on the initial depletion voltage V^0_{depl} measured in CV scans before the detector installation.

Good agreement is observed between the TT expected ageing at the experimental data. No ageing is observed in the IT, due to the smaller fluence withstood by this subdetector.

Finally, Figure 6.27(b) shows the absolute change in V_{depl} for the innermost region of TT, as measured in July 2017. The dedicated measurements performed using only tracks crossing the detector at distance $r \leq 75$ mm from the beam pipe make it possible to appreciate the occupancy- and thus the fluence-dependence of the amount of radiation damage, displaying a more important drop in V_{depl} with respect to the surrounding region.

6.8. Conclusions

Two methods were used to monitor radiation damage in the LHCb Silicon Tracker. The first method measures the detector leakage current as the current flowing in the HV channels at the end of each LHC fill. An increase in leakage current is induced by radiation damage. The observed evolution of the leakage current closely follows expectation based on phenomelogical models.

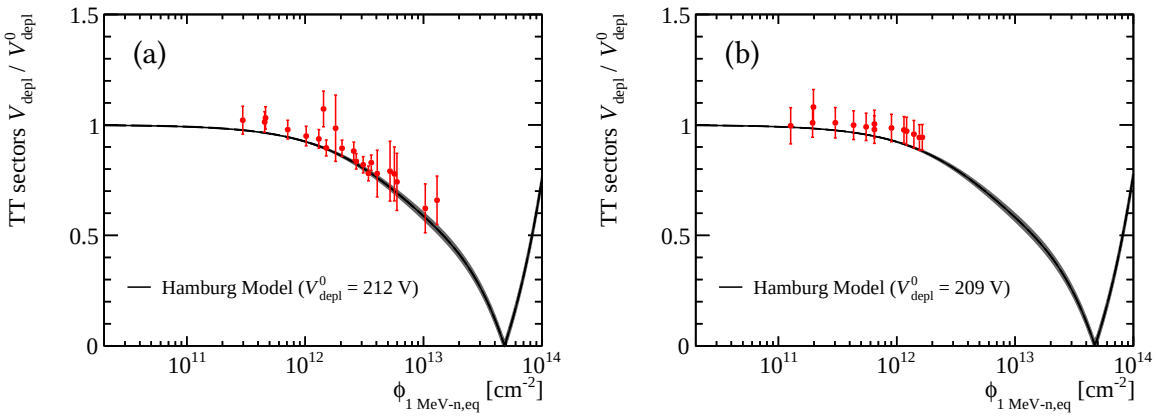

Figure 6.23: Measured evolution of V_{depl} as a function of the 1-MeV neutron equivalent fluence obtained from the running conditions and the FLUKA simulation for TT sectors 2639 (a) and 2638 (b), shown in Figure 6.27(a). The error bars of the data points display the sum of the statistical and systematic uncertainty. The solid black curve shows the predictions based on the stable damage part of the Hamburg model, the grey shaded region its uncertainty due to the parameter uncertainty of the model [62].

The second method monitors the change in charge collection efficiency. Dedicated CCE scans are performed several times a year following LHCb technical stops. A modified tracking procedure allows to search for charge deposit close to tracks crossing detector layers whose bias voltage is scanned in order to extract the current full depletion voltage of the detector layer. The results obtained match the expectations in this case as well, within the experimental uncertainties and the uncertainties on the phenomelogical model. From the CCE scan data we can estimate that TT sensors will be able to withstand five times more radiation before type inversion occurs. IT sectors show little or no radiation damage at all.

The analysis of CCE scan data could further be improved in two ways.

1. The initial depletion voltage values V^0_{depl} were measured in CV scans for each silicon sensor before the sensors were wire-bonded together to form ulti-sensor readout sectors. Attention was paid to grouping together sensors with similar initial V^0_{depl}. However, it is impossible to distinguish the characteristics of the individual sensors after wire bonding, and different sensors could evolve slightly differently with irradiation. A refined analysis could try to select tracks crossing each individual sensor based on the extrapolated track position.

2. The extraction of the depletion voltage as discussed in Section 6.6.3 is quite sensitive to the calibration parameter r, obtained from the analysis of a single CCE scan. On the other hand, there is no specific functional form to describe the collected charge *vs.* bias voltage characteristic. The straight line fit method described in Appendix B.3 removes the need for a calibration ratio, but suffers from arbitrarity in the fit procedure. A different algorithm could be implemented in order to separate the data points to be

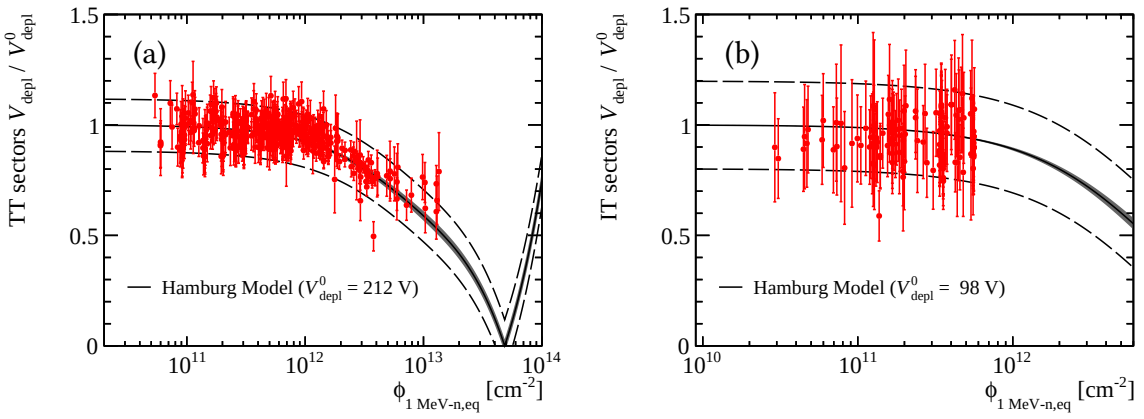

Figure 6.24: Measured evolution of V_{depl} as a function of the 1-MeV neutron equivalent fluence obtained from the running conditions and the FLUKA simulation for all of the read-out sectors of the TT (a) and of the IT (b). The innermost sectors are subdivided in concentrical annular rings with increasing distance from the beam axis. The error bars of the data points display the sum of the statistical and systematic uncertainty. The solid black curve shows the predictions based on the stable damage part of the Hamburg model, the grey shaded region its uncertainty due to the parameter uncertainty of the model. The initial depletion voltage V^0_{depl} for the Hamburg model prediction is averaged among all sectors, and the dashed black lines in show the standard deviation of the distribution of the initial V^0_{depl} values [62].

fitted with a straight line and those belonging to the full-depletion plateau, *e.g.* outlier removal. One could also fit the whole data set floating V_{depl} as a fit parameter. This could allow to reduce the impact of statistical and systematic deviation occurred during the calibration CCE scan on further analysis.

Finally, the IT CCE scans suffer from low statistics. Due to the incompatibility between physics data taking and the voltage and timing stepping procedure operated during the CCE scan, data collected in CCE scan mode cannot be used for physics analysis. Gathering a larger sample for the IT would need longer CCE scans, preventing the LHCb experiment from collecting physics data in the mean time. As no significant ageing is expected in the IT, and expectations are comfirmed by the small amount of data available, we consider it safe and more convenient not to increase the duration of the CCE scans.

The LHCb Silicon Tracker was designed with the aim of collecting data during the LHC Run I and Run II. From the results of this study we conclude that both subdetectors will easily withstand the remainder of LHC Run II. Before the start of LHC Run II, the TT will be replaced by another silicon microstrip detector, the Upstream Tracker, while a Scintillating-Fibre tracker will take the place of the IT and OT [75].

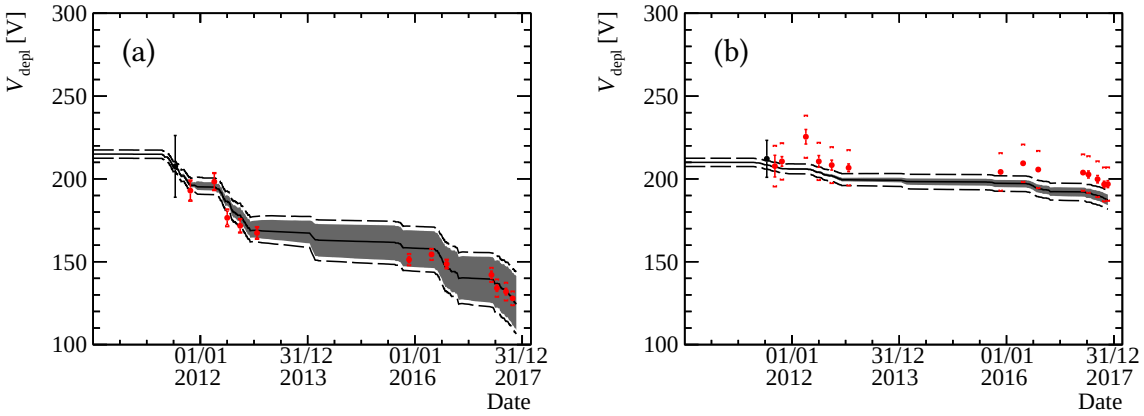

Figure 6.25: Measured effective depletion voltage (red points) in the area of two TT readout sectors: one, 2639, just next to the beam pipe, limited to tracks crossing TTaU at a distance of maximum 75 mm from the beam pipe (a), and one, 2638, slightly further away (b), whose position is indicated in Figure 6.27(a). The black dot corresponds to the CCE scan used to calibrate the ratio r. The predicted evolution of the depletion voltage based on the running conditions and the measured depletion voltage after sensor production is also shown (black curve). The grey bands show the uncertainty on the predicted evolution of V_{depl}, while the black dashed lines account for the ±2.5 V uncertainty on the initial measurement of the depletion voltage V^0_{depl} in CV scans [62].

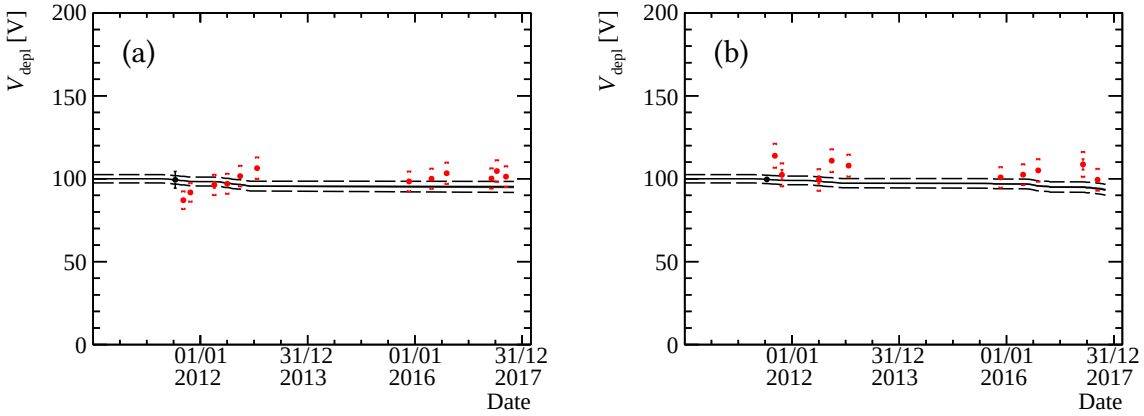

Figure 6.26: Evolution of V_{depl} as a function of time for the IT sectors 7299 (a) and 7300 (b).

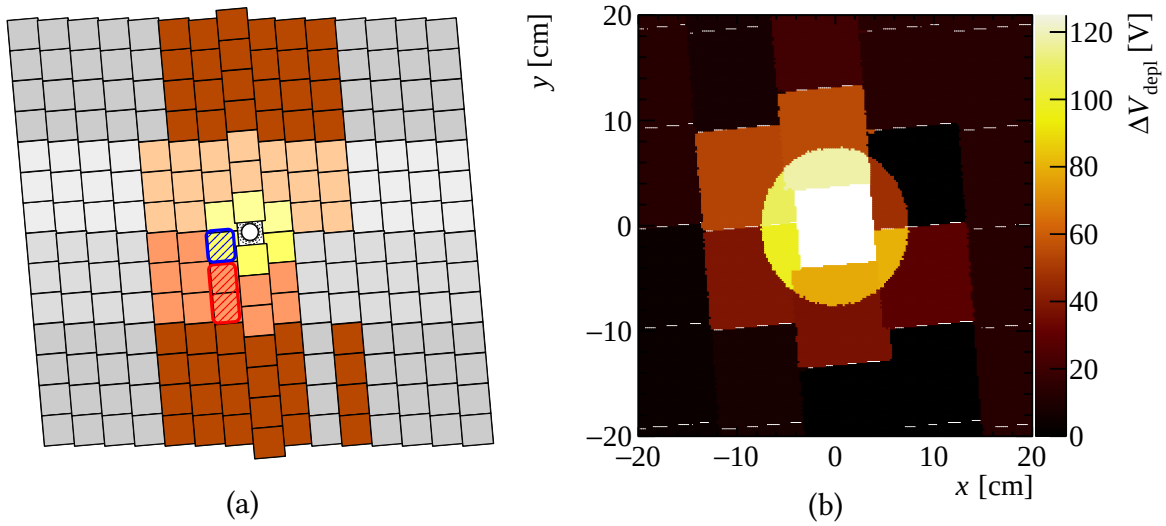

Figure 6.27: Sketch highlighting the TT sectors used during the various CCE scans (a). The greyed out sectors were excluded due to poor statistics. The two marked sectors close to the beam pipe on the left side are those whose V_{depl} evolution is shown as a function of time in Figure 6.25 and as a function of fluence in Figure 6.25: sector 2639 in blue and 2638 in red. The right panel (b) shows the absolute change in V_{depl} in the innermost region of TT in July 2017 [62].

References for the LHCb and the ST radiation damage studies

[1] *Convention pour l'établissement d'une Organisation européenne pour la Recherche nucléaire*. Paris, July 1953.

[2] cern. *CERN Accelerating science*. 2018. URL: https://home.cern/ (visited on 01/02/2018).

[3] Brüning, Oliver Sim and Collier, Paul and Lebrun, P and Myers, Stephen and Ostojic, Ranko and Poole, John and Proudlock, Paul. *LHC Design Report*. Tech. rep. Geneva, 2004. URL: https://cds.cern.ch/record/782076.

[4] Lyndon Evans and Philip Bryant. "LHC Machine". In: *JINST* 3 (2008), S08001. DOI: 10.1088/1748-0221/3/08/S08001.

[5] J R J Bennett et al. *Design concept for a 100 GeV e+e- storage ring (LEP)*. Tech. rep. Geneva, 1977. URL: https://cds.cern.ch/record/118208.

[6] G. Aad et al. "The ATLAS Experiment at the CERN Large Hadron Collider". In: *JINST* 3 (2008), S08003. DOI: 10.1088/1748-0221/3/08/S08003.

[7] O Adriani et al. "The LHCf detector at the CERN Large Hadron Collider". In: *JINST* 3 (2008), S08006. URL: https://cds.cern.ch/record/1129808.

[8] S. Chatrchyan et al. "The CMS experiment at the CERN LHC". In: *JINST* 3 (2008), S08004. DOI: 10.1088/1748-0221/3/08/S08004.

[9] G Anelli et al. "The TOTEM Experiment at the CERN Large Hadron Collider". In: *JINST* 3 (2008), S08007. URL: https://cds.cern.ch/record/1129807.

[10] A. Augusto Alves Jr. et al. "The LHCb Detector at the LHC". In: *JINST* 3 (2008), S08005. DOI: 10.1088/1748-0221/3/08/S08005.

[11] B. Acharya et al. "The Physics Programme Of The MoEDAL Experiment At The LHC". In: *Int. J. Mod. Phys. A* 29.arXiv:1405.7662. KCL-PH-TH-2014-02. LCTS-2014-02. CERN-PH-TH-2014-021. IFIC-14-16. IMPERIAL-TP-2014-AR-1 (May 2014), 1430050. mult. p. URL: https://cds.cern.ch/record/1705285.

[12] K. Aamodt et al. "The ALICE experiment at the CERN LHC". In: *JINST* 3 (2008), S08002. DOI: 10.1088/1748-0221/3/08/S08002.

[13] Christian Elsasser et al. "The Rare Decays $B^0_{(s)} \to \mu^+\mu^-$ and Z Boson Production at LHCb and Radiation Damage in its Silicon Tracker". Presented 02 Oct 2014. PhD thesis. Zurich U., Feb. 2015. URL: https://cds.cern.ch/record/2002199.

[14] Andras Laszlo. "The NA61/SHINE Experiment at the CERN SPS". In: *Nucl. Phys.* A830 (2009), pp. 559C–562C. DOI: 10.1016/j.nuclphysa.2009.09.047. arXiv: 0907.4493 [nucl-ex].

[15] Edoardo Cortina Gil et al. "The Beam and detector of the NA62 experiment at CERN". In: *JINST* 12.05 (2017), P05025. DOI: 10.1088/1748-0221/12/05/P05025. arXiv: 1703.08501 [physics.ins-det].

[16] P. Abbon et al. "The COMPASS experiment at CERN". In: *Nucl. Instrum. Meth.* A577 (2007), pp. 455–518. DOI: 10.1016/j.nima.2007.03.026. arXiv: hep-ex/0703049 [hep-ex].

[17] RE Mikkelsen, UI Uggerhoj, and TN Wistisen. *Technical Design Report, CERN NA63*. Tech. rep. CERN-SPSC-2014-033. SPSC-SR-146. Geneva: CERN, Oct. 2014. URL: https://cds.cern.ch/record/1955391.

[18] Roel Aaij et al. "LHCb Detector Performance". In: *Int. J. Mod. Phys.* A30.07 (2015), p. 1530022. DOI: 10.1142/S0217751X15300227. arXiv: 1412.6352 [hep-ex].

[19] A. A. Alves Jr. et al. "The LHCb detector at the LHC". In: *JINST* 3 (2008), S08005. DOI: 10.1088/1748-0221/3/08/S08005.

[20] Roel Aaij et al. "Measurement of the track reconstruction efficiency at LHCb". In: *JINST* 10.02 (2015), P02007. DOI: 10.1088/1748-0221/10/02/P02007. arXiv: 1408.1251 [hep-ex].

[21] R. Frühwirth. "Application of Kalman filtering to track and vertex fitting". In: *Nuclear Instruments and Methods in Physics Research Section A: Accelerators, Spectrometers, Detectors and Associated Equipment* 262.2 (1987), pp. 444–450. ISSN: 0168-9002. DOI: https://doi.org/10.1016/0168-9002(87)90887-4. URL: http://www.sciencedirect.com/science/article/pii/0168900287908874.

[22] LHCb collaboration. *LHCb website*. 2017. URL: http://lhcb.web.cern.ch/lhcb/ (visited on 01/02/2018).

[23] *LHCb VELO TDR: Vertex locator. Technical design report*. Tech. rep. 2001.

[24] *LHCb reoptimized detector design and performance: Technical Design Report*. Tech. rep. Geneva, 2003. URL: https://cds.cern.ch/record/630827.

[25] *LHCb inner tracker: Technical Design Report*. Tech. rep. revised version number 1 submitted on 2002-11-13 14:14:34. Geneva, 2002. URL: http://cds.cern.ch/record/582793.

[26] Olaf Steinkamp. *LHCb Silicon Tracker Homepage*. 2013. URL: http://lhcb.physik.uzh.ch/ST/ (visited on 01/03/2018).

[27] Jonathan Robert Harrison. "Radiation damage studies in the LHCb VELO detector and searches for lepton flavour and baryon number violating tau decays". PhD thesis. Manchester U., 2014. URL: http://inspirehep.net/record/1339905/files/CERN-THESIS-2014-068.pdf.

[28] "LHCb: Outer tracker technical design report". In: (2001).

[29] M. Adinolfi et al. "Performance of the LHCb RICH detector at the LHC". In: *Eur. Phys. J.* C73 (2013), p. 2431. DOI: 10.1140/epjc/s10052-013-2431-9. arXiv: 1211.6759 [physics.ins-det].

[30] *LHCb: RICH technical design report*. Tech. rep. 2000.

[31] *LHCb calorimeters: Technical design report*. Tech. rep. 2000.

[32] Pascal Perret and Xavier Vilasís-Cardona. "Performance of the LHCb calorimeters during the period 2010-2012". In: *J. Phys. Conf. Ser.* 587.1 (2015), p. 012012. DOI: 10.1088/1742-6596/587/1/012012.

[33] *LHCb muon system technical design report*. Tech. rep. 2001.

[34] M Clemencic et al. "The LHCb simulation application, Gauss: Design, evolution and experience". In: *J. Phys. Conf. Ser.* 331 (2011), p. 032023. DOI: 10.1088/1742-6596/331/3/032023.

[35] D. J. Lange. "The EvtGen particle decay simulation package". In: *Nucl. Instrum. Meth.* A462 (2001), pp. 152–155. DOI: 10.1016/S0168-9002(01)00089-4.

[36] Sjöstrand, Torbjörn and Mrenna, Stephen and Skands, Peter Z. "PYTHIA 6.4 physics and manual". In: *Journal of High Energy Physics* 2006.05 (2006), p. 026. URL: http://stacks.iop.org/1126-6708/2006/i=05/a=026.

[37] Sjöstrand, Torbjörn and Mrenna, Stephen and Skands, Peter Z. "A Brief Introduction to PYTHIA 8.1". In: *Comput. Phys. Commun.* 178 (2008), pp. 852–867. DOI: 10.1016/j.cpc.2008.01.036. arXiv: 0710.3820 [hep-ph].

[38] I. Belyaev et al. "Handling of the generation of primary events in Gauss, the LHCb simulation framework". In: *J. Phys. Conf. Ser.* 331 (2011), p. 032047. DOI: 10.1088/1742-6596/331/3/032047.

[39] S. Agostinelli et al. "GEANT4: A Simulation toolkit". In: *Nucl. Instrum. Meth.* A506 (2003), pp. 250–303. DOI: 10.1016/S0168-9002(03)01368-8.

[40] John Allison et al. "Geant4 developments and applications". In: *IEEE Trans.Nucl.Sci.* 53 (2006), p. 270. DOI: 10.1109/TNS.2006.869826.

[41] Albert Puig. *The LHCb trigger in 2011 and 2012*. Tech. rep. LHCb-PUB-2014-046. CERN-LHCb-PUB-2014-046. Geneva: CERN, Nov. 2014. URL: https://cds.cern.ch/record/1970930.

[42] Barbara Sciascia. "LHCb Run 2 trigger performance". In: *PoS* BEAUTY2016 (2016), p. 029.

[43] M. Agari et al. "Beetle: A radiation hard readout chip for the LHCb experiment". In: *Nucl. Instrum. Meth.* A518 (2004), pp. 468–469. DOI: 10.1016/j.nima.2003.11.058.

[44] N van Bakel et al. "Characterisation of a radiation hard front-end chip for the vertex detector of the LHCb experiment at CERN". In: *Nuclear Instruments and Methods in Physics Research Section A: Accelerators, Spectrometers, Detectors and Associated Equipment* 509.1 (2003). Proceedings of the 4th Internatonal Workshop on Radiation Imaging Detectors, pp. 176–182. ISSN: 0168-9002. DOI: https://doi.org/10.1016/S0168-9002(03)01568-7. URL: http://www.sciencedirect.com/science/article/pii/S0168900203015687.

[45] Löchner, S and Schmelling, M. *The Beetle Reference Manual - chip version 1.3, 1.4 and 1.5*. Tech. rep. LHCb-2005-105. CERN-LHCb-2005-105. Geneva: CERN, Nov. 2006. URL: http://cds.cern.ch/record/1000429.

[46] M Schmelling. *Specifications of the Front End Chip for the LHCb Vertex Detector*. Tech. rep. LHCb-2001-048. revised version number 1 submitted on 2001-05-21 14:35:51. Geneva: CERN, Apr. 2001. URL: http://cds.cern.ch/record/691610.

[47] Max-Planck Institute for Nuclear Physics Heidelberg. *Beetle - a readout chip for LHCb*. 2007. URL: http://www.kip.uni-heidelberg.de/lhcb/ (visited on 12/30/2017).

[48] G. Haefeli et al. "The LHCb DAQ interface board TELL1". In: *Nucl. Instrum. Meth.* A560 (2006), pp. 494–502. DOI: 10.1016/j.nima.2005.12.212.

[49] G. Hanson et al. "Evidence for Jet Structure in Hadron Production by e^+e^- Annihilation". In: *Phys. Rev. Lett.* 35 (24 Dec. 1975), pp. 1609–1612. DOI: 10.1103/PhysRevLett.35.1609. URL: https://link.aps.org/doi/10.1103/PhysRevLett.35.1609.

[50] Christoph Berger et al. "Jet Analysis of the Υ (9.46) Decay Into Charged Hadrons". In: *Phys. Lett.* 82B (1979), pp. 449–455. DOI: 10.1016/0370-2693(79)90265-X.

[51] R. Brandelik et al. "Evidence for Planar Events in e+ e- Annihilation at High-Energies". In: *Phys. Lett.* 86B (1979), pp. 243–249. DOI: 10.1016/0370-2693(79)90830-X.

[52] Ahmed Ali and Gustav Kramer. "Jets and QCD: A Historical Review of the Discovery of the Quark and Gluon Jets and its Impact on QCD". In: *Eur. Phys. J.* H36 (2011), pp. 245–326. DOI: 10.1140/epjh/e2011-10047-1. arXiv: 1012.2288 [hep-ph].

[53] G. Arnison et al. "Experimental observation of isolated large transverse energy electrons with associated missing energy at s=540 GeV". In: *Physics Letters B* 122.1 (1983), pp. 103–116. ISSN: 0370-2693. DOI: https://doi.org/10.1016/0370-2693(83)91177-2. URL: http://www.sciencedirect.com/science/article/pii/0370269383911772.

[54] M. Banner et al. "Observation of single isolated electrons of high transverse momentum in events with missing transverse energy at the CERN pp collider". In: *Physics Letters B* 122.5 (1983), pp. 476–485. ISSN: 0370-2693. DOI: https://doi.org/10.1016/0370-2693(83)91605-2. URL: http://www.sciencedirect.com/science/article/pii/0370269383916052.

[55] G. Arnison et al. “Experimental Observation of Isolated Large Transverse Energy Electrons with Associated Missing Energy at s**(1/2) = 540-GeV”. In: *Phys. Lett.* 122B (1983). [,611(1983)], pp. 103–116. DOI: 10.1016/0370-2693(83)91177-2.

[56] G. Arnison et al. “Experimental Observation of Lepton Pairs of Invariant Mass Around 95-GeV/c**2 at the CERN SPS Collider”. In: *Phys. Lett.* 126B (1983), pp. 398–410. DOI: 10.1016/0370-2693(83)90188-0.

[57] M. Banner et al. “Observation of Single Isolated Electrons of High Transverse Momentum in Events with Missing Transverse Energy at the CERN anti-p p Collider”. In: *Phys. Lett.* 122B (1983), pp. 476–485. DOI: 10.1016/0370-2693(83)91605-2.

[58] P. Bagnaia et al. “Evidence for Z0 —> e+ e- at the CERN anti-p p Collider”. In: *Phys. Lett.* 129B (1983), pp. 130–140. DOI: 10.1016/0370-2693(83)90744-X.

[59] Alan Astbury et al. *A 4π solid angle detector for the SPS used as a proton-antiproton collider at a centre of mass energy of 540 GeV*. Tech. rep. CERN-SPSC-78-6. CERN-SPSC-78-06. SPSC-P-92. Geneva: CERN, Jan. 1978. URL: http://cds.cern.ch/record/319371.

[60] M Banner et al. *Proposal to study antiproton-proton interactions at 540 GeV cm energy*. Tech. rep. CERN-SPSC-78-8. SPSC-P-93. Geneva: CERN, 1978. URL: http://cds.cern.ch/record/596804.

[61] P. A. Aarnio et al. “The DELPHI detector at LEP”. In: *Nucl. Instrum. Meth.* A303 (1991), pp. 233–276. DOI: 10.1016/0168-9002(91)90793-P.

[62] Elena Graverini et al. “Monitoring radiation damage in the LHCb Tracker Turicensis”. In preparation. 2018.

[63] Frank Hartmann. “Evolution of Silicon Sensor Technology in Particle Physics”. In: *Springer Tracts Mod. Phys.* 231 (2009), pp. 1–204.

[64] W. Shockley and W. T. Read. “Statistics of the Recombinations of Holes and Electrons”. In: *Phys. Rev.* 87 (5 Sept. 1952), pp. 835–842. DOI: 10.1103/PhysRev.87.835. URL: https://link.aps.org/doi/10.1103/PhysRev.87.835.

[65] R. N. Hall. “Electron-Hole Recombination in Germanium”. In: *Phys. Rev.* 87 (2 July 1952), pp. 387–387. DOI: 10.1103/PhysRev.87.387. URL: https://link.aps.org/doi/10.1103/PhysRev.87.387.

[66] H. Bethe. “Zur Theorie des Durchgangs schneller Korpuskularstrahlen durch Materie”. In: *Annalen der Physik* 397 (1930), pp. 325–400. DOI: 10.1002/andp.19303970303.

[67] F. Bloch. “Bremsvermögen von Atomen mit mehreren Elektronen”. In: *Zeitschrift fur Physik* 81 (May 1933), pp. 363–376. DOI: 10.1007/BF01344553.

[68] W. R. Leo. *Techniques for Nuclear and Particle Physics Experiments: A How to Approach*. 1987. ISBN: 9783540572800.

[69] K. A. Olive et al. "Review of Particle Physics". In: *Chin. Phys.* C38 (2014), p. 090001. DOI: 10.1088/1674-1137/38/9/090001.

[70] Sven Lochner. "Development, optimisation and characterisation of a radiation hard mixed-signal readout chip for LHCb". PhD thesis. Heidelberg U., 2006. URL: http://weblib.cern.ch/abstract?CERN-THESIS-2006-061.

[71] L. Landau. "On the energy loss of fast particles by ionization". In: *J. Phys.(USSR)* 8 (1944), pp. 201–205.

[72] U. Fano. "Ionization Yield of Radiations. II. The Fluctuations of the Number of Ions". In: *Phys. Rev.* 72 (1 July 1947), pp. 26–29. DOI: 10.1103/PhysRev.72.26. URL: https://link.aps.org/doi/10.1103/PhysRev.72.26.

[73] Gerhard Lutz. *Semiconductor radiation detectors: device physics*. Berlin: Springer, 1999. URL: https://cds.cern.ch/record/411172.

[74] Michael Moll. "Radiation damage in silicon particle detectors: Microscopic defects and macroscopic properties". PhD thesis. Hamburg U., 1999. URL: http://www-library.desy.de/cgi-bin/showprep.pl?desy-thesis99-040.

[75] LHCb Collaboration. *LHCb Tracker Upgrade Technical Design Report*. Tech. rep. CERN-LHCC-2014-001. LHCB-TDR-015. Feb. 2014. URL: http://cds.cern.ch/record/1647400.

[76] M. Moll, E. Fretwurst, and G. Lindstrom. "Leakage current of hadron irradiated silicon detectors - material dependence". In: *Nucl. Instrum. Meth.* A426 (1999), pp. 87–93. DOI: 10.1016/S0168-9002(98)01475-2.

[77] D Esperante-Pereira and A Vollhardt. *Design and development of the Control Board for the LHCb Silicon Tracker*. Tech. rep. LHCb-2007-153. CERN-LHCb-2007-153. Geneva: CERN, Jan. 2008. URL: http://cds.cern.ch/record/1082457.

[78] E Bos and E Rodrigues. *The LHCb Track Extrapolator Tools*. Tech. rep. LHCb-2007-140. CERN-LHCb-2007-140. Geneva: CERN, Nov. 2007. URL: https://cds.cern.ch/record/1070314.

[79] Michel De Cian et al. *Fast neural-net based fake track rejection in the LHCb reconstruction*. Tech. rep. LHCb-PUB-2017-011. CERN-LHCb-PUB-2017-011. Geneva: CERN, Mar. 2017. URL: https://cds.cern.ch/record/2255039.

[80] Christian Elsasser. "Extension of the TT Test Stand with a Pulsed Focused Infrared Laser". Bachelor thesis. Nov. 2009.

[81] A Ferrari et al. *FLUKA: A multi-particle transport code (program version 2005)*. Tech. rep. Geneva, 2005. URL: http://cds.cern.ch/record/898301.

[82] G. Battistoni et al. "The FLUKA code: description and benchmarking". In: *AIP Conference Proceedings* 896.1 (2007), pp. 31–49. DOI: 10.1063/1.2720455. URL: http://aip.scitation.org/doi/abs/10.1063/1.2720455.

CHAPTER 7

$R\left(\Lambda_c^*\right)$ as a test for Lepton Universality

Contents

7.1. Introduction

One of the key roles of high energy physics experiments is to look for signatures of New Physics. In this chapter, possible hints of the violation of a fundamental property of the SM, the universality of the lepton flavour (LFU), are discussed. The most recent measurements of LFU are examined. Then, a possible way to seek a solution to the so-called $R\left(D^{(*)}\right)$ puzzle through the analisys of $\Lambda_b \to \Lambda_c^* \ell \bar{\nu}_\ell$ decays is presented. The possible backgrounds for this decay are discussed, and those due to an erroneous event reconstruction[1] are quantified in detail.

The $B \to D^{(*)} \ell \bar{\nu}_\ell$ decays have been studied at BaBar [1, 2], Belle [3–5] and LHCb [6, 7]. In all cases, the ratios

$$R\left(D^{(*)}\right) \equiv \frac{\mathrm{Br}\left(B \to D^{(*)} \tau \bar{\nu}_\tau\right)}{\mathrm{Br}\left(B \to D^{(*)} \ell \bar{\nu}_\ell\right)}, \quad \text{with } \ell = \mu, e \tag{7.1}$$

[1] Specifically, misidentified particles, and combinations of tracks coming from unrelated decays.

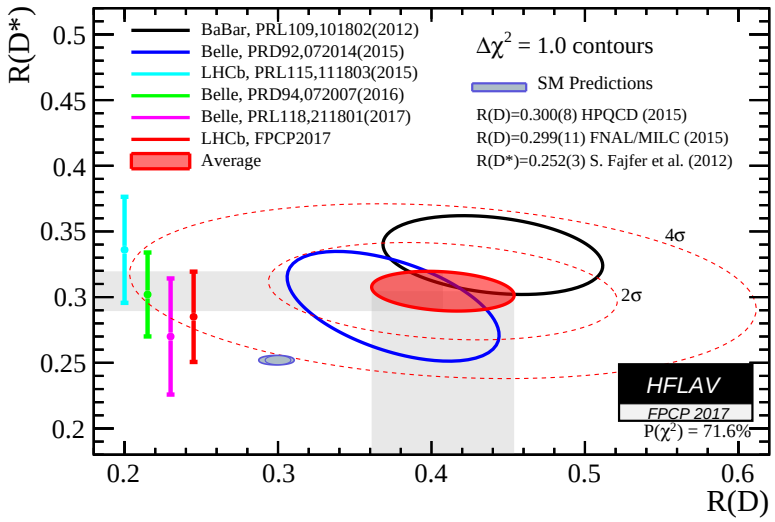

Figure 7.1: Averages of the $R(D^{(*)})$ ratios as computed in June 2017 [11].

consistently exceed SM expectations. Figure 7.1 offers an overview of all of the above cited results, comparing them with the most recently calculated SM predictions [8, 9]. The following averages are obtained [10, 11]:

$$R(D) = 0.407 \pm 0.039\ (\text{stat}) \pm 0.024\ (\text{syst}) \qquad R(D)_{SM} = 0.299 \pm 0.003 \tag{7.2}$$

$$R(D^*) = 0.304 \pm 0.013\ (\text{stat}) \pm 0.007\ (\text{syst}) \qquad R(D^*)_{SM} = 0.252 \pm 0.003 \tag{7.3}$$

where the *SM* suffix identifies the theoretical prediction. The experimental values of $R(D)$ and $R(D^*)$ exceed the SM expectactions by 1.9σ and 3.3σ, respectively, for a resulting combined tension with the SM of 4.1σ.

$B \to D^{(*)}\ell\bar{\nu}_\ell$ decays proceed through an underlying $b \to c\ell\bar{\nu}_\ell$ transition. Due to the large amount of B mesons available at B factories, only mesonic processes have been studied so far. Nevertheless, complementary tests of LFU are possible and can be performed also with baryonic decays. The $\Lambda_b \to \Lambda_c^{(*)}\ell\bar{\nu}_\ell$ decays are also governed by an underlying $b \to c$ transition, but, compared to $B \to D^{(*)}\ell\bar{\nu}_\ell$, they present a more complex spin structure and can offer complementary observables to further constrain NP models. Figure 7.2 shows the Feynman diagrams for the mesonic and baryonic processes discussed in this chapter. A simultaneous measurement using both the Λ_c and Λ_c^* baryons would allow to verify if the same tension with respect to the Standard Model predictions also exists in the baryonic sector. In particular, a measurement of the $\Lambda_b \to \Lambda_c^*\ell\bar{\nu}_\ell$ decay is necessary as a first step towards the analysis of decays involving the ground state Λ_c, since partially reconstructed Λ_c^* events would feed into the Λ_c sample.

In this chapter, the $\Lambda_b \to \Lambda_c^*\ell\bar{\nu}_\ell$ decay is investigated. Figure 7.2 shows the Feynman diagrams for the mesonic and baryonic processes discussed here. The physics interest in

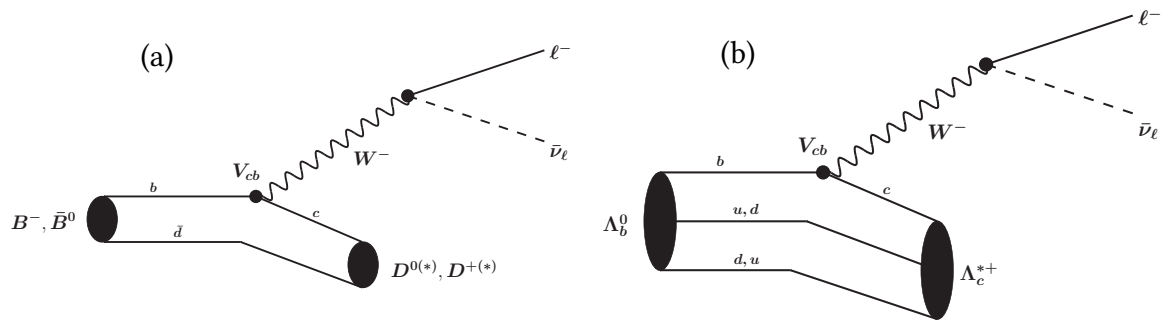

Figure 7.2: Feynman diagrams for the semileptonic $B \to D^* \ell \bar{\nu}$ (a) and $\Lambda_b \to \Lambda_c^* \ell \bar{\nu}$ (b) transitions.

such decay is discussed *e.g.* in [12–20]. The effects of individual NP couplings on $R(\Lambda_c)$ are analysed in a model-independent way in [20]. The potential of a LFU measurement in the baryonic sector as a complementary probe of NP is demonstrated in Figure 7.3, where the authors of [20] show the effects of a possible $R(\Lambda_c)$ measurement on individual NP couplings already constrained by the existing measurements of $R(D)$, $R(D^*)$ and of the lifetime of the B_c meson.

The LHCb experiment has recently studied the decay $\Lambda_b \to \Lambda_c \mu \bar{\nu}_\mu$ [21]. While analyzing backgrounds to this decay, large samples of $\Lambda_c(2595)$ and $\Lambda_c(2625)$ candidates were reconstructed. The reconstructed Λ_c^* mass peaks are visible in Figure 7.4, which demonstrates the abundance of this kind of events. The potential of LFU tests using $\Lambda_b \to \Lambda_c^* \ell \bar{\nu}_\ell$ decays lies not only in the large size of the available sample, but also in the peculiar topology of such decays, sketched in Figure 7.7. Compared to $B \to D^{(*)} \ell \bar{\nu}_\ell$ and to $\Lambda_b \to \Lambda_c \ell \bar{\nu}_\ell$, the number of daughter particles coming from the Λ_b decay vertex is larger. In fact, the Λ_c^* decays immediately to $\Lambda_c \pi \pi$, and the Λ_c decays in turn to $pK\pi$[2]. The additional particles coming from the secondary vertex increase the precision of the decay reconstruction.

This chapter presents preliminary studies aimed at investigating the ratio

$$R_{\Lambda_c^*} \equiv \frac{\mathrm{Br}(\Lambda_b \to \Lambda_c^{*+} \tau^- \bar{\nu})}{\mathrm{Br}(\Lambda_b \to \Lambda_c^{*+} \mu^- \bar{\nu})} \tag{7.4}$$

where Λ_c^{*+} denotes either the $\Lambda_c^+(2595)$ or the $\Lambda_c^+(2625)$ charmed baryon. Sections 7.1.1 and 7.1.2 will briefly introduce the properties of the baryons involved in these processes. Section 7.2 will explain the analysis strategy. Finally, Sections 7.3 to 7.5 will discuss how to deal with the main sources of background.

[2] The Λ_c^+ can decay to different final states, such as $pK^-\pi^+\pi^0$ or $\Lambda^0\pi^+\pi^0$; however, we only look at well reconstructed $\Lambda_c \to pK^-\pi^+$ final states for this analysis.

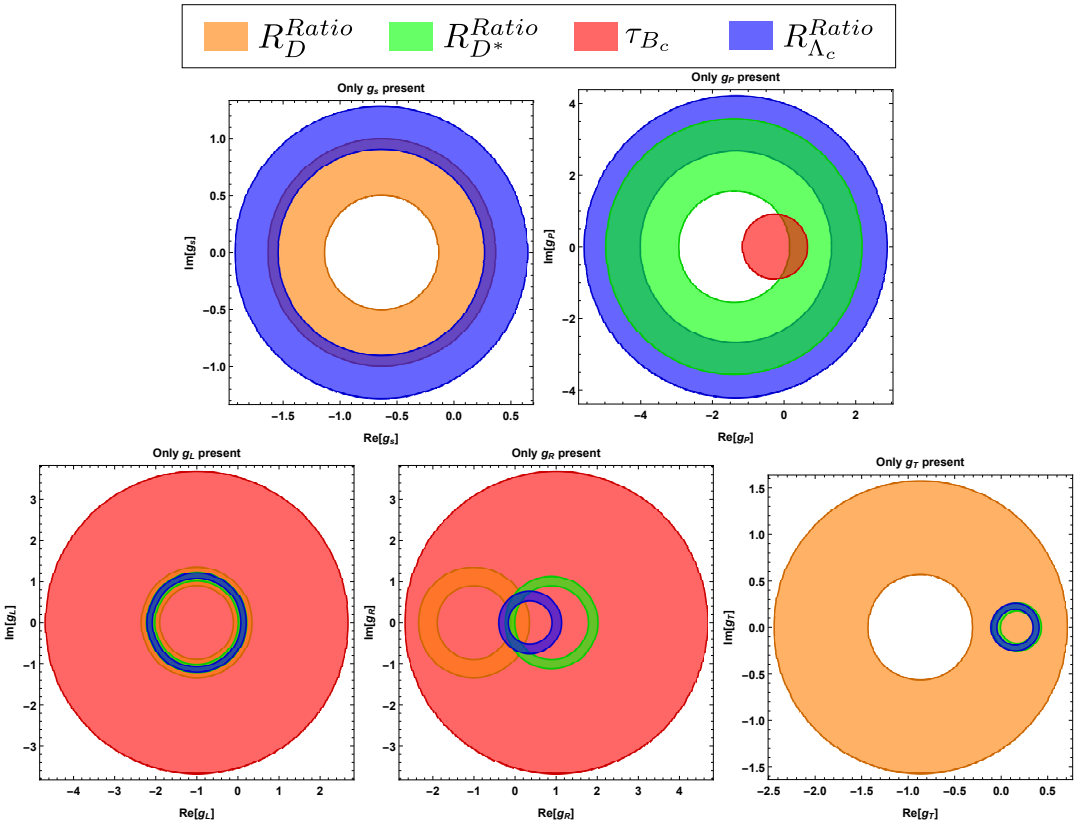

Figure 7.3: Constraints on individual new-physics couplings from existing mesonic measurementds and a possible $R\left(\Lambda_c^*\right)$ measurement (shown in blue), assuming that $R\left(\Lambda_c\right) = (1.3 \pm 3 \times 0.05)\, R\left(\Lambda_c\right)_{SM}$ where the 1σ uncertainty is 0.05 [20].

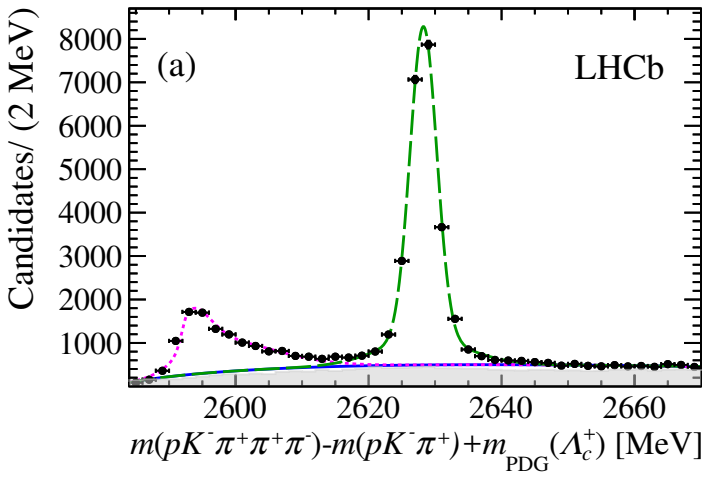

Figure 7.4: Mass difference $m\left(pK^-\pi^+\pi^+\pi^-\right) - m\left(pK^-\pi^+\right)$ for $pK^-\pi^+$ candidates within ±20 MeV of the known Λ_c^+ mass [21].

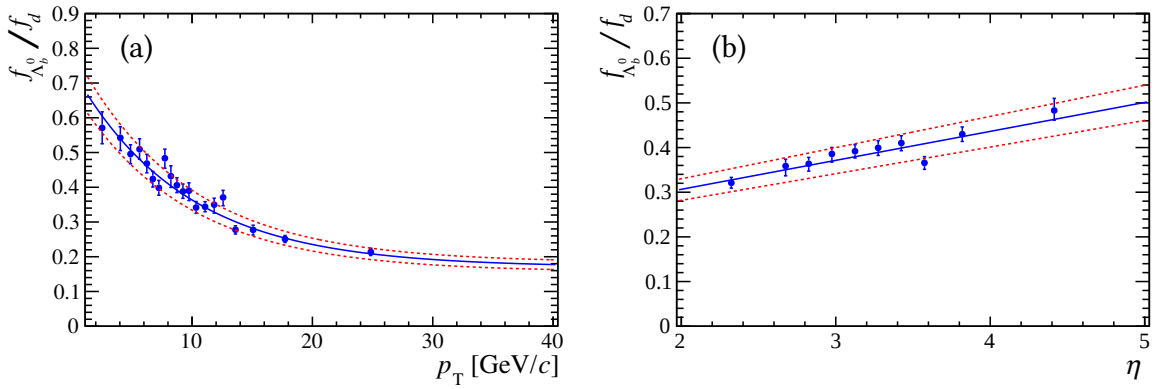

Figure 7.5: Relative production rate between Λ_b baryons and B^0 mesons as a function of the transverse momentum (a) and pseudorapidity (b) of the beauty baryon for pp collisions at $\sqrt{s} = 7$ TeV [24].

7.1.1. The Λ_b

Lambda baryons are a family of baryons containing three different quarks, among which an up- and a down-quark. The third quark can be an s, c or b quark, respectively, for Λ, Λ_c and Λ_b baryons. Lambda baryons containing the top quark were not observed, as the t lifetime is too short at $O\left(10^{-25}\text{ s}\right)$ to form bound hadronic states.

The Λ_b is the lowest mass baryon containing a b quark. It is an isospin $I = 0$ state of mass $m_{\Lambda_b} = 5.62$ GeV and spin-parity $J^P = 1/2^+$. Its lifetime is rather large, $\tau_{\Lambda_b} = 1.47 \times 10^{-12}$ s [22], which results in a mean decay distance in the mm regime with the typical boost obtained in pp collisions at $\sqrt{s} = 13$ TeV.

At the LHC, Λ_b baryons are produced in copious amount, at approximately half the rate of B^0 mesons [23, 24]. Figure 7.5 shows the ratio of Λ_b to B^0 production as a function of the b-hadron kinematics. An advantage to LFU studies using Λ_b baryons is that, due to the conservation of the baryon number, and to the Λ_b being the lowest mass b-baryon, analyses looking at specific Λ_b decay channels have to cope with background arising only from different decays of the Λ_b itself.

7.1.2. The $\Lambda_c^{(*)}$

The Λ_c as well as its excited states are charmed baryons composed by an u, a d and a c quark. In the rest of this Chapter, and in Chapter 8, the symbol Λ_c^* will collectively refer to the two states $\Lambda_c(2595)$ and $\Lambda_c(2625)$, distinguished by their masses of 2.593 GeV and 2.625 GeV. These two charmed baryons form an isospin doublet with $I = 0$ and spin-parity $J^P = 1/2^-$ and $J^P = 3/2^-$, respectively. Both states have a rather narrow decay width and decay with 100% probability to a $\Lambda_c\pi\pi$ final state. The decay of the lower mass state proceeds predominantly through an intermediate $\Sigma_c(2455)^{++}\pi^-$ or $\Sigma_c(2455)^0\pi^+$ resonance, as described in Figure 7.6. The decay $\Lambda_c^* \to \Lambda_c\pi\pi$ – including its resonant $\Sigma_c(\to \Lambda_c\pi)\,\pi$ mode – is the only strong decay allowed for a charmed baryon with this mass [22]. Table 7.1 lists the decay modes of these

Particle	Decay mode	Branching fraction
Λ_b^0	$\Lambda_c^+ \ell^- \bar{\nu}_\ell$	$\left(6.2\,^{+1.4}_{-1.3}\right)\%$
	$\Lambda_c^+ \pi^+ \pi^- \ell^- \bar{\nu}_\ell$	$(5.6 \pm 3.1)\%$
	$\Lambda_c\left(2625\right)^+ \ell^- \bar{\nu}_\ell$	$\left(1.3\,^{+0.6}_{-0.5}\right)\%$
	$\Lambda_c^+ D_s^-$	$(1.10 \pm 0.10)\%$
	$\Lambda_c\left(2595\right)^+ \ell^- \bar{\nu}_\ell$	$\left(7.9\,^{+4.0}_{-3.5}\right) \times 10^{-3}$
	$\Lambda_c^+ \pi^+ \pi^- \pi^-$	$(7.7 \pm 1.1) \times 10^{-3}$
	$\Lambda_c^+ \pi^-$	$(4.9 \pm 0.4) \times 10^{-3}$
$\Lambda_c\left(2595\right)^+$	$\Sigma_c\left(2455\right)^{++} \pi^-$	$(24 \pm 7)\%$
	$\Sigma_c\left(2455\right)^0 \pi^+$	$(24 \pm 7)\%$
	$\Lambda_c^+ \pi^+ \pi^-$	$(18 \pm 10)\%$
$\Lambda_c\left(2625\right)^+$	$\Lambda_c^+ \pi^+ \pi^-$	$\geq 67\,\%$
	$\Sigma_c\left(2455\right)^{++} \pi^-$	$< 5\,\%$
	$\Sigma_c\left(2455\right)^0 \pi^+$	$< 5\,\%$
$\Sigma_c\left(2455\right)^{+,0}$	$\Lambda_c^+ \pi^{0,+}$	$\approx 100\,\%$

Table 7.1: Main decay modes of the Λ_b, Λ_c^* and Σ_c states [22].

states. Decays of heavier charmed baryons into Λ_c^* were not observed.

7.1.3. Strategy for semileptonic measurements at LHCb

Experiments such as Belle and BaBar operate at so-called B factories. At a B factory, asymmetric e^+e^- beams collide at a centre-of-mass energy just above the mass of the $\Upsilon\left(4S\right)$ meson, *i.e.* at $\sqrt{s} \gtrsim 10.58$ GeV. The $\Upsilon\left(4S\right)$ decays almost exclusively into B^+B^- or $B^0\bar{B}^0$ pairs. In order to reconstruct semileptonic decays of a B meson, one can select events where one of the two B mesons is fully reconstructed, and use kinematic information from the fully reconstructed B decay to reconstruct the four-momentum of the missing neutrino (or neutrinos, in case of a $B \to D^*\tau\left(\to \mu\bar{\nu}_\mu\nu_\tau\right)\bar{\nu}_\tau$ decay) produced in the decay of the other B meson.

At hadronic colliders, $b\bar{b}$ quark pairs are produced in parton-level interactions. Therefore, it is impossible to know the centre-of-mass energy in the initial state. Moreover, one of the b quarks may hadronize outside of the detector acceptance. For these reasons, semileptonic decays cannot be fully reconstructed. At LHCb, an approximation is used to estimate the transverse component of the missing momentum carried by the neutrino(s). Let us consider the $B \to D^*\ell\bar{\nu}_\ell$ process as an example. The component of the B momentum parallel to the beam axis is assumed to be equal to that of the visible decay products, *i.e.* of the $D^*\ell$ pair, rescaled for the difference in mass between the B and its visible daughters:

$$p_{B,z} \equiv \frac{m_B}{m_V}\, p_{V,z}. \tag{7.5}$$

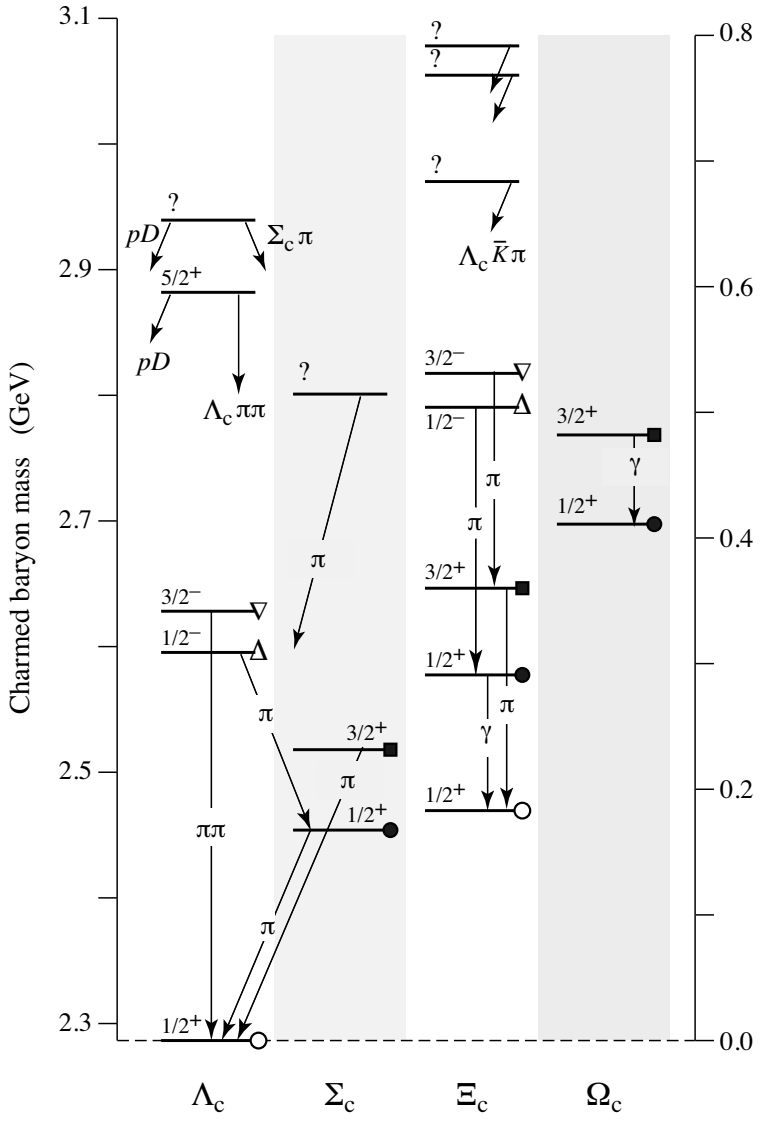

Figure 7.6: Charmed baryons spectroscopy. The Λ_c (2595) and Λ_c (2625) baryons form an isospin doublet [22].

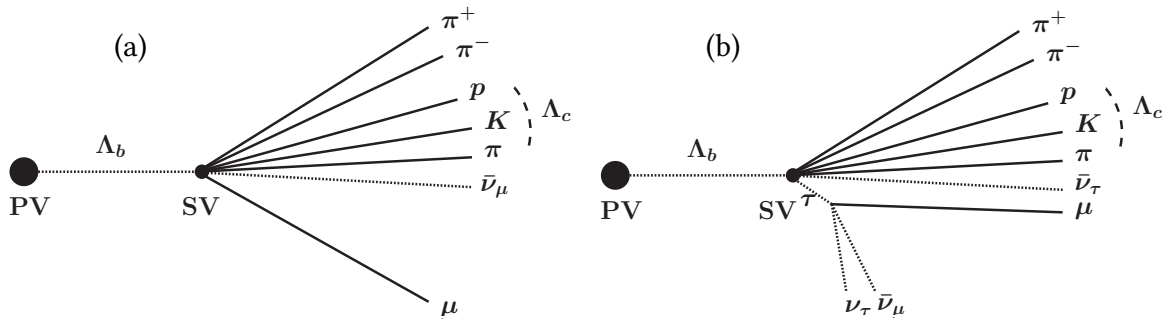

Figure 7.7: Decay topology for the $\Lambda_b \to \Lambda_c^* \mu \bar{\nu}_\mu$ (a) and $\Lambda_b \to \Lambda_c^* \tau \bar{\nu}_\tau$ (a) processes.

In Eqn. 7.5 and in the remainder of this chapter, the V subscript denotes kinematical observables calculated for the ensemble of visible particles in the final state of a semileptonic decay.

The spatial positions of the primary vertex (PV) and of the secondary vertex (SV) are then compared to determine the direction of the B momentum, using the relations

$$p_x = \frac{\Delta x}{\Delta z} p_z \quad \text{and} \tag{7.6}$$

$$p_y = \frac{\Delta y}{\Delta z} p_z, \tag{7.7}$$

where $\Delta k = k_{SV} - k_{PV}$ represents the projection along the axis $\hat{k}$ of the distance travelled by the Λ_b before decaying.

At this stage, one can measure the component of the momentum of the visible decay products transverse with respect to the direction of the B; this is equal in magnitude and opposite in direction to the transverse momentum of the unreconstructed neutrino(s). This leaves only the parallel component of the neutrino momentum to be determined. The following energy conservation relation

$$(p_\nu + p_V)^2 = m_B^2, \tag{7.8}$$

where p_ν denotes the four-momentum of the neutrino(s), allows to determine the parallel component of the neutrino momentum up to a quadratic two-fold ambiguity. In fact, by expressing the four-momenta in terms of their parallel ($p_\parallel$) and orthogonal ($p_\perp$) components as

$$p_V = \left(\sqrt{p_{V,\parallel}^2 + p_\perp^2}, 0, p_\perp, p_{V,\parallel}\right) \quad \text{and} \tag{7.9}$$

$$p_\nu = \left(\sqrt{p_{\nu,\parallel}^2 + p_\perp^2}, 0, -p_\perp, p_{\nu,\parallel}\right), \tag{7.10}$$

and solving Eqn. 7.8 for $p_{\nu,\parallel}$, one obtains

$$\begin{aligned} p_{\nu,\parallel} &= \frac{-b \pm \sqrt{b^2 - 4ac}}{2a}, \qquad \text{where} \\ a &= 4\left(p_\perp^2 + m_V^2\right) \\ b &= 4p_{V,\parallel}\left(2p_\perp^2 - m_{miss}^2\right) \\ c &= 4p_\perp^2\left(p_{V,\parallel}^2 + m_B^2\right) - m_{miss}^4, \qquad \text{and} \\ m_{miss}^2 &= (p_B - p_V)^\mu (p_B - p_V)_\mu. \end{aligned} \tag{7.11}$$

In the above notation, m_{miss}^2 indicates the total invariant mass squared of the missing particles. If there is only one missing neutrino, this value is null. However, if there is more than one neutrino in the final state, such as in the $B \to D^*\tau\left(\to \mu\bar{\nu}_\mu\nu_\tau\right)\bar{\nu}_\tau$ decay, the combination of their momenta results in $m_{miss}^2 > 0$. Although the reconstruction of the event is more problematic, one can use this aspect to discriminate between single-neutrino and multi-neutrinos final states, as described in Section 7.2.1.

7.2. Analysis strategy

As discussed in Section 7.1.3, $\Lambda_b \to \Lambda_c^*\ell\bar{\nu}_\ell$ decays cannot be exclusively reconstructed at LHCb: the initial centre-of-mass energy of the partonic collision producing the $b\bar{b}$ pair cannot be determined at a hadron collider, thus preventing any reconstruction of the momentum carried away by the final state neutrino. However, the missing mass in the decay can be determined by comparing the momentum of the Λ_b with that of the visible decay products as in Eqn. 7.11. While the single neutrino produced in the semi-muonic decay $\Lambda_b \to \Lambda_c^*\mu\bar{\nu}_\mu$ has a negligible mass, the combination three neutrinos generated in the semi-tauonic mode can result in a large missing mass. However, decays with a $\Lambda_c^*\mu X$ final state, too, where X represents any combination of particles, can carry nonzero missing mass if X contains neutrinos or X is only partially reconstructed. Therefore, $\Lambda_b \to \Lambda_c^*\mu X$ decays provide a potentially dangerous background for the signal mode $\Lambda_b \to \Lambda_c^*\tau\bar{\nu}_\tau$.

This class of background can be separated into two main contributions. The first comes from decays of the form $\Lambda_b \to \Lambda_c^{**}\mu\bar{\nu}_\mu$ followed by $\Lambda_c^{**} \to \Lambda_c^*X$, where Λ_c^{**} is any charmed baryon with mass larger than that of the $\Lambda_c(2595)$ and $\Lambda_c(2625)$ states. This type of background is referred to as "feeddown". $\Lambda_c^{**} \to \Lambda_c(2595)X$ and $\Lambda_c^{**} \to \Lambda_c(2625)X$ decays have never been observed (*cf.* Figure 7.6), but should be searched for, as their yield could be comparable to that of the expectedly small $\Lambda_b \to \Lambda_c^*\tau\bar{\nu}_\tau$ signal.

The second contribution comes from decays of the $\Lambda_b \to \Lambda_c^*X_c$ type, with X_c being any combination of particles containing a charmed hadron and resulting in a $\mu\bar{\nu}_\mu X$ final state. This source of background is referred to as "double charm", as the Λ_c^* is accompanied by another charmed particle. An example of such process is the decay $\Lambda_b \to \Lambda_c^*D_s$. The D_s has a

lifetime comparable to that of the τ lepton, and can mimic the topology of a τ decay. Even if the combined branching ratio of the $\Lambda_b \to \Lambda_c^* D_s\,(\to \ell\bar{\nu}_\ell X)$ process is expected to be small, it could be of the same order of magnitude of that of the $\Lambda_b \to \Lambda_c^*\tau\bar{\nu}_\tau$ signal.

Not only different Λ_b decays can affect the measurement of $R\left(\Lambda_c^*\right)$. An important background arises when a $\Lambda_b \to \Lambda_c^* hX$ event is recorded, h being any particle, and h is misidentified as a muon. Such events not containing a genuine muon are referred to as "mis-ID" background. Furthermore, events containing a genuine muon produced in an unrelated process, but which is incorrectly associated to a $\Lambda_b \to \Lambda_c^* X$ decay, can also leak into the $\Lambda_b \to \Lambda_c^*\ell\bar{\nu}_\ell$ signal sample. This is referred to as "combinatorial background".

While the analysis of physics background sources requires a comparison between simulated background events and the actual shape of kinematic observables reconstructed from collision data, the characteristics and yields of signal decays arising from mis-ID and combinatorial background can be estimated using only collision data. Section 7.3 describes how the mis-ID background can be handled for the $R\left(\Lambda_c^*\right)$ measurement. Section 7.4 instead analyses the contribution from combinatorial background. Section 7.2.1, finally, shows how to distinguish $\Lambda_b \to \Lambda_c^*\tau\bar{\nu}_\tau$ signal from the more abundant $\Lambda_b \to \Lambda_c^*\mu\bar{\nu}_\mu$ yield, and from the various sources of background.

7.2.1. Determination of the $\Lambda_b \to \Lambda_c^*\tau\bar{\nu}_\tau$ signal yield

The $\Lambda_b \to \Lambda_c^*\tau\left(\to \mu\bar{\nu}_\mu\nu_\tau\right)\bar{\nu}_\tau$ decay has exactly the same set of visible particles in the final state as the more abundant $\Lambda_b \to \Lambda_c^*\mu\bar{\nu}_\mu$ muonic counterpart. To be able to distinguish them, one has to exploit the difference in the kinematics of the two processes arising from the large mass difference between the μ and τ leptons, and from the presence of extra neutrinos in the semitauonic decay. This strategy is well established for mesonic measurements at B factories, such as [1, 2, 4, 5], where the simple kinematics of the $e^+e^- \to \Upsilon(4S) \to B\bar{B}$ production mechanism allows to fully constrain the fourmomentum of the decaying B meson. Even if the B fourmomentum cannot be precisely determined at LHCb, the approximation discussed in Section 7.1.3 allows to construct kinematic variables sensitive to the kinematics of the missing system, which therefore carry a certain discriminant power between muonic and tauonic processes, such as:

- the invariant mass m^2_{miss} of the missing particle(s),
- the energy E^*_μ of the muon in the rest frame of the decaying b-hadron,
- the fourmomentum transfer q^2 to the lepton system,
- the impact parameter IP_μ of the muon with respect to the Λ_b decay vertex,
- and the quality of the reconstruction of the Λ_b vertex itself, measured by means of the chi-square quantity χ^2_{SV}.

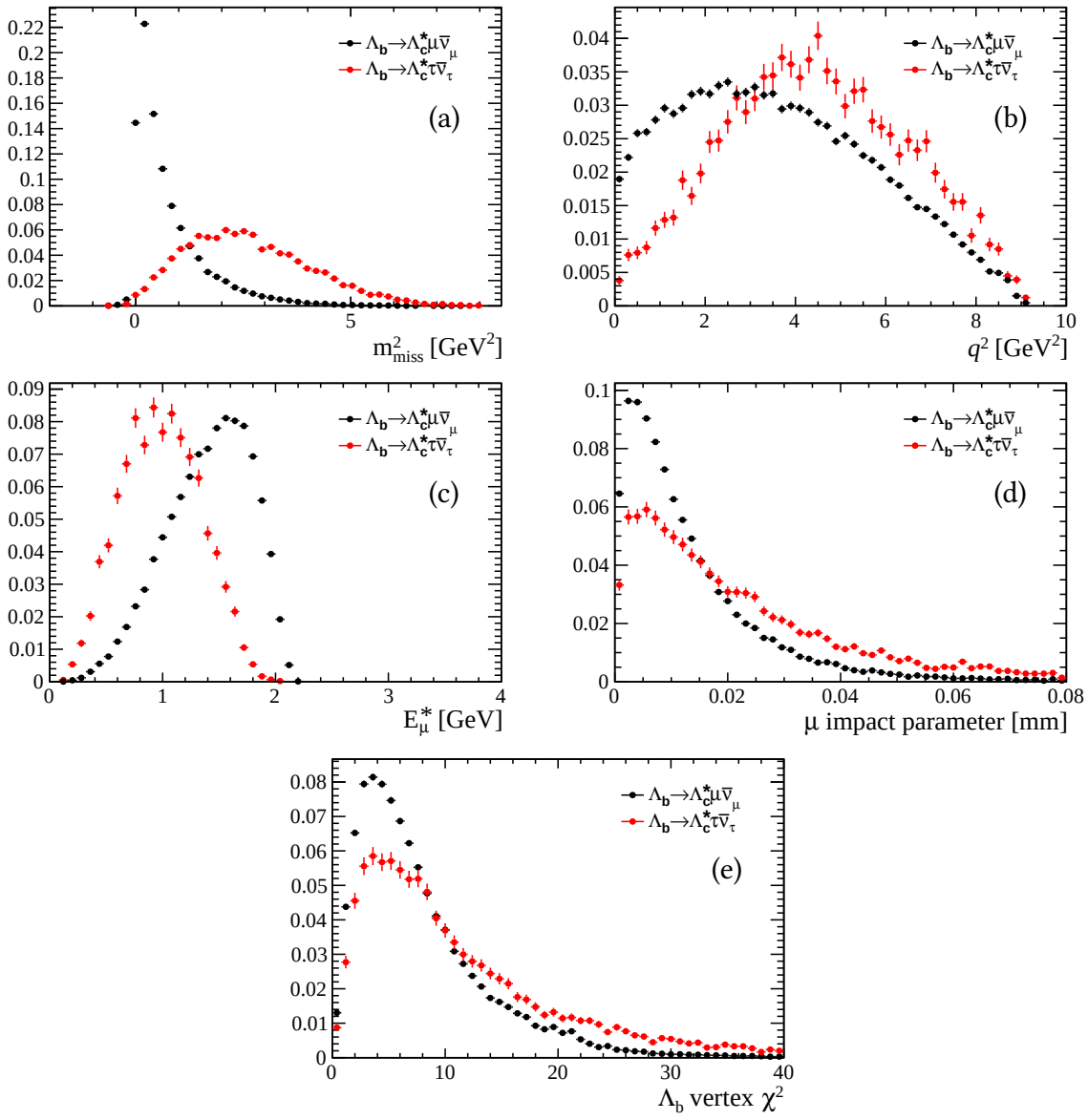

Figure 7.8: Distribution of the $\tau-\mu$ discriminating variables described in the text for a simulated sample of $\Lambda_b \to \Lambda_c^* \tau \bar{\nu}_\tau$ decays (red) *vs.* $\Lambda_b \to \Lambda_c^* \mu \bar{\nu}_\mu$ (black), following event reconstruction.

For example, the $R(D^*)$ LHCb analysis used a combination of m^2_{miss}, E^*_μ and q^2 to separate $B \to D^*\tau\bar{\nu}_\tau$ signal from the muonic channel [6]. In the case of $R\left(\Lambda_c^*\right)$, we foresee to adopt a similar strategy. In addition to that, the Λ_b decay vertex exibits slightly better quality in the muonic case, because the muon track points back to it exactly, excluding smearing effects due to the detector resolution (*cf.* Figure 7.7). Therefore, the χ^2_{SV} and the corresponding muon impact parameter IP_μ can be used to provide further discrimination.

Figure 7.8 shows the simulated distributions for all variables described above, highlighting the different shapes arising from $\Lambda_b \to \Lambda_c^*\mu\bar{\nu}_\mu$ and $\Lambda_b \to \Lambda_c^*\tau\bar{\nu}_\tau$ decays. A fit to any combination of these variables, using templates obtained from muonic and tauonic Montecarlo generated samples, will be sensitive to the ratio of events containing a τ to events where the Λ_b decays directly to a muonic final state. Correcting this ratio for the selection efficiencies of the two modes allows to measure $R\left(\Lambda_c^*\right)$:

$$R\left(\Lambda_c^*\right) = \frac{N\left(\Lambda_b \to \Lambda_c^*\tau\bar{\nu}_\tau\right)}{N\left(\Lambda_b \to \Lambda_c^*\mu\bar{\nu}_\mu\right)} \times \frac{\varepsilon_\mu}{\varepsilon_\tau} \equiv R_\tau \times \frac{\varepsilon_\mu}{\varepsilon_\tau}, \tag{7.12}$$

where $\varepsilon_{\mu,\tau}$ denotes the selection efficiency of the μ and τ modes, and N the observed number of events after background subtraction. The ratio $R_\tau \equiv N_\tau/N_\mu$ can be determined by fitting data with a model $\mathcal{F}$ containing contributions from the τ and μ channels as well as constraints on all the sources of background, with a formulation like

$$\mathcal{F}(\mathbf{x}) = N_\mu \times \left[f_\mu(\mathbf{x}) + R_\tau f_\tau(\mathbf{x}) + \sum_{i \in \text{BG sources}} R_i f_i(\mathbf{x}) \right], \tag{7.13}$$

where:

- $\mathbf{x}$ is any combination of the fit variables,
- N_μ is the number of observed $\Lambda_b \to \Lambda_c^*\mu\bar{\nu}_\mu$ candidates,
- f_k is a probability density function describing the shape of $\mathbf{x}$ for the species k, where
- k runs over μ, τ and all the sources i of background, and
- R_k denotes the ratio of yield from the species k to that of $\Lambda_b \to \Lambda_c^*\mu\bar{\nu}_\mu$ candidates.

The normalization N_μ can be obtained with a fit to the Λ_c^* mass peaks as explained in Section 7.3, including all of the known background components. Most of the components f_k of the above model can be derived from Montecarlo simulated samples (this is the case *e.g.* for physics backgrounds) or data-driven templates (*e.g.* for events with a fake muon). Figure 7.8 shows the shapes $f_\mu(\mathbf{x})$ and $f_\tau(\mathbf{x})$ obtained by the corresponding Montecarlo samples. The ratios R_i can only be constrained by identifying the corresponding components in data. In the following sections we will constrain the rates $R_{\text{mis-ID}}$ and R_{comb} of candidates from fake muons and random combinations of unrelated tracks, respectively, and provide a template for the

shapes $f_{\text{mis-ID}}(\mathbf{x})$. Finally, Section 7.5 will suggest how to constrain the physics backgrounds and summarise the further steps to measure $R\left(\Lambda_c^*\right)$.

7.2.2. Trigger, stripping and data selection

The studies presented in the following sections use LHCb data collected during the LHC Run II in 2015 and 2016, corresponding to an integrated luminosity $\int\mathcal{L} = 1.99\,\text{fb}^{-1}$. These results will be extended to the full Run I + Run II dataset, for a total integrated luminosity of $3.7\,\text{fb}^{-1}$ at $\sqrt{s} = 13$ TeV and $3.23\,\text{fb}^{-1}$ at $\sqrt{s} = 7$ and 8 TeV, in the coming months.

The selection criteria used to isolate $\Lambda_b \to \Lambda_c^*\tau\bar{\nu}_\tau$ and $\Lambda_b \to \Lambda_c^*\mu\bar{\nu}_\mu$ decays are listed in Tables 7.2 and 7.3. Table 7.2 shows the trigger decisions required to select only events with a b-hadron candidate decaying semileptonically to a final state comprising a c-hadron. After the events passing the trigger selections are saved to disk, a process called stripping partitions the data set in smaller samples according to the needs of the various classes of LHCb physics analyses. The purposes of the $R\left(\Lambda_c^*\right)$ analysis are fulfilled in Run II by the `b2LcMuX(Fake)B2DMuForTauMu` stripping line, where a b-hadron decaying to $\Lambda_c\mu X$ is constructed (X being any combination of other particles). Very loose requirements on the quality of tracks and vertices are applied at this stage. Most notably, the muon and Λ_c daughters are required to have momentum larger than 3 GeV and 2 GeV, respectively. A dedicated configuration of trigger and stripping selections (grayed out in Table 7.2) is used, additionally, to build a sample of $b \to \Lambda_c\mu X$ decays containing a fake muon, *i.e.* another particle that has been misidentified and associated with a muon hypotesis. This sample will prove useful to characterize the background due to spurious muons.

Simulated $\Lambda_b \to \Lambda_c^*\tau\bar{\nu}_\tau$ and $\Lambda_b \to \Lambda_c^*\mu\bar{\nu}_\mu$ decays were used in order to estimate the efficiency of the trigger and stripping selections. The trigger has an efficiency of about 22% for both the muonic and the tauonic mode. The stripping selections slightly favour the muonic mode, with an efficiency of 62% *vs.* 55% for the tauonic decay.

Table 7.3 lists the criteria used to further refine the data sample. The selections were tuned in order to minimise the bias towards either the muonic or tauonic mode, avoiding the use of variables that would discriminate between the two, such as the muon transverse momentum. The reconstructed Λ_c mass is required to be within a window of 30 MeV around its nominal value, and the mass difference between the Λ_c^* and the Λ_c is limited to 400 MeV. This, together with the requirement that the Λ_c^* decay vertex is well reconstructed, and that the reconstructed Λ_c points back to the same SV, limits the background from random combination of tracks and non-Λ_c^* events. The Λ_c daughter particles are required to not point back to the primary vertex, as part of the transverse momentum of the Λ_b is carried away by the two pions from the Λ_c^* decay and by the leptonic system.

After applying all selection criteria listed in Tables 7.2 and 7.3, a Λ_c^* mass fit (*cf.* Figure 7.10(f)) shows that the data sample collected by LHCb in 2015 and 2016 contains $51\,153 \pm 1132$ $\Lambda_b \to \Lambda_c^*\mu\bar{\nu}_\mu$ candidates, including $\Lambda_b \to \Lambda_c^*\tau\left(\to \mu\bar{\nu}_\mu\nu_\tau\right)\bar{\nu}_\tau$ signal, and residual background

Level	Line	Type
L0	L0HadronDecision	TIS+TOS
L0	L0Global	TIS
HLT	Hlt2XcMuXForTauB2XcMuDecision	TIS+TOS
Stripping	b2LcMuXB2DMuForTauMuLine	–
HLT	Hlt2XcMuXForTauB2XcFakeMuDecision	TIS+TOS
Stripping	b2LcMuXFakeB2DMuForTauMuLine	–

Table 7.2: Trigger decisions and stripping filter required for the selection of $\Lambda_b \to \Lambda_c^* \tau \bar{\nu}_\tau$ and $\Lambda_b \to \Lambda_c^* \mu \bar{\nu}_\mu$ decays. The grayed-out lines are used as an alternative to the normal HLT and stripping lines to evaluate the background coming from fake muons. The trigger decision can be taken either on the signal particle (TOS) or independently on another particle in the event (TIS). The stripping filter requires the presence of a b-hadron candidate decaying to a $\Lambda_c \mu X$ final state, where X is any combination of other particles.

events.

7.3. Background from fake muons (mis-ID)

Decays of the type $\Lambda_b \to \Lambda_c^* h X$ can be a background for $\Lambda_b \to \Lambda_c^* \mu \bar{\nu}_\mu$ if h is misidentified for a muon, a mistake that has a small but not negligible probability to happen. Hadrons can in fact decay in flight to a muonic final state. The identification of particles in LHCb is based on data from the PID subdetectors combined into multivariate classifiers and neural networks (*cf.* Section 5.2.2). Reference distributions of PID variables are made available in LHCb, obtained by studying well reconstructed decays such as $D^{*+} \to D^0 \left(\to K^- \pi^+\right) \pi^+$, $\Lambda^0 \to p^+ \pi^-$, $B^+ \to J/\psi \left(\to e^+ e^-\right) K^+$, and $\Lambda_b^0 \to \Lambda_c^+ \left(\to p^+ K^- \pi^+\right) \pi$ [25]. Particle identification efficiency varies as a function of the track kinematics and of the event topology [26]. Therefore, the calibration samples provide the distributions of PID variables for reconstructed particles in bins of the particle momentum (p) and pseudorapidity (η) and of the total number of tracks reconstructed in the event (n_{tracks}).

A dedicated stripping line not implementing muon PID selections is employed to asses the yield of mis-ID background. This stripping line is in every other aspect equivalent to the one used for $\Lambda_b \to \Lambda_c^* \ell \bar{\nu}_\ell$ data. After applying the selection criteria listed in Section 7.2.2, the amount of $\Lambda_b \to \Lambda_c^* \mu \bar{\nu}_\mu$ candidates found in the mis-ID stripping line is about 24000. We then partition this data sample into subsets, according to which particle was misidentified as a muon, using the selections listed in Table 7.4. Finally, the $\mathcal{sP}lot$ technique [27] is combined to a fit to the Λ_c^* mass peaks, and to the information extracted from the PID calibration samples, in order to extract the amount of fake $\Lambda_b \to \Lambda_c^* \mu \bar{\nu}_\mu$ candidates in each subset.

Montecarlo simulated $\Lambda_b \to \Lambda_c^* \mu \bar{\nu}_\mu$ decays are used in order to determine the shape of the Λ_c^* mass peaks. Systematic uncertainties related to the experimental resolution are minimised by taking the mass difference $\Delta m \equiv m_{\Lambda_c^*} - m_{\Lambda_c}$ instead of the Λ_c^* mass directly. Figure 7.9

Variable	Selection
Kinematics	
Λ_b mass	$m_{\Lambda_b} < 5.62$ GeV
Λ_c mass	2.27 GeV $< m_{\Lambda_c} <$ 2.30 GeV
Λ_c^*–Λ_c mass difference	$\Delta m < 400$ MeV
Λ_c transverse momentum	$p_{\perp,\pi_{\Lambda_c}} + p_{\perp,K} + p_{\perp,p} > 2.5$ GeV
Vertices	
Λ_c^* decay vertex quality	$\chi^2/ndf\,(SV) < 2$
Λ_c flight distance χ^2	$\chi^2_{FD}\,(\Lambda_c) > 100$
Λ_c impact parameter *w.r.t.* SV	$IP_{SV}\,(\Lambda_c) < 7.4$ mm
$\boldsymbol{\Lambda_c \to pK\pi}$	
Λ_c daughter K track quality	$\chi^2/ndf\,(K) < 5$
Λ_c daughter K kaon probability	$P_{NN,K}\,(K) > 0.2$
Λ_c daughter K ghost probability	$P_{NN,ghost}\,(K) < 0.5$
Λ_c daughter K impact parameter χ^2	$\chi^2_{IP}\,(K) > 9$
Λ_c daughter π track quality	$\chi^2/ndf\,\left(\pi_{\Lambda_c}\right) < 5$
Λ_c daughter π pion probability	$P_{NN,\pi}\left(\pi_{\Lambda_c}\right) > 0.2$
Λ_c daughter π ghost probability	$P_{NN,ghost}\left(\pi_{\Lambda_c}\right) < 0.5$
Λ_c daughter π impact parameter χ^2	$\chi^2_{IP}\left(\pi_{\Lambda_c}\right) > 9$
Λ_c daughter p proton probability	$P_{NN,p}\,(p) > 0.2$
$\boldsymbol{\Lambda_c^* \to \Lambda_c\pi^+\pi^-}$	
$\pi^\pm$ pion probability	$P_{NN,\pi}\,(\pi^\pm) > 0.2$
$\pi^\pm$ electron probability	$P_{NN,e}\,(\pi^\pm) < 0.4$
$\pi^\pm$ ghost probability	$P_{NN,ghost}\,(\pi^\pm) < 0.5$
$\boldsymbol{\mu}$ **PID** (not used for the mis-ID stripping line)	
μ muon PID	$PID_\mu\,(\mu) > 0$

Table 7.3: Event selection for the analysis of the $\Lambda_b \to \Lambda_c^* \tau \bar{\nu}_\tau$ and $\Lambda_b \to \Lambda_c^* \mu \bar{\nu}_\mu$ decays.

Subset	Selections
π	`DLLK<0`, `DLLp<0`, `DLLe<0`, `IsMuon==0`
K	`DLLK>10`, `DLLK-DLLp>0`, `DLLe<0`, `IsMuon==0`
p	`DLLp>10`, `DLLp-DLLK>10`, `IsMuon==0`
e	`DLLe>2`, `DLLe-DLLK>0`, `DLLe<0`, `IsMuon==0`
μ	`DLLmu>0`, `IsMuon==1`

Table 7.4: Selections used to partition $\Lambda_b \to \Lambda_c^* hX$ data according to the type of the h particle.

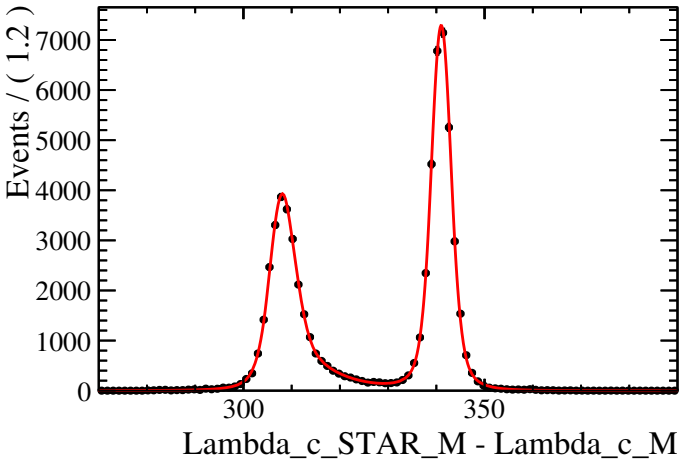

Figure 7.9: $\Delta m = m_{\Lambda_c^*} - m_{\Lambda_c}$ distribution for Montecarlo simulated $\Lambda_b \to \Lambda_c^* \mu \bar{\nu}_\mu$. The simulation takes full account of the LHCb detector geometry, and the reconstruction algorithms applied are the same used on real data. All events are required to pass the selection criteria listed in Table 7.3.

shows the Δm distribution of the Montecarlo sample. These data are fit with a double Crystal Ball function [28] for each of the two $\Lambda_c(2595)$ and $\Lambda_c(2625)$ states. The obtained model parameters are then fixed in the fit performed to the fake muons (mis-ID) data set. Here, the fit model is complemented with a threshold function first developed by the Argus collaboration and then adopted by the BaBar experiment to describe the Δm background in semileptonic $b \to c\ell\nu$ transitions [29, 30]. All fits were performed by means of the RooFit toolkit [31]. The resulting mass distributions and their fits are shown in Figure 7.10.

The $_s\mathcal{P}lot$ technique allows to assign weights to each event, representing the probability that the event belongs to one of the signal peaks. These are called $_s\mathcal{W}eights$, and are defined such that the sum $\sum_i {}_s\mathcal{W}_i$, where the symbol ${}_s\mathcal{W}$ represents the ${}_s\mathcal{W}eight$ of the event and the index i runs over all the events of the sample, is equal to the fitted amount of signal. The PID calibration samples are then used to unfold the probabilities $P(\mu|h;p,\eta,n_{tracks})$ and $P(h|h;p,\eta,n_{tracks})$, where the latter represents the probability that a particle h with momentum p and pseudorapidity η is identified as such in an event with n_{tracks} reconstructed tracks, and the former represents the probability that such particle is instead identified as a muon. The unfolded number of fake muon candidates expected to leak into the $\Lambda_b \to \Lambda_c^* \mu \bar{\nu}_\mu$ signal then reads:

$$n(\mu|h) = \sum_{i \in \text{ sample}} 10 \times \frac{P\left(\mu|h;p_i,\eta_i,n_{tracks,i}\right)}{P\left(h|h;p_i,\eta_i,n_{tracks,i}\right)} \times {}_s\mathcal{W}_i, \tag{7.14}$$

where the index i runs over the events of the sample. In the above formula, the factor 10 accounts for the difference in yield between the normal and the mis-ID stripping lines, which

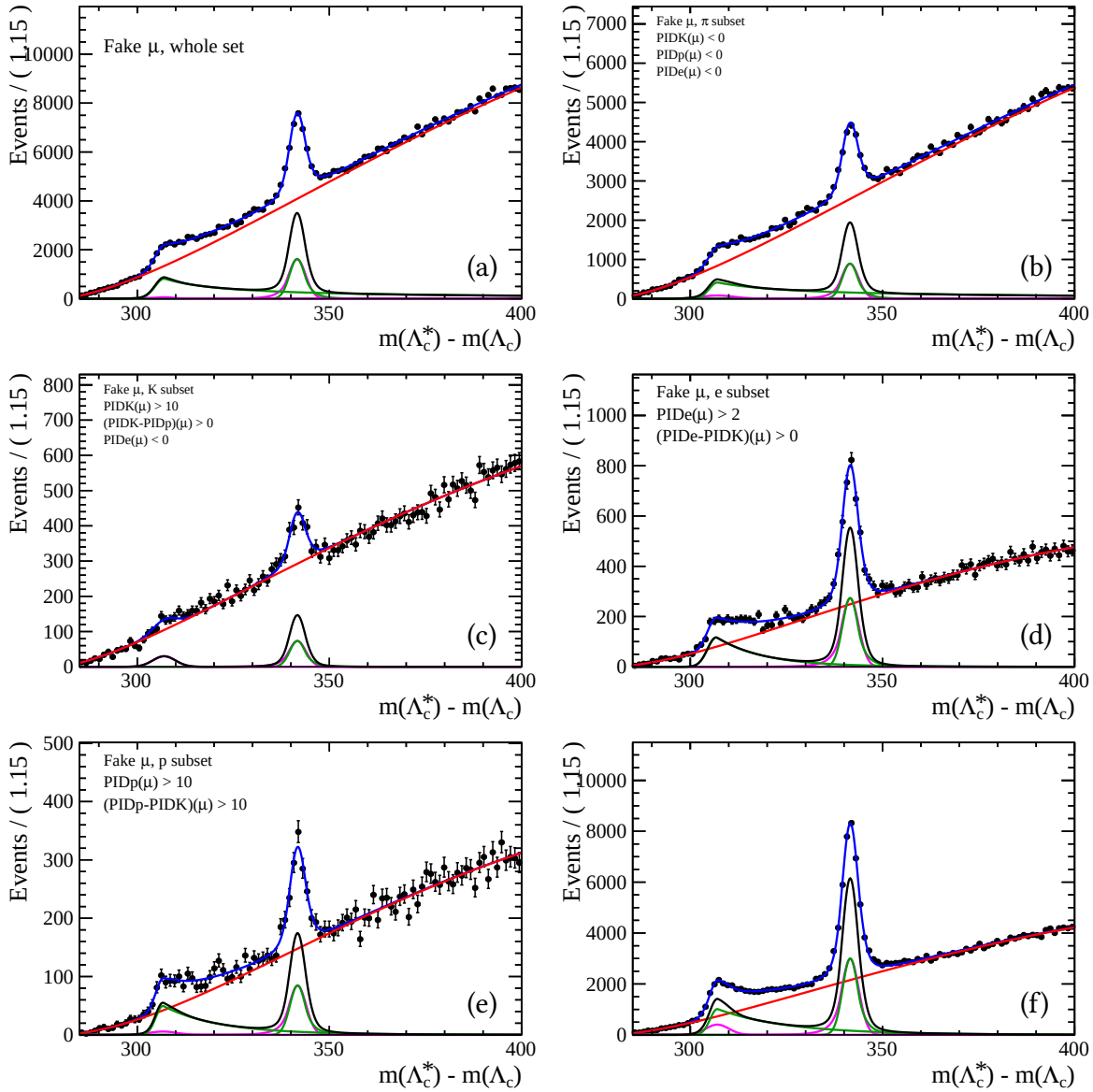

Figure 7.10: $\Delta m \equiv m_{\Lambda_c^*} - m_{\Lambda_c}$ distributions for the misidentified muon subsets listed in Table 7.4 (b–e), for the whole content of the mis-ID stripping line (a), and for the whole content of the normal stripping line (f). All events are required to pass the selection criteria listed in Table 7.3. Due to the very limited size of the sample, the K subset is fitted with a modified signal model, using a single Gaussian instead of a double Crystal Ball function to describe the Λ_c (2595) peak.

is pre-scaled by 10%. The following yields are then obtained:

$$n(\mu|\pi) = \sum_{i \in \pi \text{ sample}} 10 \times \frac{P_i(\mu|\pi)}{P_i(\pi|\pi)} \times {}_s\mathcal{W}_i = 1645 \pm 70 \quad \left(\text{fitted yield } 10 \times (23497 \pm 1000)\right) \tag{7.15}$$

$$n(\mu|K) = \sum_{i \in K \text{ sample}} 10 \times \frac{P_i(\mu|K)}{P_i(K|K)} \times {}_s\mathcal{W}_i = 259 \pm 22 \quad \left(\text{fitted yield } 10 \times (921 \pm 80)\right) \tag{7.16}$$

$$n(\mu|p) = \sum_{i \in p \text{ sample}} 10 \times \frac{P_i(\mu|p)}{P_i(p|p)} \times {}_s\mathcal{W}_i = 84 \pm 12 \quad \left(\text{fitted yield } 10 \times (1656 \pm 233)\right) \tag{7.17}$$

where the uncertainty is purely statistical, due to the size of the mis-ID data sample. Misidentified electrons are expected to contribute to the mis-ID background, but their yield could not be computed due to unavailability of $e^{\pm}$ calibration samples[3]. This contribution is nevertheless expected to be small, as electrons cannot decay in flight. The total contribution of all other misidentified particles amounts to $n(\mu|h) = 1988 \pm 74$, where the statistical errors were added in quadrature. This relates to the total signal yield via

$$R_{\text{mis-ID}} \equiv \frac{n(\mu|h)}{n_{sig}} = (3.89 \pm 0.23)\,\%, \tag{7.18}$$

where $n_{sig} = 51153 \pm 1132$ is the $\Lambda_b \to \Lambda_c^* \mu \bar{\nu}_\mu$ yield from the normal stripping line. This quantity is of the same order of magnitude of the ratio between $B \to D^* \tau \bar{\nu}_\tau$ and $B \to D^* \mu \bar{\nu}_\mu$ decays found in the LHCb measurement of $R(D^*)$ [6]. The ratio of $\Lambda_b \to \Lambda_c^* \tau \bar{\nu}_\tau$ and $\Lambda_b \to \Lambda_c^* \mu \bar{\nu}_\mu$ decays is expected to be similar. It is therefore crucial to find a way to distinguish $\Lambda_b \to \Lambda_c^* \tau \bar{\nu}_\tau$ signal from background events.

A systematic uncertainty on this result arises from the fact that ghost tracks, *i.e.* tracks composed of unrelated track segments in the tracking detectors, can pollute the mis-ID sample, and bias the PID variables. An estimate of this effect was obtained by repeating the study with an additional selection suppressing tracks with a ghost probability greater than 10%. The distribution of ghost probability for muon tracks passing all of the selection criteria listed in Section 7.2.2 is shown in Figure 7.11 for reference. Applying this additional requirement, the total mis-ID rate changes by 0.37%, amount that we assign as systematic uncertainty on $R_{\text{mis-ID}}$, obtaining:

$$R_{\text{mis-ID}} = \big(3.89 \pm 0.23\,(\text{stat}) \pm 0.37\,(\text{syst})\big)\,\%. \tag{7.19}$$

Further pollution is due to the possibility of misidentifying hadrons with each other. This

[3] At the time of this work. This contribution will be assessed in the coming months.

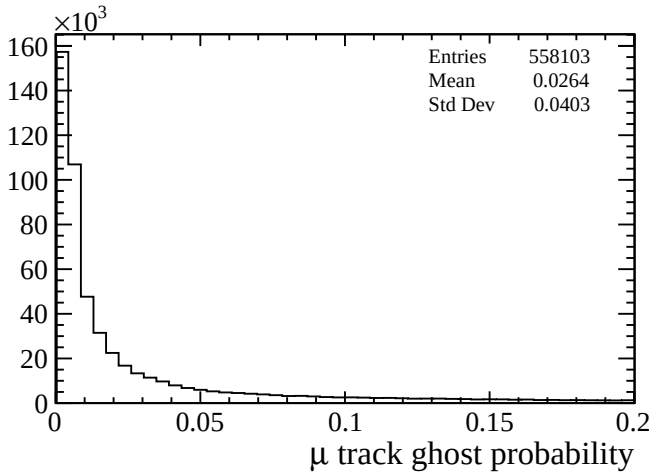

Figure 7.11: Ghost probability distribution of muon tracks passing the selection criteria listed in Table 7.3.

generates cross-feed of *e.g.* kaons or protons into the π sample, and so on. The same technique described above was used to assess the amount of fake signal yield due to mis-ID cross-feed. With the assumption that only pions, protons and kaons can be misidentified as a muon, the total amount of fake muons is given by:

$$\begin{aligned}
\begin{bmatrix} N_{\mu|\pi} \\ N_{\mu|K} \\ N_{\mu|p} \end{bmatrix} &= \begin{bmatrix} P_{\mu|\pi} & P_{\mu|\pi}P_{\pi|K} & P_{\mu|\pi}P_{\pi|p} \\ P_{\mu|K}P_{K|\pi} & P_{\mu|K} & P_{\mu|K}P_{K|p} \\ P_{\mu|p}P_{p|\pi} & P_{\mu|p}P_{p|K} & P_{\mu|p} \end{bmatrix} \cdot \begin{bmatrix} N_\pi \\ N_K \\ N_p \end{bmatrix} \\
&= \begin{bmatrix} P_{\mu|\pi}\left(N_\pi + P_{\pi|K}N_K + P_{\pi|p}N_p\right) \\ P_{\mu|K}\left(N_K + P_{K|\pi}N_\pi + P_{K|p}N_p\right) \\ P_{\mu|p}\left(N_p + P_{p|\pi}N_\pi + P_{p|K}N_K\right) \end{bmatrix} \\
&\equiv \begin{bmatrix} n(\mu|\pi) + n\big(\mu\big|\,(\pi|K)\big) + n\big(\mu\big|\,(\pi|p)\big) \\ n(\mu|K) + n\big(\mu\big|\,(K|\pi)\big) + n\big(\mu\big|\,(K|p)\big) \\ n(\mu|p) + n\big(\mu\big|\,(p|\pi)\big) + n\big(\mu\big|\,(p|K)\big) \end{bmatrix},
\end{aligned} \tag{7.20}$$

where:

- N_h is the amount of h particles found in the mis-ID stripping line,
- $N_{\mu|h}$ is the expected yield of muon candidates resulting from a misidentified h,
- the $P_{h'|h}$ symbol denotes the probability that a particle h is reconstructed as h',
- and the $n\big(\mu\big|\,(h'|h)\big)$ terms, with $h, h' \in \{\pi, K, p\}$, are cross-feed yields.

The following yields are found:

$$n\big(\mu\big|\,(\pi|K)\big) = 7.4 \pm 0.6 \tag{7.21}$$
$$n\big(\mu\big|\,(\pi|p)\big) = 6.0 \pm 0.8 \tag{7.22}$$
$$n\big(\mu\big|\,(K|\pi)\big) = 6.6 \pm 0.3 \tag{7.23}$$
$$n\big(\mu\big|\,(K|p)\big) = 27 \pm 4 \tag{7.24}$$
$$n\big(\mu\big|\,(p|\pi)\big) = 1.50 \pm 0.06 \tag{7.25}$$
$$n\big(\mu\big|\,(p|K)\big) = 0.20 \pm 0.02, \tag{7.26}$$

for a total contribution of

$$\sum_{h,h' \in \{\pi,K,p\}} n\big(\mu\big|\,(h'|h)\big) = 49 \pm 4 \tag{7.27}$$

candidates, where the statistical errors were added in quadrature. In the most pessimistic scenario, this adds $(0.010 \pm 0.001)\,\%$ to the total mis-ID rate. In fact, cross-feed yields do not add up linearly. For example, pions that feed into the reconstructed K sample and are subsequently taken as muons do not contribute to $n\,(\mu|\pi)$ directly. Therefore, we add the cross-feed yield as additional, negligible systematic uncertainty on the mis-ID yield, obtaining:

$$R_{\text{mis-ID}} = \big(3.89 \pm 0.23\,(\text{stat}) \pm 0.38\,(\text{syst})\big)\%. \tag{7.28}$$

Once the expected amount of fake muons contributing to the $\Lambda_b \to \Lambda_c^* \mu \bar{\nu}_\mu$ yield has been calculated, this background can be controlled by using the ${}_s\mathcal{P}lot$ technique to construct templates of the variables to fit in order to discriminate between $\Lambda_b \to \Lambda_c^* \tau \bar{\nu}_\tau$ and $\Lambda_b \to \Lambda_c^* \mu \bar{\nu}_\mu$. Distributions of the various fit variables observed in the sample of fake muons are ${}_s\mathcal{W}eight$-ed in order to emulate the properties of those events where the fake muon is associated to a Λ_c^* as decay products of a Λ_b candidate. The shape of the resulting distributions is shown in Figure 7.12, compared to that of simulated $\Lambda_b \to \Lambda_c^* \tau \bar{\nu}_\tau$ decays. As for $\tau - \mu$ separation in Figure 7.8, a good discriminating power is observed for all variables, except the muon impact parameter. These templates will be included in the fit model described in Eqn. 7.13 together with the measured constraint on $R_{\text{mis-ID}}$.

It is important to note that non-Λ_c^* background can skew the ${}_s\mathcal{P}lot$-ted distributions. This effect can be assessed by repeating the procedure discussed here to extract the templates with a different binning in $m_{\Lambda_c^*}$, or for example using a shorter range in mass for the Λ_c^* mass fit shown in Figure 7.10 excluding the right-hand side sideband. The different shape of the templates obtained this way can be assigned as systematic uncertainty.

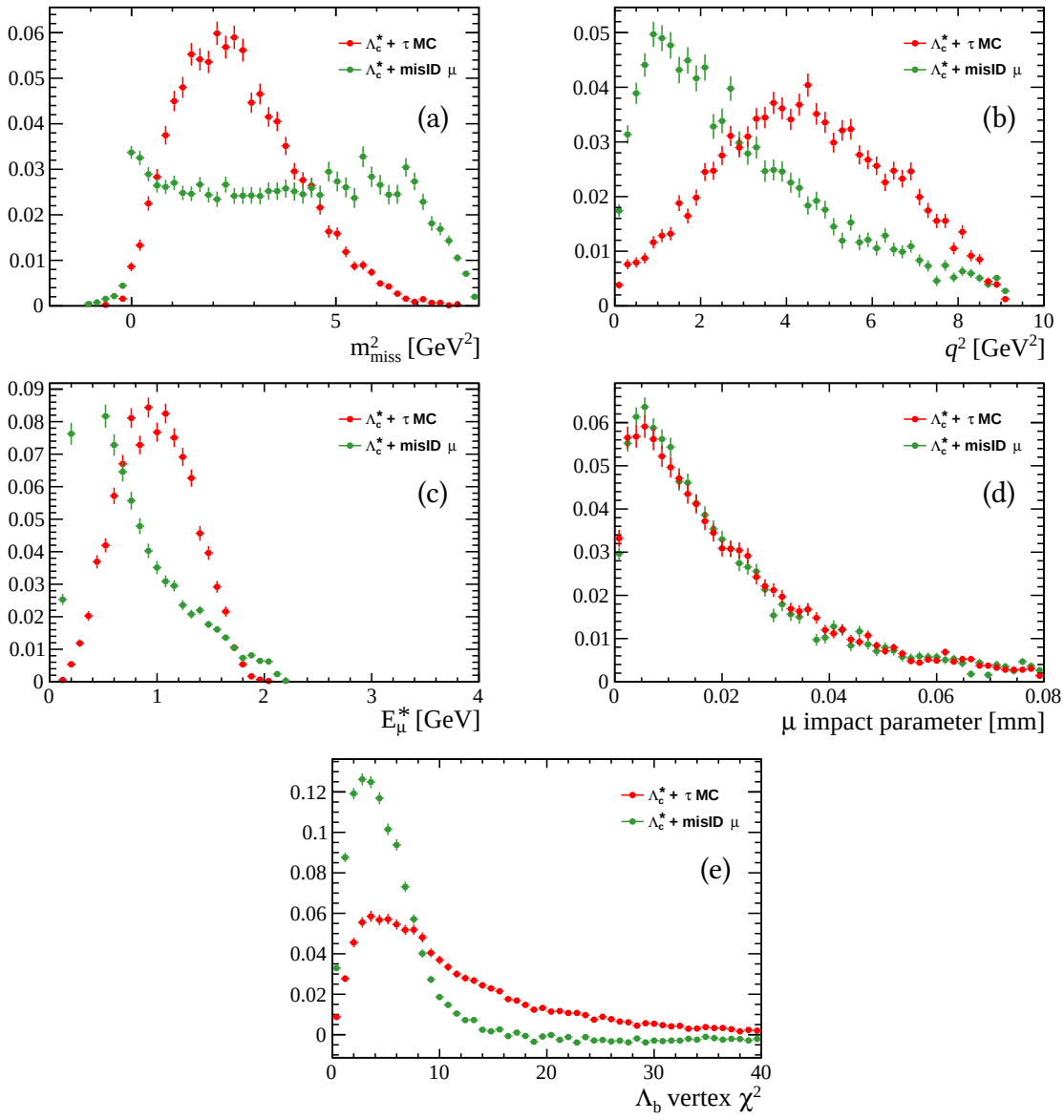

Figure 7.12: Distribution of the τ–μ discriminating variables described in Section 7.2.1 for $sWeight$-ed events with a fake muon (green) *vs.* a simulated sample of reconstructed $\Lambda_b \to \Lambda_c^* \tau \bar{\nu}_\tau$ decays (red).

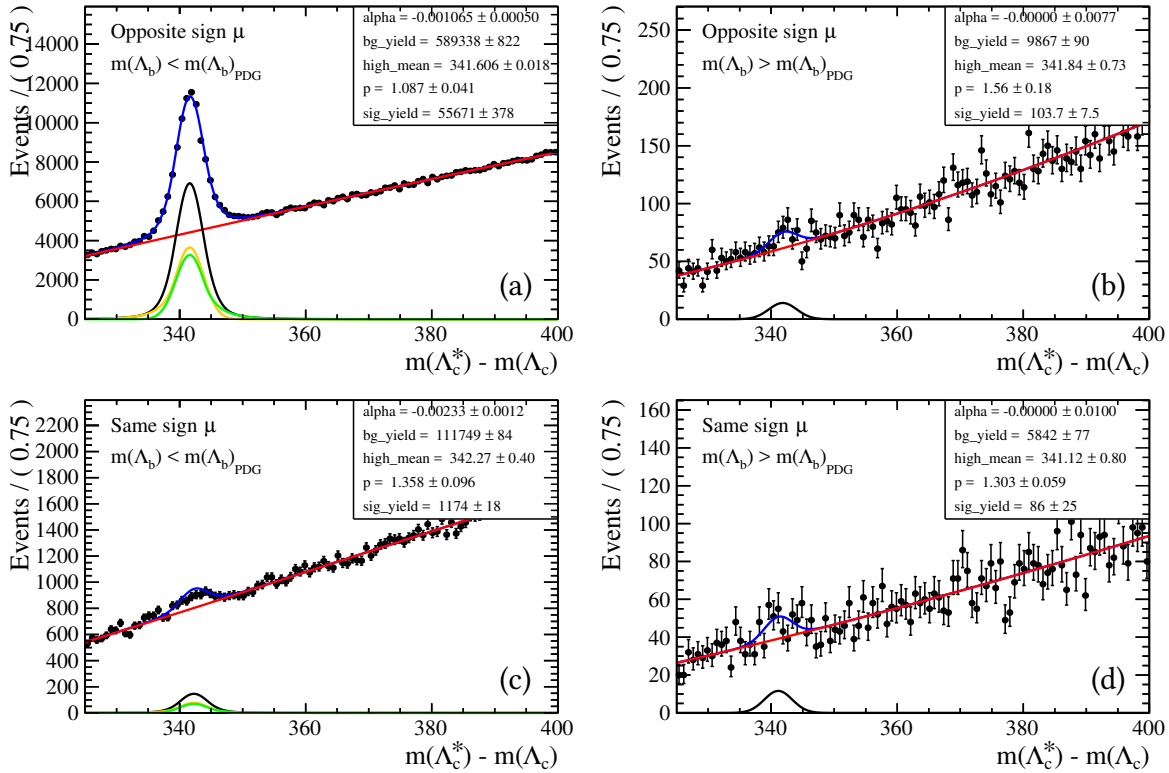

Figure 7.13: Δm distributions for: $\Lambda_c^{*+}\mu^-$ pairs with $m_V < m_{\Lambda_b}$ (a); $\Lambda_c^{*+}\mu^-$ pairs with $m_V > m_{\Lambda_b}$ (b); $\Lambda_c^{*+}\mu^+$ pairs with $m_V < m_{\Lambda_b}$ (c); $\Lambda_c^{*+}\mu^+$ pairs with $m_V > m_{\Lambda_b}$ (d). The m_V symbol denotes the mass of the $\Lambda_c^*\mu$ pair.

7.4. Background from random track combinations

The amount of combinatorial background can be assessed examining a sample of wrong-sign $\Lambda_c^{*+}\mu^+$ combinations. This type of background arises when a reconstructed particle compatible with a Λ_c^* and a muon track are associated to the same Λ_b decay, but in fact they were generated in unrelated processes. Therefore, this background can be modeled by associating particles which cannot be produced in a single $\Lambda_b \to \Lambda_c^*\mu\bar{\nu}_\nu$ decay, but that give rise to a Λ_b candidate when combined. By constructing Λ_b candidates from same-sign daughters one fulfills this requirement. Another possibility is to look for unphysical Λ_b candidates, *i.e.* candidates with a visible mass m_V larger than the Λ_b mass.

The following strategy has been adopted:

1. Estimate the amount of combinatorial background leaking into the $\Lambda_b \to \Lambda_c^*\mu\bar{\nu}_\mu$ signal by fitting Δm peaks in a sample of same-sign candidates in the physical m_V region.

2. Use the portion of data with visible mass larger than m_{Λ_b} to establish a relation between the same-sign $\Lambda_c^{*+}\mu^+$ and opposite-sign $\Lambda_c^{*+}\mu^-$ yields.

3. Combine the two above results in order to estimate the total amount of combinatorial

candidates.

As for the mis-ID case, the parameters of the double Crystal Ball model describing the Λ_c^* mass peaks are extracted by a fit to Montecarlo simulated data, shown in Figure 7.9. In this case, however, the data sample from collision data is rather small. It is therefore more convenient to focus only on the $\Lambda_c(2625)$ state, which has a more prominent yield. We assume, for this study, that the ratio between the $\Lambda_c(2595)$ and $\Lambda_c(2625)$ yield is the same for signal and combinatorial background. The resulting Δm distribution and the corresponding fits are shown in Figure 7.13. The following amount of combinatorial background leaking into the Λ_c^* peaks can be extracted from the fit to the different components:

- opposite sign $\Lambda_c^{*+}\mu^-$ combinations, $m_V > m_{\Lambda_b}$: 104 ± 8 candidates
- same sign $\Lambda_c^{*+}\mu^+$ combinations, $m_V > m_{\Lambda_b}$: 86 ± 25 candidates
- same sign $\Lambda_c^{*+}\mu^+$ combinations, $m_V < m_{\Lambda_b}$: 1174 ± 18 candidates
- opposite sign $\Lambda_c^{*+}\mu^-$ combinations, $m_V < m_{\Lambda_b}$ (signal): 55671 ± 378 candidates

In the physical $m_V < m_{\Lambda_b}$ region, the same sign yield is measured to be $(2.11 \pm 0.04)\,\%$ of the signal. In the unphysical $m_V > m_{\Lambda_b}$ region, the ratio between $\Lambda_c^{*+}\mu^-$ random combinations and $\Lambda_c^{*+}\mu^+$ random combinations is (1.2 ± 0.4). Therefore, we expect a combinatorial background yield contributing

$$R_{\text{comb}} = (1.2 \pm 0.4) \times (2.11 \pm 0.04)\,\% = (2.5 \pm 0.8)\,\% \tag{7.29}$$

of the $\Lambda_b^0 \to \Lambda_c^{*+}\mu^-\bar{\nu}_\mu$ candidates in the physical signal region.

The sample of same sign $\Lambda_c^{*+}\mu^+$ combinations has been checked for contributions due to misidentified muons. Using the same technique described in Section 7.3, data from the mis-ID stripping line has been partitioned into the three categories of combinatorial background listed above. Via a fit to the Δm distribution for the various samples (Figure 7.14) and using the $\mathcal{sP}lot$ technique combined to the PID tables, the results listed in Table 7.5 were found, for a total combinatorial mis-ID yield of:

- $R_{\text{mis-ID}} = (1.40 \pm 0.01)\,\%$ in the same sign, $m_V < m_{\Lambda_b}$ sample;
- $R_{\text{mis-ID}} = (5.67 \pm 0.06) \times 10^{-4}$ in the opposite sign, $m_V > m_{\Lambda_b}$ sample;
- $R_{\text{mis-ID}} = (3.81 \pm 0.05) \times 10^{-4}$ in the same sign, $m_V > m_{\Lambda_b}$ sample,

where the $n(\mu|h)$ contributions and the $n\big(\mu|\,(h|h')\big)$ cross-feed contributions have been conservatively added together. While the mis-ID contributions to the unphysical $m_V > m_{\Lambda_b}$ samples are negligible with respect to the signal yield uncertainty due to the Δm fit, the mis-ID contribution to the same sign sample with $m_V < m_{\Lambda_b}$ is of the same order of magnitude

	$m_V < m_{\Lambda_b}$, $\Lambda_c^{*\pm}\mu^{\pm}$	$m_V > m_{\Lambda_b}$, $\Lambda_c^{*\pm}\mu^{\mp}$	$m_V > m_{\Lambda_b}$, $\Lambda_c^{*\pm}\mu^{\pm}$
$n\left(\mu\middle\vert K\right)/n_{sig}$	$(3.79 \pm 0.03) \times 10^{-3}$	$(1.33 \pm 0.01) \times 10^{-4}$	$(7.5 \pm 0.1) \times 10^{-5}$
$n\left(\mu\middle\vert \pi\right)/n_{sig}$	$(1.005 \pm 0.009) \times 10^{-2}$	$(3.87 \pm 0.03) \times 10^{-4}$	$(2.90 \pm 0.03) \times 10^{-4}$
$n\left(\mu\middle\vert p\right)/n_{sig}$	$(8.8 \pm 0.1) \times 10^{-6}$	$(2.79 \pm 0.08) \times 10^{-5}$	$(9.3 \pm 0.7) \times 10^{-6}$
$n\big(\mu\big\vert \left(\pi\middle\vert K\right)\big)/n_{sig}$	$(3.60 \pm 0.03) \times 10^{-5}$	$(2.0 \pm 0.3) \times 10^{-6}$	$(1.8 \pm 0.2) \times 10^{-7}$
$n\big(\mu\big\vert \left(\pi\middle\vert p\right)\big)/n_{sig}$	$(1.88 \pm 0.01) \times 10^{-5}$	$(3.6 \pm 0.7) \times 10^{-7}$	$(4 \pm 1) \times 10^{-7}$
$n\big(\mu\big\vert \left(K\middle\vert p\right)\big)/n_{sig}$	$(1.25 \pm 0.02) \times 10^{-5}$	$(1.37 \pm 0.05) \times 10^{-5}$	$(4.8 \pm 0.5) \times 10^{-6}$
$n\big(\mu\big\vert \left(K\middle\vert \pi\right)\big)/n_{sig}$	$(5.91 \pm 0.05) \times 10^{-5}$	$(2.74 \pm 0.04) \times 10^{-6}$	$(8.9 \pm 0.2) \times 10^{-7}$
$n\big(\mu\big\vert \left(p\middle\vert K\right)\big)/n_{sig}$	$(7.63 \pm 0.03) \times 10^{-7}$	$(2 \pm 3) \times 10^{-8}$	$(8 \pm 5) \times 10^{-9}$
$n\big(\mu\big\vert \left(p\middle\vert \pi\right)\big)/n_{sig}$	$(8.14 \pm 0.07) \times 10^{-6}$	$(4.66 \pm 0.09) \times 10^{-7}$	$(4.6 \pm 0.1) \times 10^{-7}$

Table 7.5: Fraction of fake muons and cross-feed contributions in the three samples of combinatorial background: same sign combinations in the physical region, and same sign and opposite sign combinations in the unphysical region.

as the uncertainty on the $\Lambda_c^{*+}\mu^-$ yield. Therefore, the interplay between imperfect particle identification and erroneous combination of unrelated tracks generates an uncertainty of about 0.8% on the measured rate of combinatorial background. We get, therefore:

$$R_{\text{comb}} = \big(2.5 \pm 0.8\,(\text{stat}) \pm 0.8\,(\text{syst})\big)\%. \tag{7.30}$$

As for the mis-ID background, it would prove useful to extract templates of the fit variables from events where the Λ_b candidate is constructed from a combinatorial set of particles. However, the small size of the combinatorial sample found in 2015+2016 data makes it difficult to construct reliable templates. It will most likely be possible to add $f_{\text{comb}}(\mathbf{x})$ probability density functions to the fit model discussed in Section 7.2.1 once the full dataset from the LHCb Run II becomes available, after the end of data taking in 2018.

7.5. Strategy to assess the physics backgrounds

Downfeed from higher mass Λ_c^* states, and Λ_b decays to doubly charmed final states, are the main physics processes that can pollute the data sample for the measurement of $R\left(\Lambda_c^*\right)$.

Decays of the type $\Lambda_b \to \Lambda_c^{**}\left(\to \Lambda_c^* X\right)\ell\bar{\nu}_\ell$ are referred to as feeddown. Due to isospin conservation, Λ_c^{**} states are expected to decay into $\Lambda_c\,(2595)$ or $\Lambda_c\,(2625)$ only with the emission of two accompanying pions, resulting in $\Lambda_c^{**} \to \Lambda_c^*\pi^+\pi^-$ or $\Lambda_c^{**} \to \Lambda_c^*\pi^0\pi^0$, with similar probabilities. This decay has never been observed, but it is in principle allowed in the Standard Model. Unfortunately, the large amount of slow pions produced in every pp collision make it computationally difficult to perform a direct search of such rare Λ_c^{**} events in data. A different approach can be adopted, using the available Montecarlo samples of $\Lambda_c\,(2595)$ and $\Lambda_c\,(2625)$ and following the approach of the LHCb $|V_{ub}|$ analysis [32]. Here, the so-called

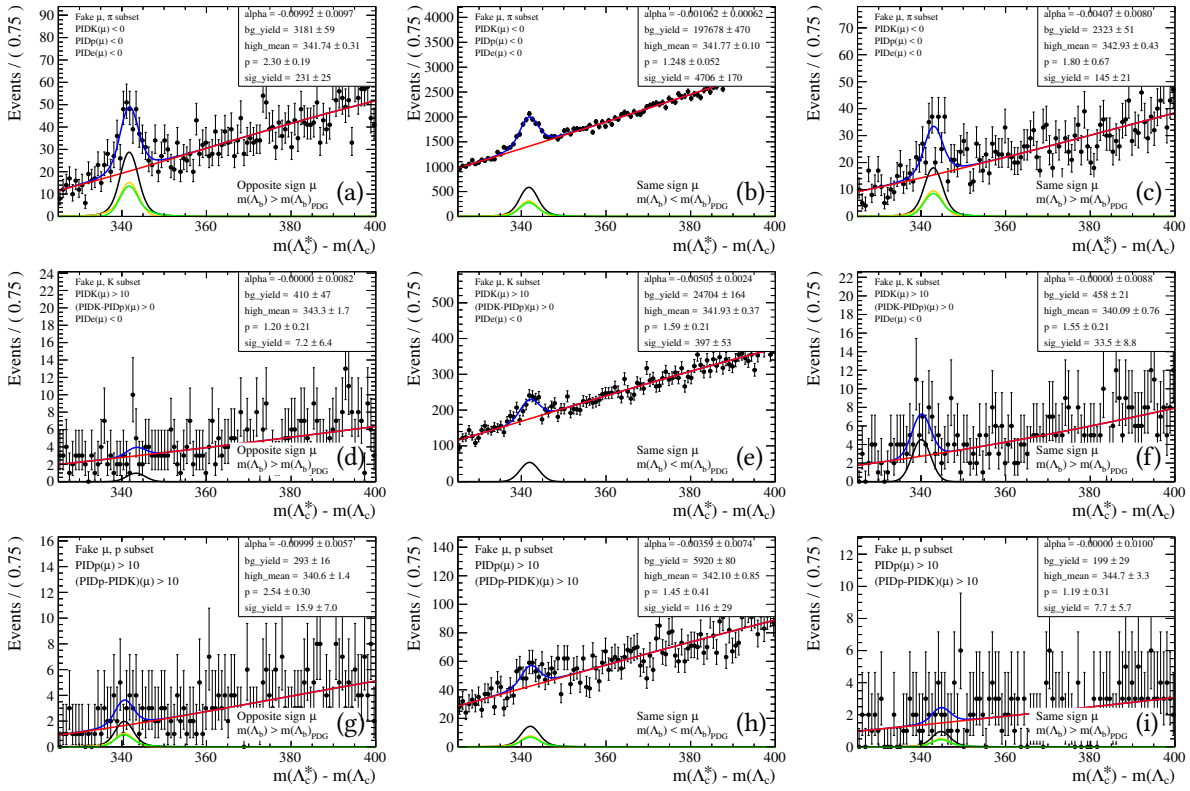

Figure 7.14: Δm distributions for: $\Lambda_c^{*+}\mu^-$ pairs with $m_V > m_{\Lambda_b}$ (a, d, g); $\Lambda_c^{*+}\mu^+$ pairs with $m_V < m_{\Lambda_b}$ (b, e, h); $\Lambda_c^{*+}\mu^+$ pairs with $m_V > m_{\Lambda_b}$ (c, f, i). The three rows correspond to different samples of particles misidentified as muons: pions (a, b, c), kaons (d, e, f) and protons (g, h, i).

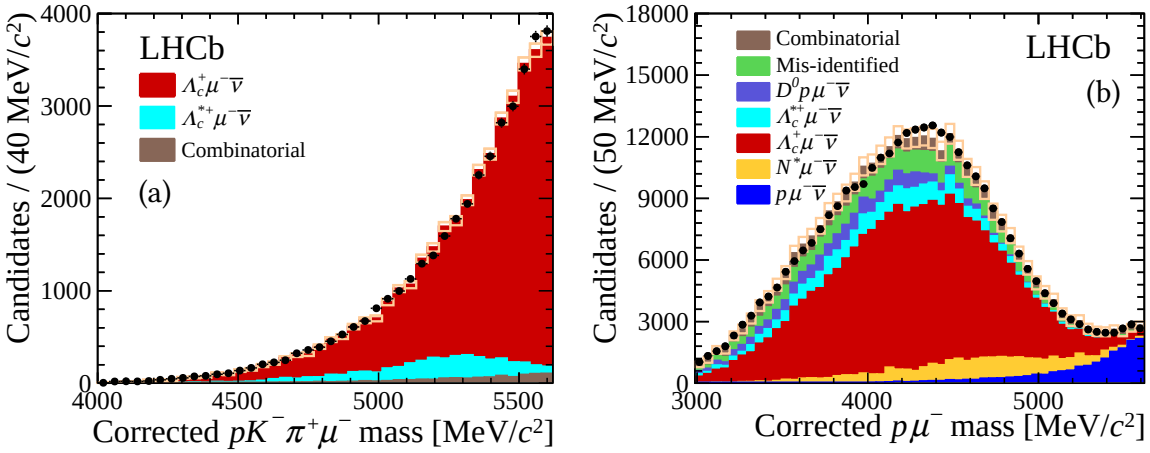

Figure 7.15: Fit to $M_{corr}\,(pK\pi\mu)$ to determine the number of $\Lambda_b \to \Lambda_c\mu\bar{\nu}_\mu$ candidates (a), and fit to $M_{corr}\,(p\mu)$ to obtain the ratio of $\Lambda_b \to p\mu\bar{\nu}_\mu$ to $\Lambda_b \to \Lambda_c\mu\bar{\nu}_\mu$ decays (b) aimed at the measurement of the $|V_{ub}|^2/|V_{cb}|^2$ ratio [32].

corrected mass [33] is used to discriminate between various Λ_b decay modes. The corrected mass, defined as

$$M_{corr}\left(\Lambda_b\right) \equiv \sqrt{m_V^2 + p_\perp^2} + p_\perp\,, \tag{7.31}$$

where m_V as usual represents the invariant mass of the visible decay products, corresponding to the mass of the Λ_b taking into account a single missing particle, which is massless and travels orthogonally to the flight direction of the Λ_b. This quantity will peak at the true mass of the Λ_b if no other particles are involved in the event, and will distribute around lower values if there are other unreconstructed decay products. Figure 7.15 demonstrates the use of M_{corr} to distinguish $\Lambda_b \to \Lambda_c\mu\bar{\nu}_\mu$, $\Lambda_b \to \Lambda_c^*\mu\bar{\nu}_\mu$, $\Lambda_b \to p\mu\bar{\nu}_\mu$ and background decays in [32].

In the case of the $R\left(\Lambda_c^*\right)$ analysis, the Λ_c^{**} yield can be assessed by fitting $M_{corr}\left(\Lambda_c^*\mu\right)$ with a model $\mathcal{M}$ containing Λ_c^* and Λ_c^{**} contributions:

$$\mathcal{M}\left(m\right) = N_{\Lambda_c^*}\left[M_{\Lambda_c^*}\left(m\right) + R_{\Lambda_c^{**}}M_{\Lambda_c^{**}}\left(m\right) + \sum_i R_i M_i\left(m\right)\right] \tag{7.32}$$

where $m \equiv M_{corr}\left(\Lambda_c^*\mu\right)$ and the index i runs over the possible backgrounds, some of which have been constrained in the previous sections. The shape of $M_{\Lambda_c^*}$ can easily be obtained from simulation. However, as Λ_c^{**} Montecarlo samples are not available, one must construct a template for $M_{\Lambda_c^{**}}$ in some other way. A viable option is to emulate the absence of the two unreconstructed pions by building $\Lambda_b \to \Lambda_c\mu\bar{\nu}_\mu$ candidates from a sample of Montecarlo data containing only $\Lambda_b \to \Lambda_c^*\mu\bar{\nu}_\mu$ events.

The M_{corr} shape can suffer from pollution from the $\Lambda_b \to \Lambda_c^*\tau\bar{\nu}_\tau$ signal and from the $\Lambda_b \to \Lambda_c^*X_c$ background. However, with the purpose of estimating the Λ_c^{**} yield, one can

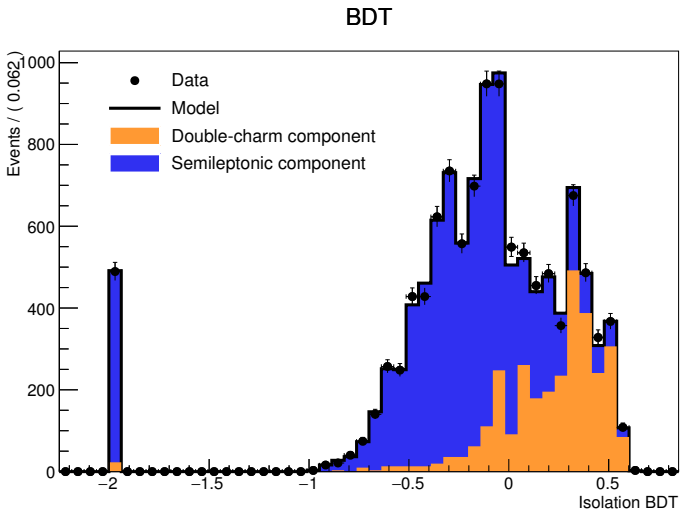

Figure 7.16: Value of the highest isolation BDT response for a mixed sample of pseudoexperiments sampled from $\Lambda_b \to \Lambda_c^* \mu \bar{\nu}_\mu$ and $\Lambda_b \to \Lambda_c^* X_c$ probability density functions obtained from simulation, fitted with templates from Montecarlo simulated $\Lambda_b \to \Lambda_c^* \mu \bar{\nu}_\mu$ and $\Lambda_b \to \Lambda_c^* X_c$ decays.

apply tight cuts on the fit quality of the Λ_b vertex and on the muon transverse momentum, allowing to decrease τ and X_c pollution to a negligible level.

The characteristics and yield of background from $\Lambda_b \to \Lambda_c^* X_c$ decays can be studied by comparing Montecarlo simulated events and collision data. A direct search in data for *e.g.* $\Lambda_b \to \Lambda_c^* D_s \left(\to \phi \mu \bar{\nu}_\mu\right)$ or other semileptonic decays of charmed mesons produced in a $\Lambda_b \to \Lambda_c^* X_c$ transition is unfeasible due to the very small number of such events expected in the 2015+2016 LHCb dataset. The strategy to measure R_{X_c} and to obtain fit variable templates f_{X_c} is therefore twofold.

Fit variable shapes f_{X_c}. The probability density functions can be obtained from Montecarlo simulated events. Currently, a limited sample of $\Lambda_b \to \Lambda_c^* X_c$ has been made available.

Double charm background rate R_{X_c}. This type of background is expected to closely resemble the event kinematics of a $\Lambda_b \to \Lambda_c^* \tau \bar{\nu}_\tau$ decay, and it is therefore the most difficult to determine based on the shape of the fit observables. It needs more careful treatment, with an accurate constraint on the expected double charm yield to be provided to the fit model in Eqn. 7.13. This can be achieved by constructing a data sample enriched in $\Lambda_c^* X_c$ content. Observables extracted from this sample can then be fitted with a model taking into account the expected shapes from $\Lambda_c^* \mu$, $\Lambda_c^* \tau$ and $\Lambda_c^* X_c$ Montecarlo samples, and templates obtained mis-ID and combinatorial background as well as from non-Λ_c^* background, *i.e.* events that do not contribute to the Λ_c^* mass peaks.

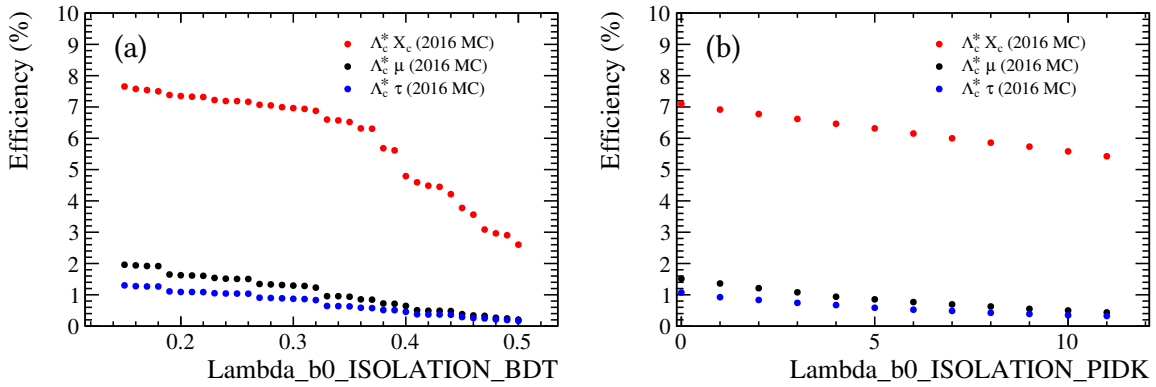

Figure 7.17: $\Lambda_c^*\mu$, $\Lambda_c^*\tau$ and $\Lambda_c^*X_c$ selection efficiency as a function of the highest isolation BDT response (a) and of the PID-kaon classifier response associated to the track with the highest BDT output (b), evaluated on Montecarlo samples.

A data sample enriched in $\Lambda_b \to \Lambda_c^* X_c$ decays can be obtained from data by designing an appropriate selection. Events containing the decay of a c-meson generally contain more charged tracks than those where the Λ_c^* is generated together with a only muon. A multivariate boosted decision tree (BDT) was developed to identify these events for the LHCb $R(D^*)$ analysis [6, 34]. This classifier is referred to as "isolation BDT". The BDT is trained to distinguish tracks coming from the same decay as the reconstructed Λ_b candidate, or from any other decay or from the primary collision, with a response going from -1 (track not associated with the Λ_b) to +1 (track associated with the Λ_b). It uses input variables related to the compatibility of the track with the Λ_b vertex, and to the angle between the Λ_b flight direction and the track considered. The BDT is applied to all of the reconstructed tracks in the event, excluding those used to construct the Λ_b candidate. By construction, in case of a candidate built from an $\Lambda_c^*\mu$ pair where the muon comes from the decay of a charmed meson, the event contains other tracks from the X_c decay that are topologically close to the Λ_b candidate and have a large BDT response. The value of the maximum BDT response in the event can be used as discriminant between events with additional tracks mistakingly not associated to the Λ_b candidates, and pure signal events. This classifier was trained with mesonic decays, but it was found efficient in distinguishing between $\Lambda_b \to \Lambda_c^*\mu\bar{\nu}_\mu$ and $\Lambda_b \to \Lambda_c^* X_c$ decays even without additional re-training on a sample of hadronic decays. Figure 7.16 demonstrates the discriminant power of this variable on a sample of pseudoexperiments containing both $\Lambda_b \to \Lambda_c^*\mu\bar{\nu}_\mu$ and $\Lambda_b \to \Lambda_c^* X_c$ contributions.

The isolation BDT can not only be used to discriminate authentic $\Lambda_c^*\mu$ signal, but also, conversely, to build a data sample enriched in $\Lambda_b \to \Lambda_c^* X_c$ decays. The selection efficiency for semimuonic, semitauonic and doubly charmed Λ_b decays has been evaluated on simulated data as a function of the highest BDT response and of the PID-kaon classifier response associated to the track with the highest BDT output, and it is shown in Figure 7.17.

A sample of data obtained with the requirement that the higher isolation BDT response is

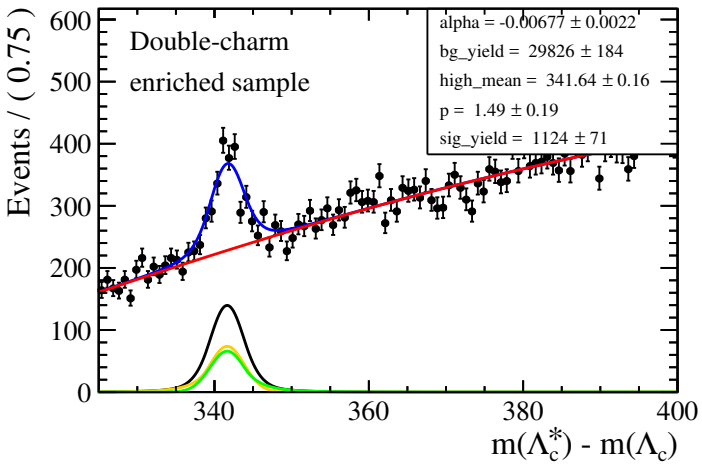

Figure 7.18: A sample of double charm enriched data obtained using `ISOLATION_BDT > 0.36 && ISOLATION_PIDK > 5`. The selected sample exhibits a Λ_c^* peak, which is fitted with a double Crystal Ball function as explained in Section 7.3.

larger than 0.36 and that the PID-kaon classifier response for the track most associated to the signal is larger than 5, on top of the signal selections discussed in Section 7.2.2, is shown in Figure 7.18, where a Λ_c^* mass peak is clearly visible and it has been fitted with the same model discussed in Section 7.3.

Observables extracted from this sample by means of the *sPlot* technique can then be modelled with a probability density function including all the contributions discussed above. Due to the smallness and limited purity of this sample, though, the determination of the R_{X_c} rate will especially benefit from increased statistical relevance when the full Run II dataset is analysed.

7.6. Conclusions and prospects

The $R(D^{(*)})$ puzzle sparked great interest in the particle physics community, with the combined tension of 4.1 σ between the measurements performed by the BaBar, Belle and LHCb experiments [1–7] and the value predicted by the Standard Model [10, 11]. A complementary measurement in the baryonic sector such as $R(\Lambda_c^*)$, with a complex spin structure, would allow to confirm or disprove the tension, and to probe possible New Physics contributions in the tensor sector.

In this work, a strategy to perform the $R(\Lambda_c^*)$ measurement at LHCb has been developed. The common $\Lambda_c^*\mu$ visible final state allows to directly determine the ratio of $\Lambda_b \to \Lambda_c^*\tau\bar{\nu}_\tau$ to $\Lambda_b \to \Lambda_c^*\mu\bar{\nu}_\mu$ decays, by means of a fit to a combination of kinematic observables sensitive to the decay topology and to the momentum of the unreconstructed neutrino(s).

The measurement of $R(\Lambda_c^*)$ requires a careful modelling of background processes. Strategies to deal with accidental background, and background from other physics processes, are

defined. In particular, the yield and kinematic characteristics of fake signal events due to particles incorrectly identified as muons have been analysed in detail, as well as the rate of background events due to random combination of tracks. Then, the necessary steps to assess the characteristics and statistical importance of other physics processes that could leak into the $\Lambda_b \to \Lambda_c^* \ell \bar{\nu}_\ell$ signal sample are discussed.

The full Run II dataset, including the 2017 and 2018 data taking periods, will enable LHCb to determine the $R\left(\Lambda_c^*\right)$ ratio. Similar techniques can be used to undertake the complementary $R\left(\Lambda_c\right)$ measurement.

Standard Model predictions for the value of $R\left(\Lambda_c^*\right)$ are not yet available, at the time of this thesis. The next Chapter will provide the necessary ingredients to measure the parameters needed to calculate such prediction.

CHAPTER 8

$\Lambda_b \to \Lambda_c^* \ell \bar{\nu}_\ell$ form factors

Contents

The interest for a study of Lepton Universality using the hadronic decays $\Lambda_b \to \Lambda_c \ell \bar{\nu}_\ell$ and $\Lambda_b \to \Lambda_c^* \ell \bar{\nu}_\ell$ has been motivated in Chapter 7. These semileptonic decays include a hadronic-level transition $\Lambda_b \to \Lambda_c^{(*)}$, whose matrix element cannot be analytically calculated. However, this transition can be factorised into short-distance contributions, embedded in the Wilson coefficients [35], and long-distance effects. The latter can be theoretically described by using form factors, perturbative expressions of which can be calculated under certain assumptions.

The decay involving the ground state charmed hadron Λ_c has been theoretically characterized in [17] using lattice QCD. In addition, the LHCb collaboration measured the parameters of the $\Lambda_b \to \Lambda_c$ form factors by measuring the differential decay rate $d\Gamma\left(\Lambda_b \to \Lambda_c \mu \bar{\nu}_\mu\right)/dq^2$ [21]. The form factors for the transition between the Λ_b and the excited states $\Lambda_c(2595)$ and $\Lambda_c(2625)$ have been parametrized in [36]; however, in that work the lepton mass was neglected, making it impossible to calculate a SM expectation for the value of the $R\left(\Lambda_c^*\right)$ ratios.

This Chapter presents a study aimed at making the calculation of such ratios possible. This work has been published in [37]. Section 8.1 presents a helicity decomposition of the $\Lambda_b \to \Lambda_c^*$ matrix element, that is convenient in describing the decay observables measurable at LHCb, such as the kinematic spectra and the $R\left(\Lambda_c^*\right)$ ratio, and for controlling the theoretical uncertainty on the SM expectation of $R\left(\Lambda_c^*\right)$. Then, Section 8.2 describes a sensitivity study for a measurement of the form factor parameters. The precision that the LHCb experiment

can achieve in measuring the parameters of the IW functions is evaluated by means of pseudoexperiments. This result is then used to estimate the experimental contribution to the uncertainty of a theoretical prediction of $R\left(\Lambda_c^*\right)$.

8.1. Parametrisation of the form factors

The transition from a quark-level decay such as $b \to c\ell\bar{\nu}_\ell$ to a hadronic final state (Λ_c^*), called hadronisation, suffers from non-perturbative QCD contributions which are difficult to calculate. Therefore, hadronic form factors are introduced, as a way to describe the hadronisation process between a given initial and final state. Form factors are perturbative functions of the process kinematics that parametrize the hadronic matrix element of the examined transition.

A significant theoretical effort has been put into developing methods to compute hadronic form factors. An example of such method is the Heavy Quark Effective Theory (HQET) [35], which is well established for mesonic $B \to D$ transitions. In HQET, heavy quarks are treated as having an infinite mass, and an effective theory is constructed by expanding around this so-called *heavy-quark limit*. This approximation is appropriate for $\Lambda_b \to \Lambda_c^*$ transitions, as both the b and c quarks have a mass larger than the typical QCD scale $\Lambda_{QCD} \approx 250$ MeV. In analogy with elecrodynamics, the heavy quark is treated as a stationary point-like source of color charge; light quarks interact with the color potential induced by the heavy quark. Assuming that the decay of the heavy quark into another heavy quark does not change the potential interacting with the light quark, form factors can be calculated to describe the hadron-level transition. This assumption works particularly well when the velocity transfer $\Delta v = v' - v$, where v and v' are the velocities of the initial and final state quarks, is small. Corrections to the heavy-quark limit are suppressed by powers of $1/m$, where m is the mass of the heavy quark.

8.1.1. Form factors for $\Lambda_b \to \Lambda_c^*$ transitions

The form factors, denoted $f_i(q^2)$ and $F_i(q^2)$ for vector transitions to the Λ_c (2595) and Λ_c (2625) states, respectively, and $g_i(q^2)$ and $G_i(q^2)$ for axialvector transitions, arise from a Lorentz decomposition of the $\Lambda_b \to \Lambda_c^*$ hadronic matrix elements onto a basis of Dirac structures

$\left\{\Gamma^{(i)}_{\mu\alpha}\right\}$:

$$\langle \Lambda_c\,(2595)|\,\bar{c}\gamma_\mu b\,|\Lambda_b\rangle = \sum_i f_i(q^2)\bar{u}^{\alpha}_{c,1/2}(k)\Gamma^{V,i}_{\mu\alpha}(p,k)u_b(p) \tag{8.1}$$

$$\langle \Lambda_c\,(2595)|\,\bar{c}\gamma_\mu\gamma_5 b\,|\Lambda_b\rangle = \sum_i g_i(q^2)\bar{u}^{\alpha}_{c,1/2}(k)\Gamma^{A,i}_{\mu\alpha}(p,k)u_b(p) \tag{8.2}$$

$$\langle \Lambda_c\,(2625)|\,\bar{c}\gamma_\mu b\,|\Lambda_b\rangle = \sum_i F_i(q^2)\bar{u}^{\alpha}_{c,3/2}(k)\Gamma^{V,i}_{\mu\alpha}(p,k)u_b(p) \tag{8.3}$$

$$\langle \Lambda_c\,(2625)|\,\bar{c}\gamma_\mu\gamma_5 b\,|\Lambda_b\rangle = \sum_i G_i(q^2)\bar{u}^{\alpha}_{c,3/2}(k)\Gamma^{A,i}_{\mu\alpha}(p,k)u_b(p), \tag{8.4}$$

where p and k are the four-momenta of the Λ_b and Λ_c^*, respectively, u_b is the spinor of the Λ_b, and $u_{c,1/2}$ and $u_{c,3/2}$ are the spinors of the $\Lambda_c\,(2595)$ and $\Lambda_c\,(2625)$. The Dirac basis chosen for this work is detailed in [37], and ensures a form factor decomposition such that each helicity amplitude[1] depends on one single form factor.

The obtained expressions for the $\Lambda_b \to \Lambda_c\,(2595)$ and $\Lambda_b \to \Lambda_c\,(2625)$ form factors are detailed in Appendix C.1.

Equations of motion allow to relate the form factors such that each of them can be expressed in terms of only two hadronic Isgur-Wise (IW) functions, a leading order one (here denoted by the ζ symbol) and a subleading order one (ζ_{SL}).

8.1.2. Isgur-Wise functions

No first principles in HQET allow to infer the q^2 dependence of the IW functions[2]. We therefore need to infer the IW functional form in other ways. Two models have been considered. The use of an exponential function is motivated in [39] for the ground state transition $\Lambda_b \to \Lambda_c$. In analogy with this, the first model we consider reads:

$$\zeta\left(q^2\right)\Big|_{\text{exp}} \equiv \zeta\left(q^2_{max}\right)\exp\left[\rho\left(\frac{q^2}{q^2_{max}}-1\right)\right] \tag{8.5}$$

$$\zeta_{SL}\left(q^2\right)\Big|_{\text{exp}} \equiv \zeta\left(q^2_{max}\right)\delta_{SL}\exp\left[\frac{\rho_{SL}}{\delta_{SL}}\left(\frac{q^2}{q^2_{max}}-1\right)\right]. \tag{8.6}$$

The second model is obtained from a first-order Taylor expansion of the exponential form around $q^2 = q^2_{max}$. For our purposes, we use an expansion up to the first order in q^2. We then

[1] The matrix element for the exchange of a virtual W boson with a defined polarization state is called *helicity amplitude*.

[2] Isgur-Wise functions were first developed to model the form factors involved in meson decays. Their use has then been introduced for baryonic processes in [38].

obtain a linear model:

$$\zeta\left(q^2\right)\Big|_{\text{lin}} \equiv \zeta\left(q^2_{max}\right)\left[1+\rho\left(\frac{q^2}{q^2_{max}}-1\right)\right] \tag{8.7}$$

$$\zeta_{SL}\left(q^2\right)\Big|_{\text{lin}} \equiv \zeta\left(q^2_{max}\right)\left[\delta_{SL}+\rho_{SL}\left(\frac{q^2}{q^2_{max}}-1\right)\right]. \tag{8.8}$$

Both models share the same parameter set: the leading order and subleading order slopes ρ and ρ_{SL}, the relative normalization δ_{SL}, and the overall multiplicative factor $\zeta\left(q^2_{max}\right)$, that drops out in ratios of observables. The two parametrizations have been chosen so that the leading order and subleading order IW functions share a common overall normalization $\zeta\left(q^2_{max}\right)$.

8.1.3. Observables

The normalized double differential $\Lambda_b \to \Lambda_c^* \ell \bar{\nu}_\ell$ decay rate can be written as

$$\frac{1}{\Gamma_0^\ell}\frac{d^2\Gamma_J^\ell}{dq^2 d\cos\theta_\ell} = a_\ell^J + b_\ell^J \cos\theta_\ell + c_\ell^J \cos^2\theta_\ell\,, \tag{8.9}$$

where the index J refers to the two states with spin-parities $1/2^-$ and $3/2^-$, ℓ corresponds to a specific final state lepton flavour ($\ell \in \{e,\mu,\tau\}$), q^2 is the invariant mass of the $\ell\bar{\nu}$ pair, and θ_ℓ is the helicity angle, *i.e.* the angle that the charged lepton ℓ forms with respect to the momentum of the $\ell\bar{\nu}$ pair calculated in the rest frame of the Λ_b. Λ_c^* polarization effects[3] are integrated upon. The normalization Γ_0^ℓ reads

$$\Gamma_0^\ell(q^2) = \frac{G_F^2 V_{cb}^2 \sqrt{s_+ s_-}\, m_{\Lambda_c^*}}{96\pi^3 m^2_{\Lambda_b}}\left(1-\frac{m_\ell^2}{q^2}\right)^2, \tag{8.10}$$

where $s_\pm \equiv (m_{\Lambda_b} \pm m_{\Lambda_c^*})^2 - q^2$, and the angular coefficients a_ℓ^J, b_ℓ^J and c_ℓ^J have the following q^2 dependence:

$$\begin{aligned} a_\ell^{1/2}\left(q^2\right) =& \frac{1}{2}\Bigg[|f_{1/2,t}|^2\frac{m_\ell^2}{q^2}\left(m_{\Lambda_b}-m_{\Lambda_c^*}\right)^2 + \left(|f_{1/2,0}|^2\left(m_{\Lambda_b}+m_{\Lambda_c^*}\right)^2 + |f_{1/2,\perp}|^2\left(m_\ell^2+q^2\right)\right) \\ &+ |g_{1/2,t}|^2\frac{m_\ell^2}{q^2}\left(m_{\Lambda_b}+m_{\Lambda_c^*}\right)^2 + \left(|g_{1/2,0}|^2\left(m_{\Lambda_b}-m_{\Lambda_c^*}\right)^2 + |g_{1/2,\perp}|^2\left(m_\ell^2+q^2\right)\right)\Bigg], \end{aligned} \tag{8.11}$$

[3] Corresponding to the angular observables of the $\Lambda_c^* \to \Lambda_c \pi\pi$ decay.

$$b_\ell^{1/2}\left(q^2\right) = \left(f_{1/2,t} f_{1/2,0} + g_{1/2,t} g_{1/2,0}\right) \frac{m_\ell^2}{q^2} \left(m_{\Lambda_b}^2 - m_{\Lambda_c^*}^2\right) - 2\, q^2 f_{1/2,\perp} g_{1/2,\perp}, \tag{8.12}$$

$$\begin{aligned} c_\ell^{1/2}\left(q^2\right) = &-\frac{1}{2}\left(1 - \frac{m_\ell^2}{q^2}\right)\Bigg[|f_{1/2,0}|^2 \left(m_{\Lambda_b} + m_{\Lambda_c^*}\right)^2 - q^2 |f_{1/2,\perp}|^2 \\ &+ |g_{1/2,0}|^2 \left(m_{\Lambda_b} - m_{\Lambda_c^*}\right)^2 - q^2 |g_{1/2,\perp}|^2 \Bigg], \end{aligned} \tag{8.13}$$

$$\begin{aligned} a_\ell^{3/2}\left(q^2\right) = &\Bigg[|F_{1/2,t}|^2 \frac{m_\ell^2}{q^2} \left(m_{\Lambda_b} - m_{\Lambda_c^*}\right)^2 \\ &+ |F_{1/2,0}|^2 \left(m_{\Lambda_b} + m_{\Lambda_c^*}\right)^2 + \left(|F_{1/2,\perp}|^2 + 3|F_{3/2,\perp}|^2\right)\left(m_\ell^2 + q^2\right) \\ &+ |G_{1/2,t}|^2 \frac{m_\ell^2}{q^2} \left(m_{\Lambda_b} + m_{\Lambda_c^*}\right)^2 \\ &+ |G_{1/2,0}|^2 \left(m_{\Lambda_b} - m_{\Lambda_c^*}\right)^2 + \left(|G_{1/2,\perp}|^2 + 3|G_{3/2,\perp}|^2\right)\left(m_\ell^2 + q^2\right) \Bigg], \end{aligned} \tag{8.14}$$

$$\begin{aligned} b_\ell^{3/2}\left(q^2\right) = &\, 2\left(F_{1/2,t} F_{1/2,0} + G_{1/2,t} G_{1/2,0}\right) \frac{m_\ell^2}{q^2} \left(m_{\Lambda_b}^2 - m_{\Lambda_c^*}^2\right) \\ &- 4\, q^2 \left(F_{1/2,\perp} G_{1/2,\perp} + 3 F_{3/2,\perp} G_{3/2,\perp}\right), \end{aligned} \tag{8.15}$$

$$\begin{aligned} c_\ell^{3/2}\left(q^2\right) = &-\left(1 - \frac{m_\ell^2}{q^2}\right)\Bigg[|F_{1/2,0}|^2 \left(m_{\Lambda_b} + m_{\Lambda_c^*}\right)^2 - q^2 \left(|F_{1/2,\perp}|^2 + 3|F_{3/2,\perp}|^2\right) \\ &+ |G_{1/2,0}|^2 \left(m_{\Lambda_b} - m_{\Lambda_c^*}\right)^2 - q^2 \left(|G_{1/2,\perp}|^2 + 3|G_{3/2,\perp}|^2\right) \Bigg]. \end{aligned} \tag{8.16}$$

In Eqns. 8.11–8.16, we indicate the form factors for vector (axialvector) transitions to the $\Lambda_c(2595)$ with the lowercase letter f (g). Uppercase form factors, denoted by F (G), correspond to vector (axialvector) $\Lambda_b \to \Lambda_c(2625)$ transitions. Finally, the t, 0 and $\perp$ subscripts denote time-line, longitudinal and transversal contributions, respectively. The form factors expressions obtained in [37] are detailed in Eqns. C.1–C.14.

By integrating Eqn. 8.9 over $\cos\theta_\ell$ one obtains the differential branching ratio

$$\frac{1}{\Gamma_0^\ell} \frac{d^2\Gamma_J^\ell}{dq^2} = 2\left(a_\ell^J + \frac{1}{3} c_\ell^J\right). \tag{8.17}$$

Finally, by integrating again over the q^2 phase space, the total decay width

$$\Gamma_J^\ell = 2 \int_{m_\ell^2}^{(m_{\Lambda_b} - m_{\Lambda_c})^2} \mathrm{d}q^2 \; \Gamma_0^\ell(q^2) \left(a_\ell^J(q^2) + \frac{1}{3} c_\ell^J(q^2) \right) \tag{8.18}$$

can be calculated as a function of the Λ_c^* state and lepton flavour considered. In this framework, the ratio $R\left(\Lambda_c^*\right)$ is given by

$$R\left(\Lambda_c^*\right)_{1/2} = \frac{\Gamma_{1/2}^\tau}{\Gamma_{1/2}^\mu} \quad \text{for the } \Lambda_c\,(2595) \text{ state, and by} \tag{8.19}$$

$$R\left(\Lambda_c^*\right)_{3/2} = \frac{\Gamma_{3/2}^\tau}{\Gamma_{3/2}^\mu} \quad \text{for the } \Lambda_c\,(2625) \text{ state.} \tag{8.20}$$

8.2. LHCb sensitivity to the form factor parameters

A precise theoretical prediction for the value of the $R\left(\Lambda_c^*\right)$ ratios can only arise from a combination of theoretical work and experimental input. In particular, the arbitrarity of the Isgur-Wise functional form and of their parameters can only be solved by means of a direct measurement of the kinematical variables involved in the $\Lambda_b \to \Lambda_c^* \mu \bar{\nu}_\mu$ decay. This section presents a study of the LHCb sensitivity to the form factor parameters defined in Section 8.1.2. Section 8.3 elaborates the estimated measurement uncertainties by assessing their effect on the $R\left(\Lambda_c^*\right)$ prediction.

Throughout this section, the expected $\Lambda_c\,(2595)$ and $\Lambda_c\,(2625)$ yields for a given luminosity are extrapolated from the values quoted in [21], *cf.* Figure 7.4. The increase of the $b\bar{b}$ production cross section for pp collisions at $\sqrt{s} = 13$ TeV is taken into account [40]. Except for the extrapolation presented in Section 8.3, a signal yield corresponding to the current LHCb dataset[4] is assumed.

Two key factors limit the precision achievable in the measurement of the IW parameters: the size of the data sample, and the experimental resolution. In Section 8.3 we evaluate the evolution of the LHCb sensitivity with the signal yields expected until the end of the first LHCb detector upgrade, corresponding to a data set approximately ten times as large as the one currently available.

8.2.1. LHCb resolution

The experimental resolution determines how finely data can be binned. Furthermore, a correlation is introduced between the bins. In fact, due to finite resolution, events belonging to bin i of a certain kinematical variable can migrate to bin j once reconstructed.

[4] Corresponding to the data collected in Run I and Run II until December 2017.

At a hadron collider, the momentum of the neutrino can be calculated up to a quadratic ambiguity, using the flight direction of the reconstructed Λ_b and its mass (*cf.* Section 7.1.3). Therefore, there are two main sources contributing to the resolution on the kinematic variables of the $\Lambda_b \to \Lambda_c^* \mu \bar{\nu}_\mu$ decay, discussed below.

- Vertex resolution: the direction of the Λ_b is reconstructed from the primary pp interaction vertex (PV) and the secondary Λ_b decay vertex (SV).
- Choice of the neutrino solution: it is difficult to know, without external information, which solution is correct; therefore, one is often chosen randomly.

In this study we estimate the LHCb resolution for the transferred momentum q^2 and the muon helicity angle $\cos\theta_\ell$, with the purpose of choosing a binning scheme to evaluate the LHCb sensitivity to the form factor parameters.

A sample of $\Lambda_b \to \Lambda_c(2625)\,\mu\bar{\nu}_\mu$ decays is simulated in Pythia [41, 42] for pp collisions at energy $\sqrt{s} = 13$ TeV. The sample is then reduced to those events where the Λ_b pseudorapidity is $2 < \eta < 5$, corresponding approximately to the acceptance of the LHCb detector. Then, a Gaussian smearing is applied to the PV and SV following the work done in [43]. The following resolution is assumed:

$$\sigma_{x,y}(PV) = 13\ \mu\text{m}$$
$$\sigma_z(PV) = 70\ \mu\text{m}$$
$$\sigma_{x,y}(SV) = 20\ \mu\text{m}$$
$$\sigma_z(SV) = 200\ \mu\text{m}$$

Finally, the decay is reconstructed. Of the two solutions for the neutrino momentum, we choose either:

1. a solution at random,
2. the solution closest (or farthest) to the simulated neutrino momentum.

Through this, we are able to study the effect of the choice of solution on the reconstruction of kinematic variables.

Figure 8.1 shows the reconstructed q^2 for a random choice of the solution, as compared to the simulated distribution. The comparison in bins of $\cos\theta_\ell$ shows that the reconstruction accuracy deteriorates at larger values of $\cos\theta_\ell$. Similarly, Figure 8.2 shows the simulated and reconstructed $\cos\theta_\ell$ distributions in four q^2 bins, demonstrating a significant migration in the higher q^2 bin. Bin migrations arise from the interplay between q^2 and $\cos\theta_\ell$. At high q^2 the $\cos\theta_\ell$ resolution is worse, due to the difficulty in reconstructing the W rest frame, *i.e.* the rest frame of the $\mu\bar{\nu}_\mu$ pair. More details about this are given in Appendix C.2.

In order to choose the most convenient binning scheme, the q^2 and $\cos\theta_\ell$ bin purities were examined for various number of q^2 and $\cos\theta_\ell$ bins. More details are given in Appendix C.3.

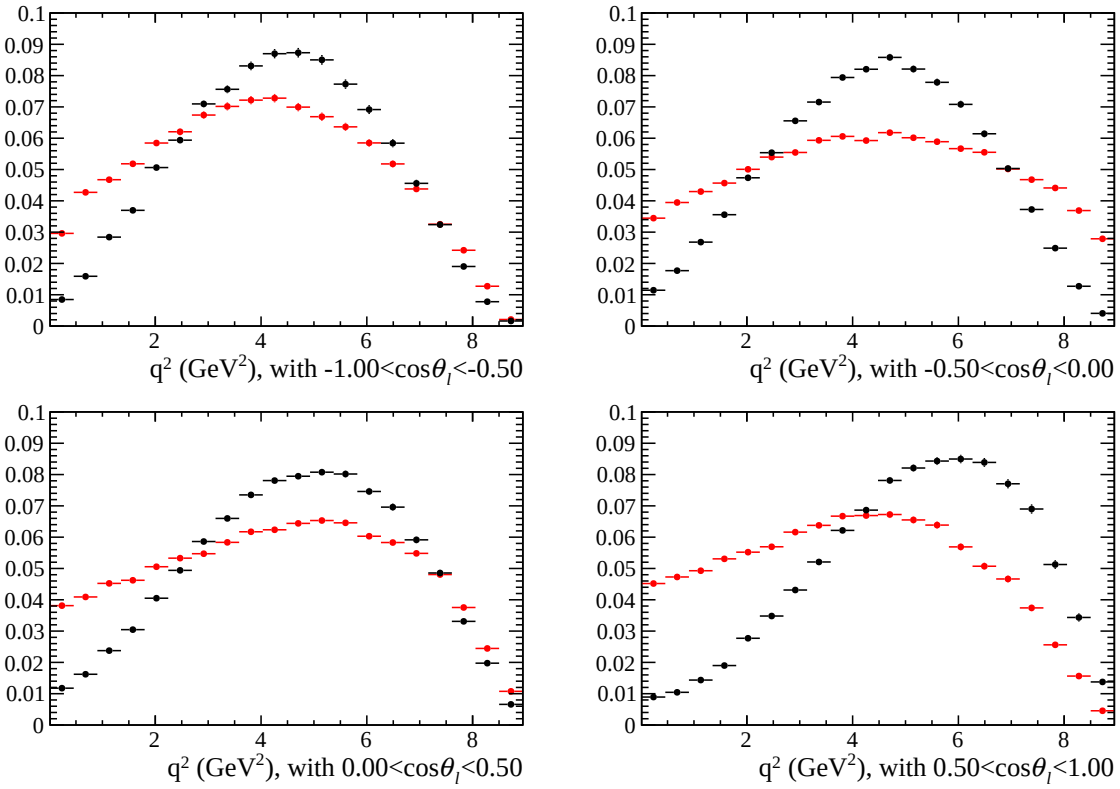

Figure 8.1: Reconstructed (red) *vs.* simulated (black) q^2 in bins of $\cos\theta_\ell$.

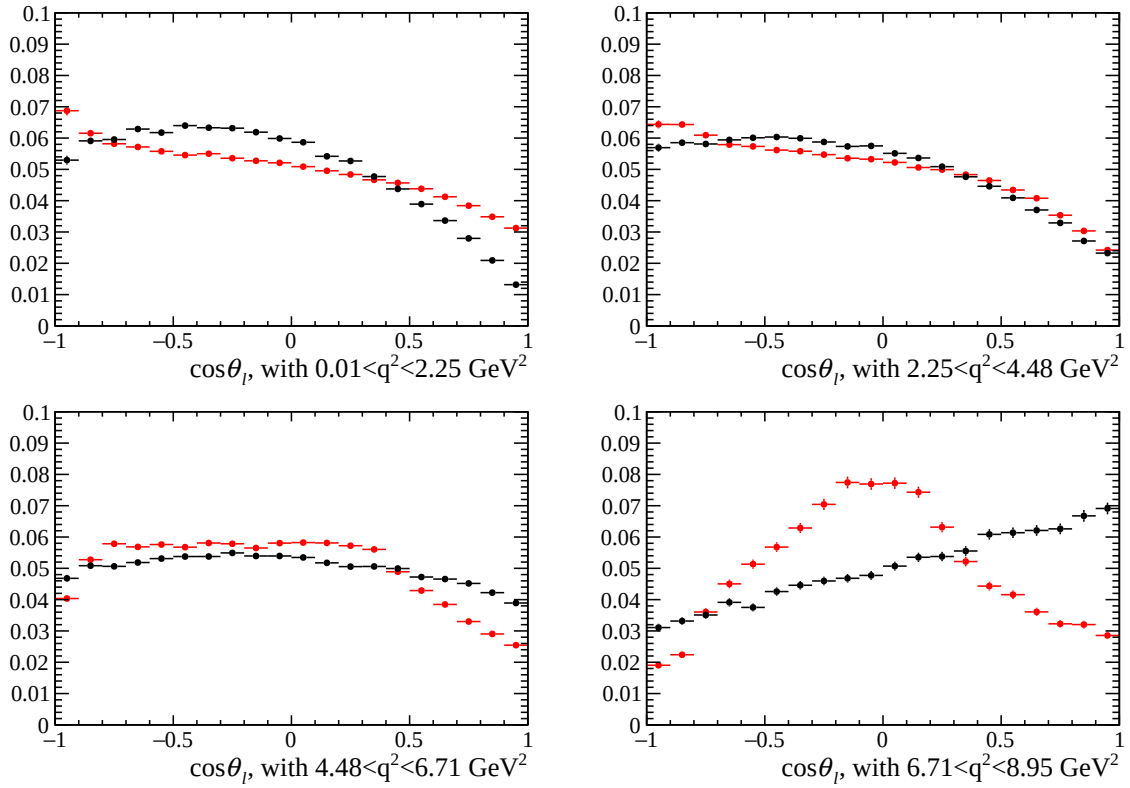

Figure 8.2: Reconstructed (red) *vs.* simulated (black) $\cos\theta_\ell$ in bins of q^2.

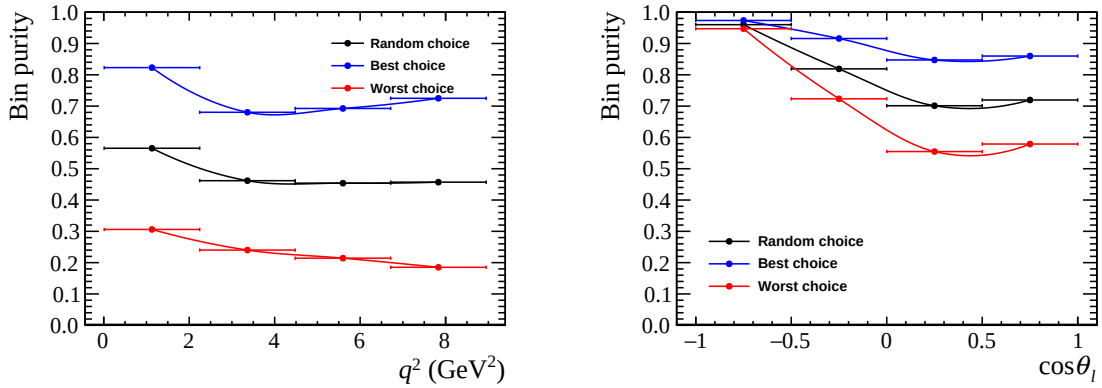

Figure 8.3: Purity as a function of q^2 and $\cos\theta_\ell$, defined as the fraction of candidates that belong in a particular kinematic bin, for four q^2 bins and four $\cos\theta_\ell$ bins.

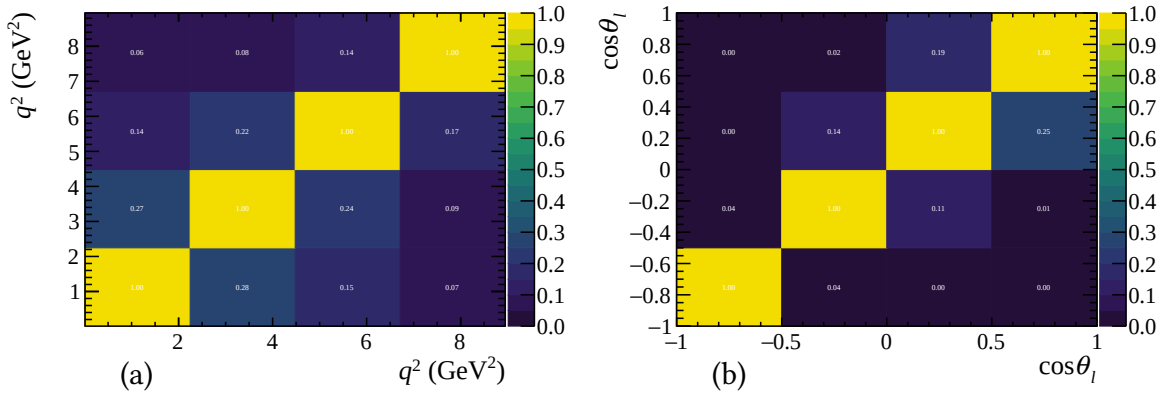

Figure 8.4: Bin correlations for a random choice of the neutrino solution: q^2 (a) and $\cos\theta_\ell$ (b).

The bin purity is defined as the fraction of simulated candidates that belong to the same kinematical bin before and after reconstruction, *i.e.* that do not migrate to another bin. We found that four bins allow to achieve a q^2 bin purity larger than 40% across the whole q^2 range. We chose to adopt the same number of bins in $\cos\theta_\ell$, as a finer $\cos\theta_\ell$ binning does not improve sensitivity (*cf.* Appendix C.3).

The resulting purities for a random choice of neutrino solution are shown in Figure 8.3. The choice of the neutrino solution plays a key role in the experimental resolution. Without any additional information, we can only choose a solution at random. Most likely the LHCb analysis will manage to improve this by means of a regression algorithm [43], allowing to obtain a bin purity lying in between the random choice and best choice purities shown in Figure 8.3.

In our study, the migration of candidates between kinematic bins is modeled with a level of correlation between bins. For a given kinematical variable, a correlation $c_{i,j}$ between bin i and bin j is assigned, calculated as the fraction of reconstructed candidates in bin j that would belong to bin i if the experimental resolution was infinite, *i.e.* that belonged in bin i when the event was simulated.

The obtained correlation levels between q^2 bins are shown in Figure 8.4(a). A maximum correlation of 28% is observed between neighbouring bins, and a correlation of 6% between third neighbours ($|i-j|=3$). The correlation between $\cos\theta_\ell$ bins is shown in Figure 8.4(b). In agreement with the better resolution, a lower correlation is observed, amounting to maximum 19% between neighbouring bins in the high $\cos\theta_\ell$ region.

8.2.2. Benchmark points

The momentum transfer q corresponding to zero hadronic recoil is of special interest, as in this point the form factors are minimally sensitive to the dynamics of the spectator quarks and the $\Lambda_b \to \Lambda_c^*$ transition is entirely determined by the heavy quarks b and c. Numerical information on the square of the form factors can be inferred following what is called a

Zero-Recoil Sum Rule (ZRSR) [44].

The ZRSR procedure analyzes the $\Lambda_b \to \Lambda_b$ forward vector and axialvector matrix elements I_V and I_A, and it is briefly discussed here taking the analysis of the vector matrix element I_V as an example. The I_V matrix element has been perturbatively calculated for mesonic decays $B \to D^{(*)}\mu\bar{\nu}_\mu$, and can be reinterpreted for baryon processes under some assumptions, neglecting corrections of order $1/m^4$ and beyond [44]. At the same time, $I_V \equiv F + F_{inel}$ can be decomposed into a term F, accounting for contributions from ground state $\Lambda_b \to \Lambda_c$ transitions and known from lattice QCD calculations [17], and a term F_{inel}, containing contributions from non-ground state transitions. The latter include Λ_b decays into $\Sigma_c(2455)$, $\Sigma_c(2520)$, $\Lambda_c(2595)$, $\Lambda_c(2625)$ and $\Sigma_c(2800)$. However, the three Σ_c states form an isospin triplet, and therefore carry an isospin $I = 1$. As a consequence, $\Lambda_b \to \Sigma_c$ transitions are suppressed by reason of isospin conservation. We therefore assume that in the point of zero recoil F_{inel} can be expressed solely in terms of $\Lambda_b \to \Lambda_c^*$ matrix elements. In the point of zero recoil, matching the presently available information on the value of I_V at the third order in $1/m$ with the sum of F and of the expression of F_{inel} in terms of the form factors calculated in Section 8.1 yields a numerical range for the parameters of the IW functions listed in Section 8.1.2. We take the central values of these intervals as benchmark points:

$$\delta_{SL} \simeq -0.14 \tag{8.21}$$

$$\zeta\left(q^2_{max}\right) \simeq 0.25. \tag{8.22}$$

A lower boundary for ρ and ρ_{SL} can be obtained taking inspiration from an expansion of the slope parameters in terms of a sum of positive definite quantities, developed for $B \to D$ mesonic transitions [45]. The lowest term of the sum has a value of about 0.25 when the IW functions are expressed as a function of q^2. Our linear parametrization for the IW function is positive within the allowed q^2 range for values of ρ up to about 0.75. We therefore chose to adopt the two extreme values 0.25 and 0.75 as benchmark points to calculate the LHCb sensitivity.

These values were obtained on the basis of a large set of assumptions further detailed in [37], and are not suited as model parameters for physics analysis. The IW parameters should instead be experimentally measured. However, these values can be used to define a set of benchmark points for the sensitivity study reported in the rest of this Chapter. We chose four different benchmark points, corresponding to the extreme values of the slope parameters:

1. $\rho = \rho_{SL} = 0.25$, $\delta_{SL} = -0.14$;
2. $\rho = 0.25$, $\rho_{SL} = 0.75$, $\delta_{SL} = -0.14$;
3. $\rho = 0.75$, $\rho_{SL} = 0.25$, $\delta_{SL} = -0.14$;
4. $\rho = \rho_{SL} = 0.75$, $\delta_{SL} = -0.14$.

8.2.3. Fit strategy

At a hadron collider, measurements of decay rates suffer from systematic uncertainty related to the imprecise knowledge of the amount of decaying particles produced in the pp collision. To overcome this problem, one can measure the ratio between the decay width of the target channel and that of a well known decay used as normalization. For this study, we normalize the decay rate to the total Λ_b decay width, as calculated in Eqn. 8.18. Therefore, we use only the shape of the differential decay rate to determine the parameters of the IW functions. This way, the absolute scale of the form factors cannot be determined, and no sensitivity is reported for $\zeta\left(q^2_{max}\right)$ [37].

Pseudo-experiments are generated for each benchmark point using the currently available number of $\Lambda_b \to \Lambda_c(2595)\,\mu\bar{\nu}_\mu$ and $\Lambda_b \to \Lambda_c(2625)\,\mu\bar{\nu}_\mu$ decays at LHCb. Several binning schemes, shown in Appendix C.3, are tested. The fit parameters are initialised to the benchmark values and allowed to float in a χ^2 fit. Both Λ_c^* states share the same IW parameters, and they are fit simultaneously, using the binning and statistical correlation discussed in Section 8.2.1. The correlation is introduced by means of a covariance matrix using Poisson uncertainties for the content of each bin. One-dimensional (1D) fits using only q^2 information and two-dimensional (2D) fits using both q^2 and $\cos\theta_\ell$ are performed.

The lower mass Λ_c^* state is experimentally more challenging, as its decay to $\Lambda_c\pi\pi$ proceeds also through the intermediate resonance $\Sigma_c(2455)$ (*cf.* Table 7.1). This makes the mass distribution of the $\Lambda_c(2595)$ more difficult to model. Together with the lower abundance of $\Lambda_b \to \Lambda_c(2595)\,\mu\bar{\nu}_\mu$ decays compared to the more frequent $\Lambda_b \to \Lambda_c(2625)\,\mu\bar{\nu}_\mu$ process, these reasons would suggest that experimental analyses aimed at measuring $\Lambda_b \to \Lambda_c^*\mu\bar{\nu}_\mu$ observables start with a study limited to the higher mass state, which would in principle give the highest sensitivity. However, the sensitivity study reported here shows that the use of only one state would yield incomplete results.

The fitted Isgur-Wise parameters are shown in Figure 8.5 for 1D fits to the q^2 distribution and for 2D fits to the q^2 and $\cos\theta_\ell$ distributions. It is clear from the bottom panel of Figure 8.5 that only the combination of the two Λ_c^* states allows to extract information on both the leading order and the subleading order contributions. This is due to the fact that the dependence of the form factors on ζ and ζ_{SL} is different for the two states (*cf.* Eqns. C.1–C.14). In Figure 8.6 the correlation between the leading order and subleading order slope parameters is investigated. The parameters present a positive correlation when measured in $\Lambda_b \to \Lambda_c(2595)\,\mu\bar{\nu}_\mu$ decays, and a negative one when measured in $\Lambda_b \to \Lambda_c(2625)\,\mu\bar{\nu}_\mu$ decays. Only a simultaneous fit to data containing both processes can solve the degeneracy between the two slopes. Moreover, Figure 8.5 shows that the $\Lambda_c(2595)$ and $\Lambda_c(2625)$ data sets are individually sensitive to the δ_{SL} parameter, but a simultaneous fit provides much better precision.

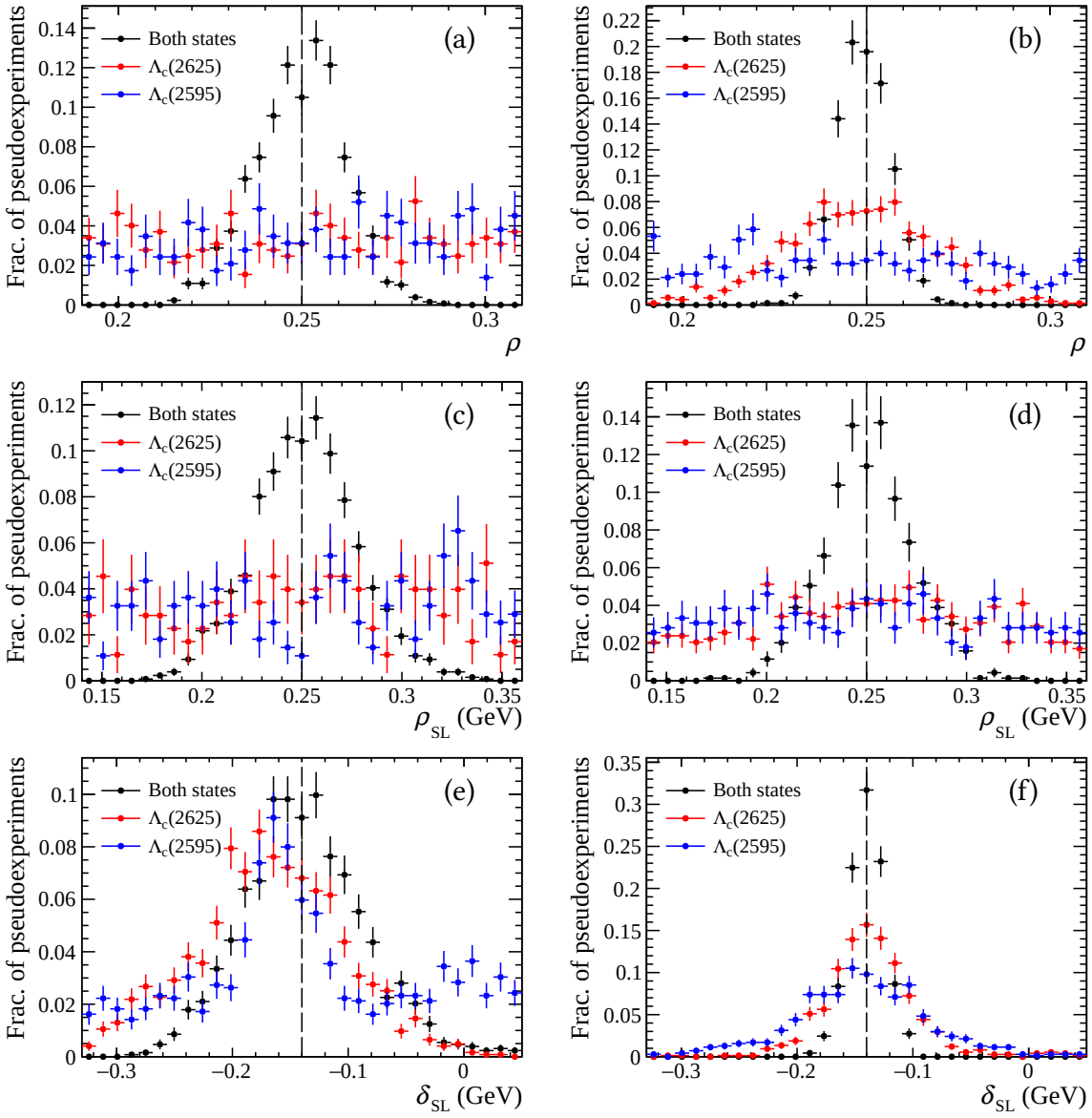

Figure 8.5: Distribution of the IW functions parameters ρ (a), ρ_{SL} (c) and δ_{SL} (e) as extracted from a 1D fit to the q^2 distribution of an ensemble of about 800 pseudo-experiments. Distribution of ρ (b), ρ_{SL} (d) and δ_{SL} (f) as extracted from a 2D fit to the q^2 and $\cos\theta_\ell$ distributions. The three distributions in each plot represent the different data samples used: only Λ_c (2595) (blue), only Λ_c (2625) (red), or both (black), in a sample size roughly equivalent to the data currently available at LHCb.

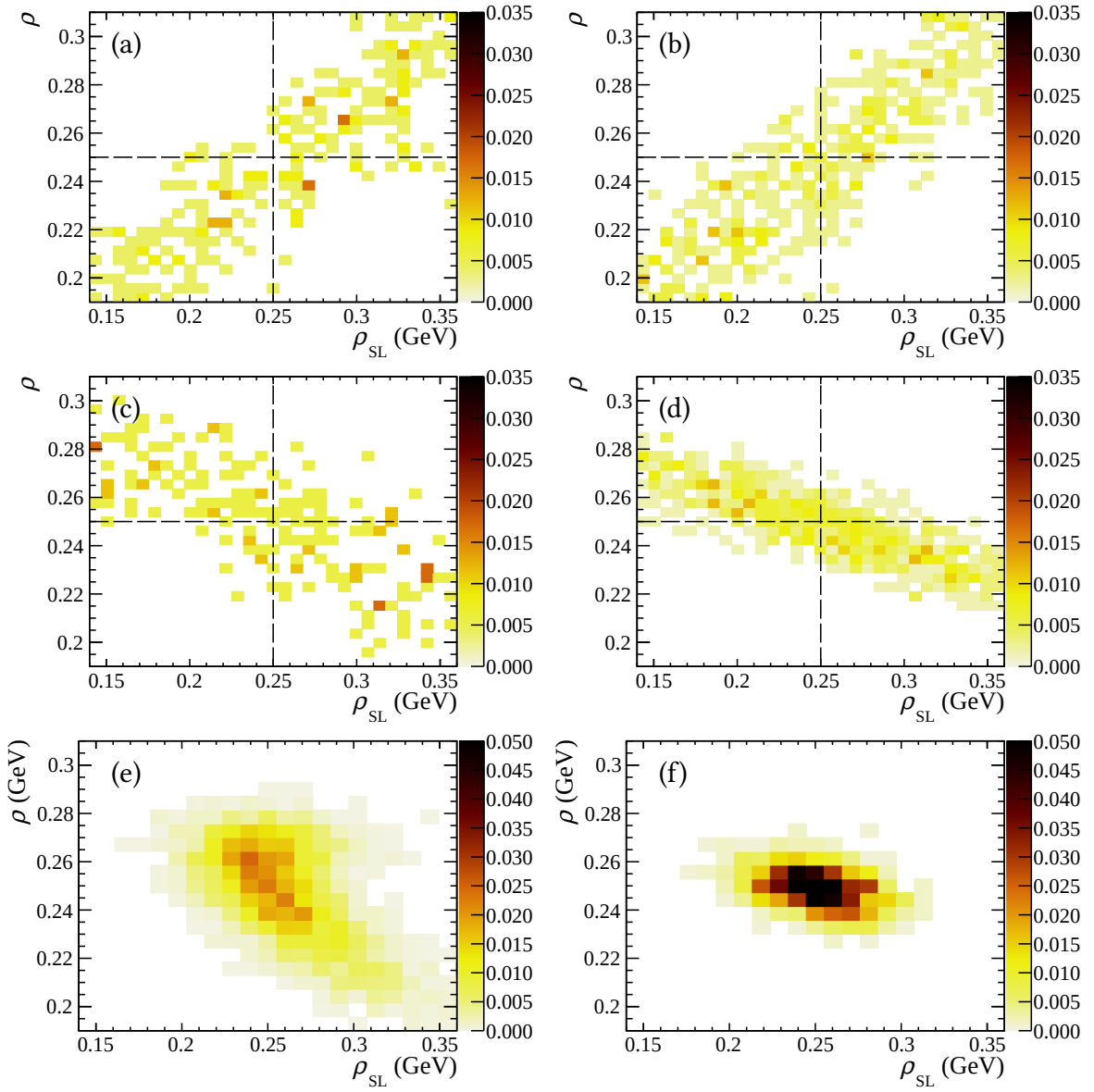

Figure 8.6: 2D distributions of the slope parameters ρ and ρ_{SL} as extracted from a 1D fit to q^2 (a, c, e) and from a 2D fit to both q^2 and $\cos\theta_\ell$ (b, d, f). Three different data samples are fitted: only Λ_c (2595) (a, b), only Λ_c (2625) (c, d), or both (e, f), in a sample size roughly equivalent to the data currently available at LHCb. The positive (negative) correlation between the slope parameters visible in decays to Λ_c (2595) (Λ_c (2625)) is solved when fitting both processes simultaneously.

8.3. Theoretical prediction of $R\left(\Lambda_c^*\right)$

The results presented in Section 8.2.3 are extrapolated in order to estimate the theoretical uncertainty on the predicted value of $R\left(\Lambda_c^*\right)$. To provide this prediction, one needs a knowledge of the form factors and thus of the Isgur-Wise functions. We tested two parametrizations of the IW functions, sharing the same parameter set (*cf.* Section 8.1.2), for both the leading order and subleading order contributions. At the same time, we evaluated the LHCb sensitivity to the form factor parameters generating pseudo-experiments based on four different benchmark sets of IW parameters (*cf.* Section 8.2.2).

The precision on the $R\left(\Lambda_c^*\right)$ ratio is calculated as a function of the luminosity collected by the LHCb experiment, by varying the $\Lambda_c\,(2595)$ and $\Lambda_c\,(2625)$ sample sizes according to the expected yields, rescaled from those quoted in [21] taking the increased luminosity into account.

We exploit the fact that the shape of the fitted parameters is almost Gaussian in order to extrapolate the uncertainty on $R\left(\Lambda_c^*\right)$. From each pseudoexperiment we extract the fitted parameter values, the associated statistical uncertainties, and the correlation between them, constructing a multivariate Gaussian distribution. We then perform an additional series of pseudo-experiments by sampling $(\rho, \rho_{SL}, \delta_{SL})$ values from the latter distribution. For each set of sampled parameters we calculate $R\left(\Lambda_c^*\right)$ according to Eqns. 8.19 and 8.20. We take the standard deviation of the calculated $R\left(\Lambda_c^*\right)$ values as a measure of the statistical uncertainty on the SM expectation for $R\left(\Lambda_c^*\right)$.

The expected precision on $R\left(\Lambda_c^*\right)$ is shown in Figure 8.7 as a function of luminosity for the various sets of pseudo-experiments. We chose to quote te maximum uncertainty obtained among all sets of pseudoexperiments as expected statistical uncertainty [37]. A theoretical precision of about 7% can be expected on $R\left(\Lambda_c\,(2625)\right)$ with Run I and Run II data, which can shrink down to about 2% with the dataset available at the time of the first LHCb upgrade. The prediction for $R\left(\Lambda_c\,(2595)\right)$ is expected to be more precise. These uncertainties ignore power-suppressed terms in the HQET expansion of the form factors, as well as experimental systematic uncertainties, that could become relevant at this level of precision [37].

8.4. Conclusions

The work presented in this chapter provides all the necessary ingredients to constrain the theoretical uncertainty on $R\left(\Lambda_c^*\right)$ by means of an experimental measurement of the form factor parameters, that can be performed at LHCb. The form factors are expressed in terms of two Isgur-Wise functions, providing leading order and subleading order contributions and sharing the same set of parameters. We demonstrated that a two-dimensional fit to the q^2 and $\cos\theta_\ell$ distributions of Λ_b decays to both Λ_c^* states is necessary in order to constrain both slope parameters, and the relative normalization between the two IW functions. A measurement of

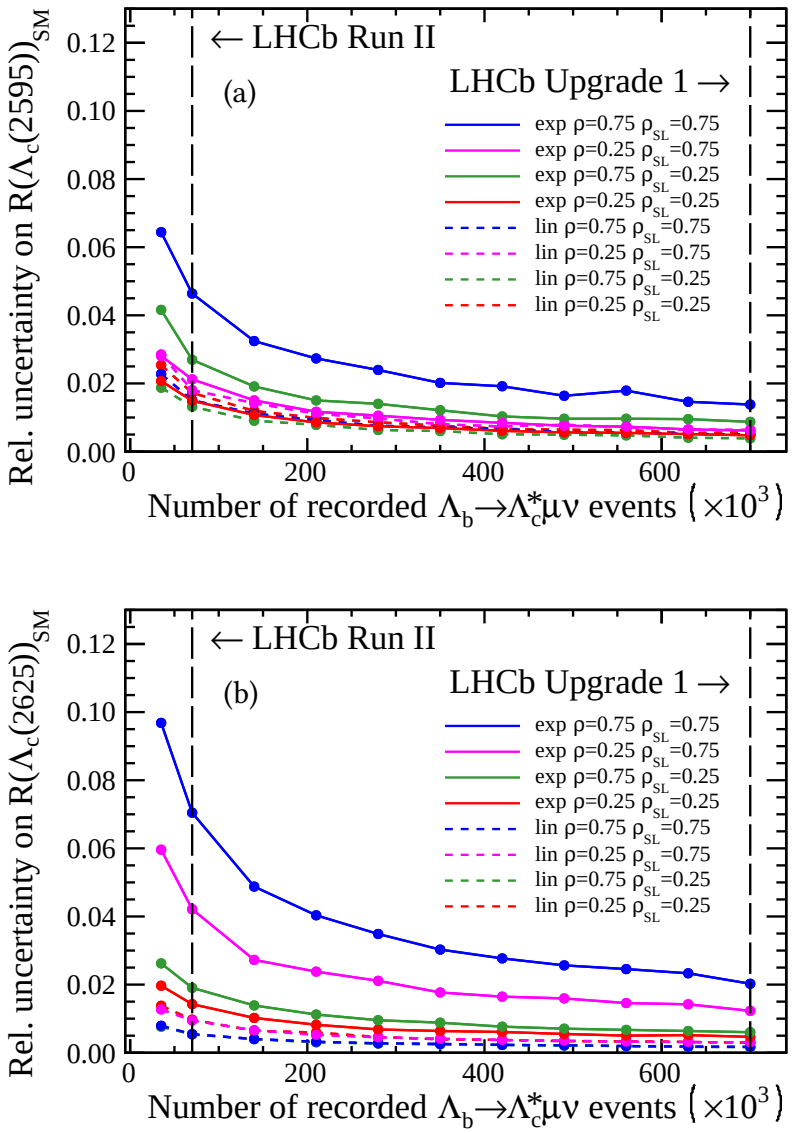

Figure 8.7: Expected statistical uncertainty on the Standard Model prediction of $R(\Lambda_c(2595))$ (a) and $R(\Lambda_c(2625))$ (b) as a function of the amount of data collected by the LHCb experiment. The various data sets correspond to linear and exponential parametetrizations of the leading order and subleading order IW functions, and to the four sets of parameters used as benchmark.

the overall normalization parameter is not feasible if we assume the use of a normalization channel to control systematic uncertainties on the experimental measurement. On the other hand, the overall normalization $\zeta\left(q^2_{max}\right)$ drops out in the calculation of $R\left(\Lambda_c^*\right)$.

In particular, this study proves that fitting angular information in addition to the q^2 spectrum can substantially improve the sensitivity to the subleading Isgur-Wise function [37]. Moreover, we motivate an LHCb analysis of the shape of the $\Lambda_b \to \Lambda_c^* \mu \bar{\nu}_\mu$ decay, showing that a measurement of the $\Lambda_b \to \Lambda_c^*$ form factors can lead to a precise theoretical determination of the $R\left(\Lambda_c^*\right)$ ratio.

References for the LFU tests in $\Lambda_b \to \Lambda_c^* \ell \bar{\nu}_\ell$ decays

[1] J. P. Lees et al. "Evidence for an excess of $\bar{B} \to D^{(*)}\tau^-\bar{\nu}_\tau$ decays". In: *Phys. Rev. Lett.* 109 (2012), p. 101802. DOI: 10.1103/PhysRevLett.109.101802. arXiv: 1205.5442 [hep-ex].

[2] J. P. Lees et al. "Measurement of an Excess of $\bar{B} \to D^{(*)}\tau^-\bar{\nu}_\tau$ Decays and Implications for Charged Higgs Bosons". In: *Phys. Rev.* D88.7 (2013), p. 072012. DOI: 10.1103/PhysRevD.88.072012. arXiv: 1303.0571 [hep-ex].

[3] M. Huschle et al. "Measurement of the branching ratio of $\bar{B} \to D^{(*)}\tau^-\bar{\nu}_\tau$ relative to $\bar{B} \to D^{(*)}\ell^-\bar{\nu}_\ell$ decays with hadronic tagging at Belle". In: *Phys. Rev.* D92.7 (2015), p. 072014. DOI: 10.1103/PhysRevD.92.072014. arXiv: 1507.03233 [hep-ex].

[4] A. Abdesselam et al. "Measurement of the branching ratio of $\bar{B}^0 \to D^{*+}\tau^-\bar{\nu}_\tau$ relative to $\bar{B}^0 \to D^{*+}\ell^-\bar{\nu}_\ell$ decays with a semileptonic tagging method". In: *Proceedings, 51st Rencontres de Moriond on Electroweak Interactions and Unified Theories: La Thuile, Italy, March 12-19, 2016*. 2016. arXiv: 1603.06711 [hep-ex]. URL: https://inspirehep.net/record/1431982/files/arXiv:1603.06711.pdf.

[5] S. Hirose et al. "Measurement of the τ lepton polarization and $R(D^*)$ in the decay $\bar{B} \to D^*\tau^-\bar{\nu}_\tau$". In: *Phys. Rev. Lett.* 118.21 (2017), p. 211801. DOI: 10.1103/PhysRevLett.118.211801. arXiv: 1612.00529 [hep-ex].

[6] Roel Aaij et al. "Measurement of the ratio of branching fractions $\mathcal{B}(\bar{B}^0 \to D^{*+}\tau^-\bar{\nu}_\tau)/\mathcal{B}(\bar{B}^0 \to D^{*+}\mu^-\bar{\nu}_\mu)$". In: *Phys. Rev. Lett.* 115.11 (2015). [Erratum: Phys. Rev. Lett.115,no.15,159901(2015)], p. 111803. DOI: 10.1103/PhysRevLett.115.159901,10.1103/PhysRevLett.115.111803. arXiv: 1506.08614 [hep-ex].

[7] Roel Aaij et al. "Measurement of the ratio of the $B^0 \to D^{*-}\tau^+\nu_\tau$ and $B^0 \to D^{*-}\mu^+\nu_\mu$ branching fractions using three-prong τ-lepton decays". In: (2017). arXiv: 1708.08856 [hep-ex].

[8] Dante Bigi and Paolo Gambino. "Revisiting $B \to D\ell\nu$". In: *Phys. Rev.* D94.9 (2016), p. 094008. DOI: 10.1103/PhysRevD.94.094008. arXiv: 1606.08030 [hep-ph].

[9] Svjetlana Fajfer, Jernej F. Kamenik, and Ivan Nisandzic. "On the $B \to D^*\tau\bar{\nu}_\tau$ Sensitivity to New Physics". In: *Phys. Rev.* D85 (2012), p. 094025. DOI: 10.1103/PhysRevD.85.094025. arXiv: 1203.2654 [hep-ph].

[10] Y. Amhis et al. "Averages of b-hadron, c-hadron, and τ-lepton properties as of summer 2016". In: *Eur. Phys. J.* C77.12 (2017), p. 895. DOI: 10.1140/epjc/s10052-017-5058-4. arXiv: 1612.07233 [hep-ex].

[11] Heavy Flavor Averaging Group (HFLAV). *Average of R(D) and R(D*) for FPCP 2017*. 2017. URL: http://www.slac.stanford.edu/xorg/hflav/semi/fpcp17/RDRDs.html (visited on 01/16/2019).

[12] R. M. Woloshyn. "Semileptonic decay of the Λ_b baryon". In: *PoS* Hadron2013 (2013), p. 203.

[13] Shanmuka Shivashankara, Wanwei Wu, and Alakabha Datta. "$\Lambda_b \to \Lambda_c \tau \bar{\nu}_\tau$ Decay in the Standard Model and with New Physics". In: *Phys. Rev.* D91.11 (2015), p. 115003. DOI: 10.1103/PhysRevD.91.115003. arXiv: 1502.07230 [hep-ph].

[14] Gutsche, Thomas and Ivanov, Mikhail A. and Körner, Jürgen G. and Lyubovitskij, Valery E. and Santorelli, Pietro and Habyl, Nurgul. "Semileptonic decay $\Lambda_b \to \Lambda_c + \tau^- + \bar{\nu}_\tau$ in the covariant confined quark model". In: *Phys. Rev.* D91.7 (2015). [Erratum: Phys. Rev.D91,no.11,119907(2015)], p. 074001. DOI: 10.1103/PhysRevD.91.074001,10.1103/PhysRevD.91.119907. arXiv: 1502.04864 [hep-ph].

[15] Gutsche, Thomas and Ivanov, Mikhail A. and Körner, Jürgen G. and Lyubovitskij, Valery E. and Santorelli, Pietro. "Semileptonic decays $\Lambda_c^+ \to \Lambda \ell^+ \nu_\ell$ ($\ell = e, \mu$) in the covariant quark model and comparison with the new absolute branching fraction measurements of Belle and BESIII". In: *Phys. Rev.* D93.3 (2016), p. 034008. DOI: 10.1103/PhysRevD.93.034008. arXiv: 1512.02168 [hep-ph].

[16] Rupak Dutta. "$\Lambda_b \to (\Lambda_c, p)\, \tau\, \nu$ decays within standard model and beyond". In: *Phys. Rev.* D93.5 (2016), p. 054003. DOI: 10.1103/PhysRevD.93.054003. arXiv: 1512.04034 [hep-ph].

[17] William Detmold, Christoph Lehner, and Stefan Meinel. "$\Lambda_b \to p \ell^- \bar{\nu}_\ell$ and $\Lambda_b \to \Lambda_c \ell^- \bar{\nu}_\ell$ form factors from lattice QCD with relativistic heavy quarks". In: *Phys. Rev.* D92.3 (2015), p. 034503. DOI: 10.1103/PhysRevD.92.034503. arXiv: 1503.01421 [hep-lat].

[18] Elvio Di Salvo and Ziad J. Ajaltouni. "Searching for New Physics in Semi-Leptonic Baryon Decays". In: *Mod. Phys. Lett.* A32.08 (2017), p. 1750043. DOI: 10.1142/S0217732317500432. arXiv: 1610.01469 [hep-ph].

[19] Xin-Qiang Li, Ya-Dong Yang, and Xin Zhang. "$\Lambda_b \to \Lambda_c \tau \overline{\nu}_\tau$ decay in scalar and vector leptoquark scenarios". In: *JHEP* 02 (2017), p. 068. DOI: 10.1007/JHEP02(2017)068. arXiv: 1611.01635 [hep-ph].

[20] Alakabha Datta et al. "Phenomenology of $\Lambda_b \to \Lambda_c \tau \overline{\nu}_\tau$ using lattice QCD calculations". In: *JHEP* 08 (2017), p. 131. DOI: 10.1007/JHEP08(2017)131. arXiv: 1702.02243 [hep-ph].

[21] Roel Aaij et al. "Measurement of the shape of the $\Lambda_b^0 \to \Lambda_c^+ \mu^- \overline{\nu}_\mu$ differential decay rate". In: *Phys. Rev.* D96.11 (2017), p. 112005. DOI: 10.1103/PhysRevD.96.112005. arXiv: 1709.01920 [hep-ex].

[22] C. Patrignani et al. "Review of Particle Physics". In: *Chin. Phys.* C40.10 (2016). including the 2017 partial update., p. 100001. DOI: 10.1088/1674-1137/40/10/100001.

[23] R. Aaij et al. "Measurement of b-hadron production fractions in 7 TeV pp collisions". In: *Phys. Rev.* D85 (2012), p. 032008. DOI: 10.1103/PhysRevD.85.032008. arXiv: 1111.2357 [hep-ex].

[24] R. Aaij et al. "Study of the kinematic dependences of Λ_b^0 production in pp collisions and a measurement of the $\Lambda_b^0 \to \Lambda_c^+ \pi^-$ branching fraction". In: *JHEP* 08 (2014), p. 143. DOI: 10.1007/JHEP08(2014)143. arXiv: 1405.6842 [hep-ex].

[25] Lucio Anderlini et al. *The PIDCalib package*. Tech. rep. LHCb-PUB-2016-021. CERN-LHCb-PUB-2016-021. Geneva: CERN, July 2016. URL: https://cds.cern.ch/record/2202412.

[26] F. Archilli et al. "Performance of the Muon Identification at LHCb". In: *JINST* 8 (2013), P10020. DOI: 10.1088/1748-0221/8/10/P10020. arXiv: 1306.0249 [physics.ins-det].

[27] Muriel Pivk and Francois R. Le Diberder. "SPlot: A Statistical tool to unfold data distributions". In: *Nucl. Instrum. Meth.* A555 (2005), pp. 356–369. DOI: 10.1016/j.nima.2005.08.106. arXiv: physics/0402083 [physics.data-an].

[28] Tomasz Skwarnicki. "A study of the radiative CASCADE transitions between the Upsilon-Prime and Upsilon resonances". PhD thesis. Cracow, INP, 1986. URL: http://www-library.desy.de/cgi-bin/showprep.pl?DESY-F31-86-02.

[29] H. Albrecht et al. "Exclusive Hadronic Decays of B Mesons". In: *Z. Phys.* C48 (1990), pp. 543–552. DOI: 10.1007/BF01614687.

[30] J. P. Lees et al. "Measurement of the $D^*(2010)^+$-D^+ Mass Difference". In: *Phys. Rev. Lett.* 119.20 (2017), p. 202003. DOI: 10.1103/PhysRevLett.119.202003. arXiv: 1707.09328 [hep-ex].

[31] W. Verkerke and D. Kirkby. "The RooFit toolkit for data modeling". In: *ArXiv Physics e-prints* (June 2003). eprint: physics/0306116.

[32] Roel Aaij et al. "Determination of the quark coupling strength $|V_{ub}|$ using baryonic decays". In: *Nature Phys.* 11 (2015), pp. 743–747. DOI: 10.1038/nphys3415. arXiv: 1504.01568 [hep-ex].

[33] K. Abe et al. "A Measurement of R(b) using a vertex mass tag". In: *Phys. Rev. Lett.* 80 (1998), pp. 660–665. DOI: 10.1103/PhysRevLett.80.660. arXiv: hep-ex/9708015 [hep-ex].

[34] Gregory Ciezarek and Mitesh Patel. "Searches for lepton number violation, and flavour violation beyond the Yukawa couplings at LHCb". Presented 10 Jun 2014. May 2014. URL: http://cds.cern.ch/record/1755654.

[35] Matthias Neubert. "Heavy quark symmetry". In: *Phys. Rept.* 245 (1994), pp. 259–396. DOI: 10.1016/0370-1573(94)90091-4. arXiv: hep-ph/9306320 [hep-ph].

[36] Adam K. Leibovich and Iain W. Stewart. "Semileptonic Lambda(b) decay to excited Lambda(c) baryons at order Lambda(QCD) / m(Q)". In: *Phys. Rev.* D57 (1998), pp. 5620–5631. DOI: 10.1103/PhysRevD.57.5620. arXiv: hep-ph/9711257 [hep-ph].

[37] Böer, Philipp and Bordone, Marzia and Graverini, Elena and Owen, Patrick and Rotondo, Marcello and van Dyk, Danny. "Testing lepton flavour universality in semileptonic $\Lambda_b \to \Lambda_c^*$ decays". In: *Journal of High Energy Physics* 2018.6 (June 2018), p. 155. ISSN: 1029-8479. DOI: 10.1007/JHEP06(2018)155. arXiv: 1801.08367 [hep-ph]. URL: https://doi.org/10.1007/JHEP06(2018)155.

[38] Adam F. Falk. "Hadrons of arbitrary spin in the heavy quark effective theory". In: *Nucl.Phys.* B378 (1992), pp. 79–94. DOI: 10.1016/0550-3213(92)90004-U.

[39] Elizabeth Ellen Jenkins, Aneesh V. Manohar, and Mark B. Wise. "The Baryon Isgur-Wise function in the large N(c) limit". In: *Nucl. Phys.* B396 (1993), pp. 38–52. DOI: 10.1016/0550-3213(93)90257-P. arXiv: hep-ph/9208248 [hep-ph].

[40] Roel Aaij et al. "Measurement of the b-quark production cross-section in 7 and 13 TeV pp collisions". In: *Phys. Rev. Lett.* 118.5 (2017). [Erratum: Phys. Rev. Lett.119,no.16,169901(2017)], p. 052002. DOI: 10.1103/PhysRevLett.119.169901,10.1103/PhysRevLett.118.052002. arXiv: 1612.05140 [hep-ex].

[41] Sjöstrand, Torbjörn and Mrenna, Stephen and Skands, Peter Z. "PYTHIA 6.4 physics and manual". In: *Journal of High Energy Physics* 2006.05 (2006), p. 026. URL: http://stacks.iop.org/1126-6708/2006/i=05/a=026.

[42] Sjöstrand, Torbjörn and Mrenna, Stephen and Skands, Peter Z. "A Brief Introduction to PYTHIA 8.1". In: *Comput. Phys. Commun.* 178 (2008), pp. 852–867. DOI: 10.1016/j.cpc.2008.01.036. arXiv: 0710.3820 [hep-ph].

[43] G. Ciezarek et al. "Reconstruction of semileptonically decaying beauty hadrons produced in high energy pp collisions". In: *JHEP* 02 (2017), p. 021. DOI: 10.1007/JHEP02(2017)021. arXiv: 1611.08522 [hep-ex].

[44] Thomas Mannel and Danny van Dyk. "Zero-recoil sum rules for $\Lambda_b \to \Lambda_c$ form factors". In: *Phys. Lett.* B751 (2015), pp. 48–53. DOI: 10.1016/j.physletb.2015.10.016. arXiv: 1506.08780 [hep-ph].

[45] Nikolai Uraltsev. "A 'BPS' expansion for B and D mesons". In: *Phys. Lett.* B585 (2004), pp. 253–262. DOI: 10.1016/j.physletb.2004.01.053. arXiv: hep-ph/0312001 [hep-ph].

CHAPTER 9

Summary and prospects

This thesis presents three projects in the scope of flavour physics. These are carried out with two different High Energy Physics experiments, SHiP and LHCb.

The first project consists of a study aimed at assessing the physics potential of the newly proposed SHiP experiment. A detailed simulation of the response of the SHiP detector to the decay of hidden particles, such as Heavy Neutral Leptons and dark photons, was developed. This study allowed to optimize the shape of the SHiP vacuum vessel, leading to substantial modifications with respect to the originally proposed design. Furthermore, a thorough study of the background induced by Standard Model neutrinos was conducted, in order to determine the efficiency of background tagging detectors and to define a selection strategy to isolate signal coming from the decay of hidden particles. Finally, the potential synergy between the SHiP physics potential and hidden particle searches that could take place at the Future Circular Collider was investigated, proving that most of the parameter space of the νMSM can be explored this way. The studies presented in this thesis have been a crucial contribution in the preparation of the SHiP Comprehensive Design Report, which has been positively received by the CERN SPS Committee.

The second project presented in this thesis addresses the challenges of operating the LHCb silicon microstrip tracker in the exceptionally radioactive LHC environment. The evolution of the radiation damage in the Silicon Tracker (ST) was monitored using measurements of the leakage current and of the effective depletion voltage. For the latter measurements, dedicated charge collection efficiency scans were performed. All measurements show a very good agreement with predictions based on phenomenological models. This analysis proves that even the ST sensors closest to the beam axis, where the irradiation level is higher, can be safely operated until the end of the LHC Run II. The ST detectors will subsequently be replaced in the context of the LHCb upgrade.

The third part of this thesis focusses on testing $\Lambda_b \to \Lambda_c^* \ell \bar{\nu}_\ell$ decays in order to confirm or disprove the tension between experimental data and the universality of lepton flavour predicted by the Standard Model. To this aim, the measurement of the ratio $R\left(\Lambda_c^*\right) \equiv \mathrm{Br}\left(\Lambda_b \to \Lambda_c^* \tau \bar{\nu}_\tau\right) / \mathrm{Br}\left(\Lambda_b \to \Lambda_c^* \mu \bar{\nu}_\mu\right)$ is proposed. The challenges with such measurements are discussed in detail, and preparatory studies assessing the expected amount and observable features of background events resembling $\Lambda_b \to \Lambda_c^* \ell \bar{\nu}_\ell$ decays are performed. This studies represent a key step towards the measurement of $R\left(\Lambda_c^*\right)$, which will be performed when the full Run II dataset is available.

The measured value of $R\left(\Lambda_c^*\right)$ will be tested against the Standard Model prediction. However, such prediction cannot be calculated without a measurement of the parameters governing the hadronic $\Lambda_b \to \Lambda_c^*$ transition. Such measurement is possible at LHCb, if a parametrisation modelling the form factors and kinematic observables of the transition is provided. Such parametrisation is given in the last chapter of this thesis, accompanied by a sensitivity study appraising the LHCb sensitivity to the $\Lambda_b \to \Lambda_c^* \ell \bar{\nu}_\ell$ form factor parameters. This study defines the strategy to extract the form factor parameters from a fit to the kinematic and angular observables of the pursued decay. In addition, the analysis reported here shows that only a simultaneous analysis of $\Lambda_b$decays to both the Λ_c (2595) and Λ_c (2625) excided states can provide the required sensitivity.

Acknowledgements

After four incredible years, the time for writing and submitting my thesis came, inexpectedly (as crazy as it may sound). The feeling of emptiness following the final delivery of the manuscript left me unable to cope with what I have always perceived as fundamental: expressing my heartfelt gratitude to all those that made these four years possible, enjoyable and productive. Out of a "I-can't-find-the-right-words" stress, I will therefore at least try to list out the people I am academically and emotionally indebted to.

When I first came to Zürich for my interview, I was mind blown by how warmly the group welcomed me. I am especially beholden to my supervisor, Prof. Straumann, for having immediately believed in me and for inviting me to join his group just a few hours after we first met. I am grateful to Prof. Steinkamp, and happy to have followed his first advice: decline all other job offerings, and come to Zürich. And I extremely owing to Prof. Serra, but also a bit angry at him, for making me love the job of a physics researcher so much!

It is probably impossible to give credit to all the colleagues who worked with me. Not once I have felt lost or lonely in my work. I especially wish to acknowledge Nico and Barbara for diving into the SHiP adventure. Preema, Mark and Michele, whose help with the ST analysis has been invaluable. Marcin and Patrick, for guiding me through the jungle of semileptonic decays. And Danny and Marzia, who opened for me the doors of the frightening world of theory with class and graciousness.

I am grateful to all of my (alphabetically ordered) Zürich friends and colleagues – Albert, Andrea, Andreas, Annarita, Barbara, Camilla, Carlos, Chris, Christian, Danny, Dario, Davide, Espen, Federica, Iaroslava, Marcin, Marco, Marzia, Michele, Patrick, Rafael –, for making my working group feel like family.

I wish to thank my Geneva friends: the NA62 family – Alina, Dario, Enrico, Jacopo, Marco, Matteo, Mattia, Nicolas, Karim, Rossella –, and Nilou, Elisabetta, Lorenzo and Michela, for making my workplace feel like home. I am truly glad we crossed paths. Tini, thanks for baptising my little furry friend; and little Otto, thanks for sitting between me and my keyboard throughout the writing of the thesis! Elizabeth, thanks for adopting and big-sistering me. Oliver, Valentin, thanks for teaching me and letting me teach you how to climb! Thanks to Giulia, Giulio, Lorenzo, I am glad that chance makes us meet often at CERN, and I hope we will always manage keep in touch.

It is difficult to say why I wish to do so in my PhD thesis, but my heart wants to thank my dearest friends from Siena and Pisa, who are always there for me, no matter where they are geographically located. Alberto, Arianna, Luigi, Sara, Marco, Pedro, Steinn, Tommaso: it sounds silly to thank you for friendship, but it is pretty much what I am doing here.

Four years of a journey through the smallest particles composing our Universe, during which I met a lot of interesting people, I lost some of them, and I learned many invaluable things. But there is something I did not need to learn. My family is my best friend. I feel lucky to have been born from them. Every time I felt seriously overwhelmed, my mum, dad and brother were immediately there for me, no matter what. I will owe much to them for the rest of my life, but it is not a burden, it is a pleasure. Mamma, Babbo, Daniele, thanks for your unending support. It is to you that this thesis is dedicated.

Appendices

APPENDIX A

Parametrization of the HNL production and decay branching ratios

Contents

This Appendix gathers the formulas used to model the production and decay of Heavy Neutral Leptons (HNLs) for the studies presented in Chapters 2 and 3. The formulas were found and reviewed from [1], while some of the model parameters can be found in [2, 3].

A.1. HNL production in two- and three-body meson decays

Let H be a charm or beauty meson. Its leptonic decay into a sterile neutrino and a lepton of flavour α has the following branching ratio:

$$\begin{aligned}\frac{d\,\mathrm{Br}\left(H^+ \to l_\alpha^+ N\right)}{dE_N} &= \tau_H \frac{G_F^2 f_H^2 M_H M_N^2}{8\pi} |V_H|^2 |U_\alpha|^2 \\ &\times \left(1 - \frac{M_N^2}{M_H^2} + 2\frac{M_l^2}{M_H^2} + \frac{M_l^2}{M_N^2}\left(1 - \frac{M_l^2}{M_H^2}\right)\right) \\ &\times \sqrt{\left(1 + \frac{M_N^2}{M_H^2} - \frac{M_l^2}{M_H^2}\right)^2 - 4\frac{M_N^2}{M_H^2}} \times \delta\left(E_N - \frac{M_H^2 - M_l^2 + M_N^2}{2M_H}\right), \end{aligned} \quad \text{(A.1)}$$

where τ_H is the meson lifetime, V_H is the CKM matrix element [2], and the meson decay constant f_H can be taken from Table A.1.

For the semileptonic decay into a sterile neutrino, a lepton of flavour α, and a pseudoscalar

H	π^+	K^+	D^+	D_s	B^+	B_s	B_c
f_H (MeV)	130	159.8	222.6	280.1	190	230	480
V_H	V_{ud}	V_{us}	V_{cd}	V_{cs}	V_{ub}	V_{us}	V_{cb}

Table A.1: Meson decay constants [2, 3] and CKM parameters involved in the decay diagram [1].

meson H', the branching ratio reads:

$$\begin{aligned}
\frac{d\,\mathrm{Br}\,(H \longrightarrow H' l_\alpha N)}{dE_N} &= \tau_H |U_\alpha|^2 \frac{|V_{HH'}|^2 G_F^2}{64\pi^3 M_H^2} \times \int dq^2 \Bigg[f_-^2(q^2) \\
&\times \left(q^2 \left(M_N^2 + M_l^2 \right) - \left(M_N^2 - M_l^2 \right)^2 \right) \\
&+ 2 f_+(q^2) f_-(q^2) \Bigg(M_N^2 \left(2M_H^2 - 2M_{H'}^2 - 4E_N M_H - M_l^2 + M_N^2 + q^2 \right) \\
&+ M_l^2 \left(4E_N M_H + M_l^2 - M_N^2 - q^2 \right) \Bigg) \\
&\times f_+^2(q^2) \Bigg(\left(4E_N M_K + M_l^2 - M_N^2 - q^2 \right) \left(2M_K^2 - 2M_\pi^2 - 4E_N M_K - M_l^2 + M_N^2 + q^2 \right) \\
&- \left(2M_K^2 + 2M_\pi^2 - q^2 \right) \left(q^2 - M_N^2 - M_l^2 \right) \Bigg) \Bigg],
\end{aligned} \tag{A.2}$$

where $q^2 = (p_l + p_N)^2$ is the momentum of the $l_\alpha N$ pair, $V_{HH'}$ is the corresponding CKM matrix element, and $f_+(q^2)$, $f_-(q^2)$ are dimensionless hadronic form factors that can be found in literature [2].

Semileptonic decays with a vector boson in the final state are currently not considered, as they are subdominant with respect to the other channels.

A.2. HNL production in τ decays

Branching ratios of two-body decays of a τ lepton into a sterile neutrino and a scalar meson can be modeled with:

$$\begin{aligned}
\frac{d\,\mathrm{Br}\,(\tau \longrightarrow HN)}{dE_N} &= \tau_\tau \frac{|U_\tau|^2}{16\pi} G_F^2 |V_H|^2 f_H^2 M_\tau^3 \left[\left(1 - \frac{M_N^2}{M_\tau^2} \right)^2 - \frac{M_H^2}{M_\tau^2} \left(1 + \frac{M_N^2}{M_\tau^2} \right) \right] \\
&\times \sqrt{\left(1 - \frac{\left(M_H - M_N \right)^2}{M_\tau^2} \right) \left(1 - \frac{\left(M_H + M_N \right)^2}{M_\tau^2} \right)} \times \delta \left(E_N - \frac{M_\tau^2 - M_H^2 + M_N^2}{2M_\tau} \right),
\end{aligned} \tag{A.3}$$

where τ_τ is the lifetime of the τ, V_H is the CKM matrix element, and the meson decay constant

f_H can be taken from Table A.1.

Three-body τ leptonic decays can happen with the exchange of a $W^{\pm}$ boson in a time-like or space-like process. In the first case, there will be a ν_τ in the final state; in the other case, the HNL will mix directly to the τ flavour. We use, respectively:

$$\frac{d\,\mathrm{Br}\,(\tau \to \nu_\tau l_\alpha N)}{dE_N} = \tau_\tau \frac{|U_\alpha|^2}{2\pi^3} G_F^2 M_\tau^2 E_N \left(1 + \frac{M_N^2 - M_l^2}{M_\tau^2} - 2\frac{E_N}{M_\tau}\right) \times \left(1 - \frac{M_l^2}{M_\tau^2 + M_N^2 - 2E_N M_\tau}\right) \sqrt{E_N^2 - M_N^2}\,, \tag{A.4}$$

$$\frac{d\,\mathrm{Br}\,(\tau \to \bar{\nu}_\alpha l_\alpha N)}{dE_N} = \tau_\tau \frac{|U_\tau|^2}{4\pi^3} G_F^2 M_\tau^2 \left(1 - \frac{M_l^2}{M_\tau^2 + M_N^2 - 2E_N M_\tau}\right)^2 \sqrt{E_N^2 - M_N^2} \times \left[(M_\tau - E_N)\left(1 - \frac{M_N^2 + M_l^2}{M_\tau^2}\right) - \left(1 - \frac{M_l^2}{M_\tau^2 + M_N^2 - 2E_N M_\tau}\right) \times \left(\frac{(M_\tau - E_N)^2}{M_\tau} + \frac{E_N^2 - M_N^2}{3M_\tau}\right)\right]. \tag{A.5}$$

A.3. HNL decay

Two-body decay modes of sterile neutrinos can be parametrized as:

$$\Gamma\left(N \to \pi^0 \nu_\alpha\right) = \frac{|U_\alpha|^2}{32\pi} G_F^2 f_\pi^2 M_N^3 \left(1 - \frac{M_\pi^2}{M_N^2}\right)^2, \tag{A.6}$$

$$\Gamma\left(N \to \pi^+ l_\alpha^-\right) = \frac{|U_\alpha|^2}{16\pi} G_F^2 |V_{ud}|^2 f_\pi^2 M_N^3 \left[\left(1 - \frac{M_l^2}{M_N^2}\right)^2 - \frac{M_\pi^2}{M_N^2}\left(1 + \frac{M_l^2}{M_N^2}\right)\right] \tag{A.7}$$

$$\times \sqrt{\left(1 - \frac{(M_\pi - M_l)^2}{M_N^2}\right)\left(1 - \frac{(M_\pi + M_l)^2}{M_N^2}\right)}, \tag{A.8}$$

$$\Gamma\left(N \to \rho^0 \nu_\alpha\right) = \frac{|U_\alpha|^2}{16\pi} \frac{g_\rho^2}{M_\rho^2} G_F^2 M_N^3 \left(1 + 2\frac{M_\rho^2}{M_N^2}\right)\left(1 - \frac{M_\rho^2}{M_N^2}\right)^2, \tag{A.9}$$

$$\Gamma\left(N \to \rho^+ l_\alpha^-\right) = \frac{|U_\alpha|^2}{8\pi} \frac{g_\rho^2}{M_\rho^2} G_F^2 |V_{ud}|^2 M_N^3 \left[\left(1 - \frac{M_l^2}{M_N^2}\right)^2 + \frac{M_\rho^2}{M_N^2}\left(1 + \frac{M_l^2 - 2M_\rho^2}{M_N^2}\right)\right] \tag{A.10}$$

$$\times \sqrt{\left(1 - \frac{\left(M_\rho - M_l\right)^2}{M_N^2}\right)\left(1 - \frac{\left(M_\rho + M_l\right)^2}{M_N^2}\right)}, \tag{A.11}$$

where $g_\rho = 0.102\ \mathrm{GeV}^2$ [2].

For three-body decays into lepton flavours α and β we have:

$$\Gamma\left(N \to \sum_{\alpha,\beta} \nu_\alpha \bar{\nu}_\beta \nu_\beta\right) = \frac{G_F^2 M_N^5}{192\pi^3} \sum_\alpha |U_\alpha|^2 \,, \tag{A.12}$$

$$\Gamma\left(N \to l^-_{\alpha\neq\beta} l^+_\beta \nu_\beta\right) = \frac{G_F^2 M_N^5}{192\pi^3} |U_\alpha|^2 \left(1 - 8x_l^2 + 8x_l^6 - x_l^8 - 12x_l^4 \log x_l^2\right) \tag{A.13}$$

$$\text{with} \quad x_l = \frac{\max\left[M_{l_\alpha},\ M_{l_\beta}\right]}{M_N} \,,$$

$$\begin{aligned}\Gamma\left(N \to \nu_\alpha l^+_\beta l^-_\beta\right) = \frac{G_F^2 M_N^5}{192\pi^3} |U_\alpha|^2 \Bigg[&\left(C_1(1-\delta_{\alpha\beta}) + C_3\delta_{\alpha\beta}\right) \\ &\times \left(\left(1 - 14x_l^2 - 2x_l^4 - 12x_l^6\right)\sqrt{1-4x_l^2} + 12x_l^4\left(x_l^4 - 1\right)L\right) \\ &+ 4\left(C_2(1-\delta_{\alpha\beta}) + C_4\delta_{\alpha\beta}\right) \\ &\times \left(x_l^2\left(2 + 10x_l^2 - 12x_l^4\right)\sqrt{1-4x_l^2} + 6x_l^4\left(1 - 2x_l^2 + 2x_l^4\right)L\right)\Bigg]\end{aligned} \tag{A.14}$$

$$\text{with} \quad L = \log\left[\frac{1 - 3x_l^2 - \left(1 - x_l^2\right)\sqrt{1-4x_l^2}}{x_l^2\left(1 + \sqrt{1-4x_l^2}\right)}\right], \quad x_l \equiv \frac{M_l}{M_N} \,, \text{ and}$$

$$C_1 = \frac{1}{4}\left(1 - 4\sin^2\theta_w + 8\sin^4\theta_w\right), \quad C_2 = \frac{1}{2}\sin^2\theta_w\left(2\sin^2\theta_w - 1\right),$$

$$C_3 = \frac{1}{4}\left(1 + 4\sin^2\theta_w + 8\sin^4\theta_w\right), \quad C_4 = \frac{1}{2}\sin^2\theta_w\left(2\sin^2\theta_w + 1\right).$$

References

[1] Dmitry Gorbunov and Mikhail Shaposhnikov. "How to find neutral leptons of the νMSM?" In: *JHEP* 10 (2007). [Erratum: JHEP11,101(2013)], p. 015. DOI: 10.1007/JHEP11(2013)101,10.1088/1126-6708/2007/10/015. arXiv: 0705.1729 [hep-ph].

[2] K. A. Olive et al. "Review of Particle Physics". In: *Chin. Phys.* C38 (2014), p. 090001. DOI: 10.1088/1674-1137/38/9/090001.

[3] Sheldon Stone. "Measurement of $D_s^+ \to \ell^+\nu$ and the Decay Constant F_{D_s}". In: *Conf. Proc.* C060726 (2006). [,1032(2006)], pp. 1032–1035. arXiv: hep-ex/0610026 [hep-ex].

APPENDIX B

Additional material about the radiation damage in the LHCb Silicon Tracker

Contents

B.1. ST sector numbering scheme and initial full depletion voltages

The TT consists of one detector box containing four detection layers arranged in two pairs. Silicon sensors within each detection layer are electronically grouped into readout sectors consisting of one, two, three or four sensors; all sensors within a readout sector are connected in series to a front-end readout hybrid that carries four 128-channel Beetle chips [1]. Each of the three IT stations consists of four independent detector boxes: one above, one below, and one to either side of the LHC beam pipe. The three stations are positioned equidistantly along the beam pipe. Each detector box contains four detection layers. Detector modules in the boxes to either side of the beam pipe consist of two 410 μm thick sensors that are connected in series to a front-end readout hybrid with three Beetle chips. Detector modules in the boxes above and below the beam pipe consist of a single 320 μm thick silicon sensor connected to a front-end readout hybrid with tree Beetle chips [2]. Each ST readout sector has a unique identifier in the LHCb software, which is embedded in the unique ID associated to the ST readout channels. For simplicity, sectors are referred to with their IDs in Chapter 6 of this thesis, and in this Appendix. Figures B.2 and B.3 relate each ID to the sector position in the TTaU and T3X2 detection layers, respectively.

Both the TT and the IT employ p^+-in-n silicon micro-strip sensors. Sensors for the TT are 500 µm thick, while sensors for the IT are either 320 µm thick (top and bottom boxes) or 410 µm thick (two-sensor modules at the two sides of the beam pipe) [2, 3]. The initial full-

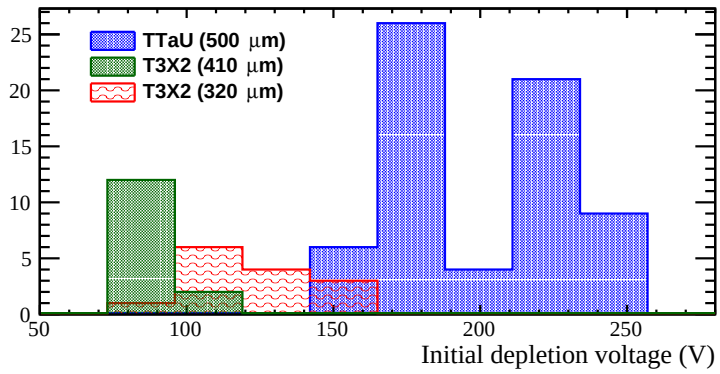

Figure B.1: Initial full depletion voltage of silicon sensors for the ST layers analyzed in the CCE scans (TTaU and T3X2), as determined from laboratory measurements of bulk capacitance as a function of the applied bias voltage [2].

depletion voltages of the sensors were determined from measurements of the bulk capacitance as a function of applied bias voltage and were found to range between 30 and 130 V for the 410 µm thick sensors, between 100 and 165 V for the 320 µm thick sensors and between 135 and 275 V for the 500 µm thick sensors. The distribution of measured full-depletion voltages is shown in Figure B.1 for the sensors of the TTaU and T3X2 layers, analyzed in the CCE scans.

B.2. Time evolution of V_{depl}

Figures 6.25 and 6.26 only show the time evolution of the depletion voltage for two TT sectors in the area close to the beam pipe, and for two IT sectors. Figure B.4 gathers results, together with the predictions, for 5 more TT sectors and 3 more IT sectors at a larger distance from the beam pipe. The integrated dose experienced by readout sectors in the outer region of the TT is significantly lower than that in the central area. Thus, the sectors shown in Figure B.4 show little radiation damage.

B.3. Alternative extraction of V_{depl}

As discussed in Section 6.8, there is a degree of arbitrarity in the choice of how to define the full depletion voltages extracted from the charge collection efficiency *vs.* bias voltage characteristics. There is no defined physical function to describe this shape, and data can fluctuate statistically due to the size of the statistical sample (especially for readout sectors in the outer detector regions) and depending on the preceding analysis steps. The chosen method used to obtain the results discussed in Chapter 6 has been an interpolation by means of a 5^{th} order spline, that is a collection of 5^{th} order polynomial segments with parameters chosen such that the first derivative is always continuous.

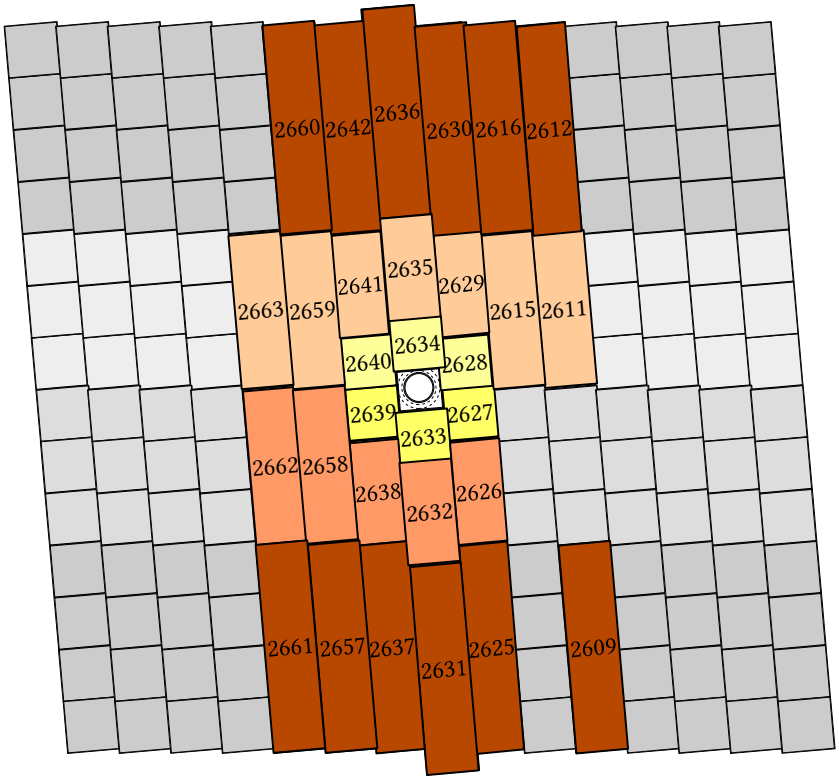

Figure B.2: TTaU readout sector numbering schemes. The greyed out sectors are not used for the CCE scan due to poor statistics or to abnormal statistical fluctuations at the time of the calibration CCE scan.

Cross-checking methods were developed and tested, in order to test the reliability of the spline method and to try to improve the handling of statistical errors. First of all, lower-order splines (2^{nd} and 3^{rd} order) were used, as well as linear interpolation. No significant difference was observed in the results. Due to the arbitrarity of the choice of the polynomials order, we assigned the difference in V_{depl} obtained by linear interpolation and with the 5^{th} order spline as systematic uncertainty on V_{depl} for each sector and each CCE scan. Second, third and fifth order splines are drawn in orange, blue and red, respectively, in Figures B.6 and B.7; linear interpolation is shown in purple.

An additional method not relying on the measurement of the calibration parameter r was developed. This method employs the same procedure to fit the charge collection efficiency plateau as the spline interpolation, but it also uses a fit to adapt a straight line to the data points corresponding to linear charge collection efficiency increase with V_{bias}. These data points are selected as follows.

1. The first data point $(V_0,\ ADC_0)$ is taken.
2. The second data point $(V_1,\ ADC_1)$ is taken. The derivative $\Delta_1 \equiv (ADC_1 - ADC_0)/(V_1 - V_0)$ is computed.
3. For each point i, with $i > 1$:

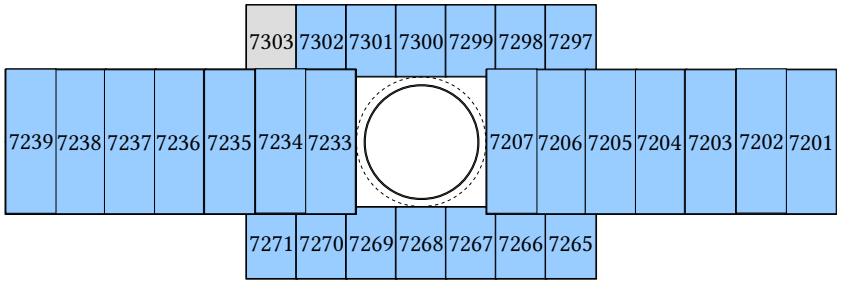

Figure B.3: T3X2 readout sector numbering schemes. The greyed out sectors are not used for the CCE scan due to poor statistics or to abnormal statistical fluctuations at the time of the calibration CCE scan.

a) the derivative $\Delta_i \equiv (ADC_i - ADC_{i-1})/(V_i - V_{i-1})$ is computed;

b) if $(\Delta_i - \Delta_{i-1})/\Delta_i < 50\%$ the point (V_i, ADC_i) is taken, otherwise the collection of data points is put an end to.

The condition $(\Delta_i - \Delta_{i-1})/\Delta_i < 50\%$ ensures that the rounded edge just before the *ADC* plateau is not included in the data set for the straight line fit. The 50% threshold was calibrated on data to ensure maximal acceptance. Different conditions, including a minimum distance from the *ADC* plateau, have been tested, with similar performance. The data points collected by the above procedure are fit with a straight line ℓ, drawn as a red dashed line in Figures B.6 and B.7. Then, the full depletion voltage is defined as the abscissa location where ℓ gets the value of the *ACD* plateau S_{max}, *i.e.*

$$\ell\left(V_{depl}\right) = S_{max} \quad \Longrightarrow \quad V_{depl} \equiv \ell^{-1}\left(S_{max}\right). \tag{B.1}$$

The difference in V_{depl} obtained by linear interpolation and with the straight line fit is added as systematic uncertainty on V_{depl} for each sector and each CCE scan, as with the 5^{th} order spline method. By definition the V_{depl} value obtained with the straight line method is on average slightly larger than that obtained using an interpolating spline method and the r calibration ratio. However, this applies systematically to all of the V_{depl} measurements obtained in the various CCE scans, hence the evolution with time (or fluence) of the difference $V_{depl} - V^0_{depl}$ is insensitive to this shift. Moreover, the choice of defining the depletion voltage after detector installation as a fraction $V_{depl} \equiv S^{-1}(r \times S_{max})$ with the spine method was also arbitrary.

The time and fluence evolutions of V_{depl} calculated with the spline method and with the straight line fit method are compared in Figures B.8 and B.9, respectively, for various TT readout sectors, and for all of the TT and IT readout sectors. The number of data points in Figure B.9 is smaller in the panels showing the results obtained with the straight line fit method. This is due to the fact that a result can be obtained only if at least three data points are used for the straight line fit, otherwise the measurement is discarded. Because of limited statistics, sometimes it happens that data fluctuate too wildly for a straight line fit to be possible.

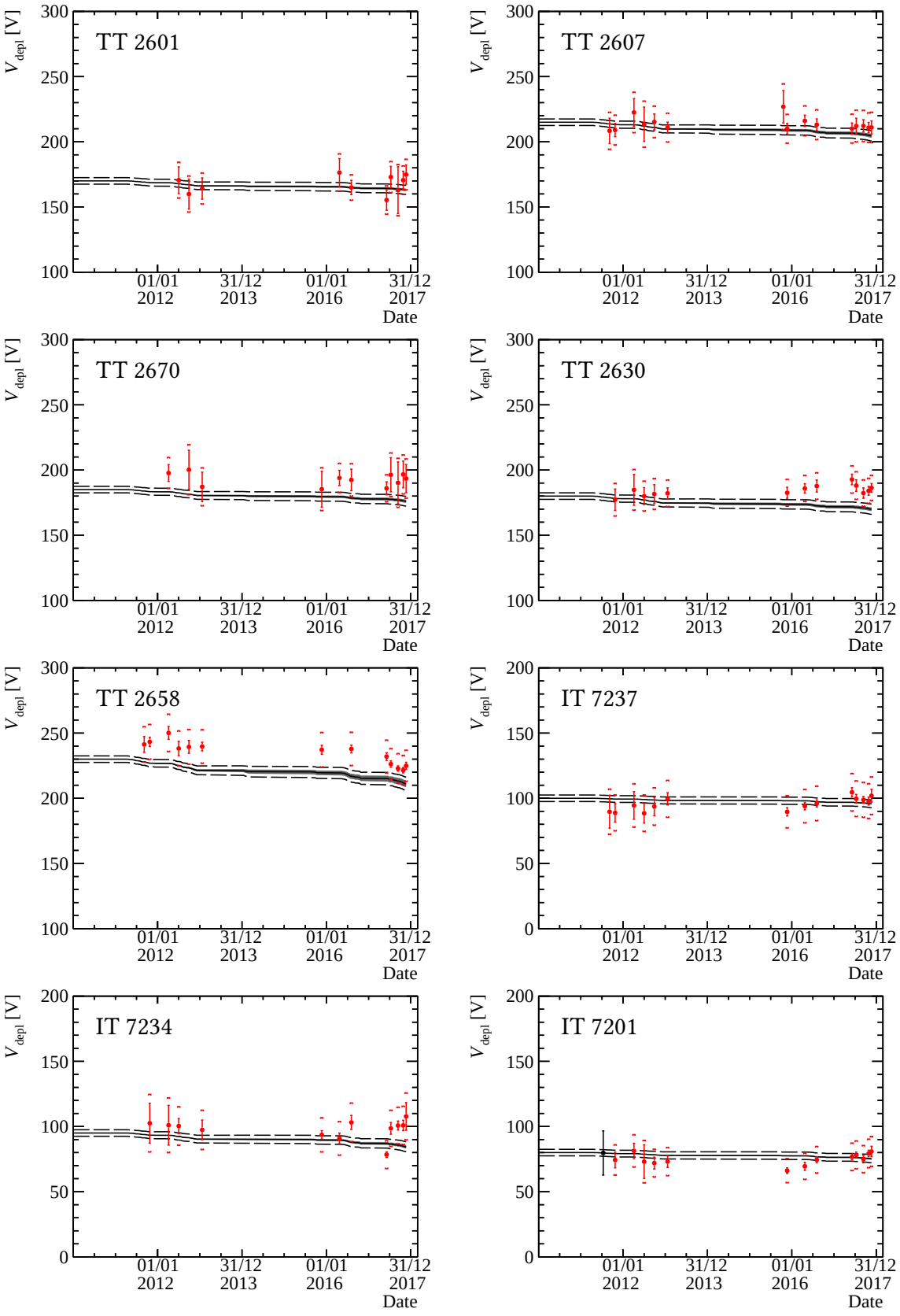

Figure B.4: Evolution of V_{depl} with time for various TT and IT readout sectors.

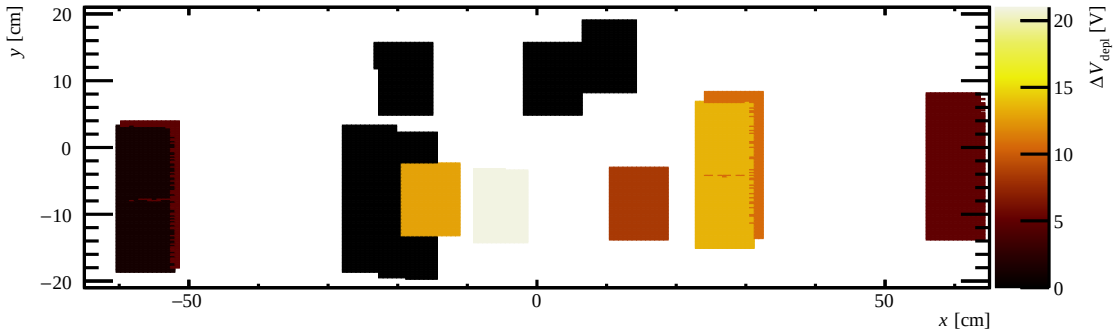

Figure B.5: Absolute change in V_{depl} in the IT in September 2017.

In general, the various order splines, the linear interpolation, and the straight line fit all result in V_{depl} measurements which are compatible with the predicted evolution within the uncertainties on the measurements and on the simulation. We conclude that the results shown in Chapter 6 are trustworthy.

References

[1] M. Agari et al. “Beetle: A radiation hard readout chip for the LHCb experiment”. In: *Nucl. Instrum. Meth.* A518 (2004), pp. 468–469. DOI: 10.1016/j.nima.2003.11.058.

[2] Elena Graverini et al. “Monitoring radiation damage in the LHCb Tracker Turicensis”. In preparation. 2018.

[3] A. A. Alves Jr. et al. “The LHCb detector at the LHC”. In: *JINST* 3 (2008), S08005. DOI: 10.1088/1748-0221/3/08/S08005.

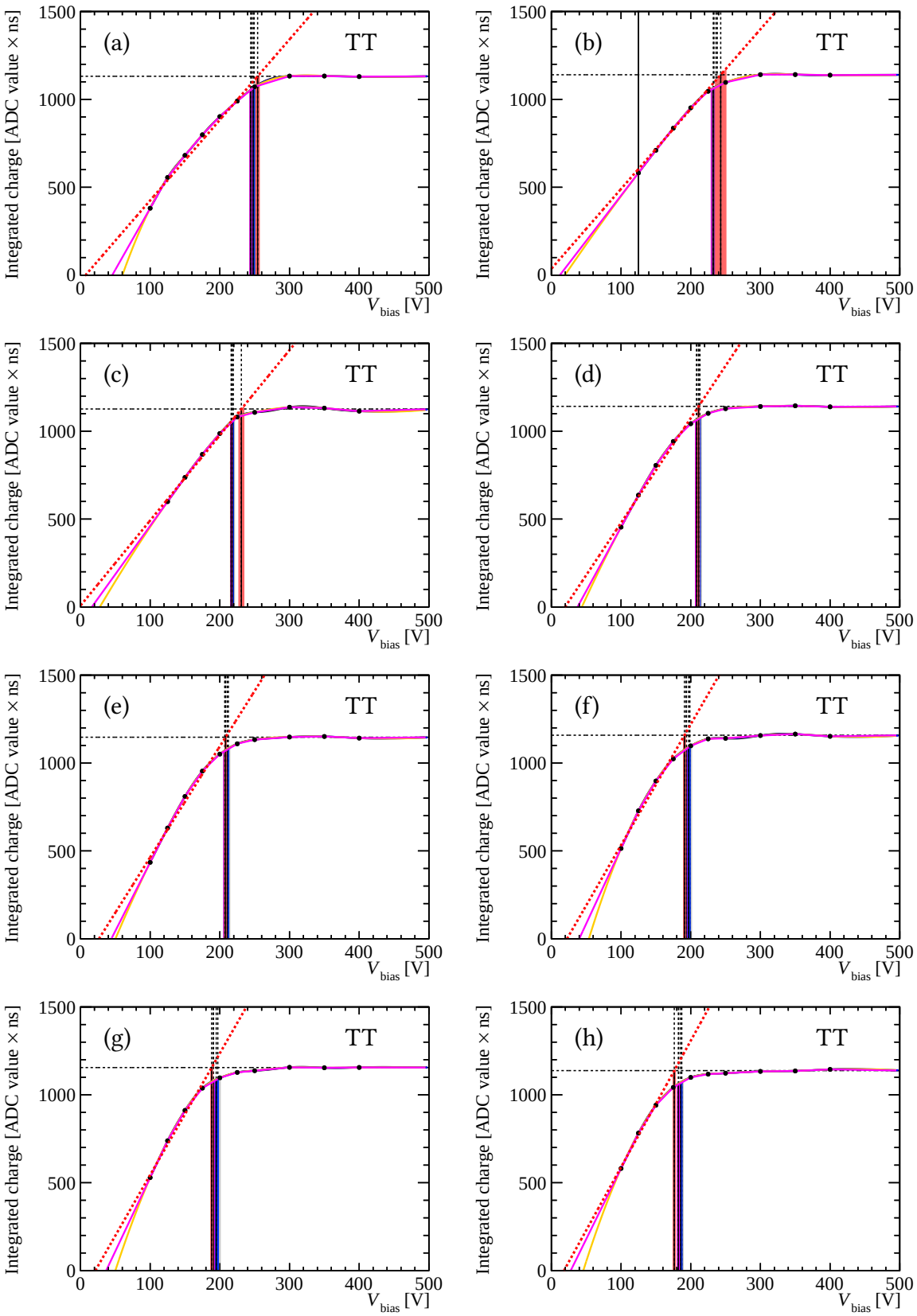

Figure B.6: Integrated collected charge as a function of the applied bias voltage for a central TT read-out sector (2634) measured in CCE scans taken in: April 2012 (a), July 2012 (b), January 2013 (c), November 2015 (d), August 2016 (e), July 2017 (f), September 2017 (g), October 2017 (h). Linear interpolation is drawn in purple; second, third and fifth order interpolating splines are drawn in orange, blue and red, respectively. The straight line fitting the rising edge of the characteristic is drawn as a dashed red line. Only statistical uncertainties are displayed.

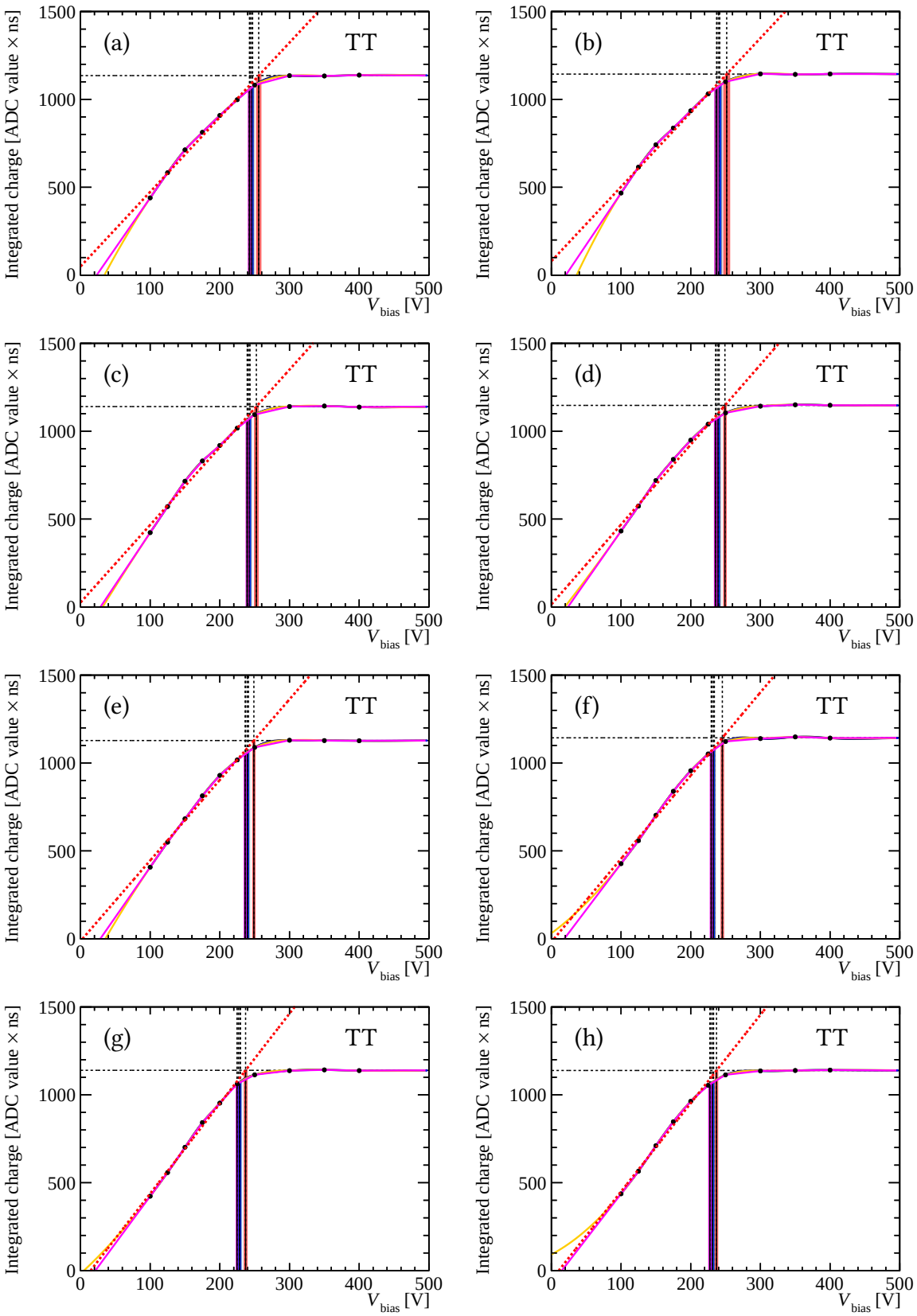

Figure B.7: Integrated collected charge as a function of the applied bias voltage for the TT readout sector 2635 measured in CCE scans taken in: April 2012 (a), July 2012 (b), January 2013 (c), November 2015 (d), August 2016 (e), July 2017 (f), September 2017 (g), October 2017 (h). Linear interpolation is drawn in purple; second, third and fifth order interpolating splines are drawn in orange, blue and red, respectively. The straight line fitting the rising edge of the characteristic is drawn as a dashed red line. Only statistical uncertainties are displayed.

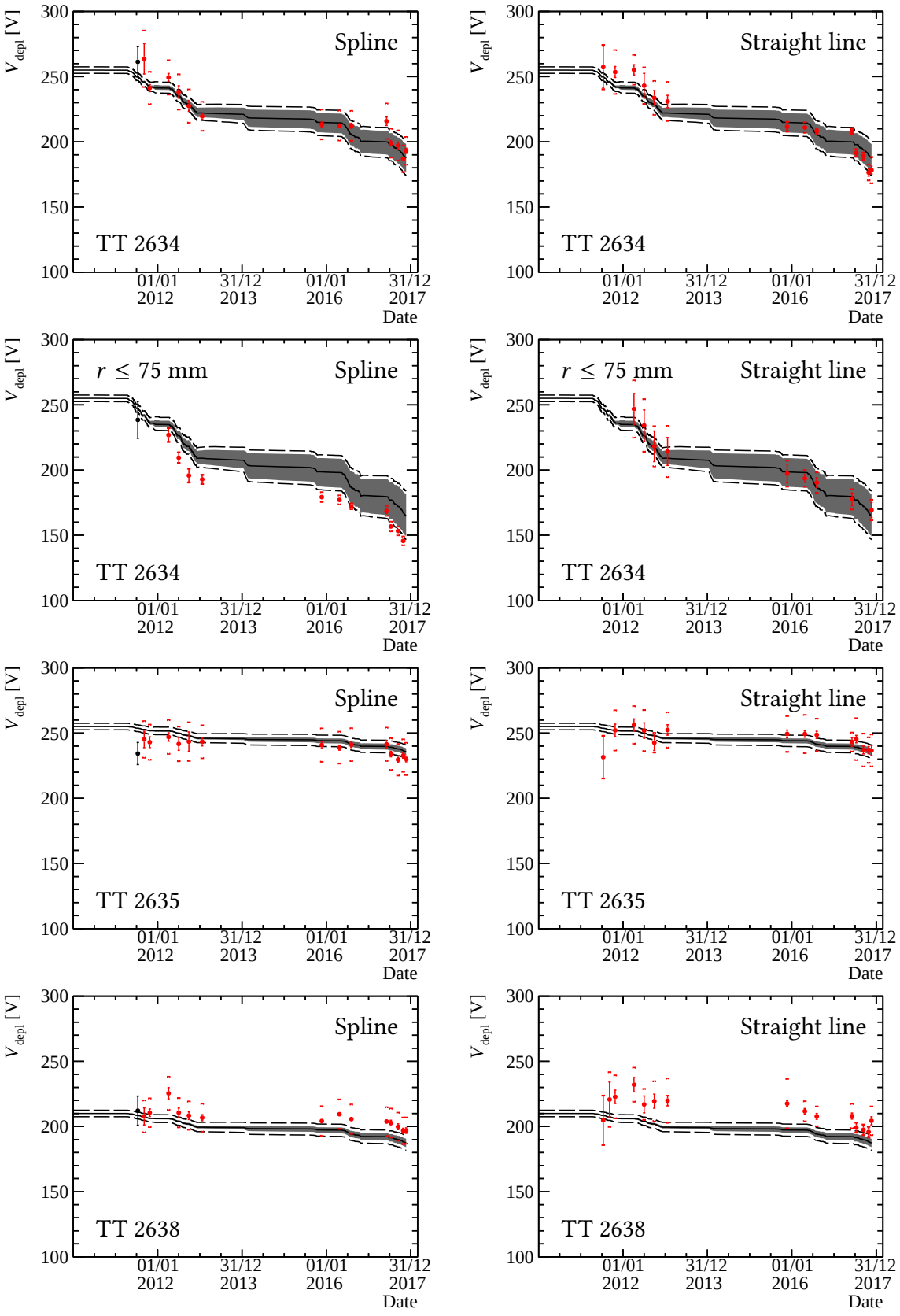

Figure B.8: Comparison of the measured time evolution of V_{depl} for various TT readout sectors obtained by interpolating with a 5th order spline and by fitting the rising edge with a straight line.

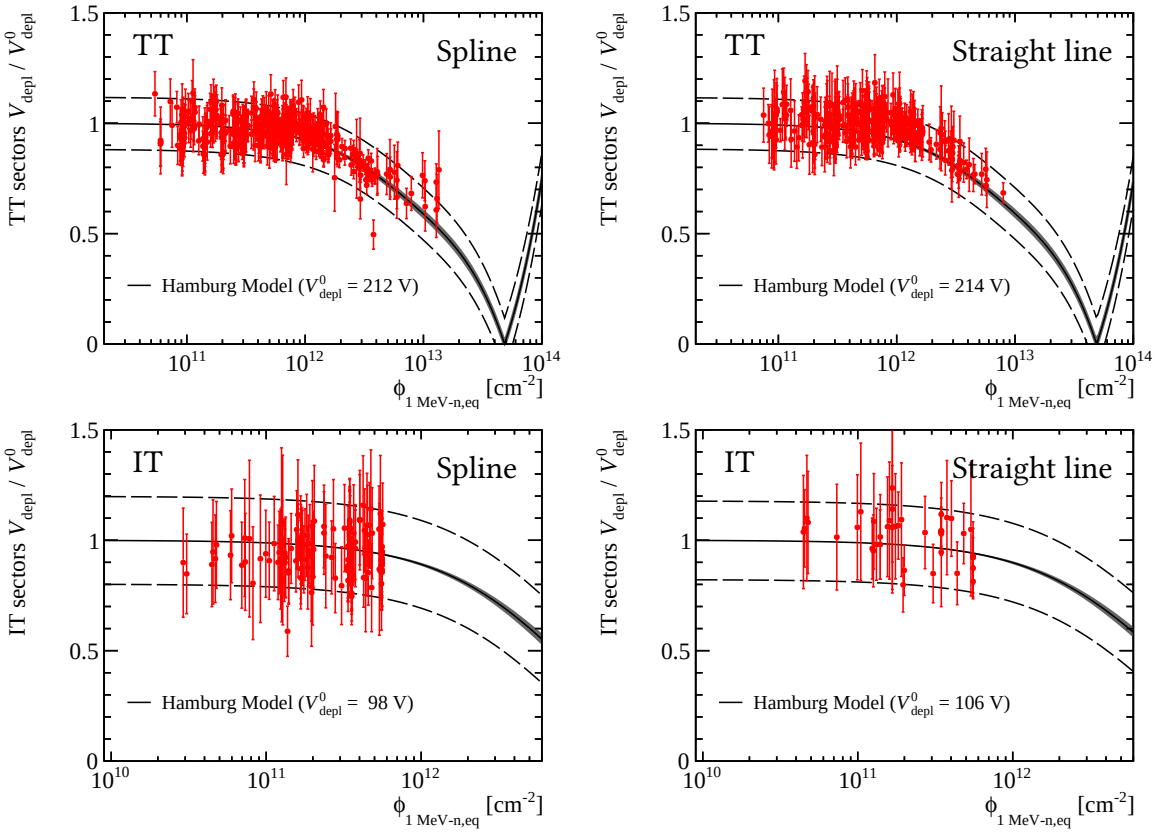

Figure B.9: Comparison of the evolution of V_{depl} with fluence, for all the TT sectors and all the IT sectors, obtained by interpolating with a 5th order spline and by fitting the rising edge with a straight line.

APPENDIX C

Additional material about the $\Lambda_b \to \Lambda_c^* \ell \bar{\nu}_\ell$ form factors analysis

Contents

C.1. Parametrisation of the $\Lambda_b \to \Lambda_c(2595)$ and $\Lambda_b \to \Lambda_c(2625)$ form factors

In the following, form factors for the $\Lambda_b \to \Lambda_c^* \ell \bar{\nu}_\ell$ transition are calculated in the framework of HQET, assuming $m_b \to \infty$, $m_c \to \infty$, and $m_c/m_b = const$. The $\Lambda_b \to \Lambda_c^*$ transition is decoupled form the subsequent $\Lambda_c^* \to \Lambda_c \pi\pi$ decay thanks to the small decay width of the two Λ_c^* states[1], and the $\Lambda_c^* \to \Lambda_c \pi\pi$ process is factorized upon.

This allows to calculate perturbative expressions of the related form factors up to order $1/m$ in Heavy Quark Expansion (HQE)[2]. With this parametrisation, all of the form factors for Λ_b transitions to both Λ_c^* states are expressed in terms of two hadronic Isgur-Wise (IW) functions [1].

Following the procedure thoroughly described in [2], the following expressions are obtained for the q^2 dependence of the $\Lambda_b \to \Lambda_c(2595)$ vector longitudinal, time-like and perpendicular

[1] This is called *narrow width approximation.*
[2] The mass considered here is the b quark mass.

form factors:

$$f_{1/2,0} = \frac{\sqrt{s_+}}{2\left(m_{\Lambda_b} m_{\Lambda_c^*}\right)^{3/2}} \Bigg\{ \Bigg[s_- \left(C_1(\bar{w}) + \frac{s_+ \left(C_2(\bar{w}) m_{\Lambda_c^*} + C_3(\bar{w}) m_{\Lambda_b} \right)}{2 m_{\Lambda_b} m_{\Lambda_c^*} \left(m_{\Lambda_b} + m_{\Lambda_c^*} \right)} \right) + \frac{\left(m_{\Lambda_b} - m_{\Lambda_c^*} \right)}{m_{\Lambda_b} + m_{\Lambda_c^*}} \left(\frac{m_{\Lambda_b}^2 - m_{\Lambda_c^*}^2 + q^2}{2 m_{\Lambda_b}} \bar{\Lambda} - \frac{m_{\Lambda_b}^2 - m_{\Lambda_c^*}^2 - q^2}{2 m_{\Lambda_c^*}} \bar{\Lambda}' \right) \Bigg] \zeta - 2 \left(m_{\Lambda_b} - m_{\Lambda_c^*} \right) \zeta_{\mathrm{SL}} \Bigg\}, \tag{C.1}$$

$$f_{1/2,t} = \frac{\sqrt{s_-}}{2\left(m_{\Lambda_b} m_{\Lambda_c^*}\right)^{3/2}} \Bigg\{ \Bigg[C_1(\bar{w}) s_+ + \frac{m_{\Lambda_b} + m_{\Lambda_c^*}}{m_{\Lambda_b} - m_{\Lambda_c^*}} \Bigg(\frac{m_{\Lambda_b}^2 - m_{\Lambda_c^*}^2 + q^2}{2 m_{\Lambda_b}} \left(\bar{\Lambda} + \frac{C_2(\bar{w}) s_+}{m_{\Lambda_b} + m_{\Lambda_c^*}} \right) - \frac{m_{\Lambda_b}^2 - m_{\Lambda_c^*}^2 - q^2}{2 m_{\Lambda_c^*}} \left(\bar{\Lambda}' - \frac{C_3(\bar{w}) s_+}{m_{\Lambda_b} + m_{\Lambda_c^*}} \right) \Bigg) \Bigg] \zeta - 2 \frac{\left(m_{\Lambda_b} + m_{\Lambda_c^*} \right)^2}{m_{\Lambda_b} - m_{\Lambda_c^*}} \zeta_{\mathrm{SL}} \Bigg\}, \tag{C.2}$$

$$f_{1/2,\perp} = \frac{\sqrt{s_+}}{2\left(m_{\Lambda_b} m_{\Lambda_c^*}\right)^{3/2}} \Bigg\{ \Bigg[C_1(\bar{w}) s_- + \frac{3 m_{\Lambda_b}^2 + m_{\Lambda_c^*}^2 - q^2}{2 m_{\Lambda_b}} \bar{\Lambda} - \frac{m_{\Lambda_b}^2 + 3 m_{\Lambda_c^*}^2 - q^2}{2 m_{\Lambda_c^*}} \bar{\Lambda}' \Bigg] \zeta - 2 m_{\Lambda_b} \zeta_{\mathrm{SL}} \Bigg\}, \tag{C.3}$$

while for the $\Lambda_b \to \Lambda_c(2595)$ axial-vector form factors we obtain:

$$g_{1/2,0} = \frac{\sqrt{s_-}}{2\left(m_{\Lambda_b} m_{\Lambda_c^*}\right)^{3/2}} \Bigg\{ \Bigg[s_+ \left(C_1(\bar{w}) - \frac{s_- \left(C_2(\bar{w}) m_{\Lambda_c^*} + C_3(\bar{w}) m_{\Lambda_b} \right)}{2 m_{\Lambda_b} m_{\Lambda_c^*} \left(m_{\Lambda_b} - m_{\Lambda_c^*} \right)} \right) + \frac{m_{\Lambda_b} + m_{\Lambda_c^*}}{m_{\Lambda_b} - m_{\Lambda_c^*}} \left(\frac{m_{\Lambda_b}^2 - m_{\Lambda_c^*}^2 + q^2}{2 m_{\Lambda_b}} \bar{\Lambda} - \frac{m_{\Lambda_b}^2 - m_{\Lambda_c^*}^2 - q^2}{2 m_{\Lambda_c^*}} \bar{\Lambda}' \right) \Bigg] \zeta - 2 \left(m_{\Lambda_b} + m_{\Lambda_c^*} \right) \zeta_{\mathrm{SL}} \Bigg\}, \tag{C.4}$$

$$
\begin{aligned}
g_{1/2,t} =& \frac{\sqrt{s_+}}{2\left(m_{\Lambda_b} m_{\Lambda_c^*}\right)^{3/2}} \Bigg\{ \Bigg[C_1(\bar{w}) s_- + \frac{m_{\Lambda_b} - m_{\Lambda_c^*}}{m_{\Lambda_b} + m_{\Lambda_c^*}} \Bigg(\frac{m_{\Lambda_b}^2 - m_{\Lambda_c^*}^2 + q^2}{2m_{\Lambda_b}} \left(\bar{\Lambda} - \frac{C_2(\bar{w}) s_-}{m_{\Lambda_b} - m_{\Lambda_c^*}} \right) \\
& - \frac{m_{\Lambda_b}^2 - m_{\Lambda_c^*}^2 - q^2}{2m_{\Lambda_c^*}} \left(\bar{\Lambda}' + \frac{C_3(\bar{w}) s_-}{m_{\Lambda_b} - m_{\Lambda_c^*}} \right) \Bigg) \Bigg] \zeta \\
& - 2 \frac{\left(m_{\Lambda_b} - m_{\Lambda_c^*}\right)^2}{m_{\Lambda_b} + m_{\Lambda_c^*}} \zeta_{\mathrm{SL}} \Bigg\},
\end{aligned} \tag{C.5}
$$

$$
\begin{aligned}
g_{1/2,\perp} =& \frac{\sqrt{s_-}}{2\left(m_{\Lambda_b} m_{\Lambda_c^*}\right)^{3/2}} \Bigg\{ \Bigg[C_1(\bar{w}) s_+ + \bar{\Lambda} \frac{3m_{\Lambda_b}^2 + m_{\Lambda_c^*}^2 - q^2}{2m_{\Lambda_b}} - \bar{\Lambda}' \frac{m_{\Lambda_b}^2 + 3m_{\Lambda_c^*}^2 - q^2}{2m_{\Lambda_c^*}} \Bigg] \zeta \\
& - 2m_{\Lambda_b} \zeta_{\mathrm{SL}} \Bigg\},
\end{aligned} \tag{C.6}
$$

where:

- $s_\pm \equiv (m_{\Lambda_b} \pm m_{\Lambda_c^*})^2 - q^2$,
- $w \equiv v \cdot v' = \left(m_{\Lambda_b}^2 + m_{\Lambda_c^*}^2 - q^2 \right) / \left(2m_{\Lambda_b} m_{\Lambda_c^*} \right)$ is the scalar product of the initial and final state four-momenta v and v', and
- $\bar{w} \equiv \left(1 + \frac{\bar{\Lambda}}{m_b} + \frac{\bar{\Lambda}'}{m_c} \right) w - \left(\frac{\bar{\Lambda}}{m_b} + \frac{\bar{\Lambda}'}{m_c} \right)$ is the recoil experienced by the heavy quark within the hadron, where $\bar{\Lambda}$ and $\bar{\Lambda}'$ are the HQET parameters in the infinite mass limit, representing the energy of the gluons and light quarks [3].

Here, the form factors are expressed in terms of the C_1, C_2 and C_3 Wilson coefficients [3]. Finally, equations of motion allow to relate the form factors such that each of them can be expressed in terms of only two hadronic Isgur-Wise (IW) functions, a leading order one (here denoted by the ζ symbol) and a subleading order one (ζ_{SL}).

The $\Lambda_c(2625)$ is a $J^P = 3/2^-$ state, and therefore it has two additional form factors $F_{3/2,\perp}$ and $G_{3/2,\perp}$. The vector form factors read for the $\Lambda_b \to \Lambda_c(2625)$ transition read:

$$
\begin{aligned}
F_{1/2,\perp} =& \frac{\sqrt{s_+}}{2\left(m_{\Lambda_b} m_{\Lambda_c^*}\right)^{3/2}} \Bigg\{ \Bigg[C_1(\bar{w}) s_- + \frac{3m_{\Lambda_b}^2 + m_{\Lambda_c^*}^2 - q^2}{2m_{\Lambda_b}} \bar{\Lambda} - \frac{m_{\Lambda_b}^2 + 3m_{\Lambda_c^*}^2 - q^2}{2m_{\Lambda_c^*}} \bar{\Lambda}' \Bigg] \zeta \\
& + m_{\Lambda_b} \zeta_{\mathrm{SL}} \Bigg\},
\end{aligned} \tag{C.7}
$$

$$F_{1/2,t} = \frac{\sqrt{s_-}}{2\left(m_{\Lambda_b} m_{\Lambda_c^*}\right)^{3/2}} \Bigg\{ \Bigg[C_1(\bar{w}) s_+ + \frac{m_{\Lambda_b} + m_{\Lambda_c^*}}{m_{\Lambda_b} - m_{\Lambda_c^*}} \Bigg(\frac{m_{\Lambda_b}^2 - m_{\Lambda_c^*}^2 + q^2}{2m_{\Lambda_b}} \left(\bar{\Lambda} + \frac{C_2(\bar{w}) s_+}{m_{\Lambda_b} + m_{\Lambda_c^*}} \right) - \frac{m_{\Lambda_b}^2 - m_{\Lambda_c^*}^2 - q^2}{2m_{\Lambda_c^*}} \left(\bar{\Lambda}' - \frac{C_3(\bar{w}) s_+}{m_{\Lambda_b} + m_{\Lambda_c^*}} \right) \Bigg) \Bigg] \zeta + \frac{\left(m_{\Lambda_b} + m_{\Lambda_c^*}\right)^2}{m_{\Lambda_b} - m_{\Lambda_c^*}} \zeta_{\mathrm{SL}} \Bigg\}, \tag{C.8}$$

$$F_{1/2,0} = \frac{\sqrt{s_+}}{2\left(m_{\Lambda_b} m_{\Lambda_c^*}\right)^{3/2}} \Bigg\{ \Bigg[s_- \left(C_1(\bar{w}) + \frac{s_+ \left(C_2(\bar{w}) m_{\Lambda_c^*} + C_3(\bar{w}) m_{\Lambda_b} \right)}{2m_{\Lambda_b} m_{\Lambda_c^*} \left(m_{\Lambda_b} + m_{\Lambda_c^*} \right)} \right) + \frac{m_{\Lambda_b} - m_{\Lambda_c^*}}{m_{\Lambda_b} + m_{\Lambda_c^*}} \left(\frac{m_{\Lambda_b}^2 - m_{\Lambda_c^*}^2 + q^2}{2m_{\Lambda_b}} \bar{\Lambda} - \frac{m_{\Lambda_b}^2 - m_{\Lambda_c^*}^2 - q^2}{2m_{\Lambda_c^*}} \bar{\Lambda}' \right) \Bigg] \zeta + \left(m_{\Lambda_b} - m_{\Lambda_c^*} \right) \zeta_{\mathrm{SL}} \Bigg\}, \tag{C.9}$$

$$F_{3/2,\perp} = -\frac{\sqrt{s_+}}{2m_{\Lambda_b}^{3/2} m_{\Lambda_c^*}^{1/2}} \zeta_{\mathrm{SL}}, \tag{C.10}$$

and the axial-vector form factors:

$$G_{1/2,\perp} = \frac{\sqrt{s_-}}{2\left(m_{\Lambda_b} m_{\Lambda_c^*}\right)^{3/2}} \Bigg\{ \Bigg[C_1(\bar{w}) s_+ + \frac{3m_{\Lambda_b}^2 + m_{\Lambda_c^*}^2 - q^2}{2m_{\Lambda_b}} \bar{\Lambda} - \frac{m_{\Lambda_b}^2 + 3m_{\Lambda_c^*}^2 - q^2}{2m_{\Lambda_c^*}} \bar{\Lambda}' \Bigg] \zeta + m_{\Lambda_b} \zeta_{\mathrm{SL}} \Bigg\}, \tag{C.11}$$

$$G_{1/2,t} = \frac{\sqrt{s_+}}{2\left(m_{\Lambda_b} m_{\Lambda_c^*}\right)^{3/2}} \Bigg\{ \Bigg[C_1(\bar{w}) s_- + \frac{m_{\Lambda_b} - m_{\Lambda_c^*}}{m_{\Lambda_b} + m_{\Lambda_c^*}} \Bigg(\frac{m_{\Lambda_b}^2 - m_{\Lambda_c^*}^2 + q^2}{2m_{\Lambda_b}} \left(\bar{\Lambda} - \frac{C_2(\bar{w}) s_-}{m_{\Lambda_b} - m_{\Lambda_c^*}} \right) - \frac{m_{\Lambda_b}^2 - m_{\Lambda_c^*}^2 - q^2}{2m_{\Lambda_c^*}} \left(\bar{\Lambda}' + \frac{C_3(\bar{w}) s_-}{m_{\Lambda_b} - m_{\Lambda_c^*}} \right) \Bigg) \Bigg] \zeta + \frac{\left(m_{\Lambda_b} - m_{\Lambda_c^*}\right)^2}{m_{\Lambda_b} + m_{\Lambda_c^*}} \zeta_{\mathrm{SL}} \Bigg\}, \tag{C.12}$$

$$G_{1/2,0} = \frac{\sqrt{s_-}}{2\left(m_{\Lambda_b} m_{\Lambda_c^*}\right)^{3/2}} \Bigg\{ \Bigg[s_+ \left(C_1(\bar{w}) - \frac{s_- (C_2(\bar{w}) m_{\Lambda_c^*} + C_3(\bar{w}) m_{\Lambda_b})}{2m_{\Lambda_b} m_{\Lambda_c^*} (m_{\Lambda_b} - m_{\Lambda_c^*})} \right) + \frac{m_{\Lambda_b} + m_{\Lambda_c^*}}{m_{\Lambda_b} - m_{\Lambda_c^*}} \left(\frac{m_{\Lambda_b}^2 - m_{\Lambda_c^*}^2 + q^2}{2m_{\Lambda_b}} \bar{\Lambda} - \frac{m_{\Lambda_b}^2 - m_{\Lambda_c^*}^2 - q^2}{2m_{\Lambda_c^*}} \bar{\Lambda}' \right) \Bigg] \zeta + \left(m_{\Lambda_b} + m_{\Lambda_c^*} \right) \zeta_{\mathrm{SL}} \Bigg\}, \tag{C.13}$$

$$G_{3/2,\perp} = -\frac{\sqrt{s_-}}{2m_{\Lambda_b}^{3/2} m_{\Lambda_c^*}^{1/2}} \zeta_{\mathrm{SL}}. \tag{C.14}$$

C.2. Reconstruction of the W rest frame in the $\Lambda_b \to \Lambda_c^* \mu\nu$ decay

This Appendix offers additional information concerning the studies of the LHCb resolution with respect to the reconstruction of the $\Lambda_b \to \Lambda_c^* \mu \bar{\nu}_\nu$ decay kinematics. The decrease in resolution at high momentum transfer is introduced in Section 8.2.1. The two kinematical variables considered are q^2, *i.e.* the invariant mass of the $\mu\bar{\nu}_\mu$ pair, and θ_ℓ, the muon helicity angle. The latter is defined as the angle between the μ momentum and the Λ_b momentum as measured in the rest frame of the exchanged W (*i.e.* in the rest frame of the $\mu\bar{\nu}_\mu$ pair).

The difficulty at high q^2 arises from the poor reconstruction of the W rest frame. In order to compute the helicity angle θ_ℓ, a boost is required with the same magnitude as the momentum of the reconstructed Λ_c^*, and opposite direction. However, the Λ_c^* is poorly reconstructed at high q^2. Figures C.1 and C.2 show the simulated (black) and reconstructed (red) momentum of the Λ_c^* in four bins of q^2 an four bins of $\cos\theta_\ell$. A significan migration towards larger Λ_c^* momenta is observed in the highest q^2 bins, and this effect is more prominent for $\cos\theta_\ell > 0$.

C.3. Additional binnings for the $\Lambda_b \to \Lambda_c^* \ell \nu$ form factor fit

In this Appendix, additional material is offered to motivate the choice of a 4×4 binning scheme for a two-dimensional fit to the q^2 and $\cos\theta_\ell$ distributions of $\Lambda_b \to \Lambda_c^* \mu \bar{\nu}_\mu$ decays. The purity of datasets divided into fewer or more bins in both variables has been studies. Figure C.3 gathers the q^2 (a–d) and $\cos\theta_\ell$ (e–h) bin purity of data samples divided into three to six bins. As the binning gets finer, the bin purity decreases. Figure C.4 shows the correlation levels corresponding to events migration among three to six bins in q^2 (a–d) and three to six bins (e–h) in $\cos\theta_\ell$.

A minimum number of four bins in q^2 and three bins in $\cos\theta_\ell$ are found required in order to obtain sensitivity to all of the parameters. The amount of available data and the good angular resolution at LHCb allow to add an extra bin in $\cos\theta_\ell$. The fitted parameter distributions shown in Figure C.5 demonstrate that additional bins in either kinematic variable do not improve the fit precision.

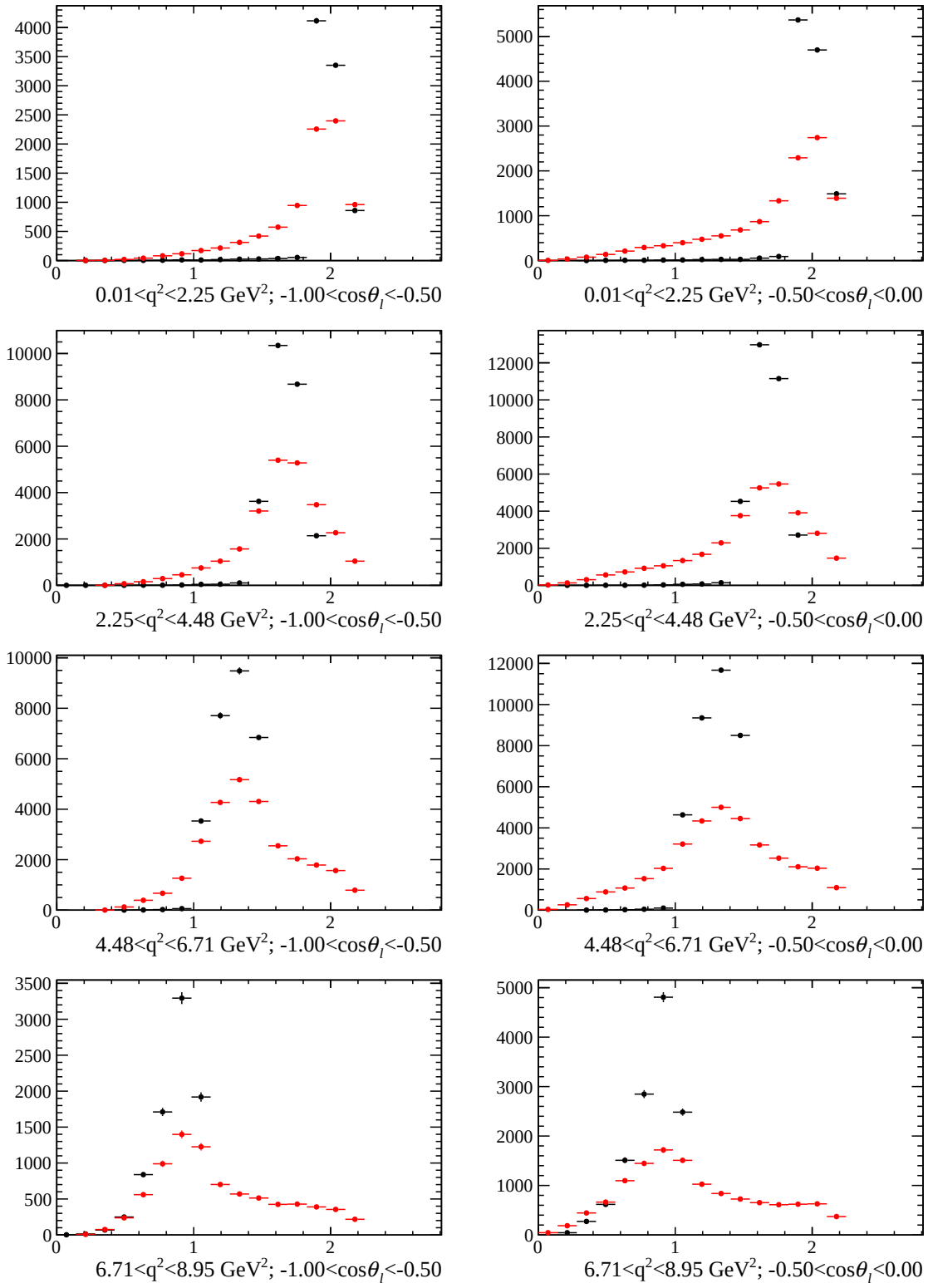

Figure C.1: Simulated (black) and reconstructed (red) Λ_c^* momentum in four bins of q^2 and four bins of $\cos\theta_\ell$. This panel displays all the q^2 bins, and the first two $\cos\theta_\ell$ bins.

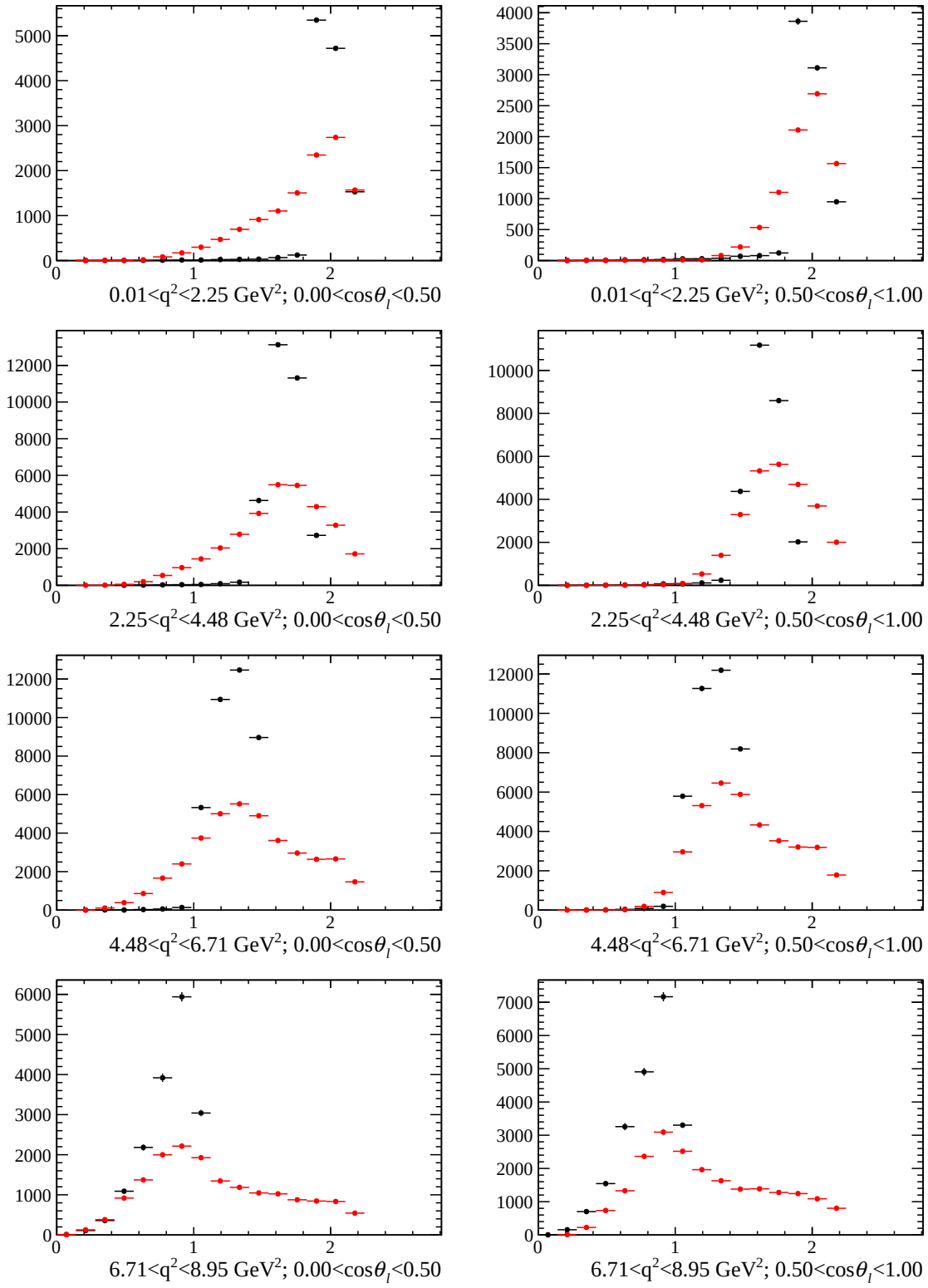

Figure C.2: Simulated (black) and reconstructed (red) Λ_c^* momentum in four bins of q^2 and four bins of $\cos\theta_\ell$. This panel displays all the q^2 bins, and the last two $\cos\theta_\ell$ bins.

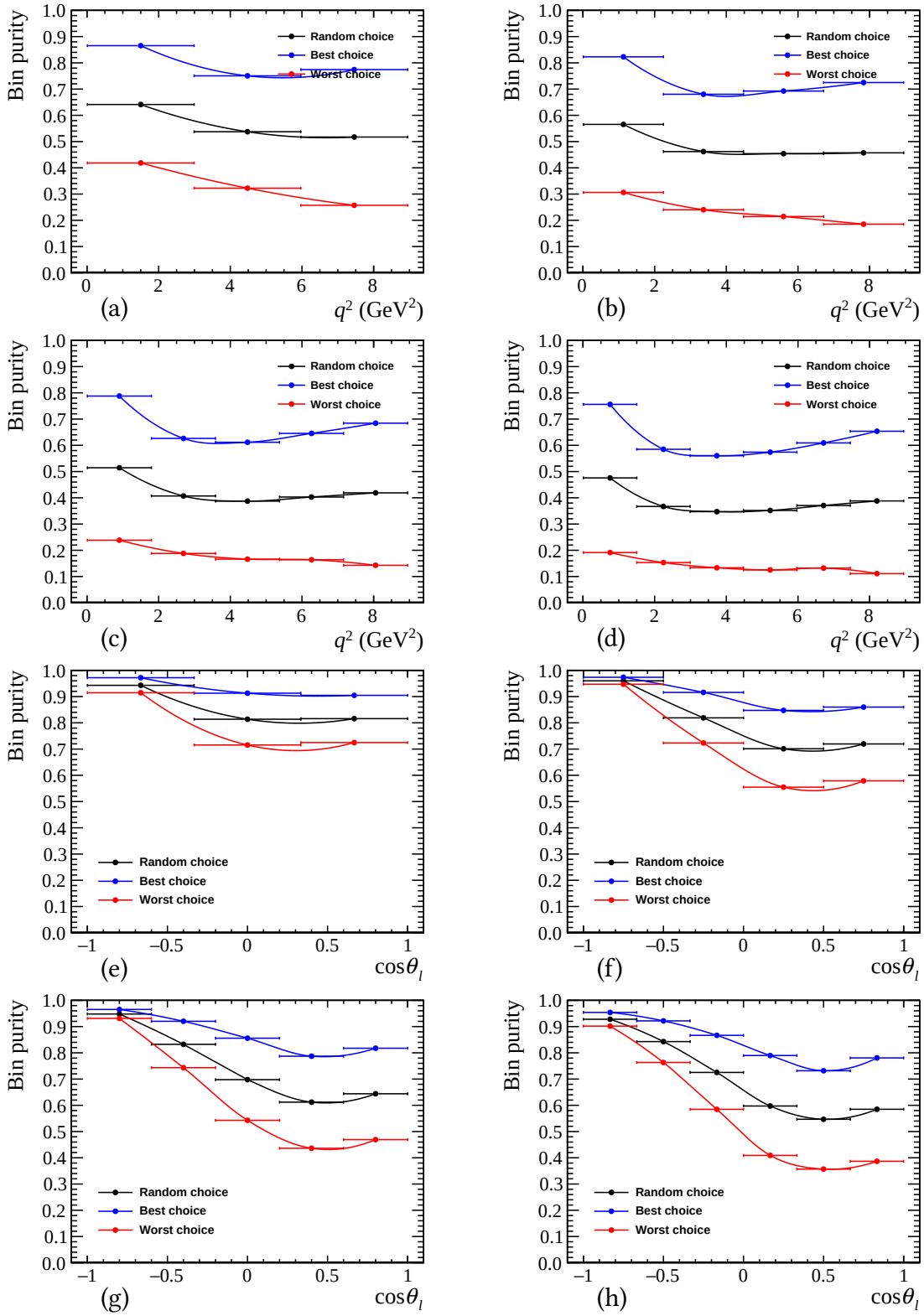

Figure C.3: Purity as a function of q^2 and $\cos\theta_\ell$, defined as the fraction of candidates that belong in a particular kinematic bin, for three to six q^2 bins (a–d) and three to six $\cos\theta_\ell$ bins (e–h).

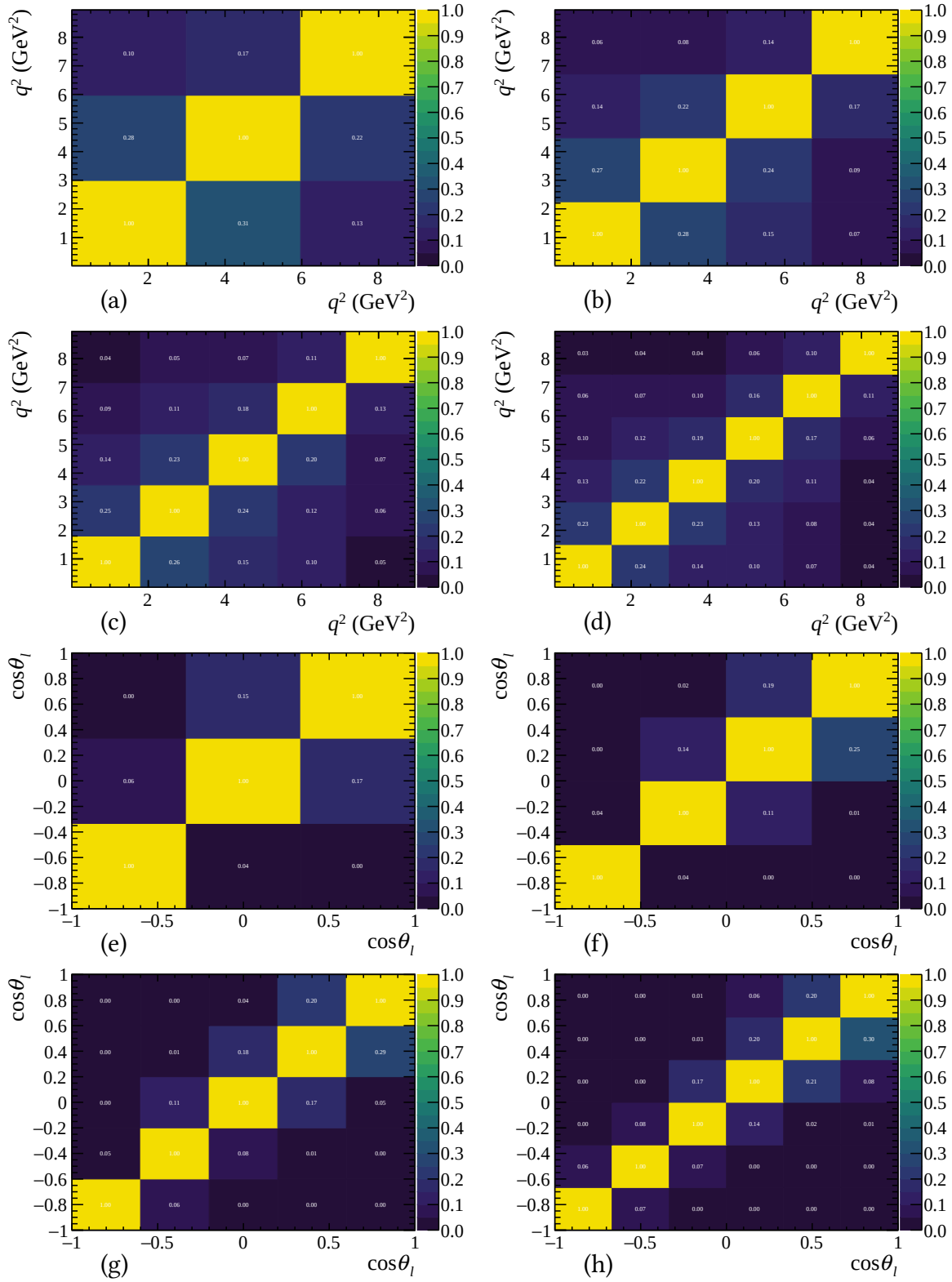

Figure C.4: Correlation between bins of q^2 and $\cos\theta_\ell$, for three to six q^2 bins (a–d) and three to six $\cos\theta_\ell$ bins (e–h).

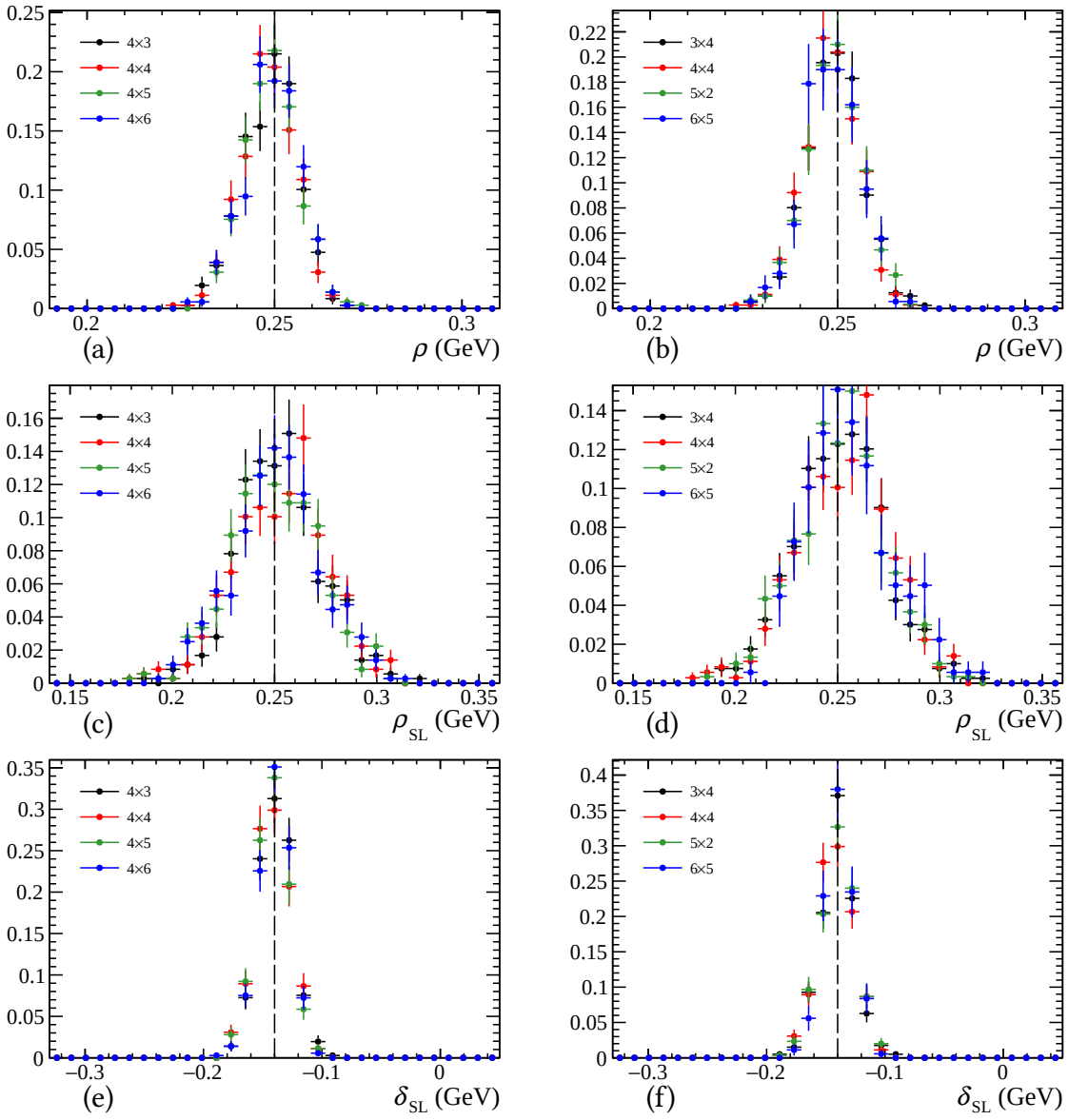

Figure C.5: Isgur-Wise parameters distributions resulting from a two-dimensional fit to both Λ_c^* states. A finer binning in q^2 or $\cos\theta_\ell$ does not improve the precision of the fit.

References

[1] Adam F. Falk. “Hadrons of arbitrary spin in the heavy quark effective theory”. In: *Nucl.Phys.* B378 (1992), pp. 79–94. DOI: 10.1016/0550-3213(92)90004-U.

[2] Böer, Philipp and Bordone, Marzia and Graverini, Elena and Owen, Patrick and Rotondo, Marcello and van Dyk, Danny. “Testing lepton flavour universality in semileptonic $\Lambda_b \to \Lambda_c^*$ decays”. In: *Journal of High Energy Physics* 2018.6 (June 2018), p. 155. ISSN: 1029-8479. DOI: 10.1007/JHEP06(2018)155. arXiv: 1801.08367 [hep-ph]. URL: https://doi.org/10.1007/JHEP06(2018)155.

[3] Matthias Neubert. “Heavy quark symmetry”. In: *Phys. Rept.* 245 (1994), pp. 259–396. DOI: 10.1016/0370-1573(94)90091-4. arXiv: hep-ph/9306320 [hep-ph].

Elena Graverini | Curriculum Vitæ

Compiled on 2018, February 6th, in compliance with the regulations of the University of Zurich

Education

2014–2018 **Ph.D. studies**, *Physik–Institut der Universität Zürich*, Switzerland.
Supervisor: Prof. Dr. Ulrich Straumann
Committee: Prof. Dr. Nicola Serra, Dr. Barbara Storaci, Dr. Olaf Steinkamp
Main research projects:

- Sensitivity to exotic particles and optimization of the SHiP detector
- Performance, alignment and radiation ageing of the LHCb silicon tracker
- Lepton universality tests using semileptonic Λ_b decays at LHCb

2011–2013 **Master's Degree in Physics**, *University of Pisa*, Italy, 110/110 cum laude.
Specialized in Physics of the Fundamental Interactions
Thesis title: *A GPU-based real time trigger for rare kaon decays at NA62*
Supervisor: Prof. Dr. Marco Sozzi

2007–2011 **Bachelor's Degree in Physics and Advanced Technologies**, *University of Siena*, Italy, 107/110.
Thesis title: *A large GEM detector prototype: test-beam results and analysis*
Supervisors: Prof. Dr. Nicola Turini and Dr. Eraldo Oliveri

2002–2007 **Diploma di Maturità Scientifica**, *Liceo Scientifico Francesco Redi*, Arezzo (Italy), 93/100.

Selected Publications

2018 **"Testing lepton flavour universality in semileptonic $\Lambda_b \to \Lambda_c^*$ decays"**, P. Böer, M. Bordone, E. Graverini, P. Owen, M. Rotondo and D. van Dyk., arXiv:1801.08367 [hep-ph].

2015 **"A facility to Search for Hidden Particles (SHiP) at the CERN SPS"**, M. Anelli *et al.* [SHiP Collaboration], arXiv:1504.04956 [physics.ins-det].
134 citations counted in INSPIRE as of 6 February 2018

2015 **"Search for New Physics in SHiP and at future colliders"**, E. Graverini *et al.*, arXiv:1503.08624 [hep-ex], JINST **10**, no. 07, C07007 (2015).
9 citations counted in INSPIRE as of 6 February 2018

2014 **"Search for Heavy Right Handed Neutrinos at the FCC-ee"**, A. Blondel, E. Graverini, N. Serra, M. Shaposhnikov [FCC-ee study Team]., arXiv:1411.5230 [hep-ex], Nucl. Part. Phys. Proc. **273-275**, 1883.
76 citations counted in INSPIRE as of 6 February 2018

2014 **"GPUs for real-time processing in HEP trigger systems"**, G. Lamanna *et al.*., J. Phys. Conf. Ser. **513**, 012017 (2014).

Summary As member of the LHCb and SHiP collaborations since 2014, and former member of the GPU Application Project, as of 6 February 2018 I am author or co-author of **181** papers published in peer-reviewed journals, **9** conference proceedings, **4** CERN notes, one INFN white paper and **19** papers awaiting publication.

Full list `inspirehep.net/author/profile/Elena.Graverini.1`

Talks at Conferences and Seminars

2016, Aug **Rencontres du Vietnam: NuFact**, *Quy Nhon, Vietnam*.
Speaker of the "Heavy neutrino searches from MeV to TeV" plenary review.

2016, Feb **Invited seminar at the Université Libre de Bruxelles**, *Bruxelles, Belgium*.
Seminar about the status and prospects of the SHiP experiment.

2016, Dec **Miami topical conference on elementary particles, astrophysics and cosmology**, *Fort Lauderdale, USA*.
Speaker of the "Semi-tauonic physics at LHCb" plenary talk on behalf of the LHCb collaboration.

2016, Jun **Rencontres de Blois**, *Blois, France*.
Speaker of the "SHiP: a new facility to search for long lived neutral particles and investigate the ν_τ properties" talk on behalf of the SHiP collaboration.

2015, Jul **EPS Conference on High Energy Physics**, *Vienna, Austria*.
Speaker of the "SHiP: a new facility with a dedicated detector to search for new long-lived neutral particles" talk on behalf of the SHiP collaboration.

Complementary education

2017, May **School of Statistics**, *Istituto Nazionale di Fisica Nucleare (INFN)*.

2017, Mar **Inverted CERN School of Computing**, *CERN*.

2016, Jun **XIII Seminar on Software for Nuclear, Subnuclear and Applied Physics**, *Istituto Nazionale di Fisica Nucleare (INFN)*.

2016, Feb **Heavy Flavour Data Mining Workshop**, *University of Zurich*.

2015, Jan **CHIPP PhD Winter School**, *Swiss Institute for Particle Physics (CHIPP)*.

2014, Jul **Intelligent Signal Processing for Frontier Research and Industry (INFIERI)**, *Université Paris Diderot*, FP7 European ITN project.

2012, Jul **Hadron Collider Summer School (HASCO)**, *Georg-August-Universität Göttingen*.

2011, Feb **Network Theory and Complexity**, *University of Siena*, PhD course in Chemistry.

2010, Mar **Challenges of astronomy and modern astrobiology**, *Siena Biotech and University of Siena*, Master's Degree course in Pharmaceutical Biotechnology.

2010, Jan **EXOWORKSHOP: research techniques for extrasolar planets**, *University of Siena*.

2009, Apr–Jun **Econophysics**, *Scuola Superiore Santa Chiara and University of Siena*, Multidisciplinary program *"Physics and Complex Systems"*.

Teaching experience

2014–2016 **Teaching Assistant**, *Physik–Institut der Universität Zürich (UZH)*, Zürich (CH).
- Excercise sessions for the course "Statistics and Data Analysis" (2014–2016)
- Design of a web-based homework platform for the course "Statistics and Data Analysis" (2015)
- Laboratory sessions for Physics majors (2014)

2016, Aug **Academic assistant**, *International Physics Olympiads (IPhO 2016)*, Zürich (CH).

Research stays

2012, Aug–Sep **Internship at Fermilab**, *Fermi Research Alliance*, Batavia (USA).
Microstrip silicon detectors R&D for the CMS inner tracker upgrade campaign.

2011, Aug **Internship at CERN**, *CERN*, Génève (CH).
Characterization of two detectors of the GEM tracker for the TOTEM experiment.

2010, Aug–Sep **Internship at CERN**, *CERN*, Génève (CH).
Characterization of a new GEM particle detector on behalf of the Gas Detector Development group of the RD51 collaboration and of the TOTEM experiment.

2008–2009 **Apprenticeship at the Astronomical Observatory**, *University of Siena*, Siena (IT).
Acquisition, calibration and photometric analysis of CCD images from astrophysical sources.

Languages

Italian	Mother tongue	
English	Proficient	*Fluent speaking, excellent reading / writing skills*
French	Advanced	*Good spoken interaction, fluent reading / writing skills*
German	Basic	*A1 basic skills*